Bioengineered Scaffold Microenvironment Promotes Assembly and Differentiation of Stem Cell-Derived Human Organoids

by

Richard L. Youngblood

A dissertation submitted in partial fulfillment
of the requirements for the degree of
Doctor of Philosophy
(Biomedical Engineering)
in The University of Michigan
2020

Doctoral Committee:

Professor Lonnie D. Shea, Chair
Assistant Professor Corentin Cras-Méneur
Professor David Kohn
Associate Professor Ariella Shikanov

Richard L. Youngblood

youngblr@umich.edu

ORCID iD: 0000-0003-4333-6199

Dedication

Dedicated to the memory of my granddad, Lloyd Youngblood, who always believed in my ability to be successful in the academic arena. You are gone but your belief in me has made this journey possible.

Acknowledgements

Firstly, I wish to express my sincere appreciation to my advisor, Dr. Lonnie Shea, for the continuous support of my Ph.D. study and related research as well as for his patience, motivation, and immense knowledge. His mentorship helped me get through my toughest times of research and writing of this thesis. He also showed me the importance of work life balance by insisting I make it to his weekly 7am basketball games. I could not have imagined having a better advisor and mentor for my Ph.D. study.

In addition to my advisor, I would like to thank the rest of my thesis committee: Dr. David Kohn, Dr. Ariella Shikanov and Dr. Corentin Cras-Méneur, for their helpful comments and encouragement, but also for their insightful questions which motivated me to widen my research from various perspectives. I also thank my fellow lab mates, specifically the Glucose Gang, for the stimulating discussions, for the sleepless nights working together before deadlines, and for all the fun we have had in the last five years.

I would also like to acknowledge my funding sources, which included a training grant for Cellular Biotechnology and Organogenesis from the National Institute of Health and various other training grants that provided funding during my graduate education.

Last but not the least, I wish to acknowledge the support and great love from my parents, sister, and grandparents. They have continually provided their moral, emotional and financial support. Thank you! I also dedicate my work to my partner, Daniella, who has been extremely supportive of me throughout this entire process and has made countless sacrifices to help me get to this point. Thank you for your wisdom, patience, and great editing skills.

Table of Contents

Page

List of Figures

List of Tables

Abstract

Human pluripotent stem cells (hPSCs) differentiated into complex three-dimensional (3D) structures, referred to as 'organoids' due to their organ-like properties, offer ideal platforms to study human development, disease and regeneration. However, studying organ morphogenesis has been hindered by the lack of appropriate culture systems that can spatially enable cellular interactions that are needed for organ formation. Many organoid cultures rely on decellularized extracellular matrices as supportive scaffolds, which are often poorly chemically defined and allow only limited tunability and reproducibility. By contrast, engineered synthetic matrices can be tuned and optimized to mimic the embryo environment in order to enhance development and maturation of organoid cultures. Herein, this dissertation primarily focuses on testing the hypothesis that using synthetic microporous polymer matrices can guide key interactions guiding stem-cell decisions for the reproducible generation and control of organoid cultures. One study showed microporous synthetic biomaterials can guide the assembly of pancreatic progenitors into insulin-producing clusters that further developed into islet organoids. Immunofluorescent analysis showed the scaffold culture facilitated cell-cell interactions by significantly increasing protein expression of ECAD compared to suspension (42 ± 5% vs 21 ± 4% of total cell population, n=4; $P<0.01$). PLG scaffold cultures supported cell-mediated matrix deposition of extracellular matrix (ECM) proteins associated with the basement membrane of islet cells as well. Furthermore, hPSC-derived β-cells cultured on the PLG scaffold showed an enhanced insulin secretion index compared to the suspension culture control (1.3 ± 0.2 vs 0.43 ± 0.06, n=3, $P<0.01$), indicating the development of functional β-cells. By modifying the stage that cells were seeded on scaffolds from pancreatic progenitor to pancreatic endoderm,

islet organoids showed increased amounts of insulin secreted per cell. In addition, seeding scaffolds with dense clusters instead of a single suspension minimized cell manipulation during the differentiation, which was shown to be influential to the development of the islet organoids. An engineered insulin reporter further identified how mechanistic changes *in vitro* influenced function within individual cells by measuring insulin storage and secretion through non-invasive imaging. Human lung organoids (HLOs) were also evaluated for *in vivo* maturation on biomaterial scaffolds, where HLOs were shown improved tissue structure and cellular differentiation. We sought to examine the contribution of polymer degradation to the number of airway-like structures with the hypothesis that faster degradation would permit more HLOs fusing in adjacent pores, thus, support larger airway-like structures. Investigative studies demonstrated slower degrading 85:15 PLG HLOs had significantly smaller airway diameter than the faster degrading 75:25 PLG (224 μm vs. 333 μm, $P<0.05$) confirming that scaffold pore interconnectivity and polymer degradation contributed to *in vivo* maturation. Polymer biomaterials were also developed to modulate local tissue and systemic inflammation through local delivery of human interleukin 4 (hIL-4)-expressing lentivirus. Microporous scaffold culture strategies improve organoid complexity and exert fine control over the system using engineering solutions, thus, allowing the community to build more realistic organoid tools. Taken together, the microporous scaffold culture has the feasibility to translate organoid culture to the clinic as a biomanufacturing platform.

Chapter 1: General Introduction

1.1 Motivation and objective

Regenerative medicine has the potential to cure untreatable illness by replacing dysfunctional organs damaged by disease, age or trauma. Being able to develop human tissue in a dish, from its early development to its organogenesis or adult stage, would be a key breakthrough in modern biology. Two dimensional (2D) monolayer cultures are prevalent in cell-based molecular investigations, however, 2D cultures often fail to capture the complexity within native three dimensional tissues[1–3]. Significant drawbacks in these systems include an inability to achieve *in vivo*-like cell-cell adhesions[4], considerable differences in gene expression profiles[5]and cellular morphologies[6], marginal nutrient and metabolite gradients[7], and an absence of extracellular matrix (ECM) interactions[8]. In order to attend to these problems, three dimensional (3D) cellular models[9] have been proposed and developed in diverse fields of developmental/embryonic biology[10], drug discovery[11], and regenerative medicine[12]. Of these models, development of multicellular three-dimensional organoids that closely mimic the native structure and function of organs has received a large focus.

The tissue engineering triad for organoid development comprises a combination of cells, scaffolds, and biologically active molecules[13]. Scaffolds are three-dimensional constructs with the prime function of being able to mimic the physico-chemical properties of the natural ECM[13]. In addition to structural stability, the ECM has been shown to provide tissue-specific biophysical and biochemical cues that are required for tissue neogenesis and homeostasis. As one of the crucial players of the microenvironment, the extracellular matrix is a dynamic ensemble of proteins and proteoglycans, which surround cells, provide anchoring sites, and control growth

factor signaling[14–17]. While the influence of soluble molecules and growth factors on cell fate is very well understood, our knowledge of the impact of the physicochemical properties of the extracellular matrix is only just beginning to emerge.

Scaffold-based platforms can play a valuable role in advancing our knowledge of the role of ECM in regulating various cellular functions. Our synthetic polymer scaffolds can provide a tunable niche, as their material properties can be tailored to mimic those of native tissues. Investigating the influence of an artificial ECM can help evaluate what complex and dynamic roles the ECM plays during organogenesis. In addition, when organoids are destined for transplantation, they should preferably be able to establish a functional niche during culture *in vitro*, and then continue proper engraftment *in vivo*. To avoid the need of disrupting cell-matrix interactions established *in vitro*, and to maintain physical support against hemodynamic shear stress, it is preferable that the matrix used for *in vitro* culture can also be transplanted together with the organoid to promote functional maturation at the ectopic site. Furthermore, the synthetic scaffolds have the potential to be functionalized to present factors that can promote cell survival and function.

Investigating the influence of a supportive matrix using scaffolds can provide new insights for a variety of tissue engineering applications being developed to treat diseases, like diabetes. Type 1 diabetes (T1DM) affects one in every 400 children and, approximately, 1.5M people in the US[18]. Pancreatic islet transplantation has emerged as a promising therapy for T1DM[19,20]. Despite impressive initial improvements in metabolic control, few islet transplant patients maintain long term insulin independence[21,22]. Furthermore, islet transplantation therapy is limited by an inadequate supply of donor islets, a problem worsened by islet loss post-transplantation. Thus, the field has turned to human pluripotent stem cells (hPSCs) as an alternative source to generate a limitless supply of islets due to their ability to self-renew and differentiate. While multiple protocols for differentiating hPSCs into insulin-producing cells have been established[23–25], these traditional culture systems can generate heterogenous populations consisting of

polyhormonal endocrine cells in addition to monohormonal β-cells. Moreover, the development of hPSCs to mature glucose-responsive, insulin-secreting β-cells is inconsistent, and not all transplant recipients return to normoglycemia[24,26]. During pancreatic development, the progenitors congregate into structures called islets that are surrounded by a dynamic, supportive extracellular matrix[27–30]. The microporous scaffold provides a 3D environment that physiological represents the architecture of the native islet environment compared to traditional culture systems, like air-liquid interfaces or suspension flasks. Thus, one objective of this research is to develop microporous scaffolds that support the differentiation of hPSC-derived pancreatic progenitor cells into 3D islet-like structures, which will lead to maturation of glucose-responsive insulin-producing β-cells.

This research can also be applied to intestinal organoid models derived from hPSCs, which have been one of the pioneering organoid models in the field[31–36]. Intestinal organoids have been used to model infectious diseases that are specific to the intestine[37–40]. Matrigel is the most common matrix used for the culture and transplantation of intestinal organoids, however this 3D matrix is derived from mouse tumor basement membrane and consists of extracellular matrix proteins and undefined growth factors[41]. Since Matrigel contains undefined materials and may have tumorigenic affects, it cannot be easily translated into the clinic. Also, the properties of Matrigel cannot be easily modified. For these reasons, another objective of this research is to define a scaffold matrix comprised of synthetic polymer materials suitable for *in vivo* intestinal organoid maturation. Scaffold technologies can also be paired with existing immunosuppressive therapies, or with emerging tolerance therapies to prevent rejection. In order to translate this technology, scaffolds should be designed offer the necessary signals to achieve the goal of regenerating complex tissues that can fully integrate with the host. Thus, our last objective is focused on demonstrating that polymer biomaterials implanted into adipose tissue have the potential to modulate local tissue and systemic inflammation and metabolism to regulate immune tolerance. It is in this context that the work presented in this thesis is concerned.

1.2 Thesis Outline

The cell culture system microenvironment can facilitate and/or promote three-dimensional structures and cellular organization by recapitulating the native environment of the tissue both physically and chemically. Biomaterial systems, the focus of this thesis dissertation, were developed to direct the cellular organization and influence the cell phenotype within the organoid cultures. **Chapter 2** is a review article that summarizes the current applications of biologic and synthetic biomaterials utilized for different 3D organoid systems and discusses mechanical and biochemical material properties relevant for tissue formation. In **Chapters 3 and 4**, microporous synthetic scaffolds are designed to develop early-stage islet organoids then investigate their maturational heterogeneity using a novel fluorescent insulin reporter cell line. The *in vitro* differentiation of the pancreatic progenitors to early-stage islet organoids on the scaffolds will be compared to suspension cultures. **Chapter 5** then investigates the physico-chemical properties of microporous scaffolds that influence late-stage human lung organoids to form airway structures *in vivo*. **Chapter 6** focuses on local delivery of immunomodulatory cytokine Il-4 from scaffold implants that can be used to regulate a specific set of immune cells for tolerance induction after organoid transplantation. Finally, in **Chapter 7**, a conclusive summary of the thesis research is provided along with a discussion on future directions and potential challenges that must be addressed before these strategies are tested in humans.

1.3 Significance

Our research will use microporous scaffolds to create a 3D environment for the consistent and efficient differentiation of hPSCs into functional organoids that can help transform cell-based therapies. The 3D environment provided by the scaffolds can be easily changed to recapitulate the native environment to promote the maturation of progenitor cells *in vitro* and *in vivo*. The cells in contact with the material can obtain signals from cell-matrix interactions, while those cells not in contact with the material will receive signals from cell-cell interactions. This organization of cells into a tissue, rather than a collection of cells, would also facilitate direct

transplantation of the scaffold without manipulating the cell within the pores of the scaffold, unlike cell aggregates which are dissociated and reassembled before transplantation. Thus, less manipulation combined with maintaining cell-cell contacts and providing ECM signals is anticipated to improve organoid survival and function post-transplantation. An engineered fluorescent reporter tool provided non-invasive assessments of maturation and function of the organoid cultures, as well. *In vivo*, insights on how the scaffold pore interconnectivity and material degradation rate influences organoid tissue growth and maturation can be utilized to inform future engineered matrices. Scaffold cultures also offer the potential to create controllable environments with the appropriate immunomodulatory cues required to promote tissue viability and function *in vivo*. The biomaterials, thus, provide a tool that may be capable of directing tissue formation from organoids for the purpose of modeling normal development, and for enhancing cell-based therapies.

Chapter 2: Designing Biologic and Synthetic Scaffolds to Guide Stem Cell-Based Organogenesis

2.1 Introduction

Advances in human pluripotent stem cell (hPSC) biology over the past two decades has led to many new and exciting opportunities for engineering human tissue from hPSCs. The ability for hPSCs to self-renew *in vitro* and differentiate into cell types from all three germ layers makes them an attractive source for generating a wide variety of tissues. Continued advancements in differentiation protocols have made it possible to obtain fairly enriched or highly pure populations of hPSC differentiated cell types for tissue engineering constructs, including neurons[42,43], cardiomyocytes[44–46], liver hepatocytes[47,48], and pancreatic endocrine cells[23–25]. In recent years, several examples of various organoids derived from hPSCs provide an alternative strategy for direct engineering of tissues from hPSC sources[49–51]. Functional organoid tissues are inherently comprised of multiple cell populations that interact within and between populations as well as with their extracellular environment to dictate tissue form and function. These heterogenous cell mixtures are organized in three-dimensional arrangements that can cover multiple scales and ultimately work cooperatively together to carry out specific functions.

Organoids are physiologically relevant and can allow the study of biological processes, such as cell behavior, tissue repair and response to drugs or mutations, holding great promise in both basic research and translational therapies. As a result, there are a wide range of applications. In terms of developmental biology, organoids derived from hPSCs that retain features of their developmental stage can help in studying the process of embryonic development[52], lineage specification[53] and tissue homeostasis[54]. This research can also help investigate the development

of stem cells and their niche. Organoids are also suited to study infectious diseases affecting specialized human cell types. Lung organoids derived from iPSCs from a healthy child carrying null alleles of interferon regulatory factor-7 gene were developed to study influenza virus replication[55]. In regards to personalized medicine, organoids derived from hPSCS derived from individual patients could allow ex vivo testing of drug response[56]. Tumor organoids, for example. can be employed to assess the drug response for individual patients.

Despite these significant advances shown by hPSC-derived organoids in different manners, organoids are in an early stage of development and need more robust and dependable culturing practices. Substantial differences that set them apart from their *in vivo* counterparts indicate the need for technologies that improve organoid generation and reliability and that allow the development of key tissue- specific features[57]. Influencing specific stem-cell signaling pathways that drive organoid formation requires a precise niche environment. *In vivo*, the extracellular matrix (ECM) plays a critical role in the development of the complex cellular phenotypes, while abnormal changes within the ECM have been considered a driver of disease[58,59].

Given the essential role that the ECM has in maintaining the physiological stability of the microenvironment and guiding tissue-specific function, biomaterial scaffolds have been designed to mimic this environment in an effort to enhance tissue development.[60] Compared to traditional 2D culture, the novel 3D biomaterial scaffolds create a more satisfactory microenvironment for stem cells by including both chemical and physical signals across the ECM. Based on the design, scaffolds can be used to directly regulate cell signaling and elicit lineage-specific differentiation of stem cells through chemical cues or cell-matrix interactions.[61] Furthermore, the cell adhesion, cell transportation, cell differentiation and matrix organization can be modulated within the scaffold to direct stem cell differentiation. Hence, surface, mechanical, morphological and chemical properties must be precisely considered when designing a new scaffold for *in vitro* stem cell development.

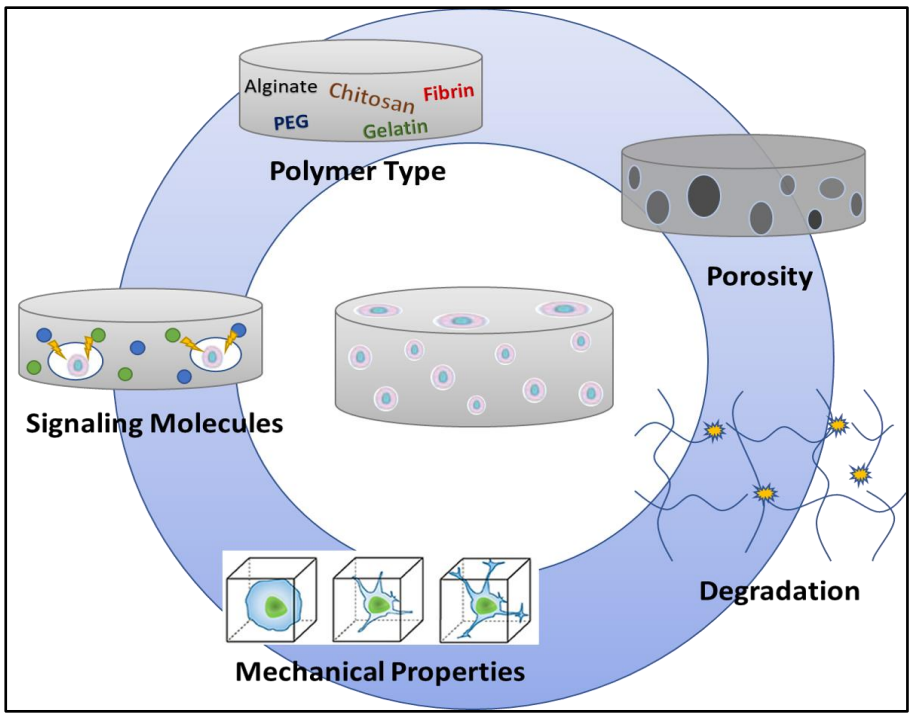

Figure 2.1 *Design considerations*
The hydrogel design for delivery in tissue engineering applications is dictated by the biocompatible polymer type, porosity, mechanical properties, degradability, and signalling factors in the microenvironment.

For transplantation, scaffold designs largely depend on the site of implantation (e.g. tissue type to be repaired or type of stem cell to be delivered). These design parameters can be manipulated to mimic the native ECM and consequently function to promote new tissue formation and stem cell engraftment (**Fig 2.1**)[62,63]. On the most fundamental level, biomaterial scaffolds should define a three-dimensional (3D) space for tissue formation, as the 3D architecture can support the infiltration and assembly of host cells into structures and induce gene expression programs associated with normal growth or development. Cell seeding and infiltration of the scaffold can be facilitated by micron-scale porosity and/or cell-mediated degradation cues introduced into the design. Furthermore, ECM derived adhesion peptides, protein fragments, or native proteins can promote cell adhesion leading to a number of specific cell processes such as vascularization, bone regeneration, or the creation of a tissue-specific niche[64,65]. Trophic factors may also be necessary within the environment to drive cellular responses leading to stem cell differentiation and tissue formation. Finally, tissue engineering

and regenerative medicine may be nearing a tipping point based on recent investments by industry and an increasing number of clinical trials. For translational purposes, the design approach should consider manufacturing issues such as availability, reproducibility, processing strategies and generally the issues that will be needed for FDA regulatory approval and commercial viability.

This section will provide an overview for how to design scaffolds to guide cell development and promote organoid generation. We also discuss the scaffold design parameters that are available to enhance transplanted cell survival and appropriate interactions with the host tissue. We highlight engineered material systems for culturing organoids with the aim to establish organoid cultures as powerful research platforms.

2.2 Scaffold Designs to Promote *In vitro* Organoid Development

The *in vitro* organoid model is a major technological innovation that has quickly become an essential tool in many basic biology and clinical applications. This near-physiological 3D cell culture system facilitates the investigation of a range of *in vivo* biological processes including tissue renewal, stem cell/niche functions and tissue responses to drugs, mutation or damage[66–68]. Organoids offer a valuable bridge between traditional 2D cultures and *in vivo* human models, as they are more physiologically relevant than monolayer culture models and are far more receptive to manipulation of niche components and signaling pathways than *in vivo* models.

Much importance has been placed on the self-organizing nature of hPSC-derived organoids, while the surrounding extracellular environment has been largely regarded as a passive matrix in which a pre-determined cellular program can play out. However, these mini-organs are currently imperfect models, which would suggest that their native tissue counterparts depend on both the self-organizing potential of the stem cells as well as complementary effects from the microenvironment niche to establish complete organization and function.

Biomaterial matrices are often used as a 3D culture environment for organoid development in order to recapitulate the scaffolding support provided by the native ECM tissue.

Both biological and polymeric materials have demonstrated the ability to establish a complex microenvironment for the cells to develop. Hydrogels made of natural biologic materials, like reconstituted decellularized ECM, present sufficient cell adhesive-domains to promote cell attachment and can be remodeled by enzymes expressed in the developing organoid. Alternatively, engineered synthetic matrices are a suitable alternative to conventional organoid culture scaffolds because they provide better tunability, are fully chemically defined and can be easily produced with minimal batch-to-batch variability. Designing the appropriate biomaterial-based strategy is advantageous towards optimizing organoid growth and controlling the geometrical, biomechanical, and biochemical properties of the organoid's three-dimensional environment. We highlight systems that have the potential to develop organoid models suitable for different types of manipulations and high-throughput applications.

2.2.1 Biologic materials utilized for organoid development

The intended function of an *in vitro* organoid system determines the design specifications. Modeling developmental processes in tissues to generate functional organoids dictates that closely mimicking the *in vivo* tissue is a top priority. In that case, recapitulating complex niche components and interactions will be crucial. This niche environment should be designed to permit the cells to mature, remodel their environment and undergo self-directed cell sorting. As the complexity of the native ECM cannot be easily replicated, a growing body of work has examined the use of scaffolds derived from decellularized tissues for stem/progenitor cell culture[69,70]. Biologic scaffold matrices derived from the ECM, like reconstituted decellularized tissue, help provide this complex extracellular microenvironment through the retention of compositional, biomechanical, and structural properties specific to the native ECM. Increasingly, studies have investigated the use of ECM-derived scaffolds as instructive substrates to recapitulate properties of the stem cell niche and guide cell proliferation, paracrine factor production, and differentiation in a tissue-specific manner.

Techniques for tissue decellularization have been reviewed previously[71,72], but commonly include enzymatic, chemical and mechanical steps to destroy antigenic cellular material while preserving the construct and composition of the native ECM as much as possible. In addition to being utilized in their intact form, decellularized tissue can be designed in a variety of modified ECM-derived biomaterial formats including sheets[73], hydrogels[74,75], microcarriers[76], porous foams[77,78], and 3D-printed scaffolds[79]. In order to closely mimic the *in vivo* microenvironment for cell maturation, DeQuach et al. designed a myocardial matrix consisting of a nanofibrous and mesoporous structure with re-assembled nanofibers approximately 40-100nm in diameter[80]. They used this method to generate tissue-specific extracellular matrix coatings by decellularizing skeletal and cardiac tissues. These decellularized matrices facilitated the maturation of committed skeletal myoblast progenitors and hPSC-derived cardiomyocytes in 3D culture. In a similar study by Rajabi-Zeleti et al., 3D microporous scaffolds derived from enzyme-digested decellularized human pericardium were shown to enhance the survival, proliferation, and differentiation of human Sca-1^{+} cardiac progenitor cells in comparison to collagen scaffold controls that had a similar porous structure, as well as intact decellularized pericardium[81].

Tissue-specific ECM provides a good scaffold model for organoid development as they have been widely hypothesized to promote lineage-specific differentiation *in vitro*. Flyn et al. showed that decellularized adipose tissue (DAT) established an adipo-inductive environment for human adipocyte stem cells (ASCs), inducing the expression of the key transcription factors CCAAT/enhancer-binding protein alpha (C/EBPα) and peroxisome proliferator-activated receptor gamma (PPARγ) in the absence of exogenous differentiation factors[82]. They then tested a variety of DAT-based bioscaffolds to confirm that adipose-derived ECM displays both adipo-conductive and adipo-inductive properties by improving the *in vitro* differentiation of human ASCs in adipogenic culture medium and by promoting adipogenic differentiation in proliferation medium that would normally inhibit adipogenesis[83]. Thus, decellularized organ scaffolds have been shown to provide structural cues and ECM components for 3D tissue morphogenesis.

Another commonly used biologic scaffold material is Engelbreth–Holm–Swarm (EHS) matrix, which is a reconstituted basement membrane harvested from mouse sarcoma[84]. The EHS matrix, also known by one of its trade names Matrigel, consists of a mixture of many different ECM components, which provide a complex environment for embedded cells[85]. Matrigel provides a physiologically relevant microenvironment of soluble growth factors, hormones, and other molecules with which cells interact in an *in vivo* environment[86]. Matrigel has been widely used as the gold standard scaffold material to provide 3D cell cultures for a wide range of cell types. To generate cerebral organoids, studies have used Matrigel to demonstrate the feasibility to derive complicated tissue patterns through a process involving dynamic patterning and structure self-organization in 3D hPSC culture[52,57,87]. Recently, Sasai and colleagues recapitulated aspects of eye development *in vitro* by culturing aggregates of mouse embryonic stem cells (ESCs) in Matrigel and minimal growth factors[87]. Their studies showed that mouse ESCs were able to self-organize into a bilayered optic cup-like structure when cultured in 3D. Beyond the morphological similarities, the outer and inner layers expressed retinal pigment epithelial (RPE) and neural retina (NR) markers, respectively, indicating that cell differentiation followed that of the developing retina *in vivo.* Using a similar approach, they have also generated distinct cortical neurons[88]. These studies have laid the groundwork to organogenesis that may be used for therapy of patients with neuronal disorders. The organoids can also function as an *in vitro* model to understand the intricacies of brain function in a culture dish.

In vivo, a variety of extracellular matrices provides support for epithelia and significantly influence epithelial and stem cell behavior. It is therefore not surprising that the choice of extracellular matrices in three-dimensional intestinal organoid culture systems matters a great deal[89]. Sato et al. showed the self-renewal and differentiation of Lgr5 intestinal stem cells (ISCs) is cooperatively controlled by signals from the underlining mesenchyme matrix as well as cells in the epithelium, specifically Paneth cells (e.g., Notch and Wnt signals)[90]. Thus, isolated ISCs were cultured in Matrigel along with medium conditions that permitted the self-renewal and

differentiation of the stem cells, followed by self-organization of the generated cells, which collectively led to the establishment of intestinal organoids. Ultimately, there studies found Matrigel to be indispensable for epithelial organoid culture.

While Matrigel has provided key insights for the influence of a 3D scaffold matrix on organoid development, the disadvantages associated with Matrigel are commonly occurring lot-to-lot variability during manufacturing and the complexity in composition, which are often ill-defined, making it difficult to determine exactly which signals are promoting cell function. The mouse tumor basement membrane-derived matrix might not be ideal for cell therapy and drug screening applications also because of regulatory issues (animal product). Other natural gels such as fibrin, hyaluronic acid, chitosan, alginate, or silk fibrils have also been used for 3D cell culture; however, these natural gels have less versatility to promote 3D culture than Matrigel.

2.2.2 Synthetic polymeric matrices developed for in vitro organoid culture

The ECM used in stem cell-derived organoid cultures is in most cases a 'one-size-fits-all' type of matrix: physicochemical properties cannot be controlled to accommodate dynamic tissue-specific needs, nor can the course of the morphogenetic processes be manipulated. Thus, researchers have started to utilize synthetic ECMs, with compositions that can be customized to reflect organ-to-organ microenvironmental variations. This synthetic matrix could provide better control of vital cell niche cues to direct stem cell fate decisions within organoids during their formation, thus steering the overall development of the organoid at will.

As an alternative to biologic scaffolds, vital signals from native ECMs can be incorporated into synthetic polymer matrices with specifically tailored compositions. PEG hydrogels, a class of synthetic biomaterial scaffolds, are highly hydrated crosslinked polymer networks that have been constructed for a wide range of applications[91–94]. Several key characteristics of PEG hydrogels make them particularly well suited for mimicking the extracellular matrix, namely their biocompatibility[95–97]; their permeability to oxygen, nutrient growth factors, and metabolic

waste[98,99]; their tunable mechanical properties[100–102]; and their tissue-like viscoelastic characteristics[103,104]. This tunable design allows for engineered biomaterials to present features similar to the natural ECM, like a multitude of cell-adhesive ligands. Peptides, like the fibronectin-derived peptide sequence RGD[105], the collagen-derived peptide GFOGER[106] or the laminin-derived peptides IKVAV[107] and YIGSR[108], can be incorporated into synthetic biomaterials to provide cell-adhesive ligands and to influence cell phenotype. The concentration[109], spacing[110,111], patterning[112,113] and timing of ligand presentation[114] all impact the behavior of cultured cells. For example, RGD ligands that are presented as pendant groups from a PEG matrix lead to statistically significant improvements in MSC viability compared with RGD peptides that are confined within the matrix[115]. In another study, the MSCs required RGD for survival early during 3D culture on PEG scaffolds; however, the removal of RGD ligands at later time points did not cause a decrease in viability[114].

Signaling proteins can be engineered into the synthetic scaffolds as well to render these otherwise bioinert environments permissive to biological processes, like degradation and matrix remodeling. This process occurs via chemical/enzymatic crosslinking through adhesive or proteolytically cleavable sites. For example, cross-linking PEG with cell-signaling components and oligopeptides that are susceptible to proteolytic degradation endows the resulting 3D scaffold with biofunctionality, making it permissive to cell migration, proliferation and tissue morphogenesis[116]. Cruz-Acuña et al. prepared hydrogels for growing human intestinal organoids using 4-armed PEG-maleimide (PEG-MAL) monomers containing bioactive ligands (e.g., laminin and RGD) that were then cross-linked with dithiol (bis-cysteine) protease-degradable peptides[117]. For investigating organoid growth within these hydrogels, spheroids were encapsulated in situ during the hydrogel synthesis, and the organoid's survival and development were systematically evaluated in a variety of hydrogels with different biochemical and mechanical properties. Hydrogels with low polymer concentration resembling the mechanical properties of Matrigel showed high organoid viability[117]. This was also observed in gels with degradable cross-linkers

and RGD adhesive peptides. The organoid viability achieved with the optimized materials was comparable to that using Matrigel, while organoid formation was strongly dependent on the mechanical properties of the scaffold material. Similarly, enzymatically formed hydrogels were used to demonstrate the importance of the hydrogel stiffness on the expansion of intestinal stem cells and organoid formation by the Lutolf laboratory[31]. While more rigid scaffolds (G′ = 1.3 kPa) encouraged the expansion of stem cells as shown by the activation of mechano-sensitive yes-associated protein 1 (YAP), softer hydrogels (190 Pa) were more suitable for organoid growth, highlighting the influence of the 3D microenvironment during organoid formation. By tethering microenvironmental signals such as ECM components, soluble factors, and cell-cell interaction proteins to discrete locations, an array of artificial scaffolds can be generated to support organoid cultures[118,119].

While these defined synthetic matrices offer the means to control organoid formation, current scaffold systems have largely focused on control over the bulk properties and have not provided spatiotemporal control over local mechanical cues or signaling gradients. Interestingly, a recent study used bioengineered scaffolds to provide controlled positional information to guide the formation of human brain organoids[120]. Fiber microfilaments comprised of poly(lactide-co-glycolide) (PLGA) were used as floating constructs to pattern embryoid bodies from hPSCs. This strategy facilitated the shaping of brain organoids from the inside at an early stage. They also found that by increasing the surface-area-to-volume ratio with these microfilament scaffolds, reproducible induction of neuroectoderm from micropatterned embryoid bodies was observed. Another study focused on generating extrahepatic cholangiocyte organoids (ECOs) to generate biliary tissue suitable for surgical reconstruction and found that organoids seeded on biodegradable polyglycolic acid (PGA) scaffolds formed tissue-like structures retaining biliary characteristics[121]. PGA is one of the most widely used synthetic polymers because it does not induce inflammatory responses in surrounding tissue, is biodegradable, and is more flexible and easier to process than natural polymers[122]. ECOs were seeded on PGA scaffolds where they

attached to the PGA fibers within 48 h and continued to grow for 4 weeks until they reached confluency. The cells populating the scaffolds retained expression of biliary markers such as CK7 and CK19, demonstrated no evidence of EMT, and maintained their functional properties. Thus, PGA scaffolds were shown to guide ECOs formation towards a bioengineered tissue resembling the biliary epithelium. These studies demonstrate the potential for bioengineered synthetic constructs to guide and control organoid self-assembly.

Similar to biologic scaffolds, the structure of the synthetic scaffold is another major design consideration for 3D organoid culture. Scaffold structures can be designed using a variety of techniques, such as 3D printing[123], particulate leaching[124], or electrospinning[125]. Alternative approaches include gas foaming, fiber meshes/fiber bonding, phase separation, melt molding, emulsion freeze drying, solution casting, or freeze drying[126]. These fabrication techniques are utilized based on what structure is needed for the 3D scaffold culture. For example, electrospinning is generally used for fabricating fibrous scaffolds whereas particulate leaching or solution casting can be used to create porous scaffolds and 3D printing produces scaffolds with a more defined shape and geometry. Of note, cells grown on fibrous scaffolds typically adhere and elongate along the fibers, which means they are often not considered to truly represent 3D culture[127].

A challenge that comes with the prefabricated design of porous scaffolds is uniformly distributing cells throughout the scaffold to promote effective regeneration of highly intricate tissues. While encapsulation strategies allow for cells to be uniformly distributed during initial fabrication, microporous hydrogel designs with a tunnel-like network could diminish the ability to achieve heterogeneous cell distribution. Several seeding techniques have been established to improve uniform cell distribution, but many are lengthy and restrict clinical applicability[128,129]. The most common method for seeding microporous scaffolds is static seeding, in which a concentrated cell suspension is passively introduced on a scaffold. This technique, however, has several limitations that result in low seeding efficiency and poor cell penetration.[130]

To improve cell seeding efficiency, Tokatlian et al. utilized a two-phase hydrogel technique where μ-pore 3.5% hyaluronic (HA) hydrogels were formed and then seeded with mouse MSCs mixed into a thin 2.5% nano-pore HA-MMP hydrogel precursor solution[131]. Due to the fluid nature of the precursor solution initially at room temperature, the gel solution flows throughout the pores of the porous hydrogel and distributes the cells uniformly. In sharp contrast to the classical approach of seeding cells on a preformed hydrogel, 3D bioprinting can simultaneously seed cells while fabricating the hydrogel to produce highly organized cellular constructs[132]. This strategy helps to overcome obstacles derived from low cell densities, uncontrollable seeding positions and a heterogenous distribution of cells throughout the scaffold. Kolesky et al. recently demonstrated a new bioprinting method using cell-laden GelMA inks as a bioprintable bulk matrix to build vascularized heterogeneous tissue constructs[133]. These 3D microengineered systems consisting of vasculature, multiple types of cells, and extracellular matrix are able to generate an environment for cell adhesion, remodeling, and migration.

Clearly, organoid cultures on scaffolds represent a valuable approach to achieve tissue and organ morphogenesis *in vitro*. Strategies using 3D matrices to help organize stem cell cultures will provide critical information about dynamic local interactions during emergent organogenesis, in a complementary manner to *in vivo* studies. With continued efforts focused on developing efficient protocols for hPSC expansion, differentiation, maturation, and 3D cultures on scaffolds, organogenesis can be an emerging resource for tissue replacement. One of the major challenges at this current stage is that this integrated approach requires a comprehensive understanding of spatial-temporal signaling networks to engineer optimal 3D environmental cues that efficiently regulate stem cell fate commitments.

2.3 Scaffolds as Vehicles for Cell Delivery

Tissue regeneration following disease or injury may require exogenous inputs to augment natural healing programs and suppress inhibitory processes. The delivery of cells has most typically involved the injection of high-density cell suspensions into the target diseased or injured

site. However, such direct cell injection methods often have a poor therapeutic response due to a rapid decrease in cell viability, low or modest engraftment of transplanted cells, and limited control over cell fate due to the local environment[134,135]. The delivery of transplanted cells in a scaffold comprised of biocompatible materials addresses these limitations by initially providing protection to the transplanted cells that can enhance survival and prolong retention at the site[136]. Moreover, scaffolds can often have physical properties that are similar to the native extracellular matrix, such as their mechanical properties and water content[137]. This mimicry of the niche environment can have a considerable impact on cell fate by influencing the morphology, viability, differentiation, and function[138,139]. The two main strategies in utilizing scaffolds for cell transplantation are non-integrating approaches that isolate cells from the host tissue through encapsulation within the hydrogel and integrating approaches that allow for the transplanted cells to directly contact host tissue either immediately through a microporous design or over time through biodegradation[140]. Several examples of systems designed for delivering cells in a range of regenerative medicine applications are listed in **Table 2.1**. The number of systems investigated in pre-clinical models is large and cannot be listed exhaustively, thus, we have focused on relatively recent publications that are approaching large animal or clinical translation. This section will discuss considerations in these scaffold designs related to the survival of transplanted cells as well as their ultimate function.

Table 2.1 Cell Delivery Applications In Natural and Synthetic Hydrogels

	Hydrogel Material(s)	Cells Delivered	Delivery Strategy	Target Application	*Ref*
Encapsulated Hydrogels	Alginate	Pancreatic Islets	Laparoscopic implant of microcapsules	Diabetes	141
		Adipose-derived and Mesenchymal stem cells	Injection co-delivered with BMP-2	Bone regeneration	142
		CAR-programmed T cells	implanted into the peritoneal or tumor resection cavity	Cancer	143
	Polyethylene Glycol and Alginate	Ovarian follicles	Encapsulated scaffold	Ovarian Function	144
Tissue-Integrating Microporous Hydrogels	Gelatin	Adipose-derived Stromal Cells	microporous microribbon hydrogel injected into cranial defect	Bone Regeneration	145
	Collagen	Autogenous chondrocytes	Porous scaffold matrix	Cartilage Repair	146
	Alginate	Mesenchymal stem cells	Injectable, void-forming microporous hydrogel	Bone Regeneration	147
Biodegradable Hydrogels	Collagen	iPSC-derived hepatocytes and endothelial cells	Encapsulated polyelectrolyte fiber scaffold transplanted into liver	Liver Tissue Regeneration	148
		neonatal astroglial cells	Transplanted gel into lesion of spinal cord	Spinal Cord Regeneration	149
	Hyaluronic Acid	Cardiac Progenitor Cells	Subcutaneous injection	Angiogenesis	150
		Neural progenitor cells	Injection into stroke cavity	Neural regeneration from stroke	151
	Gelatin	Cardiac-derived stem cells	intra-myocardial injection with the controlled release of bFGF	Cardiac regeneration	152
	Polyethylene Glycol with degradable peptide crosslinker	Adipose-derived stem cells	In-situ injection with encapsulated siRNA	Bone regeneration	153
		iPSC-derived endothelial cells	Injection co-delivered with VEGF	Muscle Repair	154
	Fibronectin and Agarose	Cardiac stem cells	In-situ injection	Cardiac regeneration	155
	Fibrin	Human embryonic stem cells	Epicardial Delivery of Encapsulating Gel	Cardiac regeneration	156
		adipose-derived mesenchymal stromal cells	Patch applied to surface of skin	Wound Healing	157

2.3.1 Cell Delivery in Encapsulating Scaffold Biomaterials

The key role of an encapsulation device is to create an environment that allows for normal cell function, while acting as an immune-regulatory barrier through isolation or modulation of the local area for better survival of the transplanted cells[158–162]. This function can be manipulated by the structure as well as material composition[140]. A common encapsulation approach is illustrated by the TheraCyte Device, which has a porous vascularizing outer membrane that promotes tissue integration and an inner impermeable, membrane that protects the transplanted allogeneic islets.[54] Neonatal pancreatic tissue was implanted in non-obese diabetic mice, survived and had a response to glucose levels for at least 50 days[164]. While this original device was not successful in clinical trials, the general strategy has evolved over the course of several companies, including Living Cell Technologies, Beta Logics, Viacyte, and Encaptra. This Encaptra device consists of a single membrane that is immunoisolating while permitting oxygen and nutrients to pass. ViaCyte is currently carrying out a phase I/II clinical trial using this device with stem cell-derived cell sources to assess the safety and efficacy in humans[165]. Other encapsulation devices that have reached clinical trials have been recently reviewed in detail[166]. While these devices provide a clinically translational design for encapsulation delivery, they are still limited in their ability to provide enhanced transport and more tunable properties. For example, in a hydrogel, adhesion sites and biomechanical properties can be manipulated within the gel to enhance cell viability and therapeutic efficacy. Scaffolds are now being developed that utilize the foundational delivery approach provided by the TheraCyte design while offering tunable properties for not only the exterior but the interior of the device to enhance cell motility, viability, and function.

Alginate is a natural polymer derived from algae that has been extensively investigated for cell encapsulation due to its biocompatibility, low toxicity, relatively low cost, and mild gelation by addition of divalent cations such as Ca^{2+} [167–169]. Alginate can also be modified to improve cell attachment and motility. A double-layered alginate hydrogel system consisting of matrix-metalloproteinases and RGD peptide in the inner layer was designed to allow transplanted stem

cells to proliferate and mobilize to the outer layer following the inflammatory storm caused from surgery[170]. Following transplantation of neural stem cells (NSCs) into a rat brain trauma model, the double-layered alginate hydrogel promoted survival and differentiation of the NSCs. This overall approach focused on NSCs, which have a reduced risk of teratoma formation compared to hESCs and iPSCs, but the design could be easily adapted to other types of transplanted cells. Alginate-based biomaterials have had great success in rodent models; however, the translation to larger animal models such as monkeys and humans have not been immediate successes[171]. Although there were no detectable inflammatory responses in human blood[63,64], the limited efficacy of two clinical transplantations of human islets in barium-alginate and calcium/barium-alginate spheres has been partially attributed to a foreign body response after transplantation.[65,66] Recently, fibrosis has been reported to be reduced or eliminated based on the diameter of the spheres [176]. Alternatively, alginate has been functionalized with a range of chemical groups in order to screen for chemistries that would avoid a fibrotic response[177,178]. Vegas et al. recently identified chemically-modified alginates such as triazole-thiomorphiline dioxide (TMTD) as scaffolds that resisted fibrosis around the implant in both rodents and non-human primates[179]. The TMTD alginate scaffold was then used to transplant hPSC-derived β-cells into immune-competent STZ-treated C57BL/6J diabetic mice. The scaffold showed no observable foreign body response and supported the engraftment and long-term glycemic correction (174 days with the mice still euglycemic at the end of the experiment) from hPSC-derived β-cells in immune-competent mice[180]. These results lay the groundwork for studies in autoimmune animal models and future human studies using formulations that overcome the immunological barrier inhibiting long-term cell function.

Materials derived from natural polymers have had a long history as scaffold delivery devices, however, synthetic polymers have become a popular substitute since they provide a more clinically translatable model and more reproducible properties. For these purposes, non-degradable polyethylene glycol (PEG) hydrogels have been widely used for encapsulation. Also,

PEG's tunable viscoelastic properties provide a tissue-like permeable membrane with minimal inflammatory response. By applying a conformal coating around islets consisting of PEG and Matrigel, Manzoli et al. demonstrated a strategy for long-term reversal of diabetes with allogeneic islets transplanted in the epidydimal fat pad in mice [181]. The incorporation of Matrigel into the PEG coating provided supportive ECM interactions while keeping the permselectivity low, which resulted in a lack of immune cell penetration and T cell allogeneic priming. In addition to biocompatibility, PEG-based hydrogels are also utilized for their structural support[182] and ease of functionalization[183]. Studies focused on artificial ovarian tissue delivery have shown encapsulated immature ovarian follicles in PEG-RGD hydrogels can enhance primordial follicle development and graft survival compared to non-encapsulated follicles[184]. After a subcutaneous transplant of encapsulated ovarian tissue, ovariectomized adult mice showed restoration of the estrous cycle within two weeks. In contrast to islets, ovarian follicles are avascular and relatively resistant to hypoxia, allowing them to maximize the benefits of immunoisolation methods.

For cells that are more dependent on graft vascularization, a PEG hydrogel was designed using lithography techniques in order to develop an encapsulating gel that had microchannels for vascularization**.** This encapsulating strategy combines encapsulation with printing systems to generate microchannels in pre-defined regions of the nano-porous hydrogel.[185] The scaffold architecture presented here can be designed to improve the transport of nutrients and oxygen to encapsulated cells. Furthermore, the network of larger sized channels could facilitate the invasion of the host vasculature after implantation or be employed for pre-vascularization *in vitro*. Their studies revealed that transplanted islets in these gels had tissue and vascular in-growth within the microchannels, which promoted normoglycemia after transplantation and sustained glucose control over the two-month period of study until removal of the device. Collectively, numerous cell encapsulation systems are being developed for the treatment of various diseases. Current advances in material design, immunomodulation and encapsulation strategies will be critical in

addressing the many challenges that are involved in transitioning these cell-based therapies to the clinic.

2.3.2 Cell Delivery with Tissue-Integrating Scaffolds

Scaffolds are also formulated into either a microporous structure or are made degradable in order to facilitate integration with the host tissue (**Fig 2.2)**. The integration with the host tissue can be advantageous for vascularization to provide nutrient transport necessary for survival and appropriate cell-cell contact that can direct differentiation[186–188].

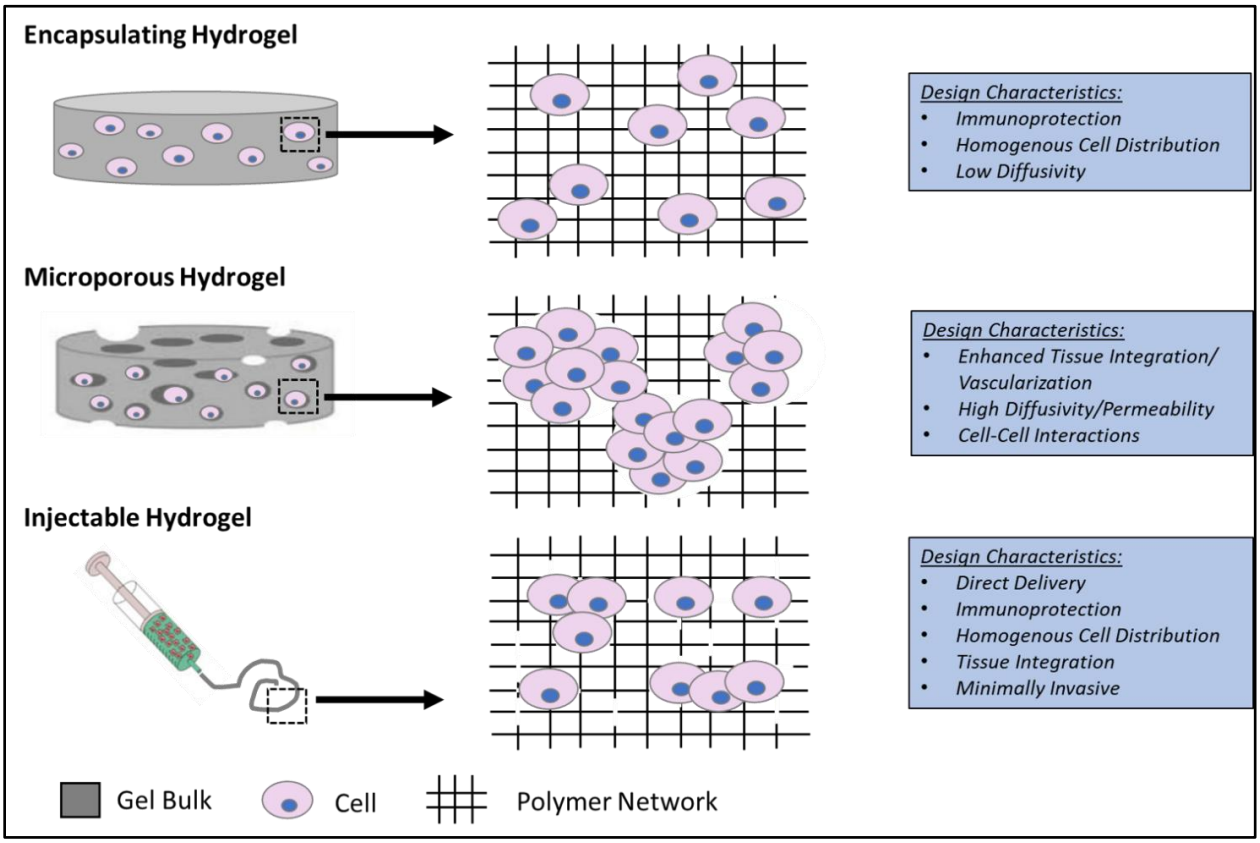

Figure 2.3 *Schematic representation and design characteristics of cell-laden hydrogels.*

Scaffolds with an interconnected microporous structure can be seeded with cells, and upon transplantation, host cells can infiltrate for integration with the transplanted cells[80]. The microporous structure allows for nutrient transport and waste removal, while also providing a substantial surface for cell adhesion and space for tissue growth[81,82]. Compared to encapsulated

designs, porous hydrogels can encourage cell migration and cell–cell interactions, which can help with regulating cell proliferation, differentiation, and the organization of some engineered tissues (e.g., cartilage and liver)[192,193]. These cellular activities can be inhibited or delayed when cells are encapsulated into gel scaffolds since they are entrapped in the 3D polymer networks. As a result, the incorporation of cell living spaces that are larger than tens of microns in diameter in gel constructs can support cell spreading, migration, proliferation, and then vascularization for the establishing access to nutrients and other systemic cues[194].

One recent innovation demonstrated that the shortcomings of human lung organoid maturation could be overcome by using a combination of synthetic, porous scaffolds and *in vivo* growth in mice[195]. Prior to transplantation on the scaffold, these organoids contained many of the cell types that are found in mature airway epithelia but, notably, they did not contain mature goblet cells (the cells that produce mucus) or a number of other secretory cells[32]. However, they showed that incorporating a porous PLG scaffold into the process of culturing the organoids then transplanting into the epididymal fat pad encouraged organoids to develop tubes that resembled the adult airway. Moreover, they contained a wider range of mature cell types than had been produced before. The PLG scaffold served as a physical niche to support survival and maturation of the transplanted lung organoids, which displayed enhanced epithelial organization, morphology and differentiation into proximal airway lineages. This result suggested that the scaffold was required, along with *in vivo* cues, to support organoid maturation.

Cocultures on scaffolds allows organoids to receive both a supportive microenvironment as well as cues from missing human cell types that have been shown to influence functionality *in vivo*. Aurora et al. showed human intestinal organoids (HIO) cultured on scaffold matrices developed multiple epithelial and mesenchymal lineages that are found in the developing human intestine[196]. However, while the HIO possessed many of the key cell types that are found in the native intestine, they lacked an enteric nervous system (ENS), immune cell lineages and vasculature. Recently, neuro-epithelial interaction in HIO-ENS co-cultures was accomplished

through the use of enteric neural crest cell (ENCC) spheres, which are 3D progenitor cultures that are capable of differentiating into the ENS lineages, along with hPSC-derived small intestine seeded on poly L-lactic acid (PLLA)/polyglycolic acid (PGA) microporous scaffolds[197,198]. The coculture was transplanted into the intestinal mesentery to aide maturation. ENCC supplementation with HIO transplants established submucosal and myenteric ganglia, repopulated various subclasses of neurons, and restored neuroepithelial connections in the organoid. This study showed improved organoid complexity by introducing an ENS and porous scaffold platform to begin studying human intestinal motility and associated human ENS neuropathies.

A common caveat of the microporous design, however, is that these scaffolds are formed into a specific shape prior to implantation, which limits the ability to target a specific site[199]. Interestingly, granular materials can be used to generate injectable yet porous materials by injecting microscale hydrogel particles and having them assemble into a bulk granular material. The first example of this approach was termed microporous annealed particle (MAP) scaffolds, where microscale hydrogel spherical beads are injected into a cavity and subsequently annealed to each other to form a bulk gel with the space between the beads serving as pores in the gel. While the void fraction in MAP scaffolds is limited to approximately 20% rather than 80% for other porous hydrogels[200], MAP scaffolds have a continuous micron-sized porous structure that allows both transplanted cells and surrounding host tissue to infiltrate the scaffold without the need for material degradation. In addition, MAP gels have the ability to conform to the wound shape and promote integration to form cellular structures within days after injection[101]. As a result, MAP hydrogel injection into skin and brain wounds have shown lower inflammation at the wound sites [101,102]. The microporous injectable hydrogel design could expand the applicability of microporous hydrogels through its injectable nature. Recently, another example of granular hydrogels utilizes particle jamming to avoid the need for particle annealing.[203] This work utilizes the phenomenon that jammed granular material behaves as a solid.

Similarly, a cytocompatible fabrication process was recently developed for generating microporous scaffolds with encapsulated cells using gelatin as a leachable porogen[104]. The scaffold was designed with a wide range of porosities and pore sizes by crosslinking oligo(poly(ethylene glycol)fumarate) in the presence of mesenchymal stem cells and varying sizes of gelatin microspheres. Encapsulated mesenchymal stem cells exhibited high viability immediately following the fabrication process, and culture of cell-laden hydrogels revealed improved cell viability with increasing porosity. An alternative technology is based on using microribbon (μRB)-like gelatin as scaffolds, in which the ribbons are building blocks forming a macroporous structure.[145] Their results suggested that enhancing cell survival and proliferation using a μRBs microporous design further promoted the paracrine-signaling effects of adipose-derived stem cells for stimulating endogenous bone repair. A commercially translated microporous design has been utilized for NeoCart® (Histogenics Corporation, Waltham, MA, USA), in which autologous chondrocytes are cultured on porous bovine Type 1 collagen scaffolds for the repair of cartilage defects in the adult knee[205]. While the 3D matrix bears load, its open structure allows for influx of MSCs, which ideally differentiate into chondrogenic lineage[206]. A FDA phase II trial comparing NeoCART® to microfracture showed significantly better results in all clinical outcome measures in the NeoCART® treated patients.[146] Histogenics recently completed patient enrollment of its NeoCart® Phase 3 clinical trial in accordance with the Special Protocol Assessment (SPA) agreement with the United States Food and Drug Administration (FDA).[207] The efficacy of these novel design methods for microporous scaffolds demonstrates the promise of cell-based therapies for enhanced long-term tissue regeneration outcomes.

Encapsulating gel scaffolds that are degradable can initially function as an immunoisolation barrier similar to the encapsulating gels of section 2.1, yet their degradability over time can allow for improved cell infiltration and integration with the host. Scaffold degradation can lead to changes in mechanics and swelling over time, which will in turn affect cell behavior[208].

By utilizing degradable reagents (i.e. peptides, ligands or proteases) to form unstable bonds, scaffolds can undergo degradation through hydrolytic or enzymatic mechanisms[209]. A common principle is that the degradation rate of the scaffold should match the rate at which the tissue grows or infiltration is desired. Recently, Lima et al. used biodegradable alginate to fabricate beads encapsulating rat mesenchymal stem cells and fibronectin and implanted the particles in a calvarial bone defect in order to evaluate their potential for bone tissue regeneration.[110] The hydrogel's rate of degradation could be controlled to permit accelerated bone tissue growth while preventing cell loss and any toxic exchange of molecules with the surrounding environment.

Many natural polymers are biodegradable; yet their utility in tissue engineering applications can be constrained by the intrinsic properties of the materials. In contrast, synthetic polymers provide an opportunity to control degradation through well-defined mechanisms, such as controlling the crosslinking density of such segments[211,212]. For example, the hydrogel can be crosslinked by reacting the backbone polymer with a peptide sequence that can be degraded by specific cell-secreted proteases endogenous to the wound healing microenvironment, such as matrix metalloproteinases[113–115]. In a recent study, PEG gels co-encapsulating chondrocytes and MSCs were crosslinked with an MMP-degradable peptide in order to match the resorption of the scaffold with the rate of matrix production by cells during cartilage repair[116]. Relative to non-degradable hydrogels, those that allowed for cell-mediated degradation showed significantly increased GAG and collagen deposition, which are key markers for chondrogenesis[117]. Another design consideration utilizing degradative properties evaluated a two-component synthetic PEG hydrogel macrodevice for the delivery of islets to an extrahepatic transplant site[218]. The hydrogel consists of an inner layer crosslinked with a non-degradable PEG dithiol and a degradable outer layer crosslinked with a proteolytically sensitive peptide to enhance localized vascularization. Encapsulated islets demonstrated high viability within the device and implementation of a vasculogenic, degradable hydrogel layer increased the vascular density around the transplant

site. While normoglycemia was not achieved with the device, suggesting that parameters like islet load require further optimization, the results highlight the benefit of degradable interfaces for the promotion of engraftment.

Another application for biodegradable scaffolds is as injectables, which have an unparalleled advantage for delivering cells to specific sites with minimally invasive procedures by undergoing gelation *in vivo*.[119] Injectable hydrogel polymerization can occur as a response to temperature or pH change, ionic cross-linking, solvent exchange or crystallization, or simply thickening upon removal of the injection shear[220,221]. One of the most common polymers used for these biomedical applications is Poly (N-isopropylacrylamide) (PNIPAM) due to its lower critical solution temperature being very close to body temperature[222,223]. A recent study evaluated PNIPAM-containing hydrogels used as carriers for intramyocardial delivery of brown adipose derived stem cells in rats with myocardial infarction[224]. The hydrogel displayed rapid, subphysiological phase transition temperatures and was capable of noninvasively delivering a liquid suspension of cells that gels in situ forming a cell-loaded scaffold, essentially isolating treatment to the injection site. In addition, engraftment around the transplanted cells was significantly enhanced and therapeutic efficacies were augmented in the myocardial infarction. This research provides new treatment opportunities for diseases like cardiac ischemia, which have seen limited therapeutic success in part due to poor targeting. Gaffey et al. addressed this concern by developing an injectable, shear-thinning HA hydrogel that delivers endothelial progenitor cells to ischemic myocardium[225]. The hydrogel was designed to flow through a syringe with the application of shear force and then re-assemble at the injection site. *In vivo* improvements from this delivery strategy included enhanced cell retention and vasculogenesis, limited adverse remodeling and improved cardiac function.

These injectable biodegradable scaffolds may also be modified with trophic factors to enhance cell survival or function. VEGF has been incorporated into degradable PEG hydrogels encapsulating islets in order to promote localized vascularization.[226] Transplantation of the in-situ

forming injectable hydrogel at an extrahepatic site supported engraftment and reversal of diabetes, which was not achieved without VEGF. Xu et al. applied a similar approach by using a basic fibroblast growth factor (bFGF) release system to increase MSC survival in a thermoresponsive, biodegradable hydrogel.[227] The incorporation of the pro-survival factor bFGF within the hydrogel improved MSC viability after intramuscular injection, as well as increased blood vessel density, limb perfusion, and muscle diameter. While the functionalization of these hydrogels enhances both oxygen and nutrients to the target site, the hydrogel's ability to promote neovascularization is still being investigated since the process of angiogenesis typically requires days to weeks. These recent studies demonstrate the critical role that local degradation seems to play within tissue engineering constructs.

Scaffolds have received increasing interest as a leading candidate for engineering tissue due to their superior biocompatibility and inherent similarity to the natural ECM, in addition to their conducive framework for cellular proliferation and survival. These recent advances discussed above highlight important considerations for designing hydrogels for effective cell delivery. Encapsulation approaches can potentially eliminate the barriers preventing transplantation of xenogeneic or stem cell-derived allogeneic cells. However, hypoxia can occur at the core of the scaffold and limit the duration that these cells function. Meanwhile, scaffolds that promote tissue integration through microporous structures or biodegradation are challenged by the immune response but can enhance vascularization and *in vivo* tissue growth. Also, incorporating therapeutic molecules and particles into these scaffolds is another method to guide transplanted cell behavior and function. With continued research in these areas focused on incorporating the benefits of both approaches, scaffold-based tissue engineering will continue to make advances toward clinical restoration of tissue function.

2.4 Conclusions

Some of the primary defining characteristics of a tissue include the physical assembly of multiple cells, heterogeneity of cell phenotypes, and higher-order organization of tissue architecture. With recent advances in design, scaffold properties such as porosity, cell-mediated degradability, and tethered bioactive cues not only provide structural support for organoid tissue development but also influence and direct cell-cell interactions, proliferation, migration, and differentiation. A scaffold delivery system no longer represents only a mere static structural support for cells but rather a dynamic and versatile environment. However, several challenges remain in controlling the dynamics of the scaffold in the complexity of the tissue environment *in vitro* and *in vivo*. Currently, no universal material fulfills all the mechanical needs to improve cell survival and functionality during the different phases of tissue generation and transplantation. While some material mechanical properties, such as stiffness, may be optimal for enhanced long-term retention and differentiation, these same mechanical properties may inhibit the progression of earlier regenerative processes. Regulating the cellular processes and guiding the development of new tissue growth in parallel with the dynamic changes of the tissue environment would be pivotal in determining the outcome of the regenerative therapy. A number of scaffold designs are being investigated to achieve this control as well, such as self-assembling peptides and peptide amphiphiles that provide for controllable gelation, degradation, and presentation of cell adhesion motifs[228,229].

A promising future research direction is the development of layered biomaterials that can recapitulate the zonal organization of native tissue in order to fulfill multiple mechanical requirements throughout the multiple stages of *in vitro* and *in vivo* organoid development. A layered scaffold consisting of different ECM proteins as well as mechanical properties could offer better delivery properties to direct cell fate and regulate processes such as tissue maturation and engraftment[230]. MSCs and chondrocytes encapsulated in multi-layered scaffolds with spatially varying matrix compositions and mechanical cues have demonstrated promising results in zonal-

specific differentiation[231,232]. Another useful functionality that can be incorporated is the ability to increase or decrease hydrogel stiffness after initial crosslinking and implantation. This has been achieved through stimulus-triggered secondary chemistries between functional groups or by incorporating a secondary reaction mechanism that occurs at a much larger time scale than the first primary crosslinking mechanism[233–236]. The stiffness of the hydrogel can therefore be made time-dependent and can be tuned to the different stages of the regenerative process.

Recent efforts to study the host response to implanted biomaterials can use these insights to design materials which can proactively direct the immune response upon implantation to be favorable to the regenerative process and the survival and functionality of any co-transplanted cells in the material. Examples include the tuning of material properties which can increase the presence of pro-remodeling versus pro-inflammatory phenotypes of macrophages in implant site and can also control transplanted stem or progenitor cell behavior and differentiation[237]. Finally, with emerging technologies such as CRISPR, transplanted organoids can undergo genetic engineering to regulate the immune response as a means to prevent or avoid rejection[238].

In summary, organoid cultures have the potentially to transform drug discovery and development. Three-dimensional cell cultures would have enormous potential to model development and disease, as advanced cell models under development may fully capture the *in vivo* functions of organs and tissues. Scaffolds offer great promise in designing suitable environments that provide not only structural support for cells and new tissue growth, but also control over organoid development to promote differentiation and improve therapeutic outcomes. The optimization of organoid cultures for scaling-up cell production would improve quality, quantity, and efficacy, thus making cells as therapeutics a reality. As these scaffold design considerations continue to be investigated, this system could provide a promising platform for organoid cultures for a wide range of applications in tissue engineering.

Chapter 3: Microporous Scaffolds Support Assembly and Differentiation of Pancreatic Progenitors into β-cell Clusters

3.1 Abstract

Human pluripotent stem cells (hPSCs) represent a promising cell source for the development of β-cells for use in therapies for type 1 diabetes. Current culture approaches provide signals to mimic a temporal control of organogenesis to drive the differentiation towards β-cells. However, spatial control may represent an opportunity to improve the efficiency and manufacturing of β-cells. Herein, we adapted the current culture systems to microporous biomaterials with the hypothesis that the pores can guide the assembly of pancreatic progenitors into clusters of defined size that can influence maturation. The scaffold culture allowed hPSC-derived pancreatic progenitors to form clusters at a consistent size as cells differentiated. By modulating the scaffold pore sizes, we observed 250-425 μm pore size scaffold cultures augmented insulin expression and key β-cell maturation markers compared to cells cultured in suspension. Furthermore, when compared to suspension cultures, the scaffold culture showed increased insulin secretion in response to glucose stimulus indicating the development of functional β-cells. In addition, scaffolds facilitated cell-cell interactions enabled by the scaffold design and supported cell-mediated matrix deposition of extracellular matrix (ECM) proteins associated with the basement membrane of islet cells. We further investigated the influence of ECM on cell development by incorporating an ECM matrix on the scaffold prior to cell seeding; however, their presence did not further enhance maturation. These results suggest the microporous scaffold culture provides a conducive environment that drives *in vitro* differentiation of hPSC-derived insulin-producing glucose-responsive β-cells and demonstrates the feasibility of these scaffolds as a biomanufacturing platform.

3.2 Introduction

Type I diabetes (T1D) is a chronic metabolic disorder characterized by autoimmune destruction of the pancreatic β-cells that results in the need for life-long insulin therapy. This disease represents 5–10% of the diagnosed cases of diabetes, corresponding to more than 1.25 million individuals in the United States [239]. Several secondary metabolic disorders can arise from this disease, as well, such as retinopathy, neuropathy, nephropathy, stroke and heart failure [240,241]. Although exogenous insulin injections have decreased mortality, severe hypoglycemic events and macrovascular complications persist [242–244]. Thus, recent research has turned to cell-based therapies focused on replacing lost insulin-producing cells. Enthusiasm in cell replacement therapies for diabetes was driven, in part, by the progress in allogeneic islet transplantation with the Edmonton protocol [245–249]. Recently, promising results from a European consortium of islet transplant centers showed excellent glycemic control and absence of hypoglycemia reported in approximately 80% of patients at 1 year and 60% at 5 years [250]. However, the widespread application of islet transplantation has been tempered by the lack of availability of islets and the need for life-long immunosuppression [251,252].

The lack of available islets has led to the investigation of human pluripotent stem cells (hPSCs) as an unlimited source of functional β-cells. Initial findings from the Kieffer and Baetge/D'Amour groups demonstrated the production of pancreatic progenitors and, subsequently, insulin-producing β-like cells *in vitro*. In the Kieffer lab, these cells could further differentiate following transplantation to normalize blood glucose levels after approximately 3-4 months [253,254]. More recently, *in vitro* culture protocols have developed hPSC-derived β-cells that induce normoglycemia over shorter times after transplantation [255–258]. Additionally, suspension cultures utilized for aggregated hPSC-derived β-cell production provide procedures that are scalable to generate sufficient glucose-responsive cells [255,257]. While numerous protocols have been established, the *in vitro* production of β-cells can result in a heterogenous population consisting of polyhormonal endocrine cells in addition to monohormonal β-cells [254,259,260].

Furthermore, the increasing culture volumes can influence the size of cell aggregates, which has previously been linked to apoptosis-related cell loss, cellular differentiation, and heterogeneity[261]. These challenges indicate the need to further investigate approaches that can promote maturation of insulin-producing β-cells.

The current stepwise hPSC differentiation approach aims to mimic a temporal control of organogenesis observed during embryonic development, and spatial control may represent an opportunity to enhance the efficiency and consistency of β-cell maturation. *In vivo* spatial control is achieved with cell-cell and cell-extracellular matrix (ECM) interactions. The ECM forms a three-dimensional (3D) environment and offers a niche for cell adhesion, colonization, proliferation, and differentiation[262–264]. This 3D environment has been shown to enhance hPSC differentiation and promote the assembly of functional tissues[23,265]. Recent advances in 3D cultures have generated tissues called organoids, which possess several advantages including cellular organization similar to the native organ while possessing the specified cell types[32,34,52,266,267]. These same cell types cultured on plastic and allowed to self-assemble are not able to form the same complex tissue architectures that are permitted by 3D cultures.

Recently, porous scaffolds have been utilized to provide a 3D environment to facilitate the assembly of hPSCs into multicellular structures, or organoids[268–270]. In addition, culture on scaffolds represents an alternative manufacturing platform that has shown translational capabilities with other tissue engineered products[271]. Microporous scaffolds allow for both cell-cell and cell-matrix signaling that supports the self-organization of the cells into functional tissue structures[272,273]. hPSC-derived β-cells have currently been obtained through either a 2D monolayer culture that is subsequently transformed into large clusters on an air-liquid interface or as 3D aggregates in low attachment plates or suspension cultures[23–25,274]. However, during pancreas organogenesis, islets are surrounded by a supportive extracellular matrix[27,275,276]. Mimicking the spatial cues in the pancreatic niche environment has the potential to augment the

in vitro hPSC differentiation toward functional β-cells.

Herein, we investigated microporous polymer scaffolds as an *in vitro* platform for the efficient differentiation of hPSC-derived pancreatic progenitor cells to insulin-producing glucose-responsive β-cells. Our scaffolds were formed from synthetic polymeric materials, with the walls supporting the assembly of pancreatic progenitors into β-cell clusters. The pore size was investigated for the ability to form clusters of distinct sizes. The cell structures within the pores of the scaffold were analyzed by histology and gene expression. The influence of ECM-coated scaffolds on β-cell maturation was evaluated as well to investigate the role of the matrix in cellular assembly and differentiation. Finally, we assessed the maturation and function of these cells through glucose stimulated insulin secretion assays. These studies provide insight on cell-cell and cell-matrix interactions that influence the differentiation of hPSCs to β-cells on microporous scaffolds, which may ultimately provide a platform for biomanufacturing the cells as a therapy for diabetes.

3.3 Materials and Methods

3.3.1 *Microporous scaffold fabrication*

Two types of scaffolds were used poly(lactide-co-glycolide) (PLG) scaffolds and polyethylene glycol (PEG) scaffolds. Microporous scaffolds were fabricated as previously described[277,278]. Briefly, PLG microporous scaffolds were fabricated by compression molding PLG microspheres (75:25 mole ratio D,L-lactide to glycolide) and micron-sized salt crystals in a 1:30 ratio of PLG microspheres to salt. The mixture was humidified in an incubator for 7 min and then thoroughly mixed again. Scaffolds were compression molded with 77.5 mg of polymer–salt mixture into cylinders 5 mm in diameter by 2 mm in height using a 5 mm KBr die (International Crystal Laboratories, Garfield, NJ) at 1500 psi for 45s. Molded constructs were gas foamed in 800 psi carbon dioxide for 16 h in a pressure vessel. The vessel was depressurized at a controlled rate for 30 min. On the day of cell seeding, scaffolds were leached in water for 1.5 h, changing the

water once after 1 h. Scaffolds were disinfected by submersion in 70% ethanol for 30 seconds and rinsed multiple times with phosphate buffer solution (PBS).

For the PEG hydrogels, PEG-maleimide (4-arm, molecular weight 20kDA, 20% wt/wt) polymer was dissolved in a HEPES buffer solution, mixed with NaCl crystals and a photoinitiator (Irgacure-2959) then cast into a PDMS mold (diameter: 5mm, thickness 2mm). The solution is irradiated with UV light to photo-crosslink the PEG-maleimide and then washed to remove the sodium chloride and unreacted photoinitiator. The pore size of the scaffolds can be readily controlled through the dimensions of the porogen, and we propose to investigate scaffold pore sizes using porogens of 63 to 108 µm, 108 to 225 µm, 225 to 450 µm, and 500 to 600 µm.

3.3.2 *Differentiation of hPSCs and scaffold seeding*

The H1 hESC line used for these studies was obtained from the WiCell Research Institute (Madison, WI). Pluripotent cells were maintained on Matrigel (BD Biosciences, San Jose, CA) in mTeSR1 medium (STEMCELL Technologies, Vancouver, Canada). When ~80% confluent (~3-4 days after plating), cells were passaged using Gentle Cell Disassociation Reagent (STEMCELL Technologies). The differentiation of pluripotent hPSCs (Stage 0) to pancreatic progenitor cells (Stage IV) were performed as described [256].

To initiate scaffold culture differentiations, Stage IV pancreatic progenitor cells were single-cell dispersed using TrypLE Express (Life Technologies) and then seeded on scaffolds at concentrations ranging from 12.5-125 million cells/cm^3. Prior to cell seeding, scaffolds were washed in cell media solution then briefly dried on sterile gauze to improve the absorption of the cell solution into the scaffold. Cells were distributed across both faces of the scaffold and then incubated for 10min to allow cell solution to be further absorbed into the scaffold before differentiation media was added. The differentiation towards insulin-producing glucose-responsive β-cells (Stages V-VI) on scaffolds required 1-2 weeks based on the established protocol [256]. A traditional hPSC suspension culture was differentiated per the described protocol

to provide an internal control [256]. Briefly, undifferentiated hPSCs were initially seeded at 1.0 million cells/mL in ultra-low attachment 6 well plates (Corning, VWR), placed on an Orbi-Shaker (Benchmark), and set at rotation rate of 95 rpm in a 37°C incubator, 5% CO2, and 100% humidity. Cells were cultured for 48 hr in mTeSR1 and then cultured in the differentiation media. Human islets were acquired from Cell Trans Inc. for comparison.

3.3.3 Protein adsorption to scaffolds

For coating scaffolds with ECM proteins, scaffolds were fabricated and then disinfected in 70% ethanol and dried again before being placed into individual wells of a 24-well tissue culture dish. Proteins were then coated per manufacturer's recommendations to be consistent with our previous report that demonstrated enhancement in islet function following transplantation on ECM protein-modified scaffolds[279,280]. Collagen IV (25µL at 1mg/mL; Sigma), laminin-332 (25µL at 1mg/mL, formerly termed laminin-5 and hereafter referred to as "laminin"; Sigma), 25µL of Matrigel (Corning, Cat#: 354277) or PBS were added to the scaffold. The scaffolds were then incubated at 37°C for 1 h, followed by the addition of 25 µL of the same component to each scaffold. Scaffolds were then incubated with 95% humidity at 37°C overnight to facilitate protein adsorption to the scaffold surface. Prior to cell seeding, control and ECM-coated scaffolds were washed in cell culture media.

3.3.4 Cell viability

The viability of cells on the scaffolds was qualitatively assessed using a Live/Dead® viability/cytotoxicity kit (Life Technologies). Cells were stained with a solution consisting of 5 µL of 4 mM acetomethoxy derivate of calcein (calcein-AM) and 20 µL of 2 mM ethidium homodimer-1 (EthD-1) in 10mL of sterile PBS. Cells cultured on microporous scaffolds were incubated at 37°C and 5% CO_2 in the live/dead solution for 30 min, followed by a wash in PBS and then the viability was assessed using a fluorescent microscope (Olympus, Center Valley, PA, United States).

3.3.5 qRT-PCR Analysis

For gene expression analysis, cell-laden scaffolds were mechanically homogenized in Trizol® reagent (Life Technologies), and RNA was isolated using Direct-zol™ RNA MiniPrep Plus (Zymo Research Corporation, Orange, CA, USA) according to the manufacturer's instructions. RNA concentration was determined using a NanoDrop spectrophotometer. The iScript™ Reverse Transcription Supermix was used to transcribe RNA into cDNA. Universal RT microRNA PCR assays were performed using SYBR Green MasterMix Universal RT (Exiqon), according to the manufacturer's instructions. The amplification profile was assessed using a LightCycler® 480 (Roche, Germany). Gene expression was quantified using the ΔΔCt method and fold change was calculated using the formula $2^{-\Delta\Delta Ct}$. Values for the genes of interest were normalized to the housekeeping gene (GAPDH) followed by normalization to marker expression in pluripotent hPSCs. Primers used for qPCR analysis are listed in **Table 3.1**.

Table 3.1 Primers of Pancreatic Differentiation Markers Used for qRT-PCR

gene	primer	sequence (5' to 3')
PDX1	forward	CCTTTCCCATGGATGAAGTC
PDX1	reverse	CGTCCGCTTGTTCTCCTC
Nkx6.1	forward	GGGGATGACAGAGAGTCAGG
Nkx6.1	reverse	CGAGTCCTGCTTCTTCTTGG
MafA	forward	GAGAGCGAGAAGTGCCAACT
MafA	reverse	TTCTCCTTGTACAGGTCCCG
Insulin	forward	TTCTACACACCCAAGACCCG
Insulin	reverse	CAATGCCACGCTTCTGC
Glucagon	forward	TGCTCTCTCTTCACCTGCTCT
Glucagon	reverse	AGCTGCCTTGTACCAGCATT
ECAD	forward	TTGACGCCGAGAGCTACAC
ECAD	reverse	GACCGGTGCAATCTTCAAA
PCSK1	forward	CTCTGGCTGCTGGCATCT
PCSK1	reverse	CGGGTCATACTCAGAGGTCC

3.3.6 Immunostaining

Immunostaining of *in vitro* cell differentiation was performed on end-stage β-cell clusters. Scaffold cultures were cryopreserved in isopentane and cooled on dry ice, while suspension clusters were fixed with 4% paraformaldehyde (Electron Microscopy Sciences; Hatfield, PA, United States) then embedded within OCT embedding medium (Tissue-Tek, Sakura Finetech, Torrance, CA) and cryosectioned to 14 µm sections. Scaffold tissue sections and cells differentiated in suspension cultures were fixed with 4% paraformaldehyde for 30 min, blocked and permeabilized for 30-min with staining buffer (5% donkey serum, Jackson Immunoresearch; 017-000-121) and 0.1% Triton-X 100 (Acros Organics; 327371000 in PBS), stained overnight with primary antibodies at 4 °C, stained for 4 hr with secondary antibodies at 4 °C, and treated with mounting solution DAPI Fluoromount-G (SouthernBiotech; 0100-20). Digital images were acquired with a MicroFire digital camera (Optronics, Goleta, CA) connected to an Olympus BX-41 fluorescence microscope (Olympus, Center Valley, PA, United States). Image quantification was conducted with MATLAB software using an object-based colocalization analysis. $DAPI^+$ cells were identified per total area of the sectioned tissue and quantified by applying Otsu's thresholding method, the watershed transform, and individual cluster thresholding. Then, each cell's colocalization with immunofluorescent markers was quantified. For confocal imaging, whole tissue samples were fixed in 4% paraformaldehyde then stained with primary and secondary antibodies as described above. The labeled samples were then cleared in Murray's clear solution for optical clearing for 45 min before being imaged via confocal microscopy (Nikon A1Si laser scanning confocal microscope, Nikon Instruments Inc, Tokyo, Japan).

Primary antibody solutions were made in staining buffer with the following antibodies at a 1:250 dilution: guinea pig-anti-Insulin (Dako, A05654), mouse-anti-ECAD (Novus Biologicals; 7H12), rabbit-anti-Collagen IV (Thermo Fisher, PA128534), rabbit-anti-Laminin (Thermo Fisher, PA516287), rabbit-anti-Fibronectin (Abcam, AB23750). Secondary antibody solutions were made in staining buffer with the following antibodies at 1:500 dilution: anti-guinea pig-alexa fluor 488

(Life Technologies; A11073), anti-mouse-alexa fluor 555 (Life Technologies, A31570), anti-rabbit-alexa fluor 555 (Life Technologies, A31572).

3.3.7 Static Glucose-Stimulated Insulin Secretion Assay

For GSIS testing, scaffold cultures and suspension clusters were first washed twice with KRB buffer (125 mM NaCl, 3 mM KCl, 1.2 mM $CaCl_2$ 1.2 mM $MgSO_4$, 1 mM NaH_2PO_4, 22 mM $NaHCO_3$, 10 mM HEPES (Gibco; 15630-080), and 0.1% BSA), exposed to a basal level of glucose (2.8 mM) in a 24 well plate for 30 minutes, then transferred to a second, fresh basal glucose solution and incubated for an hour. Samples from this basal glucose solution were retained. The cells were then washed in fresh basal level glucose for 10 minutes and next exposed to a high-level glucose concentration (28 mM) for an hour. Samples from the retained second basal glucose solution and high-level glucose solution were collected to measure insulin levels using a Human Insulin ELISA kit (Mercodia Inc. 10-1113-01). The cells were single cell dispersed by TrypLE treatment, counted in a hemacytometer, and viable cell counts were used to normalize insulin secretion.

3.3.8 Statistics

All statistical analyses were conducted using Prism graphing and data analysis software (GraphPad Software, Inc., La Jolla, CA, United States). Statistical differences were determined using non-parametric testing; an unpaired two-tailed Student t test or one-way ANOVA with Dunnett test for multiple comparisons. Values were reported as the mean ± SEM. n indicates the total number of biological replicates.

3.4 Results

3.4.1 Cluster formation of hPSC-derived pancreatic progenitors within scaffold pores

Two commonly used biomaterials, PLG and PEG, were investigated for the *in vitro* scaffold culture of pancreatic progenitors to β-cells. These two materials provided a similar microporous structure (**Fig 3.1A**) with distinct material properties that can distinguish the role of structure

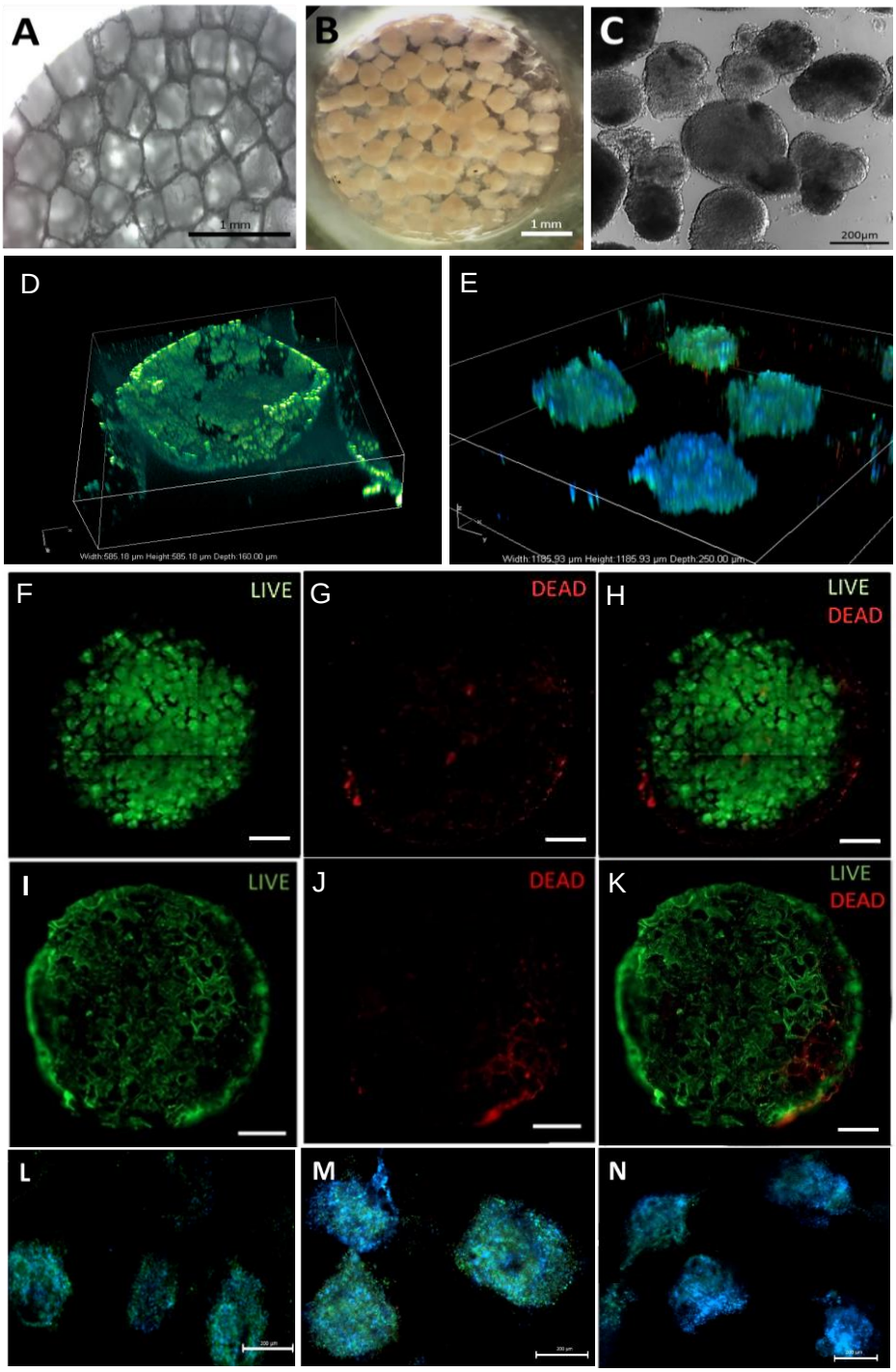

Figure 3.1 *In vitro* culturing of hPSC-derived pancreatic progenitors on microporous scaffolds

(A) SEM image of empty porous PLG scaffold shows highly porous structure with 250-425 µm pores. Microscope images of PEG scaffold culture (B) and suspension culture (C) display formed β-cell clusters. (D) Confocal imaging shows cell localization within a PEG scaffold pore at $12.5x10^6$ cells/cm^3 and (E) multiple scaffold pores at $125x10^6$ cells/cm^3. Cells were stained 2wks after seeding onto a PEG scaffold (F-H) and PLG scaffold (I-K) and examined using a live/dead assay to demonstrate minimal cell death during culture. Confocal imaging shows cell clusters distributed within a 2mm thick PEG scaffold pore at 0.5mm depth (L), 1mm depth (M) and 1.5mm depth (N).

relative to the role of the material. We first evaluated cluster formation within the microporous

scaffold cultures (**Fig 3.1B**) compared to the traditional suspension culture (**Fig 3.1C**). hPSC-derived pancreatic progenitors dissociated into single cells were initially seeded onto microporous scaffolds at a density of 12.5 million cells/cm^3 for culture. The use of single cells allows the proper infiltration of cells into the pores of the scaffolds while providing relatively uninhibited access of media to the cells. Through confocal microscopy, we found that this seeding density was not sufficient for cluster formation to occur as cells were localized to the surface of the pores (**Fig 3.1D**). Increasing the seeding density 10-fold to 125 million cells/cm^3 resulted in the cells assembling into 3D clusters within one day after seeding (**Fig 3.1E**), which resembles the self-organization that occurs in suspension cultures. Cell viability was consistently high (>90%) throughout the 14-day experiment for both PEG and PLG scaffold conditions (**Fig 3.1F-K**). These observations indicated that the assembly of cells into clusters could be supported within the micropores yet was dependent on the cell density. This high cell seeding density resulted in a uniform distribution of cells and clusters throughout the scaffold (**Fig 3.1L-N**). At densities greater than 125 million cells/cm^3, cells began to clump on the surface.

3.4.2 *Maturation of β-cell clusters within scaffolds*

We next investigated the feasibility of generating β-cell clusters in microporous scaffolds by measuring the expression of β-cell marker genes, which were compared with cells generated in suspension culture and human islets. Using qRT-PCR analysis, we found cells cultured within PEG and PLG scaffolds had an increased expression level of the endocrine hormone marker gene for insulin relative to Stage IV pancreatic progenitors. Additionally, β-cell maturation markers (*MafA, G6PC2, and PCSK1*) had expression levels on scaffold cultures that were at least comparable to suspension culture controls if not significantly increased. On average, the suspension culture produced clusters around 234 ± 63 μm in diameter (n=48 individual clusters). We used the tunable design of the scaffold pores to assess how varying the cluster size would

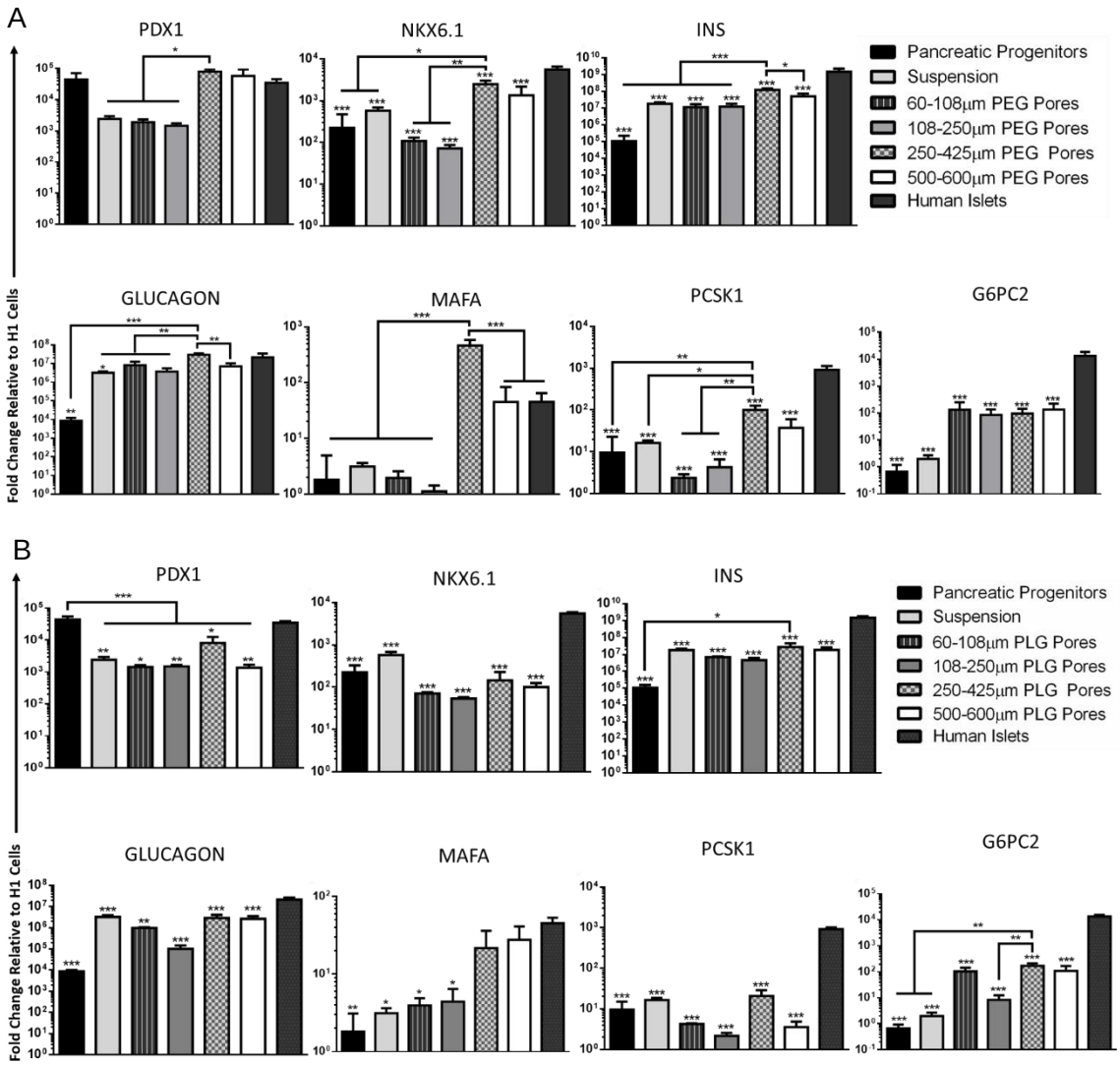

Figure 3.2 *Augmenting scaffold pore sizes enhances pancreatic progenitor differentiation*

Gene expression of pancreatic endocrine hormones, β-cell-associated transcriptional factors, and β-cell function-related proteins in hPSC-derived Stg 4 pancreatic progenitors and Stg 6 β-cells cultured on (A) PEG and (B) PLG microporous scaffolds with varying pore sizes. (*P≤0.05, **P≤0.01, ***P≤0.001 for each condition versus human islets using one-way ANOVA with Dunnett test for multiple comparisons, n = 6-7 biological replicates for all genes). Error bars represent the standard error of mean (SEM).

influence maturation within the scaffold. A correlation between scaffold pore sizes and the expression of key β-cell markers was observed with larger pore sizes promoting higher expression levels. For PEG scaffolds, pore sizes in the range of 250-425 μm had increased expression of pancreatic transcription factors (*PDX1* and *Nkx6.1*) compared to suspension and scaffolds with pore size smaller than 250 μm *(***Fig 3.2A**). The expression of *Nkx6.1* was lower than human islets for both suspension and scaffold conditions suggesting the cells have not

fully matured. However, the expression of insulin had a significant increase on scaffolds with pore sizes of 250-425 µm compared to suspension clusters and the other scaffold conditions. This trend between scaffold pore size and cell development was observed in the expression of β-cell maturation markers as well. Scaffolds with a pore size of 250-425 µm resulted in the highest expression of the insulin gene transcription factor, *MafA,* with the 500-600 µm pore size scaffolds exhibiting the second highest expression out of the *in vitro* conditions. The maturation marker proprotein convertase 1 (*PCSK1*) is one of the key enzymes associated with insulin processing and showed expression levels to be higher in scaffold cultures with 250-425 µm pore sizes compared to the scaffolds with smaller pore sizes as well as suspension clusters.

hPSC-derived pancreatic progenitors cultured on PLG scaffolds similarly demonstrated the development of β-cells with maturation showing a correlation with pore size (**Fig 3.2B**). Insulin expression for PLG scaffold cultures with 250-425 µm pore sizes was significantly increased relative to the pancreatic progenitors. The expression of pancreatic β-cell transcription factor *PDX1* and *Nkx6.1* in all four PLG scaffold conditions were lower than human islets but comparable to suspension clusters. While this suggests maturation could be improved, PLG scaffolds with 250-425 µm pore sizes showed increased expression in the key maturation marker, *G6PC2*, relative to pancreatic progenitors and suspension clusters. Overall, cells cultured in PEG and PLG microporous scaffolds generally showed increased expression levels of β-cell maturation markers. While the maturation was still not comparable to human islets, this deficit relative to islets is to be expected as, per the protocol used, *in vivo* transplantation is necessary to reach full maturation. This analysis revealed that pancreatic progenitors differentiated to β-cells in the PLG and PEG microporous scaffold show, at a minimum, comparable gene expression levels to the traditional suspension culture. Our observations also identified a relationship between scaffold pore size and β-cell maturation with 250-425 µm pore

size showing more significant improvements in β-cell development than in suspension culture. Since this pore size measurement was based on the salt porogen size used during fabrication, we also performed measurements after the scaffolds had been exposed to media. Using imaging analysis, we determined the pore size distribution for PLG and PEG scaffold cultures fabricated with 250-425 µm salt porogens were 371 ± 33 µm (n=30 individual pores) and 468 ± 62 µm (n=32 individual pores), respectively, after 24 hours in cell media. The pore size for wet PLG scaffolds remained within the estimated range while wet PEG gels had an average pore size distribution slightly above the range, likely due to swelling. Overall, based on these findings, the following studies focused on scaffolds with a relative pore size of 250-425 µm.

3.4.3 Cell-cell communication in microporous scaffold cultures during β-cell maturation

Next, we investigated cell-cell interactions within the scaffold culture that drive maturation in the pancreatic niche environment. The cell surface adhesion protein epithelial cadherin (ECAD) plays a critical role in the development of islets and intra-islet communication and is implicated in efficient insulin secretion from β-cells[281–283]. Thus, we assessed the presence of ECAD through qRT-PCR analysis in both scaffold cultures and suspension clusters. ECAD gene expression

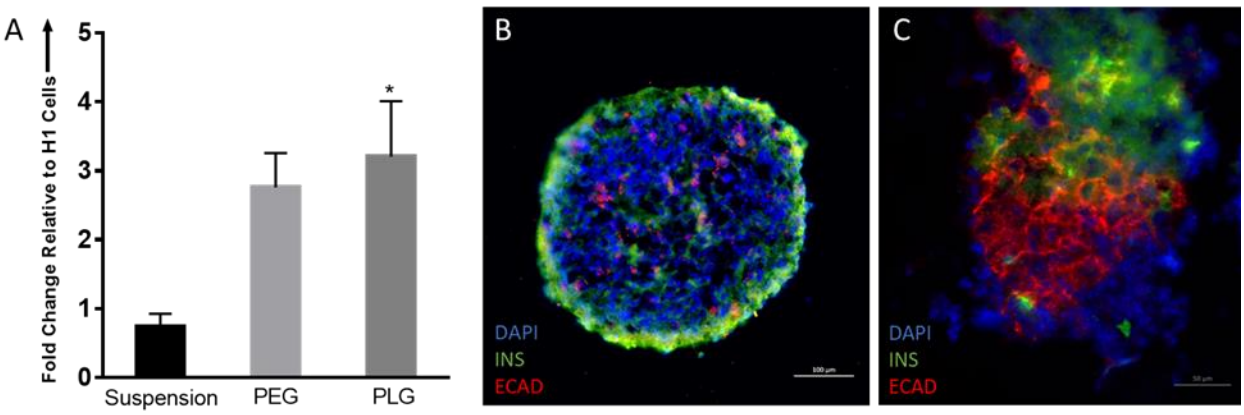

Figure 3.3 *Scaffold culture influences E-cadherin interactions in β-cell clusters*

(A) The effect of scaffold cultures versus suspension control on ECAD in maturing β-cells was determined by quantitative RT-PCR. ECAD gene expression levels of cells cultured in suspension or on PEG and PLG microporous scaffolds (*P≤0.05 compared to suspension using one-way ANOVA with Dunnett test for multiple comparisons, n = 4 biological replicates). Error bars represent the SEM. Immunofluorescent staining of suspension cluster (B) and PLG scaffold culture (C) for insulin (green), ECAD (red) and DAPI (blue).

levels were increased in cells cultured in PLG microporous scaffolds compared to suspension clusters (3 ± 1 vs 0.57 ± 0.03, n=4, *P*<0.05). (**Fig 3.3A**). PEG scaffold cultures showed comparable levels of ECAD expression relative to suspension clusters (2.8 ± 0.9 vs 0.57 ± 0.03, n=3-4). Cell-cell interactions were further investigated through immunostaining where E-cadherin was shown to be localized in small regions in the interior of the suspension clusters with increased co-expression with insulin-positive cells around the exterior of the clusters (**Fig 3.3B**). Alternatively, in PLG scaffold cultures, ECAD was distributed throughout the interior of the clusters and with co-expressed insulin-positive cells (**Fig 3.3C**). Imaging analysis of $DAPI^+$ cells expressing ECAD per the total area confirmed PLG scaffold cultures significantly increased protein expression of ECAD compared to suspension (42 ± 5% vs 21 ± 4% of total cell population, n=4; P<0.01). Our data suggests that microporous scaffold cultures, particularly PLG, promote cell-cell interactions that can play a role in driving β-cell maturation.

3.4.4 hPSC-derived β-cell glucose-responsive in vitro function within microporous scaffolds

The function of these β-cell clusters in scaffolds was next examined by their ability to secrete insulin in a glucose-responsive manner through a GSIS assay. Scaffold cultures and suspension clusters at the end of the six-stage differentiation were exposed to 2.8 mM and 28 mM glucose solutions, respectively. At the low glucose concentration, the cells in suspension or on scaffolds secreted similar quantities of insulin (**Fig 3.4A**). At the high glucose concentration, we observed an increase in insulin secretion per cell from both the PLG and PEG scaffold cultures, averaging 0.8 ± 0.2 and 0.7 ± 0.1 $\mu IU/10^3$ cells, respectively. Whereas the suspension clusters in a high glucose solution secreted low amounts of insulin, 0.3 ± 0.1 $\mu IU/10^3$ cells, and were not glucose responsive. hPSC-derived β-cells cultured on the PLG scaffold had the highest insulin secretion index, with a threefold increase compared to the suspension culture control (1.3 ± 0.2 vs 0.43 ± 0.06, n=3, *P*<0.01) (**Fig 3.4B**). PEG scaffold cultures also showed higher insulin secretion compared to the suspension control (1.11 ± 0.09, n=3, *P*<0.05) yet lower insulin secretion than

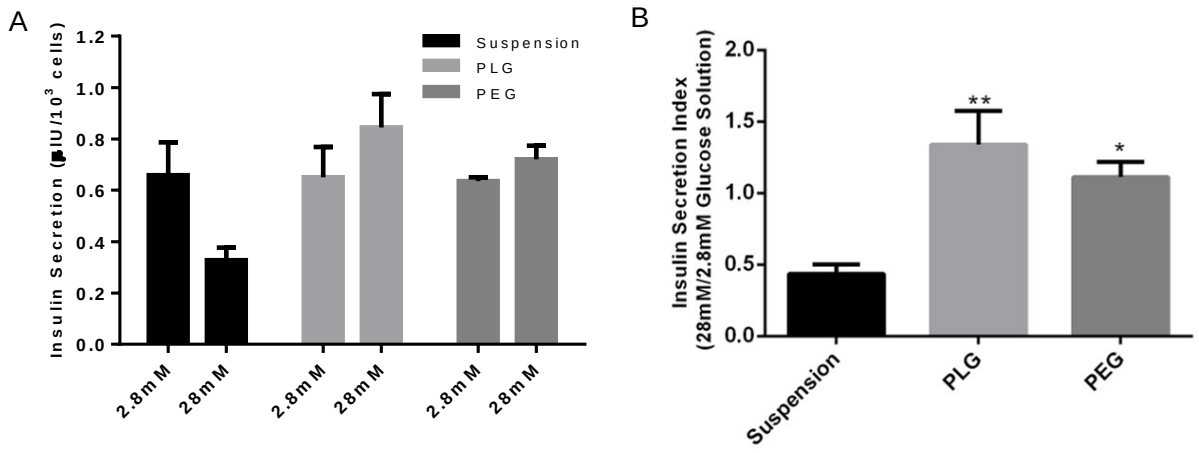

Figure 3.4 *Efficient generation of glucose-responsive β-Cells from human pancreatic progenitors differentiated on microporous scaffold cultures*

(A) Human insulin secretion from PLG and PEG scaffold cultures and suspension clusters in response to low and high glucose concentrations under static conditions (scaffold cultures: n = 4 biological replicates, suspension: n = 5 biological replicates). (B) The stimulation index was calculated as the ratio of insulin release in high to low glucose concentrations (*P≤0.05, **P≤0.01 compared to suspension, n=3-4 biological replicates). Error bars represent the SEM.

PLG. It is important to note that while the β-cells on scaffold cultures demonstrate a capacity for glucose-stimulated insulin secretion, the magnitude of response suggests these cells may not be the same as fully mature functional β-cells. Since the PLG scaffold demonstrated increased ECAD expression, had a higher degree of function, and is better for protein adsorption compared to PEG [284,285], subsequent studies employed this material for further investigation of the matrix environment supporting β-cell maturation.

3.4.5 ECM deposition by hPSC-derived β-cell clusters

We subsequently assessed the ECM within the cultured cells, as ECM basement membrane proteins are a critical component of the pancreatic environment supporting islets. Since cells cultured on PLG scaffolds showed signs of β-like development and function, we used immunofluorescence analysis to investigate if the cells were establishing a matrix similar to the pancreas within the scaffold. The presence of insulin-positive cells within the clusters were first evaluated to confirm the pancreatic progenitors were developing into β-like cells. We observed an increase in insulin-expression of $DAPI^+$ cells in PLG scaffold cultures (**Fig 3.5A-C**) compared

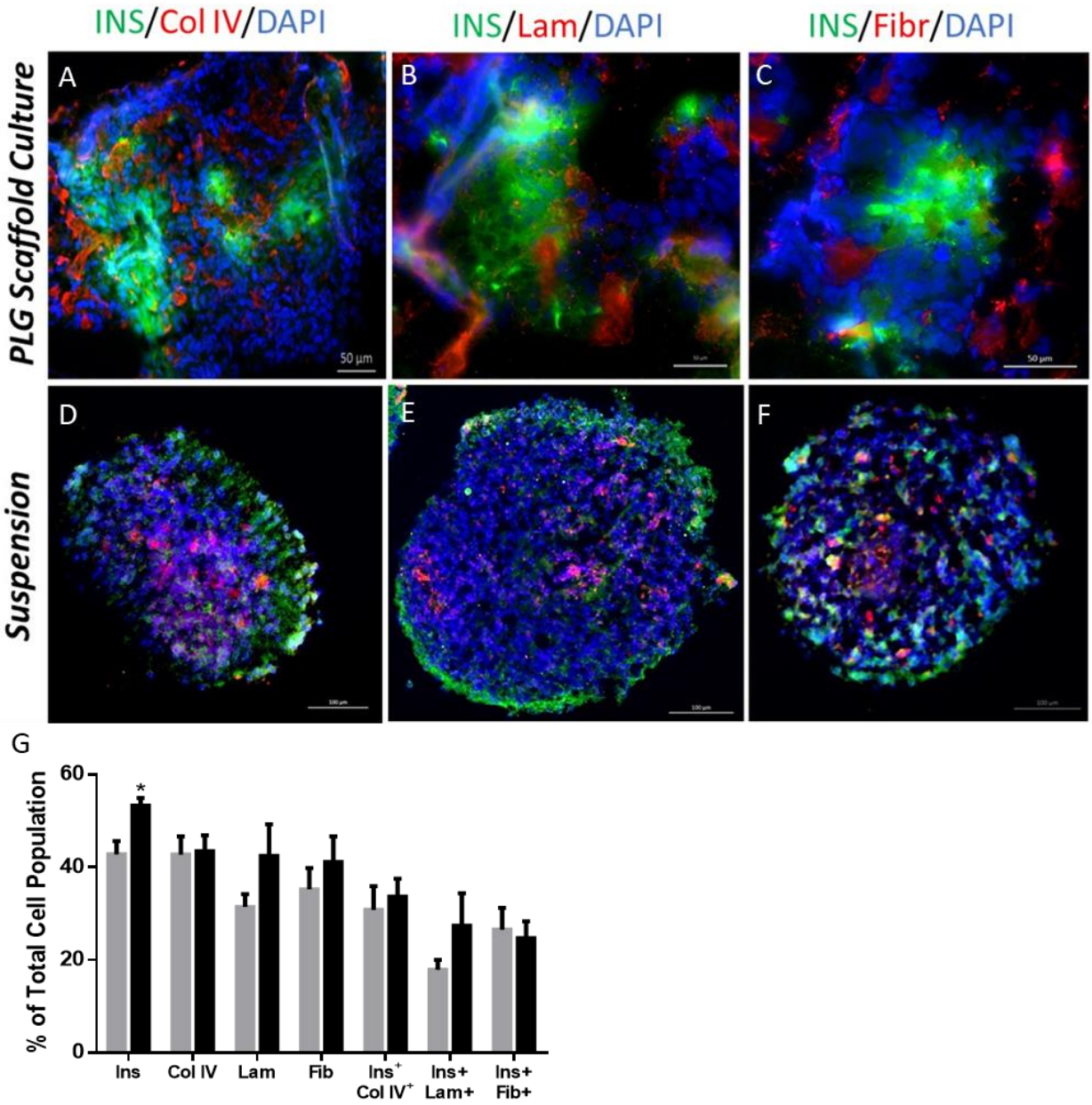

Figure 3.5 *Scaffold cultures permit hPSC-derived β-cell-secreted ECM deposition*

(A-F) Matrix composition surrounding β-cells is shown by representative immunofluorescent staining of PLG scaffold culture (A-C) and suspension cluster (D-F) for insulin (green), ECM protein (collagen IV, laminin, or fibronectin) (red) and DAPI (blue). (G) Immuno-histological analysis was performed using the percentage of $DAPI^+$ cells expressing insulin, ECM proteins and cells colocalized with insulin and ECM proteins in suspension (gray) and PLG microporous scaffolds (black) (*P≤0.05 compared to suspension, n = 4 biological replicates) with error bars representing SEM.

to suspension cultures (**Fig 3.5D-F**) (53 ± 2% vs 44 ± 3%, n=4, P≤0.05). Our results also showed ECM proteins commonly found in the extracellular matrix surrounding islets, i.e. collagen IV, laminin and fibronectin, were present in both suspension and scaffold cultures. Imaging analysis

confirmed that the percentage of $DAPI^+$ cells localized to ECM protein expression in the PLG scaffold cultures was comparable to suspension (collagen IV: 44 ± 4% vs 43 ± 4%; n=4; laminin: 42 ± 6% vs 31 ± 3%, n=4; fibronectin: 41 ± 5% vs 35 ± 5%, n=4) (**Fig 3.5G**). ECM protein was uniformly distributed across the cell cluster in both conditions as well. Thus, relative to suspension cultures, the scaffold provides a similar supportive matrix for β-cell clusters that consists of ECM proteins commonly found in the pancreas tissue.

3.4.6 β-cell maturation on ECM-modified microporous scaffolds

The presence of ECM protein deposition on the naked scaffold motivated studies in which ECM proteins commonly found in the pancreas were deposited on the scaffold prior to cell seeding as a means to further enhance maturation. Using qRT-PCR analysis, we investigated pancreatic progenitor maturation to β-cells on PLG scaffolds coated with either collagen IV, laminin or Matrigel. Naked microporous scaffolds and scaffolds coated with ECM proteins showed comparable levels of expression for endocrine transcription factors (*PDX1 and Nkx6.1)* (**Fig 3.6A**). However, only naked scaffolds and Matrigel coated scaffolds exhibited an increase in insulin expression relative to pancreatic progenitors. Evaluating cell maturation on the scaffolds also showed that, relative to pancreatic progenitors, only the naked scaffold cultures enhanced the expression of *PCSK1*. An analysis of the expression of pancreatic-related ECM genes demonstrated that the expression of *COL4A1* gene, coding for collagen type IV, in naked scaffolds as well as scaffolds coated with collagen IV and laminin was comparable to human islets. However, a decrease of *COL4A1* gene expression was observed in suspension cultures and scaffolds coated with Matrigel (**Fig 3.6B**). Laminin production, indicated by *LamA5* gene, was observed to be comparable to human islets across all culture conditions. Finally, we assessed cell maturation through glucose-responsive function. At the low glucose concentration, the cells on ECM-coated scaffolds and naked scaffolds secreted similar quantities of insulin (**Fig 3.6C**). However, for the high glucose concentration, we observed insulin secretion per cell increase for

only the laminin-coated, collagen IV-coated and naked scaffold cultures, averaging 0.6 ± 0.2, 0.6 ± 0.2 and 0.8 ± 0.2 μIU/10^3 cells, respectively. Interestingly, insulin secretion per cell on scaffolds coated with Matrigel (0.5 ± 0.2 μIU/10^3 cells) failed to respond to the individual glucose challenges.

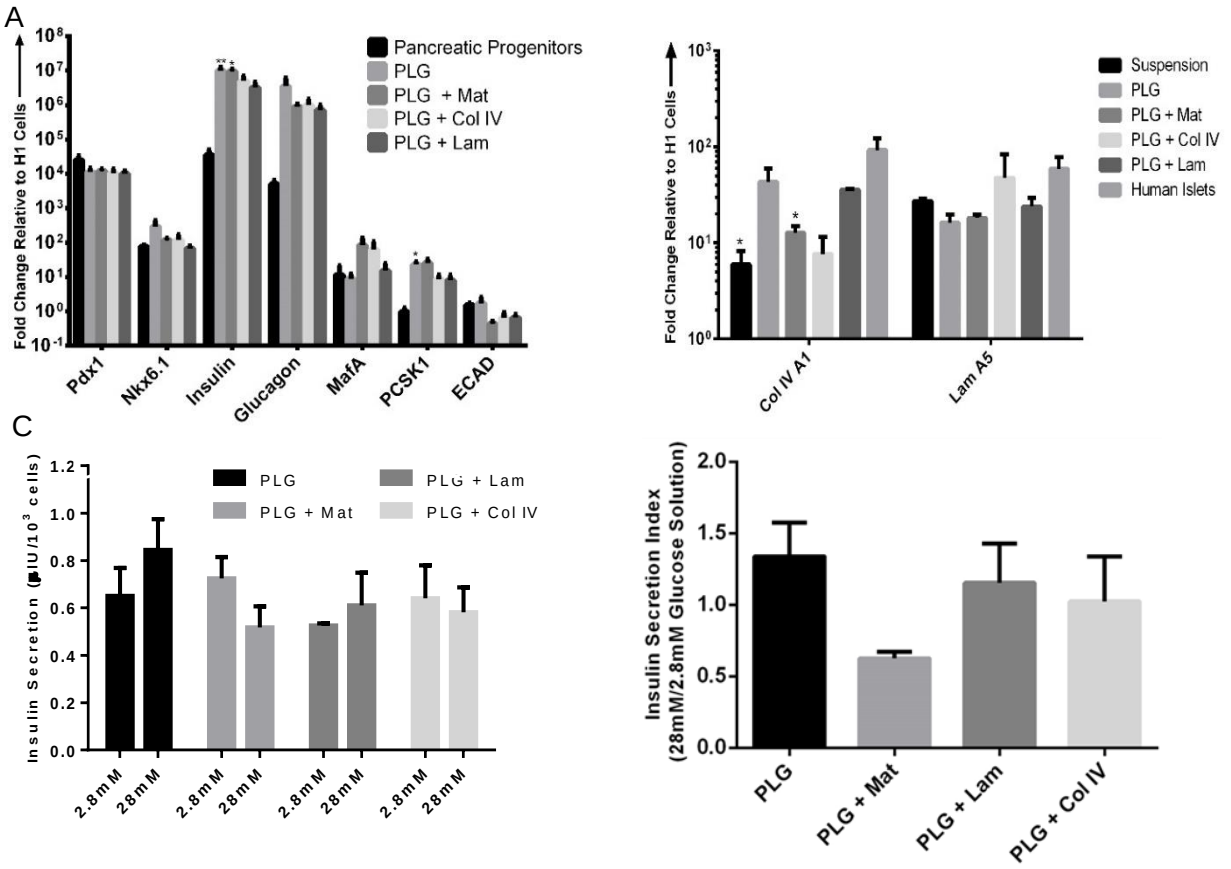

Figure 3.6 *Effects of ECM-modified scaffold cultures on pancreatic progenitor differentiation*

Pancreatic gene expression profile of pancreatic progenitor cells cultured on ECM-coated microporous PLG scaffolds (*P≤0.05, **P≤0.005 versus pancreatic progenitors using one-way ANOVA with Dunnett test for multiple comparisons, n = 4 biological replicates for all genes). (A) Gene expression for ColIVA1 and LamA5 of Stg6 β-cells. (*P≤0.05 compared to human islets using student t-test comparisons, n = 4 biological replicates for all genes) (B) Human insulin secretion in response to low and high glucose concentrations from PLG scaffold cultures coated with either Matrigel (Mat), laminin (Lam) or collagen IV (Col IV) under static conditions and compared to a non-coated PLG scaffold as a control (n = 3 biological replicates) (C) The stimulation index was calculated as the ratio of insulin release in high to low glucose concentrations (D) Error bars represent the SEM.

Using the stimulation index, we observed scaffold cultures pre-coated with ECM proteins did not have a significant improvement in β-cell function compared to naked scaffolds (0.63 ± 0.03 for PLG with Matrigel, 1.2 ± 0.2 for PLG with laminin, 1.0 ± 0.2 for PLG with collagen IV compared to 1.3 ± 0.2 for PLG, n=3) (**Fig 3.6D**). These findings indicate the initial introduction of ECM prior to

cell seeding on the scaffold does not substantially improve maturation at the end of the scaffold culture, which could be potentially due to deposition of cell-secreted matrix proteins throughout the culture.

3.5 Discussion

Our findings demonstrate that microporous scaffolds formed from synthetic materials can serve as a supportive matrix to promote the differentiation of hPSC-derived pancreatic progenitors toward insulin-producing glucose-responsive β-cells *in vitro.* Synthetic materials were used for these studies as they provide flexibility in synthesis and modification, have been widely applied for islet transplantation [286–288] and are generally easy to manufacture for large scale production. The scaffolds were designed to have a high porosity, a fully interconnected geometry, structural integrity, and a defined three-dimensional shape. Additionally, the microporous structure allows the 3D organization of cells into β-cell clusters, provides a high surface area-to-volume ratio for polymer–cell interactions, and allows nutrients to diffuse into the scaffold to support the growth of the seeded cells.

hPSC-derived β-cells cultured on the scaffold showed significantly increased gene expression levels of pancreatic endocrine hormones, insulin and glucagon, relative to pancreatic progenitors. Furthermore, the gene expression of β-cell maturation markers (*MAFA, PCSK1*, and *G6PC2*) were increased on the scaffold compared to the suspension clusters. Immunohistochemical stains showed that the percentage of Ins^+ cells in the PLG scaffold culture was increased compared to suspension cultures, suggesting that the scaffold cultures may have a higher efficiency at generating β-cells during differentiation. β-cell maturation was further investigated through glucose-responsive functional tests that demonstrated cells cultured on the scaffold had higher insulin secretion than suspension clusters. Our suspension control had gene expression that was comparable to the initial report by Rezania in 2014[256]. Unlike adult islets, this initial report indicates that suspension cultured cells do not secrete insulin in response to high concentrations of glucose either under static or perifusion conditions[256], consistent with our

results. While we demonstrate scaffold-based cultures can influence maturation down a β-cell lineage that can drive glucose stimulated insulin secretion, the insulin index ratio of scaffold cultures does not resemble the function of human islets, 3.2 ± 0.1, on average[24,25]. Future studies can further assess if the scaffold cultures are equipped to properly sense glucose and confirm if this factor is limiting insulin secretion at high glucose concentrations. The application of more recent protocols[255,289] to scaffold-based culture also offers the opportunity to further enhance glucose stimulated responses.

Despite their similar biomaterial design, the microporous PLG and PEG scaffolds also exhibited a few differences in how they influenced cell differentiation. Relative to suspension clusters, PEG scaffold cultures showed a more significant increase in the gene expression of β-cell maturation markers than PLG scaffolds. On the other hand, when investigating cell-cell interactions, only ECAD gene expression from PLG scaffold cultures showed a significant increase relative to the suspension cultures. This difference could have played a role in the higher insulin secretion observed in PLG scaffolds versus PEG scaffold cultures. Additionally, PLG scaffolds are a degradable material, unlike PEG, which could play a role in improved function as these scaffolds may allow for remodeling of the local environment. Both PEG and PLG are amenable to our fundamental objective – supporting β-cell maturation in a 3D environment– yet PLG and PEG have some differences. These variances may be due to their different mechanical and physical properties (i.e. hydrophobicity and protein adhesion) that could influence cell-cell and cell-matrix interactions. With this evidence of phenotypic differences between PLG and PEG scaffold cultures, these studies support future studies that investigate the mechanisms by which the distinct materials are directing the cellular responses.

In this study, we also show microporous scaffolds provide an environment conducive to controlling the size of the structures that could be essential for maturation. The size of transplanted islets has been previously reported to impact insulin secretion and viability [290–292].

Small islet clusters can exhibit low amounts of insulin secretion, which has been attributed to limited cell-cell contact, while excessively large clusters are considered to have limitations from nutrient availability [293]. Based on these results with islets, the influence of pore size, which would determine the hPSC-derived β-cell cluster size, was investigated. Our results suggest that clusters forming in pores with diameters greater than 250 μm maximized maturation toward β-cells. These results may reflect a contribution from the surface area to maturation. In addition, a scaffold with larger pores could have a greater interconnected porosity, thus, aiding diffusion of growth media as well as enabling a more uniform distribution of seeded cells into the scaffold. The seeding density, in combination with the pore size, was also shown to be critical for promoting cell-cell interactions. At low seeding densities, the cells were observed to primarily attach to the walls of the pores. However, increasing the cell density increasingly favored cluster formation and cell-cell interactions within the pore. Expression of E-cadherin was increased within scaffold culture relative to suspension culture, and E-cadherin staining was observed primarily between cells within the pores and not at the material surface. E-cadherin is a key player in maturation as studies have shown that E-cadherin immune-neutralization reduces both basal and glucose-stimulated insulin secretion [294]**.** Collectively, the microporous scaffold can be employed to control the formation of clusters, and to favor cell-cell interactions that are influential in maturation.

Protocols generally rely on hPSCs to spontaneously cluster in suspension resulting in the clusters varying in size [295–297], though efforts have started to focus on establishing a mechanism for controlling the size of the end-stage β-cell clusters due to the influence on long-term viability and the secretion of sufficient insulin [255,289]. While physical manipulation and shear have largely been employed to provide control of cluster size, the pores of the scaffold can provide direct control on cluster size, which may be advantageous for manufacturing. For large scale cell manufacturing in industrial or clinical settings, shear stress has been associated with challenges due to low cell viability and differentiation potential or abnormal morphology or gene expression

[298–300]. In our studies, the scaffold serving as a strategy to control cell cluster size could function in part to protect against adverse effects of shear during large scale manufacturing.

Similar to cell-cell interactions, interactions between stem cells and the extracellular matrix can induce lineage-specific differentiation and support the function of differentiated cells by providing a composite set of chemical and structural signals[301]. Herein, we report that differentiating cells deposited ECM proteins within the scaffold, with the composition resembling that found in the basement membrane around islets. Furthermore, we found ECM proteins were homogeneously distributed throughout the scaffold culture, thus, available for interaction with β-cells throughout the cluster. By culturing maturing β-cell clusters in microporous scaffolds versus suspension, cells are able to maintain a 3D morphology while interacting with a supportive matrix. A supportive matrix with which the clusters can interact could enhance cell maturation, as studies have shown ECM proteins such as collagen IV support the formation of cell structures, while also stimulating cell surface receptors to influence pancreatic cell processes[302]. Scaffold cultures also offer the opportunity to modify the local microenvironment surrounding the β-cell cluster that can be used to investigate the role of cell-matrix interactions during differentiation. Finally, suspension clusters will undergo manipulation during the transplantation process that could disrupt cell-cell and cell-matrix interactions. Whereas, for cells cultured in scaffolds, the scaffolds can maintain their niche that has been established within the pores, which can support the cell structures during transplantation.

Matrix deposition by the cells is likely a key step in maturation, as key integrins change over developmental stages [303]. This deposition of matrix initiates the formation of a niche, which is normally present in islets and influences maturation and function. Attachment of cells to ECM may also benefit β-cells by maintaining tissue architecture and preserving specific intercellular relationships within the pores. Interestingly, scaffolds coated with either collagen IV, laminin or Matrigel showed comparable gene expression levels of maturation markers to naked scaffolds

relying on cell-secreted ECM, which contained collagen IV, laminin and fibronectin. This was supported by the analysis of glucose-responsive insulin secretion on ECM coated scaffolds and naked scaffolds that showed β-cell function was similar across all conditions as well. These results suggest the matrix deposited by the cells on the PLG scaffold has the potential to mimic more of the complex niche environment during pancreatic development compared to the individual ECM proteins, and the ECM deposition may mask the impact of the adsorbed ECM proteins.

3.6 Conclusion

This research demonstrates that scaffolds have the potential to serve as a component within the process of manufacturing β-cells. The scaffold design can be tuned to control cluster size, promote cell-cell interactions and permit ECM deposition on the scaffold to create a supportive niche. Similar to organoid development in three-dimensional cultures, the pancreatic progenitors establish a functional niche during *in vitro* scaffold culture. Furthermore, the scaffolds are formed from materials that have been used *in vivo*, and thus the cell-material construct could be directly transplanted, which would have the added advantage of maintaining the niche that has developed within the scaffold. Collectively, microporous scaffolds demonstrate the feasibility as a biomanufacturing platform to generate insulin-producing glucose-responsive β-cells.

Chapter 4: *In Vitro* Modifications to Pancreatic Progenitor Cluster Maturation and Seeding on Microporous Scaffold Cultures for Enhancing Islet Organoid Maturation

4.1 Abstract

Patients with type 1 diabetes could benefit from cell-based insulin treatments, but the supply of human islet tissue is limited. Recently, we developed microporous scaffold culture procedures that generate functional islet organoids derived from a limitless source of human pluripotent stem cells (hPSCs). However, obstacles still need to be overcome in order to improve the maturation process efficiency of the final product. One critical hurdle is to ascertain that the hPSC-derived β-cells function equivalently to their endogenous counterparts. Herein, our studies focused on modifying differentiation protocols and process techniques to better understand mechanisms that can enhance the functional maturation of islet organoids cultured on microporous scaffolds. An engineered insulin reporter helped assess the function of individual cells by measuring insulin storage and secretion *in vitro*. By modifying the timing of cell seeding from pancreatic progenitor to pancreatic endoderm, islet organoids showed increased amounts of insulin secreted per cell. In addition, cluster integrity and minimized cell manipulation during the differentiation was shown to be influential to the development of the islet organoids. Finally, we evaluated seeding scaffolds with dense clusters instead of a single suspension. We found that dissociating clusters to seed as single cells on scaffolds can hinder islet organoid maturation. Together, these *in vitro* modifications to the scaffold culture differentiation process provide rational guidelines towards recapitulating the complexity of mammalian organogenesis to generate cells that more closely resemble mature human islets.

4.2 Introduction

Over the past few decades, the process of differentiating human pluripotent stem cells (hPSCs) down specific cell lineages has shown significant improvements, though some limitations have been observed with organoid formation on traditional culture systems. These breakthroughs have allowed the differentiation of various hPSC populations into somatic cell derivatives *in vitro*[23,25,304]. However, studying tissue patterning and organ morphogenesis *in vitro* has been hindered by the lack of appropriate culture systems that would allow the cell-cell and cell-matrix interactions needed for organoid formation[305]. Organoids are 3D cell culture systems that mimic some of the structural and functional characteristics of an organ. In order to produce these appropriate 3D culture systems, the field has turned to engineered biomaterials that can spatially enable cellular interactions that are needed for organ formation[67]. Many organoid cultures are grown without any spatial constraints in ill-defined 3D matrices, which allow only limited tunability and reproducibility[306,307]. By contrast, the biochemical and biophysical properties of engineered matrices can be tuned to support the development and maturation of organoid cultures that could transform drug development and research for diseases, like diabetes.

Islet organoids are being developed as treatment for Type 1 diabetes (T1D), which is a metabolic syndrome characterized by elevated blood glucose levels that result from reductions in insulin production or action. To date, insulin-expressing cells can be generated from hPSCs *in vitro* to provide a therapeutic source however the difficulty of controlling the fate and development of these cells in the body poses a challenge to diabetes treatment. Recently, islet organoids consisting of pancreatic α, β, and δ cells were able to be generated in Matrigel-collagen scaffolds but neither material is Food and Drug Administration–approved for clinical applications[308]. Synthetic polymer scaffolds provide flexibility in synthesis and modification, have been widely applied for islet transplantation[278,280,309,310] and are clinically-translatable. The scaffolds can be designed to have a high porosity, a fully interconnected geometry, structural

integrity, and a defined three-dimensional shape. Our prior studies demonstrated the ability to direct pancreatic differentiation of hPSCs on microporous scaffolds in order to generate functional early-stage islet organoids [311]. However, while we demonstrated scaffold-based cultures can enhance maturation, we remained unable to obtain functional human pancreatic – particularly insulin-producing – cells performing on par with native islets. The application of more recent protocols[25,312] to scaffold-based culture offers the opportunity to further enhance glucose stimulated responses. In addition, it has been shown that only a subset of pancreatic progenitor cells, marked by $Pdx1^+$ and $Nkx6.1^+$ expressing cells, may be competent to generate mature, insulin-expressing cells[313]. This suggests the need for tools that can help further investigate mechanisms that influence the production of a heterogenous population of mature and immature cells within the derived pancreatic clusters.

In this chapter, we present the application of improved culture systems for islet organoid formation, as well as the engineering of the hPSCs for monitoring the maturation and function of islet organoids non-invasively. This investigation will help identify subtle differences that exist at the transcriptomic and protein expression levels that can affect β-cell survival/proliferation and insulin release. Prior studies assessed heterogenous function in islets using human proinsulin with C-peptide-bearing superfolder green fluorescent protein (sfGFP-Cpep) expressed in transgenic mice[314]. By a moderate decrease in fluorescence intensity, the insulin reporter was used to reveal a rapid dispossession of insulin in only a small subset of the islet population in the mouse pancreas when challenged by glucose. This technology for assessing functional heterogeneity between individual cells can be applied towards our studies in order to help identify environmental influences that control the commitment of pancreatic progenitor cells towards a final functional fate. Thus, we developed an insulin reporter that provides unprecedented insight into cellular interactions that drive the maturation process within a 3D matrix, and can also assess dynamic insulin secretion by individual cells.

We then use this reporter cell line to characterize the environmental influences that affect hPSC differentiating into islet organoids, specifically insulin-producing β-cells. The derivation of functional islet organoids cultured on synthetic microporous scaffolds can provide a tool to molecularly dissect islet organoid development. This technology may also enable therapeutic advances by supporting the generation of a high-quality source of cells for regenerative medicine.

4.3 Materials and Methods

4.3.1 Microporous scaffold fabrication

Poly(lactide-co-glycolide) (PLG) microporous scaffolds were fabricated as previously described[277]. Briefly, PLG microporous scaffolds were fabricated by compression molding PLG microspheres (75:25 mole ratio D,L-lactide to glycolide) and 500 to 600 μm micron-sized salt crystals in a 1:30 ratio of PLG microspheres to salt. The mixture was humidified in an incubator for 7 min and then thoroughly mixed again. Scaffolds were compression molded with 77.5 mg of polymer–salt mixture into cylinders 5 mm in diameter by 2 mm in height using a 5 mm KBr die (International Crystal Laboratories, Garfield, NJ) at 1500 psi for 45s. Molded constructs were gas foamed in 800 psi carbon dioxide for 16 h in a pressure vessel. The vessel was depressurized at a controlled rate for 30 min. On the day of cell seeding, scaffolds were leached in water for 1.5 h, changing the water once after 1 h. Scaffolds were disinfected by submersion in 70% ethanol for 30 seconds and rinsed multiple times with phosphate buffer solution (PBS).

4.3.2 Culture of undifferentiated cells

All cell culture work was performed with the HUES8 hESC line, generously provided by Dr. Douglas Melton (Harvard University) and has been previously published on[24,25], and H1 hESC line obtained from the WiCell Research Institute (Madison, WI). Undifferentiated hPSC lines were cultured using mTeSR1 (StemCell Technologies; 05850) in 30-mL spinner flasks (REPROCELL; ABBWVS10A or ABBWVS03A) on a stirrer plate (Chemglass) spinning at 60

rpm in a humidified 5% CO2 37°C incubator. Cells were passaged every 3–4 days by single-cell dispersion using TrypLE Express (Life Technologies).

4.3.3 Differentiation of hPSCs and scaffold seeding

hPSC differentiations were performed in 30-mL spinner flasks on a stirrer plate set at 60 RPM in a humidified incubator set at 5% CO_2 and 37 °C. hPSCs were differentiated to SC-β cells using the protocol previously described[25]. Briefly, undifferentiated cells were single-cell dispersed and seeded at 6×10^5 cells/mL in a 30-mL spinner flask. Cells were cultured for 72 hr in mTeSR1 and then cultured in the differentiation media for 6 stages. To initiate scaffold culture differentiations, Stg5 pancreatic endoderm clusters were seeded either as single cells or dense clusters on scaffolds at 125 million cells/cm^3 then further differentiated according to the protocol[2]. Prior to cluster seeding, scaffolds were washed in cell media solution then briefly dried on sterile gauze to improve the absorption of the cell solution into the scaffold. Clusters were distributed across both faces of the scaffold and then incubated for 10min to allow cell solution to be further absorbed into the scaffold before differentiation media was added. Traditional hPSC suspension culture was differentiated per the described protocol to provide an internal control[25].

4.3.4 Designing sfGFP-Cpep fluorescent insulin reporter hPSC line

Briefly, HEK293FT cells were co-transfected using lentiviral packaging vectors (pMDL-GagPol, pRSV-Rev, pIVS-VSV-G, with a sfGFP-Cpep construct[314,315] using Lipofectamine 2000 (Life Technologies, Grand Island, NY,) for 48 h. The sfGFP-Cpep construct (i.e., with the Superfolder-GFP cDNA[316] ligated into the XhoI site of the human C-peptide coding sequence[315]) driven by the upstream 2.2-kb rat Ins1 promoter included a phosphoglycerol kinase (PGK)-promoter-mCherry selection marker. Using PEG-it (System Biosciences, Mountain View, CA), supernatant was concentrated for 24 h. Then it was precipitated using ultracentrifugation, resuspended in PBS and stored at −80 °C until use. Through viral transfection and FACS

sorting, clones can be identified in which the vector was correctly integrated into the cell line. The sfGFP-Cpep cell line was then expanded into a subclonal population and characterized.

4.3.5 qRT-PCR analysis

Gene expression analysis on fixed, sorted cells was obtained by first centrifugation of the cell pellet at 60 g for 1min at 4°C. The supernatant was discarded. Total RNA was isolated from the pellet using the RecoverAll Total Nucleic Acid Isolation kit (Ambion), starting at the protease digestion stage of manufacturer recommended protocol. The following modification to the isolation procedure was made: instead of incubating cells in digestion buffer for 15 minutes at 50°C and 15 minutes at 80°C, we carried out the incubation for 1 hour at 50°C. RNA concentration was determined using a NanoDrop spectrophotometer. The iScript™ Reverse Transcription Supermix was used to transcribe RNA into cDNA. Universal RT microRNA PCR assays were performed using SYBR Green MasterMix Universal RT (Exiqon), according to the

Table 4.1 Primers used for qPCR analysis

gene	primer	sequence (5' to 3')
PDX1	forward	CCTTTCCCATGGATGAAGTC
PDX1	reverse	CGTCCGCTTGTTCTCCTC
Nkx6.1	forward	GGGGATGACAGAGAGTCAGG
Nkx6.1	reverse	CGAGTCCTGCTTCTTCTTGG
MafA	forward	GAGAGCGAGAAGTGCCAACT
MafA	reverse	TTCTCCTTGTACAGGTCCCG
Insulin	forward	TTCTACACACCCAAGACCCG
Insulin	reverse	CAATGCCACGCTTCTGC
Glucagon	forward	TGCTCTCTCTTCACCTGCTCT
Glucagon	reverse	AGCTGCCTTGTACCAGCATT
ECAD	forward	TTGACGCCGAGAGCTACAC
ECAD	reverse	GACCGGTGCAATCTTCAAA
PCSK1	forward	CTCTGGCTGCTGGCATCT
PCSK1	reverse	CGGGTCATACTCAGAGGTCC
NEUROD1	forward	GCCCCAGGGTTATGAGACTAT
NEUROD1	reverse	ATCAGCCCACTCTCGCTGTA
NGN3	forward	CTATTCTTTTGCGCCGGTAG
NGN3	reverse	CTTCGTCTTCCGAGGCTCT

manufacturer's instructions. The amplification profile was assessed using a LightCycler® 480 (Roche, Germany). Gene expression was quantified using the ΔΔCt method and fold change was calculated using the formula $2^{-\Delta\Delta Ct}$. Values for the genes of interest were normalized to the housekeeping gene (GAPDH) followed by normalization to marker expression in hPSCs.

4.3.6 Static glucose-stimulated insulin secretion

This assay was performed in KRB buffer consisting of 128 mM NaCl, 5 mM KCl, 2.7 mM $CaCl_2$ 1.2 mM $MgSO_4$, 1 mM Na_2HPO_4, 1.2 mM KH_2PO_4, 5 mM $NaHCO_3$, 10 mM HEPES (Gibco; 15630-080), and 0.1% BSA. After preincubating the cells at 2 mM glucose, clusters were incubated for 1 hr at 2 mM glucose followed by 1 hr at 20 mM glucose. Insulin in the supernatant from these 1 hr incubations was quantified with a Human Insulin ELISA (ALPCO; 80-INSHU-E10.1). Viable cell numbers were determined using a hemocytometer. For monitoring dynamic function, cells containing the sfGFP-Cpep construct or control cells (no construct) in basal culture media were imaged on a Leica DM IRB fluorescence microscope to establish the baseline insulin levels. Subsequently, the sfGFP-Cpep cells or control cells will be treated with saline or culture media containing 20 mM glucose for 1 hour, and then imaged again. The time series images were presented as a stack of multiple images which were analyzed as a hyperstack using ImageJ/Fiji software, version 1.8[317]. They were first corrected for translational movement using the StackReg feature, and then a thresholded-base mask was used defining the insulin-positive area superimposed on the scaffold culture area. Then this area was analyzed with Regions of Interest (ROI) for each entire islet cluster, and a fluorescence intensity profile was generated using the data. Flow-thru was also collected for insulin quantification.

4.3.7 Flow Cytometry

Clusters were single-cell dispersed with Trypsin, fixed with 4% paraformaldehyde for 30 min at 4 °C, blocked and permeabilized with staining buffer for 30 min at 4 °C, incubated with primary antibodies in staining buffer overnight at 4 °C, incubated with secondary antibodies in staining buffer for 2 hr at 4 °C, resuspended in staining buffer, and analyzed. Scaffold cultures

were washed in ice-cold RPMI media, then minced and digested in 10 mL of 1mg/ml Type II collagenase (Sigma-Aldrich Inc., St. Louis, MO, USA) at 37°C, 30 minutes with vigorous shaking. Tissue homogenate was then strained through a 100μm filter and washed in PBS. Samples were then fixed, stained with antibodies and analyzed using a LSR Fortessa flow cytometer (Becton, Dickinson & Co., Franklin Lakes, New Jersey, USA). Compensation and data analysis were completed using FlowJo software (FlowJo, LLC, Becton, Dickinson & Co., Franklin Lakes, NJ, USA). All antibodies were used at 1:300 dilution except where noted. The antibodies used were: rat-anti-C-peptide (DSHB; GN-ID4-S), mouse-anti -nkx6.1 (1:100; DSHB, F55A12-S), goat-anti-pdx1(R&D Systems; AF2419), anti-mouse-alexa fluor 647 (Invitrogen; a31571), anti-goat-alexa fluor 405 (Abcam; ab175664), anti-rat-alexa fluor 405 (Abcam; ab175671),

4.3.8 Animals

Male NSG mice (Jackson Laboratories, Bar Harbor, ME, United States) between 8 and 10 weeks of age received an intraperitoneal injection of 130 mg/kg streptozotocin 4–7 days prior to transplant. (Sigma-Aldrich, St. Louis, MO). Each day leading up to surgery, blood glucose levels were measured using the tail vein prick technique (Accu-chek/Roche, Basel, Switzerland), and body weight was recorded. The criteria to include a mouse in the study was the following: glucose readings above 350 mg/dL on 2 consecutive days leading up to transplant surgeries, and no more than a 20% reduction in weight since streptozotocin injection. Following surgery, glucose and body weight for each mouse were measured three times per week. All studies involving mice were approved by the University of Michigan Animal Care and Use Committee.

4.3.9 Transplantation studies

Cell-laden scaffolds were implanted as previously described[318]. Briefly, mice were anesthetized with 2% isoflurane until loss of consciousness was confirmed by pinch reflex test.

The abdominal area was shaved and sterilized with betadine and ethanol. An approximate 5 mm incision was made in the peritoneal wall, in the middle of the abdominal region, and the epididymal fat pads (EFP) were located and unwrapped outside of the abdominal wall. Scaffolds were wrapped within the epididymal fat pad, then placed back into the peritoneal cavity. The incision was then closed in 2-layers using absorbable suture. Mice were given a dose of 0.005 mg/gram body weight Rimadyl carprofen (Zoetis, Florham Park, NJ, United States) and allowed free access to food and water postoperatively. After 30 days, blood serum was collected to quantify circulating human C-peptide levels. Mice were fasted 5 h before blood collection. Thirty minutes prior to blood collection, mice received an intraperitoneal injection of 2 g/kg glucose in the form of 20% glucose. Approximately 200 µL of blood was collected from the saphenous vein during the period between 30 and 60 min post glucose stimulation. Serum was collected from whole blood by 20 min of coagulation followed by centrifuging at 2000g for 20 min. Isolated serum was analyzed for human C-peptide levels using the manufacturer's provided ELISA protocol (AbCam, Cambridge, MA, United States).Mice were euthanized between 30-50 days post-transplant for post-analysis.

4.3.10 Statistics

All statistical analyses were conducted using Prism graphing and data analysis software (GraphPad Software, Inc., La Jolla, CA, United States). Statistical differences were determined using non-parametric testing; an unpaired two-tailed Student t test or one-way ANOVA with Dunnett test for multiple comparisons. Values were reported as the mean ± standard error of mean (SEM). n indicates the total number of biological replicates.

4.4 Results

4.4.1 Transplantation of islet organoid scaffold cultures for in vivo maturation

We previously detailed an approach generating islet organoids on microporous PLG scaffolds that produced hPSC-derived β cells capable of undergoing glucose-stimulated insulin

secretion (GSIS) in static incubations. We sought to further assess the maturation of islet organoids cultured on scaffolds by testing their capacity to function *in vivo*. The transplantation process consisted of transplanting the islet organoids in the epididymal fat pad of immunocompromised mice that had been chemically induced to be diabetic with streptozotocin (STZ). The implantation process involved minimal manipulation on the islet organoids as they were already supported by the biomaterial scaffold for delivery. After transplantation in the diabetic mice, we evaluated function by assessing fasting blood glucose levels over 50 days (**Fig 4.1A**). Human C-peptide in the blood was detected after 30 days, 0.58 ± 0.16 ng/mL, however after 50 days it was no longer detectable. (**Fig 4.1B**). We observed that, after 50 days, the grafts did not demonstrate a systemic effect on glucose metabolism. qRT-PCR analysis was conducted on cells after 30 days and 50 days post implantation to characterize islet organoid *in vivo* maturation. We found, after 30 days, transplanted cells showed increased gene expression levels of the endocrine hormone marker gene for insulin relative to the *in vitro* control. (**Fig 4.1C**). Additionally, expression of a key β-cell maturation marker, MafA, increased relative to the *in vitro* scaffold culture control. MAFA (a basic leucine zipper transcription factor) is expressed in adult β-cells and is thought to be critical in establishing β-cell function in adult islets[319–322]. After 50 days, however, we no longer observed an increase in the expression of β-cell function in the transplanted cells relative to the *in vitro* control.

These results suggest the maturing scaffold cultures were able to secrete insulin *in vivo* up to 30 days but not at a therapeutic dose capable of restoring euglycemia in diabetic mice. Further *in vitro* maturation could enhance the development of the islet organoids *in vivo*. The current differentiation protocol generated scaffold cultures with an *in vitro* glucose-responsive insulin secretion index ratio of 1.3 ± 0.2, which is significantly lower than human islets, 3.2 ± 0.1, on average[24,25]. Thus, we sought to utilize a protocol described in Velazco-Cruz et al. (2019), referred to here as the Velazco-Cruz protocol, and, with modifications to either the protocol or

our process techniques, better understand how to enhance islet organoid maturation on microporous scaffolds.

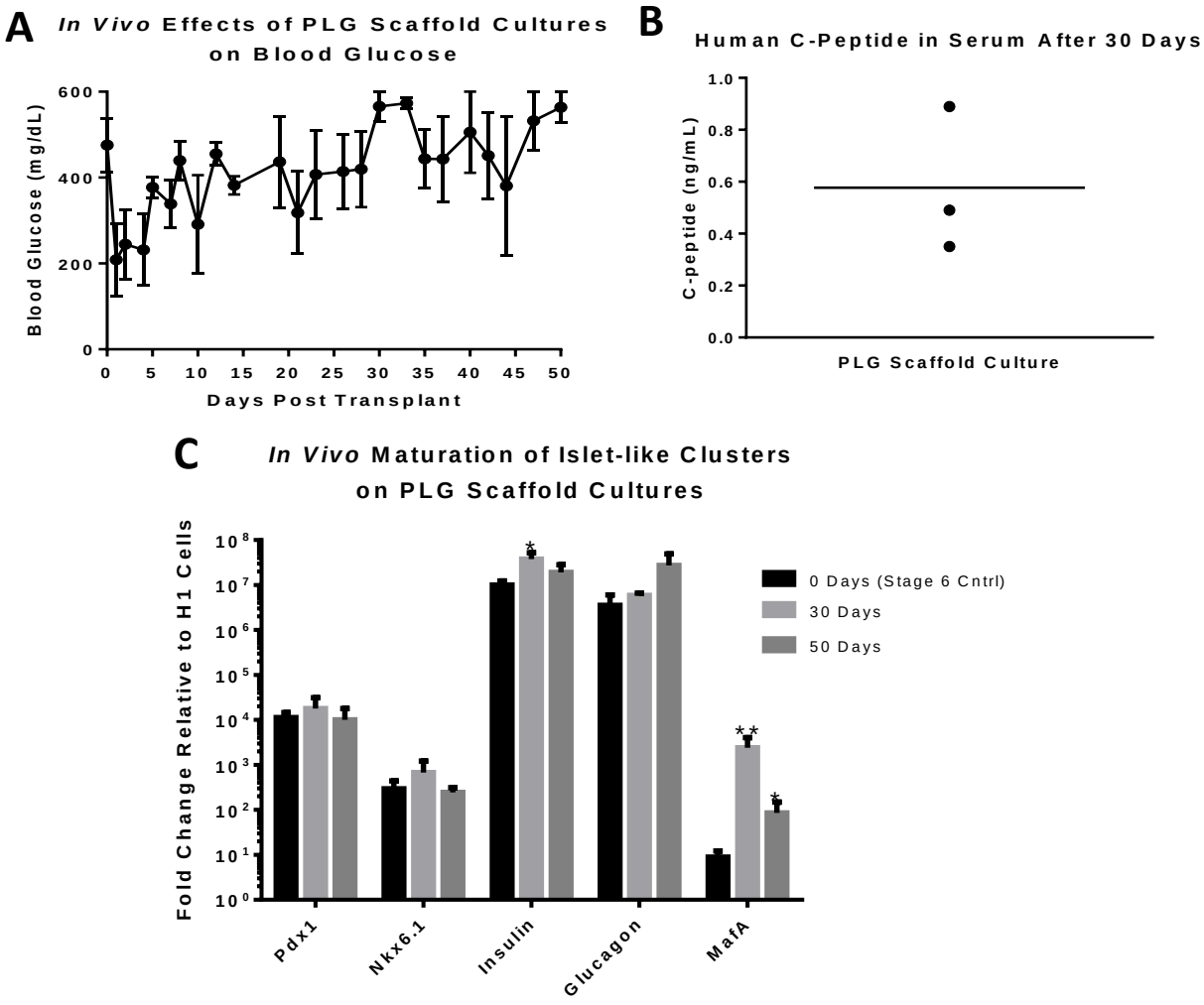

Figure 4.1 *In vivo function and maturation of hPSC-derived insulin-producing clusters on scaffold cultures*

(A) Blood glucose measurements of mice transplanted with PLG scaffold cultures over 50 days (n=3). (B) Human C-peptide levels from individual mice are shown on a box and whisker plot. (C) Gene expression of pancreatic endocrine hormones, β-cell-associated transcriptional factors, and β-cell function-related proteins in hPSC-derived insulin-producing clusters prior to transplantation (stage 6), 30 days after transplantation and 50 days after transplantation. (*P≤0.05, **P≤0.01 compared to pre-transplantation control using one-way ANOVA with Dunnett test for multiple comparisons, n = 3 biological replicates for all genes). Error bars represent the standard error of mean (SEM).

4.4.2 Characterization of islet organoid maturation on scaffolds using fluorescent insulin reporter

We first assessed if seeding scaffolds with cells resembling a more mature stage 5 pancreatic endoderm rather than stage 4 pancreatic progenitors could better utilize the scaffold microenvironment and, thus, enhance functional maturation. The Velazco-Cruz protocol

incorporates 3D cultures that were shown to help maintain cluster integrity and enhance progenitor development[25]. The six-stage protocol also involves a dissociation step where pancreatic progenitor clusters are reaggregated to help generate almost pure populations of endocrine cells containing β-like cells that secrete high levels of insulin and express β cell markers. However, we did not perform this dissociation step as we found reaggregating clusters to be a challenging process. This could be attributed to the amount of manipulation required to dissociate the clusters into single cells. Flow analysis was conducted to characterize the development of pancreatic endoderm cells prior to seeding on scaffolds. hPSCS were induced into pancreatic progenitors with approximately 29.9 ± 3.1% $PDX1^{+}Nkx6.1^{+}$ cells and, subsequently, pancreatic endoderm with an increased $PDX1^{+}Nkx6.1^{+}$ population, 36.1 ± 1.1% cells, and 22.3 ± 2.0% $C\text{-}pep^{+}Nkx6.1^{+}$ cells (**Fig. 4.2A**). Thus, the protocol showed an increase in C-peptide^{+} cell populations, a protein produced by the insulin gene, in addition to β-cell markers, $PDX1^{+}$ and $NKX6\text{-}1^{+}$, as the cells differentiated. Pancreatic endoderm cells were then dissociated into single cells and seeded on porous PLG scaffolds. Clusters formed within the first 24 hours and were then cultured for 10-14 days in order to generate functional, insulin-producing clusters. Notably, analysis of protein expression in cells cultured on scaffolds revealed an increase in pancreatic transcription factors, PDX1 and Nkx6.1, relative to the pancreatic progenitor control (**Fig. 4.2B**). Additionally, we observed increased expression of endocrine hormone marker genes, insulin and glucagon. Maturation markers commonly used to indicate insulin processing were assessed and showed MafA expression in cells cultured on scaffolds increased compared to progenitor controls.

A sfGFP-Cpep construct[323,324] was then used to investigate the differentiation efficiency, heterogeneity in maturation and reproducibility of this approach. The construct includes a phosphoglycerol kinase (PGK)-promoter-mCherry marker for selection through FACS. This construct was transduced into the H1 line using a lentivirus, sorted and a subclonal population was then generated. Flow analysis of insulin-producing cells cultured on scaffolds confirmed the

GFP marker could be used as a reporter for C-peptide since the percentage of GFP$^+$ cells was comparable to the percentage of C-peptide$^+$ cells within the total cell population (**Fig. 4.2C**). Gene

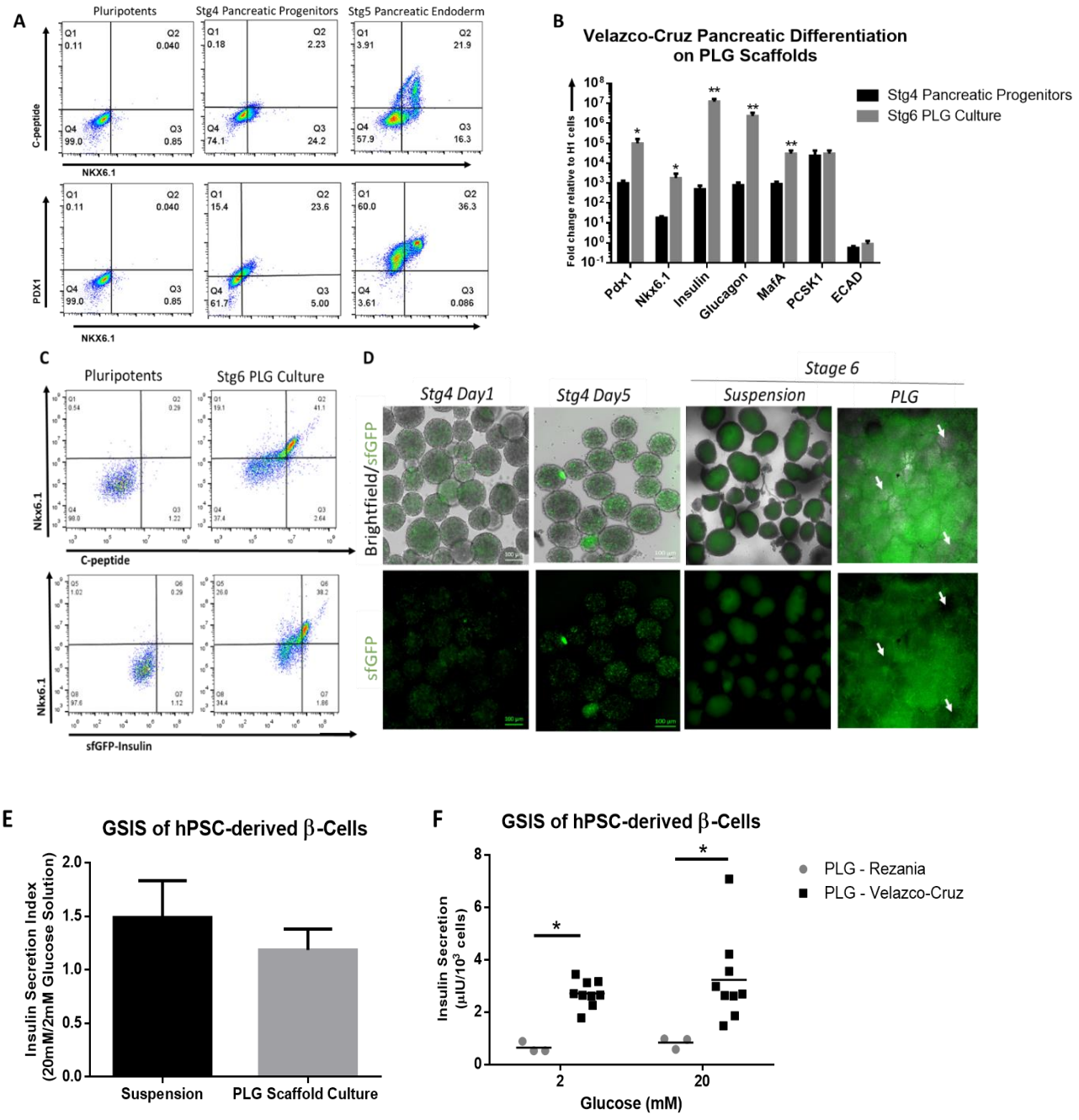

Figure 4.2 *hPSC-derived β-cell maturation using Velazco-Cruz protocol on PLG scaffolds with sfGFP-Cpep reporter*
(A) Representative flow cytometric dot plots of dispersed stage 4 and stage 5 clusters immunostained for the indicated markers. (B) Gene expression of pancreatic markers in stage 4 pancreatic progenitors and insulin-producing stage 6 clusters (*P≤0.05, **P≤0.01 compared to pancreatic progenitor, n = 6). (C) Differentiated stage 6 insulin-producing clusters derived from sfGFP-Cpep hPSC cells were analyzed by flow cytometry. Undifferentiated sfGFP-Cpep hPSCs were used for negative gating of sfGFP-Cpep expression. (D) Bright-field and fluorescent images of differentiated clusters in suspension and scaffold cultures are shown; scale bars, 100 μm. White arrows show scaffold matrix. (E) Human insulin secretion from PLG scaffold cultures generated with either the Rezania or Velazco-Cruz protocol in response to low and high glucose concentrations under static conditions (Rezania scaffold cultures: n = 3 biological replicates, Velazco-Cruz: n = 8 biological replicates). (F) The stimulation index was calculated as the ratio of insulin release in high to low glucose concentrations (*P≤0.05, **P≤0.01 compared to suspension, n=3-4 biological replicates). Error bars represent the SEM.

expression analysis of transduced cells and non-transduced cells demonstrated that the viral transduction did not affect the ability for hPSCs to differentiate down the pancreatic lineage (data not shown). Live imaging shows insulin content within sfGFP-Cpep cells as they differentiated towards a pancreatic lineage (**Fig. 4.2D**). After stage 5, we observed GFP^+ cells uniformly distributed within the clusters and an increase in GFP^+ cells as pancreatic progenitors underwent maturation in both suspension and on scaffold cultures.

The functional maturation of these insulin-producing clusters in scaffolds was examined by their ability to secrete insulin in a glucose-responsive manner through GSIS. Scaffold cultures generated using the protocol detailed in either the Velazco-Cruz protocol or Rezania et al. 2014, referred to here as the Rezania protocol, were exposed to 2 mM and 20 mM glucose solutions. We found the insulin index ratio for the scaffold cultures, 1.2 ± 0.3, was similar to both the suspension, 1.5 ± 0.4, (**Fig. 4.2E**) and the prior scaffold cultures generated using the Rezania protocol[311]. At the low glucose concentration, the cells generated on scaffolds with the Velazco-Cruz protocol secreted increased quantities of insulin relative to cells generated with the Rezania protocol (2.7 ± 0.2 versus .7 ± 0.1 μIU/10^3 cells, P≤0.05, n= 4-7) (**Fig. 4.2F**). At the high glucose concentration, we also observed an increase in insulin secretion per cell from the Velazco-Cruz scaffold cultures relative to the Rezania protocol (3.2 ± 0.6 and 0.8 ± 0.1 μIU/10^3 cells, P≤0.05, n= 4-7). Thus, we were able to show that scaffold cultures seeded with a more

mature progenitor cells resembling pancreatic endoderm were able to enhance the maturation of the insulin-producing clusters indicated by increased MafA gene expression and enhanced insulin secretion per cell. However, the glucose-responsive insulin index ratio did not show a significant improvement, thus, we sought to modify the protocol to address the challenges with reaggregating clusters that could be limiting the generation of cells with enhanced glucose-responsive function.

4.4.3 Modifications to the Velazco-Cruz protocol for aggregating dissociated pancreatic progenitors to influence islet organoid maturation

Reaggregating clusters after the pancreatic progenitor state has been shown to act as a endocrine purification process that improves cluster maturation[25,312,325,326]. Thus, we aimed to investigate if incorporating this protocol step, thereby removing non-endocrine cells, would influence islet organoid development and function. Since this step was challenging with 3D dense clusters, we utilized the 2D culture detailed in the Rezania protocol to generate stage 4 pancreatic progenitors then transitioned the cells to a 3D culture using the Velazco-Cruz protocol for further maturation. This modified protocol, referred to here as the Rezania-Cruz protocol, leveraged some of the established processes used for traditional 2D cultures that were still being developed for a 3D environment. As a result, we found dissociating pancretic progenitors in a 2D monolayer required less manipulation and generated higher cell viability compared to dissociating 3D clusters.

Using the sfGFP-Cpep cell line, we generated pancreatic progenitor cells on a 2D plate and observed trace amounts of cells expressing insulin (**Fig. 4.3A**). However, after progenitors were dissociated and allowed to aggregate in suspension, we observed cluster formation and an increase in GFP^+ cells within the clusters. Enhanced cluster maturation after the aggregation step was assessed by qRT-PCR analysis. Aggregated clusters showed an increase in insulin expression as well as the maturation marker, MafA, relative to the prior day's progenitor cells in 2D monolayer (**Fig. 4.3B**). We found clusters did not form without including Y27632, a

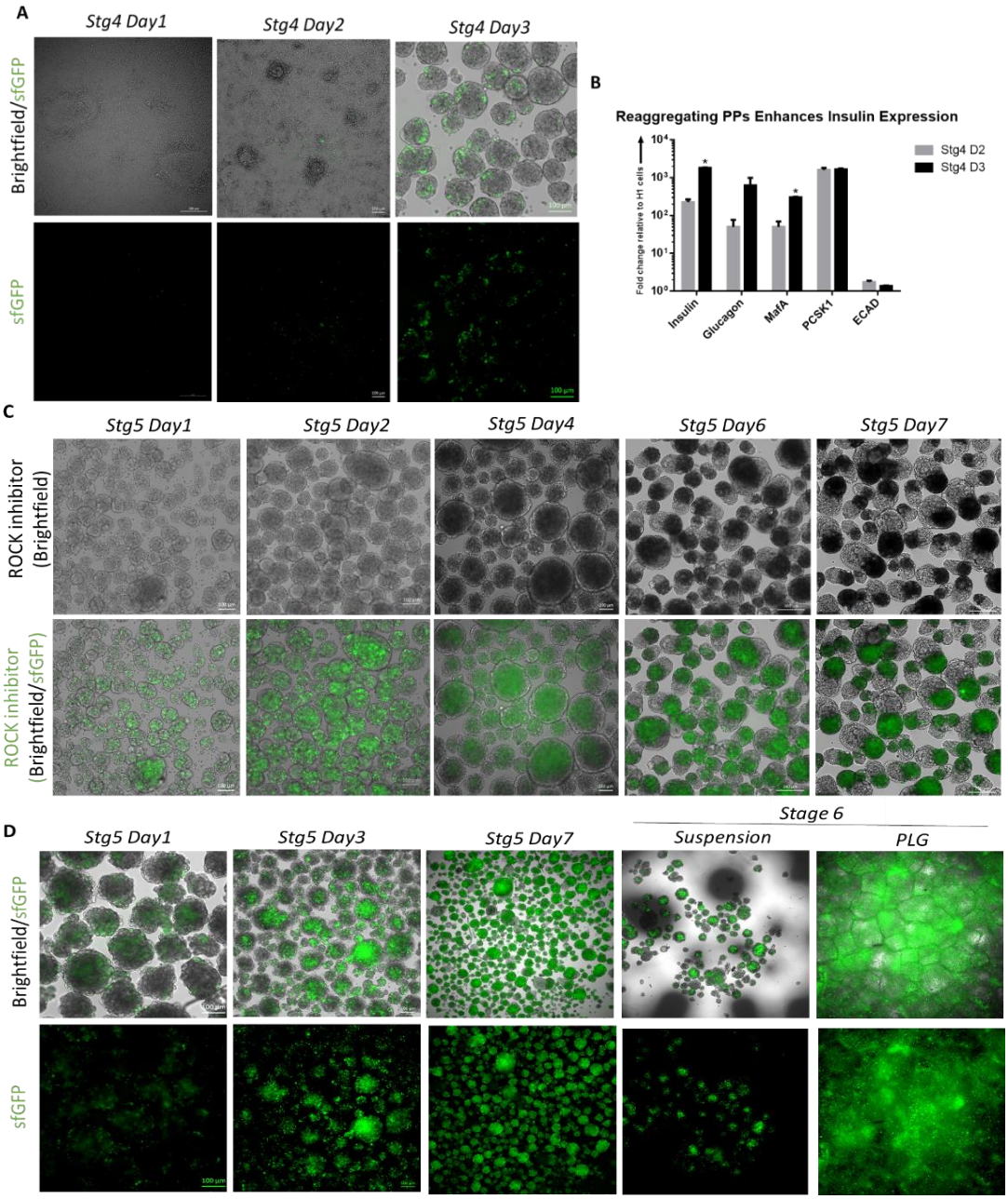
A
Stg4 Day1
Stg4 Day2
Stg4 Day3
Brightfield/sfGFP
sfGFP
B
Reaggregating PPs Enhances Insulin Expression
Stg4 D2
Stg4 D3
Fold change relative to H1 cells
Insulin
Glucagon
MafA
PCSK1
ECAD
C
Stg5 Day1
Stg5 Day2
Stg5 Day4
Stg5 Day6
Stg5 Day7
ROCK inhibitor (Brightfield)
ROCK inhibitor (Brightfield/sfGFP)
D
Stg5 Day1
Stg5 Day3
Stg5 Day7
Stage 6
Suspension
PLG
Brightfield/sfGFP
sfGFP
E
Q1 41.0
Q2 28.4
Q4 31.8
Q3 2.19
FL26-A :: Alexa Fluor 647-A
FL03-A :: Alexa Fluor 488-A
Fraction of total cells (%)
sfGFP-Cpep-/Nkx6.1+
sfGFP-Cpep+/Nkx6.1-
sfGFP-Cpep+/Nkx6.1+
F
GSIS of Stg6 hPSC β-Cells in Suspension Cultures
Insulin Secretion Index (20mM/2mM Glucose Solution)
Velazco-Cruz
Rezania-Cruz

Figure 4.3 *sfGFP-Cpep reporter characterizes modified protocol for enhanced PLG scaffold culture function*
(A) Bright-field and fluorescent images of differentiated clusters in 2D monolayer and in suspension are shown; scale bars, 200 and 100 µm. (B) Gene expression of pancreatic markers in day 2 and day 3 of stage 4 pancreatic progenitors (*P≤0.01 compared to stage 4 day 2 pancreatic progenitor, n = 4) (C) Representative images of differentiated clusters in suspension during stage 5 with exposure to ROCK inhibitor are shown. (D) Differentiated clusters of suspension and scaffold cultures during stage 5 and stage six without ROCK inhibitor; scale bars, 500 and 100 µm. (E) Differentiated stage 6 insulin-producing clusters generated on scaffold cultures using the modified protocol were analyzed by flow cytometry. Bar plot quantifies fraction of cells expressing the indicated markers. (F) Stimulation index shows human insulin secretion from PLG scaffold cultures generated with either the modified or unmodified Velazco-Cruz protocol in response to low and high glucose concentrations under static conditions (unmodified scaffold cultures: n = 5 biological replicates, modified : n = 3 biological replicates).

RHO/ROCK pathway inhibitor that has been found to prevent apoptosis. As a result, we added Y27632 throughout stage 5 to investigate if this would help maintain cluster integrity and shape as cells recovered from the dissociation process. By the end of stage 5, most pancreatic endoderm clusters expressed the fluorescent insulin reporter. However, brightfield images at stage 5 day 7 showed irregular shaped clusters with fluorescent cells congregated to one region of the cluster indicating cellular polarization (**Fig. 4.3C**)[327]. This morphology differs from the native human islet that consists of pancreatic cells distributed throughout the cluster[328,329]. Thus, we reduced Y27632 administration to only the day cells were transfered to suspension for aggegration to investigate if overexposure caused the cellular polarization to occur. As the stage 5 differentiation continued without Y27632, the cluster size reduced from 172.1 µm ± 9.6 to 57.1 µm ± 2.6 while the population of GFP^+ cells increased throughout the clusters (**Fig. 4.3D**). By the end of stage 5, the clusters retained their round shape, were predominately GFP^+ but there was a significant reduction in cell density. These results indicate modifying the protocol with Y27632 improved cell survival after manipulation on the cells but overexposure can lead to cluster polarization of endocrine cells, GFP^+ cells, and non-endocrine cells, GFP^- cells.

Stage 5 pancreatic endoderm clusters were dissociated and seeded on scaffolds or maintained in suspension for futher maturation. While cells continued to express the insulin reporter on both scaffolds and in suspension, we observed the cell density in suspension continued to decrease during stage 6 relative to the scaffold cultures. We then characterized the

maturation of islet organoids on scaffold cultures generated with the modified protocol. The majority of GFP^+ cells expressed NKX6.1 (**Fig. 4.3E**). However, the fraction of cells co-expressing C-peptide and NKX6.1, 29.3 ± 3.8%, was lower than the cell population from islet organoids generated using the unmodified Velazco-Cruz protocol. The static GSIS indicated islet organoids cultured using the modifed protocol generated an insulin secretion index, 1.7 ± 0.6, with a heterogenous population of mature and immature cells that resulted in a wide variation in function (**Fig. 4.3F**). Thus, reaggregating clusters at the pancreatic progenitor stage prior to seeding scaffold cultures was able to generate functional islet organoids that resembled human islet function but further studies would need to be completed to improve the consistency.

4.4.4 Scaffold culture process modifications reduce manipulation on clusters to augment islet organoid function

Based on the influence cell manipulation had on organoid development, we modified how we seeded scaffolds to investigate if reducing cell processing steps would affect the generation of functional, mature cells. The modified process step consisted of seeding intact pancreatic progenitor clusters on scaffolds rather then dissociating the clusters into a single cell solution for seeding. In addition, cells could benefit from the supportive scaffold matrix while leveraging their pre-established cell-cell interactions. Pancreatic progenitor clusters were generated using the Velazco-Cruz protocol with a small population of cells expressing the insulin fluorescent reporter (**Fig. 4.4A**). Clusters were then transplanted on scaffolds at the same density as prior single cell suspensions, 125 million cells/cm^3. We observed an increase in GFP^+ cells during stage 5 in both suspension and on scaffolds. We then performed gene expression analysis at the end of stage 5 and found β cell genes, including insulin, NKX6.1, glucagon, MAFA, and PCSK1, were increased in islet organoids cultured on scaffolds compared to the suspension control (**Fig. 4.4B**). NeuroD1 and NGN3 are pancreatic endocrine markers that were also increased on scaffold cultures relative to suspension. In addition, E-cadherin had increased expression levels on scaffold cultures indicating the cell-cell interactions within

seeded clusters were enhanced relative to suspension clusters.

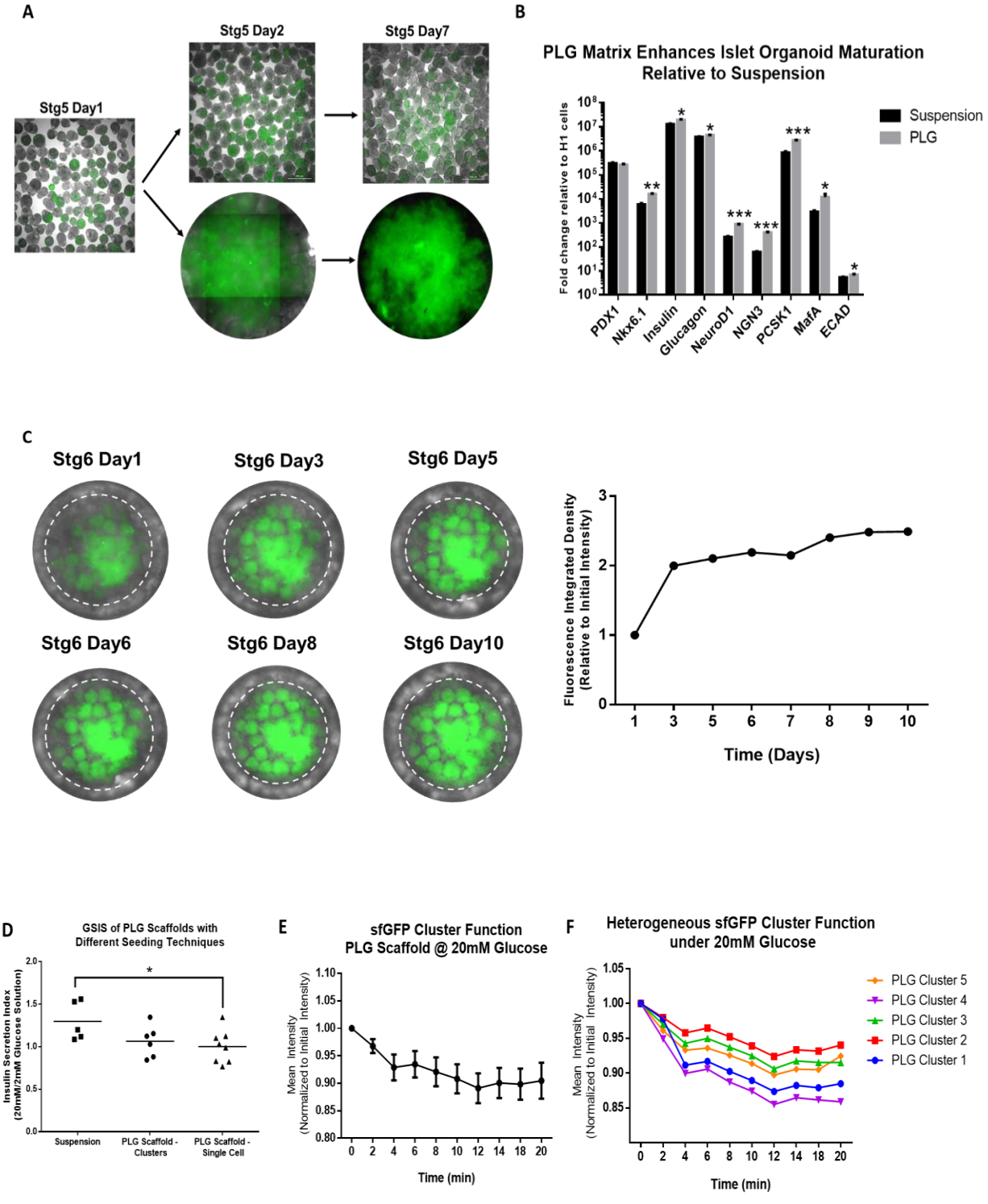

Figure 4.4 *Effect of seeding pancreatic progenitors as dense clusters on PLG scaffold cultures*

(A) Bright-field and fluorescent images of sfGFP-Cpep differentiated clusters in suspension and on scaffold cultures at stage 5 are shown; scale bars, 500 μm. (B) Gene expression of pancreatic endocrine and maturation markers as well as ECAD gene expression in pancreatic progenitors at the end of stage 5 (*P≤0.05, **P≤0.01, ***P≤0.001 compared to suspension, n = 4) (C) Representative images of differentiated clusters on a scaffold culture during stage 6. Cell-laden area on scaffold is indicated by white dashed circle. Fluorescence integrated density of scaffold culture is plotted over the duration of stage 6 and normalized to initial intensity (D) Stimulation index shows human insulin secretion from suspension and PLG scaffold cultures seeded with either pancreatic progenitors in single cell suspension or dense clusters in response to low (2mM) and high (20mM) glucose concentrations under static conditions (*P≤0.05 compared to suspension, n = 5-7 biological replicates). (E) Fluorescent imaging of scaffold cultures in response to high glucose (20mM) measured fluorescence integrated density over 20 minutes. Fluorescence intensity was normalized to initial intensity. (F) Different regions, or clusters, of a representative scaffold were assessed for changes in fluorescence integrated density over 20 minutes.

Analysis of the insulin reporter during stage 6 provided dynamic insights to how the cells functionally matured. Representative images of sfGFP-Cpep cells on scaffolds were analyzed over time for fluorescent intensity where increases in intensity mean increases in insulin biosynthesis and decreases correlate with insulin secretion (**Fig. 4.4C**). We found the fluorescence intensity doubled between day 1 and day 3 of stage 6 then increased again by a quarter around day 8 before plateauing. Static GSIS analysis assessed function of PLG scaffold cultures seeded with

clusters or single cells (**Fig. 4.4D**). PLG scaffolds seeded with clusters were comparable to clusters in suspension (1.1 ± 0.1 vs 1.3 ± 0.2, n=5-6), while PLG scaffolds seeded with a single cell suspension showed a decreased insulin index ratio, (1.0 ± 0.1 vs 1.3 ± 0.2, n=5-8, $P<0.05$).

We evaluated cluster function further by monitoring dynamic C-Peptide secretion in sfGFP-Cpep clusters under a high glucose concentration. Imaging analysis showed a gradual 10% decrease in fluorescence intensity over a 20minute stimulation period in 20mM glucose, which together with the GSIS data confirms the PLG scaffolds generated glucose-responsive insulin-secreting cells (**Fig. 4.4E**). Synchronous insulin release is typically observed with islets following *in vitro* glucose stimulation. As a result, we investigated this response in the islet organoids. Due to the integrated nature of the scaffold culture, we considered different regions of the islet organoid as clusters and found the clusters exhibited asynchronous responses (**Fig.**

4.4F). We observed heterogenous functional maturation on the scaffold with some clustered regions, like Cluster 1 and 4, showing more than 10% loss in fluorescence intensity while other regions, like Cluster 2 and 3, were closer to 5% loss. These results suggest that scaffold culture function could be improved if there was a homogenous population of clusters that resembled the clusters with more insulin secretion during GSIS.

4.5 Discussion

Our studies demonstrate the support of the scaffold microenvironment during organoid maturation could be enhanced by adjusting the differentiation stage of cells seeded on scaffolds as well as the seeding technique. With the support of a novel fluorescent insulin reporter stem cell line, these findings provide mechanistic insights regarding material design and β-cell development during the *in vitro* maturation of islet organoids on scaffolds. Scaffold cultures seeded with a more mature progenitor cell resembling pancreatic endoderm were able to enhance the secretion of insulin per cell in the islet organoids. These results indicate organoid development could benefit from incorporating scaffold cultures near the end of the differentiation process rather than during early cell fate decisions. Reaggregated pancreatic endoderm cells cultured on scaffolds also enhanced islet organoid maturation with similar insulin secretion function to human islets however functional variability from this modified protocol needs to be further evaluated. We also found glucose-responsive functional tests showed the insulin secretion index of scaffolds seeded with dense clusters were comparable to the suspension clusters while scaffolds seeded with dissociated cells had decreased function.

Microporous scaffold cultures provide a supportive 3D niche that promotes cell-cell and cell-matrix interactions to facilitate islet organoid maturation[311]. This organization into a tissue, rather than a collection of cells, facilitated transplantation as the scaffolds could be directly transplanted, which contrasts with the cells that are manually aggregated and then transplanted[23,25]. Thus, the scaffold-based transplantation exposed the cells to significantly less manipulation, particularly around the time of transplant, which can be a challenging transition for

cell survival under the best of conditions. However, low quantities of human C-peptide present in the blood demonstrated that transplanted islet organoids were functionally, mature but not capable of processing insulin to regulate blood glucose metabolism under *in vivo* conditions. Key characteristics of β-cell function include the sensing of physiological glucose levels, the rapid release of stored insulin vesicles, and the immediate cessation of insulin secretion once glucose levels have been normalized. This complex process requires optimal coordination of multiple regulatory processes that exist in endogenous β-cells. Thus, we transitioned differentiation protocols to the Velazco-Cruz protocol and evaluated mechanistic modifications to enhance islet organoid maturation prior to transplantation. hPSC-derived stage 5 pancreatic endoderm clusters generated prior to scaffold seeding showed increased $PDX1^{+}Nkx6.1^{+}$ cell populations, as well as, $Cpep^{+}$ cell populations compared to stage 4 pancreatic progenitor cells. By modifying the timing of cell seeding from pancreatic progenitor to pancreatic endoderm, islet organoids showed increased amounts of insulin secreted per cell.

In order for the islet organoid's response to culture manipulations to be directly monitored, we engineered an insulin reporter hPSC line with the insertion of a human Pro-insulin C-peptide-modified super folded green fluorescent protein. This tool helped establish a baseline for hPSC-derived β-cell function that was used to assess the impact of varying the differentiation protocol. In order to enhance organoid function demonstrated by the insulin secretion index, protocol modifications were made to incorporate a 2D monolayer of pancreatic progenitors that required less cell manipulation to dissociate cells. After pancreatic progenitors were dissociated and allowed to aggregate in suspension, we observed cluster formation and an increase in GFP^{+} cells within the clusters. The increasing density of GFP^{+} cells in the overall cell population could be the result of the non-endocrine cells being removed during the reaggregation step. While cells continued to express the insulin reporter on both scaffolds and in suspension throughout stage 6, we observed the cell density in the suspension culture

continued to decrease relative to the scaffold cultures. Cell maintainence on the scaffolds is likely attributed to the supportive matrix consisting of a cell-secreted ECM niche. While the modified Rezania-Cruz protocol facilitated cluster formation by incoporating a less harsh dissocation process on a 2D monolayer, the scaffold culture differentiation led to a heterogenous population of mature and immature cells. This was demonstrated by GSIS and suggests that the aggregation step could generate cells more akin to neonatal islets that are still on the path to full maturation.

Since modifying the protocol to support cluster integrity showed improvement in function, we evaluated a less manipulative process step for seeding scaffold cultures. Gene expression of scaffold cultures seeded with dense clusters rather than dissociated cells demonstrated scaffold cultures enhanced maturation during pancreatic endoderm development relative to suspension clusters. While the maturation markers used were helpful in establishing function, further assessment of the scaffold cultures with a more expansive group of glucose sensing markers can provide more insight on limited insulin secretion quantities at high glucose concentrations. For any given scaffold, the initial seeding influences cell density, retention, and spatial distribution within the scaffold, which eventually will affect the function of the construct[330]. A single cell suspension allows for easy infiltration and uniform distribution throughout a porous scaffold. However, seeding scaffolds with a single cell suspension requires dissociating cell-cell and cell-matrix bonds within differentiated clusters, thus a harsh manipulation process is used that could impair the cell's development. Modifying this process to seed intact clusters on scaffolds reduces the strain put on cells as they differentiate to insulin-producing organoids. As a result, the modified seeding technique led to islet organoids with increased insulin secretion indexes. Though, while scaffold cultures seeded with clusters demonstrated glucose-responsive function, the insulin index ratio was relatively low compared to human islets. This functional response could be attributed to one of the challenges with seeding clusters on scaffolds, which

is that infiltration rates can be very low, resulting in poor loading, and non-uniform distribution of cells within the scaffolds. This is due in part to the hydrophobicity of the polymer material and, in some degree, to the plugging of the porous scaffold by cells trapped at the outer surface of the construct. Since the scaffold has tunable properties, a future study can increase the scaffold pore size to identify if cluster infiltration could be inhibiting organoid maturation.

Developing an insulin reporter allowed us to carry out non-invasive assessments of maturation heterogeneity between clusters rather than relying on traditional methods that either assess an entire cell population or require the study to end. The sfGFP-Cpep containing cells provided for easy and dynamic quantification of insulin secretion to assess the effect of culture modifications on islet organoid's ability to process insulin. We found the fluorescence intensity of islet organoids cultured on scaffolds doubled between day 1 and day 3 of stage 6 then increased again by a quarter around day 8. These observations align with prior studies showing that cells are considered mature once they reach stage 6 day 9 of this protocol[25]. Immunofluorescence imaging during GSIS showed GFP-positive cells in islet organoids exhibited varying decreases in intensity, indicative of a heterogenous response of organoids throughout the scaffold. This observation was corroborated by ELISA testing that showed islet organoids secreted insulin under glucose-challenged environments, but the insulin secretion index ratio was not comparable to human islets. This loss in intensity shown by the islet organoids resembles the 10% loss shown by islets in prior studies[323]. The kinetics of the release of sfGFP-Cpep from isolated islets appear identical however individual clusters on the scaffold culture show the response between clusters is not identical. Future studies can then take this information and further characterize these scaffold cluster regions using RNA-seq analysis to help identify β-cell heterogeneity and how the microenvironment influences development.

The sfGFP insulin reporter tool could enhance our understanding of beta-cell maturation by faithfully representing normal trafficking, processing, insulin storage, and secretion. Because sfGFP-Cpep is a parallel marker of endogenously stored insulin, we can exploit survival surgery

using epifluorescence imaging of the pancreatic surface *in vivo* to estimate insulin content in the pancreatic tail region similar to our *in vitro* studies. *In vivo*, fluorescence imaging of the implant would allow visual assessment of islet organoid insulin content within the transplant site. This could help demonstrate if euglycemia is not reached in a diabetic model as a result of only a small population of maturing cells are efficiently secreting insulin or a large population are secreting trace amounts of insulin. As a result, future studies of these maturing pancreatic progenitors *in vivo* will lead to invaluable insights about the function of the scaffold culture and help determine the heterogeneity of cell populations after transplantation. Continuous, long-term observation —over several differentiation stages — could also help provide the temporal information to help further decode the function of the organoid responses for insulin storage and release within individual clusters. Taken together, these studies provide insight into the activity of islet organoids, as well as individual hPSC-derived β-cells, as they develop through maturation on microporous scaffolds before and after transplantation. In addition, we prove the feasibility of evaluating insulin content and secretion, key β-cell indicators, as the islet organoids differentiate under varying scaffold conditions. Once we can consistently demonstrate that stem cell-derived β-cells are the true equivalent of the endogenous β-cells, then transplantation into human diabetic patients can become a reality.

Chapter 5: Human Lung Organoids Develop into Adult Airway-Like Structures Directed by Physico-Chemical Biomaterial Properties

5.1 Abstract

Tissues derived from human pluripotent stem cells (hPSCs) often represent early stages of fetal development, but mature at the molecular and structural level when transplanted into immunocompromised mice. human lung organoids (HLOs) transplantation has been further enhanced with biomaterial scaffolds, where HLOs had improved tissue structure and cellular differentiation. Here, our goal was to define the physico-chemical biomaterial properties that maximally enhanced transplant efficiency, including features such as the polymer type, degradation, and pore interconnectivity of the scaffolds. We found that transplantation of HLOs on microporous scaffolds formed from poly(ethylene glycol) (PEG) hydrogel scaffolds inhibit growth and maturation, and the transplanted HLOs possessed mostly immature lung progenitors. On the other hand, HLOs transplanted on poly(lactide-co-glycolide) (PLG) scaffolds or polycaprolactone (PCL) led to tube-like structures that resembled both the structure and cellular diversity of an adult airway. Our data suggests that scaffold pore interconnectivity and polymer degradation contributed to the maturation, and we found that the size of the airway structures and the total size of the transplanted tissue was influenced by the material degradation rate. Collectively, these biomaterial platforms provide a set of tools to promote maturation of the tissues and to control the size and structure of the organoids.

5.2 Introduction

Human lung organoid models facilitate the study of cell fate decisions during development and for modeling diseases such as cystic fibrosis and goblet cell metaplasia, and infections such as respiratory syncytial virus[32,331–337]. We have previously demonstrated that human pluripotent stem cell (hPSC)-derived human lung organoids (HLOs) possess a complex tissue structure *in vitro*, which includes both the epithelium and supporting tissue (cartilage, smooth muscle, fibroblasts) [32,195,331–337].

Notably, *in vitro* HLO cultures reflect the fetal airway, with adult airway-like structures generated only after *in vivo* transplantation[195]. Maturation following *in vivo* transplantation of HLOs reflects observations with numerous other organoid and hPSC-based systems[32,338–341],. While many other studies have shown successful transplantation of hPSC-derived tissues under the kidney capsule or other vascular sites within the murine host, HLOs required the assistance of a PLG microporous polymer scaffold to support engraftment and vascularization following transplant into the epididymal fat pad of immunocompromised mice. After 8 weeks, the transplanted HLO (tHLO) had airway-like structures that resembled native adult airways including proper cellular organization, epithelial cellular ratios and airway cell types. Airway-like structures were also surrounded by smooth muscle and possessed cartilage, as would be the case in the human airways[195]. However, these previous studies did not identify the polymer scaffolds design parameters that conferred an engraftment and growth advantage for HLOs.

In this report, we investigated the physico-chemical properties of microporous scaffolds that support HLO maturation into airway structures. Polymers have different degradation rates and may have distinct interactions with the host, so microporous scaffold support of transplanted HLO were tested using diverse materials including poly(lactide-co-glycolide) (PLG), polycaprolactone (PCL), and poly(ethylene glycol) (PEG). The interconnected pore size was varied, as well, through the initial scaffold fabrication and also through the degradation rate of the polymers. For these

material platforms, we investigated airway maturation, immune response, as well as overall explant and airway size. Identifying the biomaterial design parameters that influence airway maturation and structure will enable the development of platforms that can direct the structure to better model airway homeostasis and disease environments.

5.3 Materials and Methods

5.3.1 Maintenance of hESCs, generation of HLOs, and seeding on scaffolds

H1 human embryonic stem cell (hESC) line (NIH registry #0043) and H9 (NIH registry #0062) was obtained from the WiCell Research Institute. H1 hESC line was used to derive all HLOs for these experiments except for **Fig 5.2** where H9 hESC and H9 GFP hESC lines were used to derive HLOs. H9 GFP hESC line was generated by infecting H9 hESCs with pLenti PGK GFP Puro virus generated from the plasmid purchased from AddGene (Cat#: 19070)[342]. H9 GFP hESC clonal line was generated by puromycin selection flow cytometry analysis sorting (FACS) for GFP high expressing cells. All hESC lines were approved by the University of Michigan Human Pluripotent Stem Cell Research Oversight Committee. hESCs were maintained as previously described[34]. HLOs were derived as previously described[32]. Foregut spheroids, which grow into HLOs, were seeded on scaffolds as previously described [195].

5.3.2 Scaffold fabrication

75:25 PLG scaffolds were fabricated as previously described[195,343]. 85:15 (Resomer® RG 858 S, Poly(D,L-lactide-co-glycolide), Sigma, Cat#: 739979-1G) and 50:50 PLG (Resomer® RG 505, Poly(D,L-lactide-co-glycolide) ester terminated, MW: 54,000-69,000, Sigma,Cat#: 739960) were fabricated the same as 75:25 PLG scaffolds. 20% (w/v) 4-arm PEG maleimide, 20,000MW (JenChem, Cat#: A7029-1) hydrogels were fabricated as previously described[278]. PCL scaffolds were fabricated as previously described[344]. Large interconnected PCL were commercially bought (National Institute of Standards and Technology, Cat#:8394).

5.3.3 Scaffold transplantation

Scaffolds were implanted as previously described[195]. Briefly, mice were anesthetized and prepped as for omental transplants. The epididymal fat pads of male 7–10 week old NOD-scid IL2Rgnull (NSG) were exposed using a lower midline incision. Scaffolds were then placed along the epididymal blood vessels and covered with epididymal fat. An intraperitoneal flush of Zosyn (100 mg/kg; Pfizer Inc.) was administered after which the incision was closed in 2-layers using absorbable suture. Mice were euthanized between 1-8 weeks post-transplant.

5.3.4 Immunohistochemistry, hematoxylin and eosin stain (H&E), and imaging

Immunostaining and H&E were carried out as previously described[345]. Antibody information and dilutions can be found in **Table 5.1**. All images and videos were taken on a Nikon A1 confocal microscope or the Zeiss Axio Observer.Z1.

Table 5.1: Primary and secondary antibody information

Primary Antibody	**Source**	**Catalog #**	**Dilution**	**Clone**
Chicken anti-GFP	Aves Lab	GFP-1020	1:500	polyclonal
Mouse anti-Acetylated Tubulin (ACTTUB)	Sigma-Aldrich	T7451	1:1000	6-11B-1
Mouse anti-E-Cadherin (ECAD)	BD Transduction Laboratories	610181	1:500	36/E-Cadherin
Mouse anti- Human Mitochondria (huMITO)	Millipore	MAB1273	1:500	113-1
Mouse anti-PLUNC	R&D Systems	MAP1897	1:200	monoclonal
Rabbit anti-Cytokeratin5 (CK5)	Abcam	ab53121	1:500	polyclonal
Rabbit anti-NKX2.1	Abcam	ab76013	1:200	EP1584Y
Rabbit anti-P63	Santa Cruz Biotechnology	sc-8344	1:200	H-129
Secondary Antibody	**Source**	**Catalog #**	**Dilution**	
Donkey anti-chicken 488	Jackson Immuno	703-545-155	1:500	

Donkey anti-mouse 488	Jackson Immuno	715-545-150	1:500	
Donkey anti-mouse 647	Jackson Immuno	415-605-350	1:500	
Donkey anti-mouse Cy3	Jackson Immuno	715-165-150	1:500	
Donkey anti-rabbit 488	Jackson Immuno	711-545-152	1:500	
Donkey anti-rabbit Cy3	Jackson Immuno	711-165-102	1:500	

5.3.5 Flow Cytometry

Cell disassociation and flow cytometry was previously described[344]. Antibodies used are as follow: Fluor® 700 anti-CD45 (1:125, clone 30-F11, Biolegend), V500 anti-CD11b (1:100, clone M1/70, BD Biosciences), FITC anti-Ly6C (1:100, clone HK.14, Biolegend), PE-Cy7 anti-F4/80 (1:80, clone BM8, Biolegend), APC anti-CD11c (1:80, clone N418, Biolegend), and Pacific Blue™ anti-Ly-6G/Ly-6C (Gr-1) (1:70, clone RB6-8C5, Biolegend).

5.3.6 Quantification

Airway diameters were measured using ImageJ software. The longest and shortest diameter was measured per airway structure and then averaged together. Explant size was measured using a ruler by placing the longest side of the tHLO on the ruler. $Ki67^+$ cells and $ECAD^+$, $Ki67^+$ cells were quantified using a program developed in lab by Kevin Rychel, previously described[277].

5.3.7 Experimental replicates and statistics

All experiments were done on at least three (n=3) independent biological samples for each experiment. All error bars represented SEM while the long bar represented the average. Statistical differences were assessed with Prism software using unpaired t-test.

5.4 Results

5.4.1 PLG, PEG and PCL have varying extents of HLO derived airway maturation

Microporous scaffolds with similar architectures and formed from either 75:25 (lactide:glycolide) PLG or 20% (w/v) 4-arm PEG-maleimide microporous scaffold were tested for

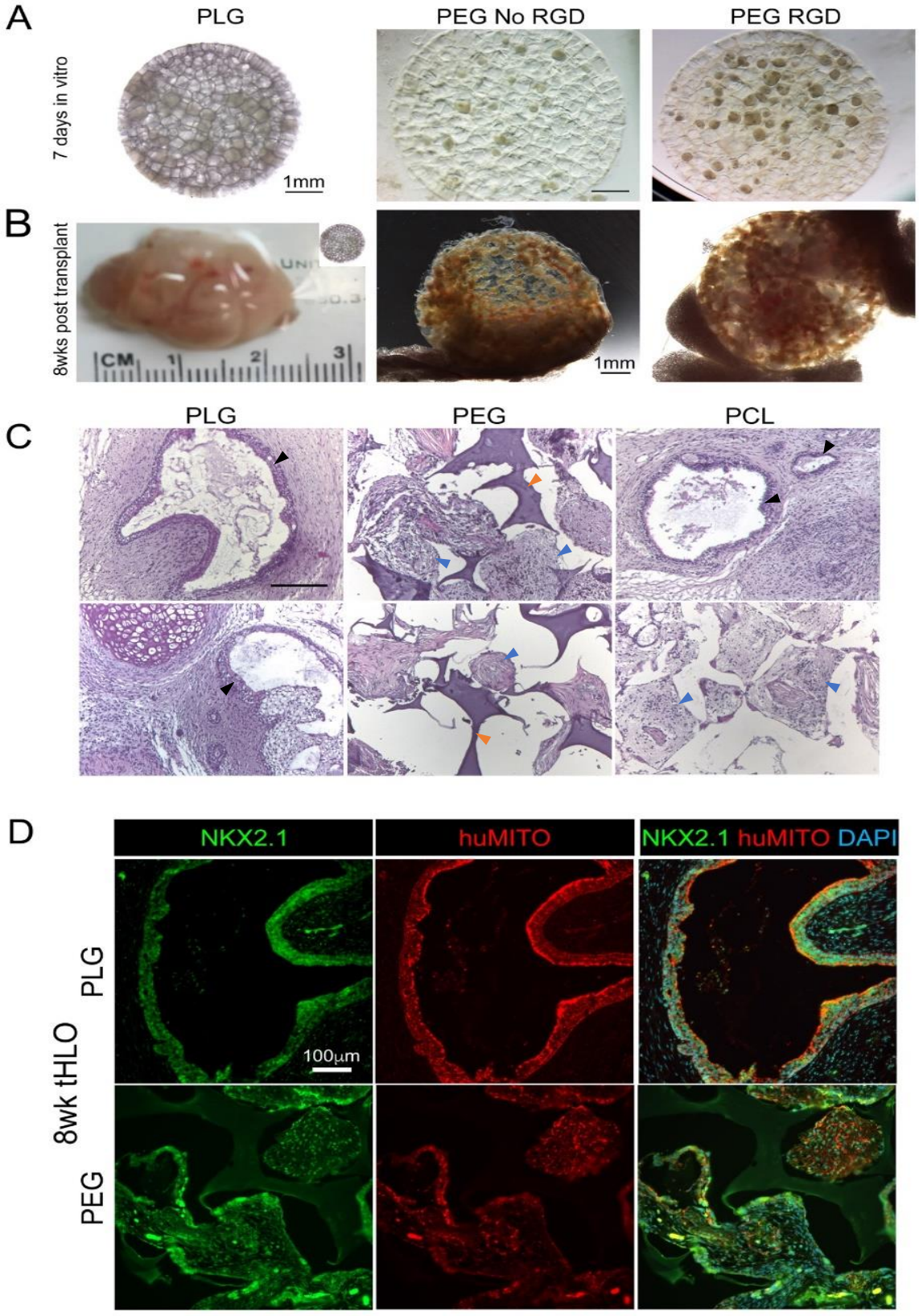
A
PLG
PEG No RGD
PEG RGD
7 days in vitro
1mm
B
8wks post transplant
CM
1mm
C
PLG
PEG
PCL
D
NKX2.1
huMITO
NKX2.1 huMITO DAPI
8wk tHLO
PLG
PEG
100μm

Figure 5.1 *HLOs seeded on PLG, PEG, and PCL scaffolds affects airway structure formation.*
(A) Approximately 50 foregut spheroids were seeded onto PLG and PEG with or without RGD. Wholemount images were taken after 1 week in culture. (B) Scaffolds were transplanted into the epididymal fat pad of immunocompromised mice and retrieved 8 weeks later. The PLG tHLO grew up to 2.5cm while the tissue remained within the PEG scaffolds with or without RGD. (C) The histology of the PLG and PCL tHLOs had organized pseudostratified epithelium resembling native airway epithelium (shown by black arrows). The PEG tHLOs showed intact scaffold (shown by orange arrows) and both the PEG and the tissue within the pores of the PCL had no organized epithelium but remained as clusters of cells (shown by blue arrows). (D) Some of the clusters of cells within the PEG scaffold were lung marker NKX2.1^{+} and human mitochondria (huMITO)$^{+}$. Scale bars for A-B:1mm, C:200μm, and D:100μm.

their ability to support transplantation of foregut spheroids. Both scaffolds had pores ranging in size from 225 μm to 450μm, and were cylinder shaped with a diameter of 5mm diameter and a thickness of 2mm. PLG is a degradable, hydrophobic polyester that will adsorb proteins while PEG scaffolds are non-degradable hydrogels and were formed with or without the adhesion peptide RGD. PLG and PEG scaffolds were seeded with foregut spheroids and cultured for 7 days *in vitro,* during which time the foregut spheroids grew to fill the pores (**Fig 5.1A**). Scaffolds were then transplanted into the epididymal fat pad of NSG mice. This highly vascularized implant site[346] is accessible by a minimally invasive surgery, has a large surface area[347] and the presence of pro-angiogenesis cytokines[348], which has supported the use of this site for transplantation. After 8 weeks, tissue was found within and around the PLG scaffold, and histological examination revealed that the tHLO tissue contained airway-like structures. The majority of the PLG scaffold should be degraded by this time point[349,350] and, accordingly, the material was not detected in histological sections (**Fig 5.1C**).

Growth of the transplanted PLG scaffolds contrasted with the PEG-seeded scaffolds. 8 weeks after transplantation, PEG scaffolds appeared intact and the spheroids remained within the pores independent of whether the scaffold was modified with RGD (**Fig 5.1B**). We hypothesized that the individual HLOs would grow together on the surface of the PEG scaffold and form airway-like structures. However, the transplanted spheroids remained within the separate pores. We investigated the possibility that smaller airways formed within the pores of the PEG scaffold;

however, the PEG hydrogels only had clusters of cells within the pores and did not possess tissue resembling airway structures (**Fig 5.1C**). The tissue within the PEG pores was derived from both spheroids and host (murine) cells, as we observed cells expressing the human-specific mitochondria marker (huMITO) along with huMITO-negative cells. huMITO$^+$ cells co-expressed NKX2.1, an early lung epithelial–specific transcription factor[351,352], yet no mature cell types or airway-like structures were observed in the PEG explants (**Fig 5.1D**). In comparison, the organized airway structures observed in the PLG explants expressed the lung marker NKX2.1 and were huMITO$^+$. Further characterization of the lung tissue was previously described in Dye et al.[195].

We next tested the ability of PCL scaffolds to support transplantation and lung organoid growth *in vivo*. Both PLG and PCL are polyester polymers that degrade predominantly by simple hydrolysis of the ester bond into acidic monomers. However, due to its higher molecular weight and higher hydrophobicity, PCL has a slower degradation rate than PLG[353,354]. PCL scaffolds were seeded with spheroids and transplanted for 8 weeks. Similar to the PEG, PCL scaffolds were still intact after 8 weeks *in vivo* (**Fig 5.1C**). No organized epithelial structures were observed within the pores of the PCL grafts but the scaffolds had clusters of cells similar to what is observed in the PEG transplants (**Fig 5.1C**). On the other hand, there were airway-like structures that formed on the outside of the scaffolds where tHLOs had expanded. Collectively, these results suggest that the polyester polymers (PLG, PCL) supported the spheroid engraftment and development of airway structures after 8 weeks, but that failure of the scaffold to degrade prevented the growth and development of spheroids into airway-like structures.

5.4.2 Initial immune response at microporous scaffolds may contribute to HLO responses

The initial immune response within the microporous scaffolds was investigated as a potential mechanism underlying the differential maturation on the various materials. Note that these studies were performed within NSG mice that lack an adaptive immune system in order to prevent rejection, yet these mice retain innate immune cells that respond to transplantation of the

construct. Lung organoids were transplanted and collected after 1 week *in vivo*, with analysis of the innate immune response. PEG tHLOs had a significantly greater percentage of leukocytes ($CD45^+$) than PLG and PCL tHLOs (**Fig 5.2A**), which indicates greater cell recruitment from the

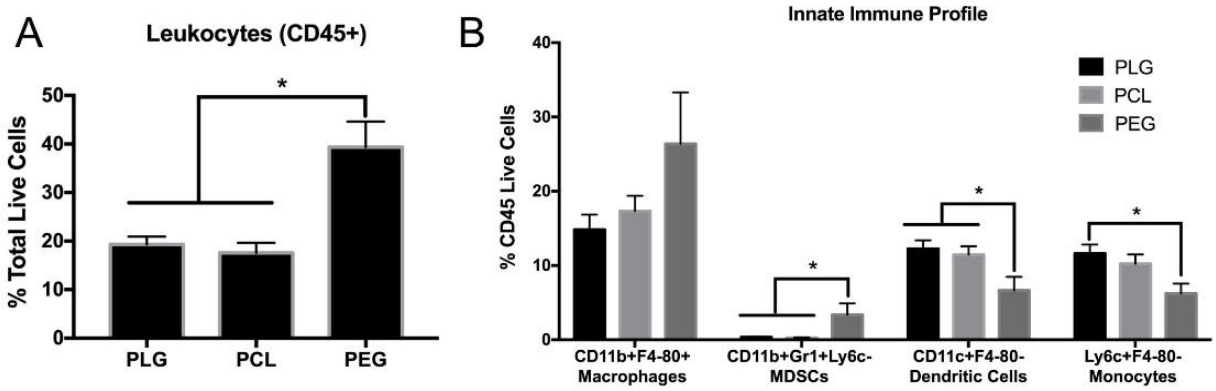

Figure 5.2 *The innate immune profile for PEG, PLG, and PCL tHLOs.*
Foregut spheroids were cultured on scaffolds for 1 week *in vitro*, transplanted into the mouse epididymal fat pad, and then retrieved after 1 week to observe the innate immune response. (A) The PEG tHLOs had 39% $CD45^+$ Leukocytes (n=6) compared to 17% $CD45^+$ cells in PLG tHLOs (n=7) and 19% $CD45^+$ cells in PCL tHLOs (n=7) $P \leq 0.005$ (B) PEG, PCL and PLG and similar percent of macrophages ($CD11b^+F4\text{-}80^+$). PEG tHLOs had significantly higher MDSCs ($CD11b^+GR1^+Ly6c^-$) compared to PLG and PCL tHLOs, $^*P \leq 0.05$. In contrast, PEG tHLO had significantly lower dendritic cells ($CD11c^+F4\text{-}80^-$) and monocytes ($Ly6c^+F480^-$) $^*P \leq 0.05$. All error bars represent SEM.

host tissue. From the $CD45^+$ population, the PEG tHLOs had significantly higher percent of $CD11b^+GR1^+Ly6c^-$ cells, often referred to as myeloid derived suppressor cells, and significantly less $CD11c^+F4\text{-}80^-$ (dendritic) cells and $Ly6c^+F4\text{-}80^-$ (monocyte) cells compared to PLG and PCL tHLOs (**Fig 5.2B**). No differences were observed between the PLG and PCL scaffolds. While the immune cell population at the graft may not fully recapitulate the immune-response of biomaterials in an immunocompetent environment, these data suggest that the immune response could be a contributing factor to the inhibition of HLO maturation in PEG scaffolds relative to PLG and PCL scaffolds.

5.4.3 HLO fusion during formation of airway-like structures

We subsequently investigated the contribution of HLO interaction in adjacent pores to the formation of airway structures, which was motivated by the observations of airway structures

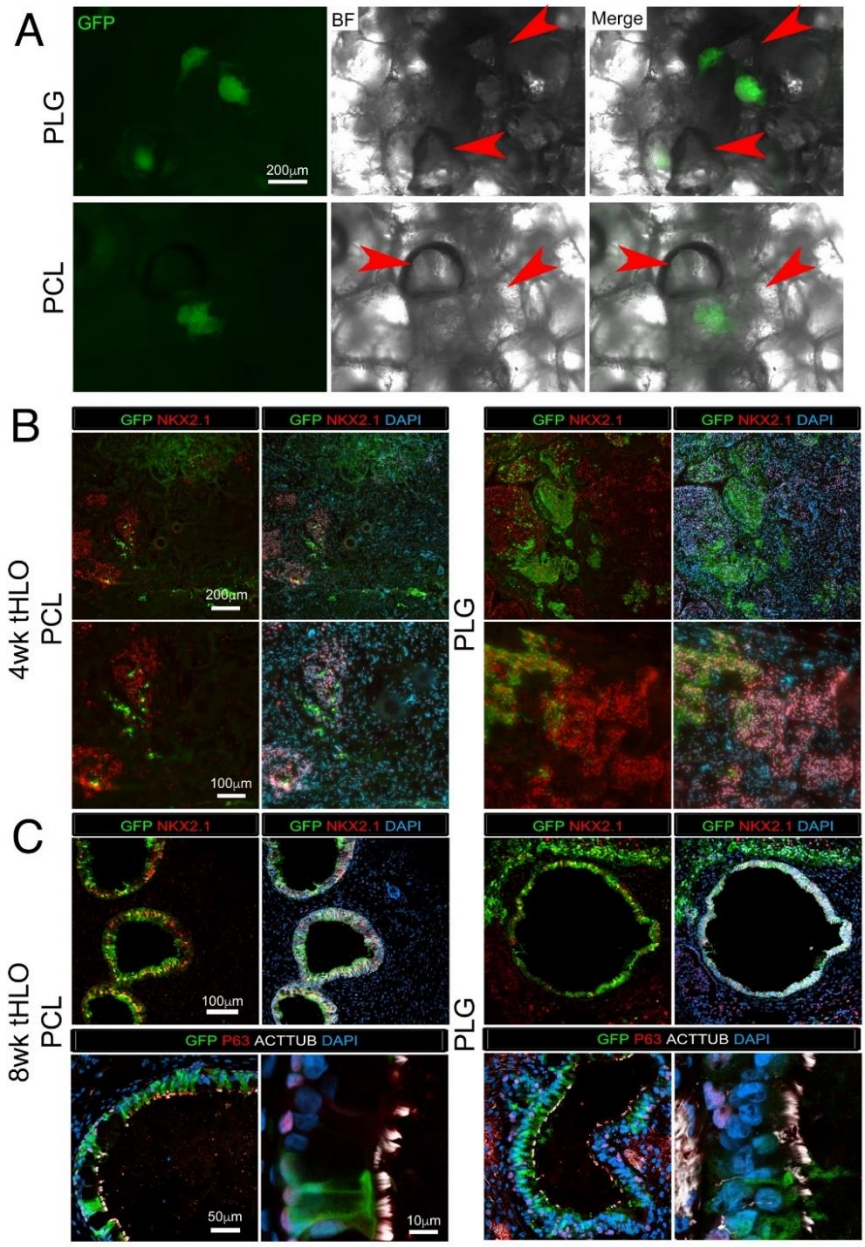

Figure 5.3 *HLOs fuse together to form airway structures*

(A) GFP H9 hESC line and H9 hESC derived HLOs were seeded onto 75:25 PLG and PCL scaffolds. Wholemount images of the scaffolds cultured for 1 week *in vitro* had GFP+ HLOs next to a pore of GFP- HLOs indicated by the red arrow head in both PLG and PCL conditions. (B) After transplanted for four weeks, the GFP+ cells were mixing with the GFP- cells and both expressed early lung marker NKX2.1 (red). No organized epithelial structures were observed for either scaffold. (C) After transplanted for 8 weeks, airway structures formed and were comprised of GFP^+ and GFP- cells in both PLG and PCL tHLOs. The airway structures expressed NKX2.1 (red). The fused GFP^+ and GFP^- HLOs in both PLG and PCL had multiciliated cells labelled by acetylated tubulin (ACTTUB, white) and basal cell marker P63 (red). Scale bars for A-B: 200μm, B-C: 100μm, and C: 50μm, 10μm.

forming on the surface of slow degrading PCL scaffolds, but not within the pores. In order to

analyze the fusion of multiple organoids into an airway structure, scaffolds were seeded with HLOs constitutively expressing GFP (GFP^+) and GFP^- HLOs. Following culture of HLOs in PLG and PCL scaffolds for 1 week *in vitro*, we observed pores seeded with GFP^+ HLOs that were adjacent to pores containing GFP^- HLOs (**Fig 5.3A**). Scaffold were transplanted and retrieved after 4 and 8 weeks *in vivo*. After 4 weeks *in vivo*, airway structures were not present, yet there were populations expressing the lung marker NKX2.1 that were either GFP^+ or GFP^- indicating both HLO populations survived and successfully generated lung progenitors (**Fig 5.3B**). After 8 weeks, airway structures were observed in PLG and on the outside of PCL tHLOs, and these structures contained airway-like structures that possessed multiciliated cells ($ACTTUB^+$) and basal cells ($P63^+$). These airway structures had both GFP^+ and GFP^- cells both in PCL and PLG tHLOs (**Fig 5.3C**), indicating that the airway structures form by the HLOs fusing from adjacent pores in both the surface pores of PCL and in the degrading pores of the PLG tHLOs.

5.4.4 Scaffold degradation affects the HLO derived airway size

We next investigated the contribution of polymer degradation to the number of airway-like structures with the hypothesis that faster degradation would permit more HLOs fusing in adjacent pores, thus, support larger airway-like structures. Previously, the 75:25 PLG scaffolds were used to transplant HLOs and were thoroughly characterized in Dye et al. 2016[195]. Yet, now with the use of multiple types of polymers with varying degrees of degradation, we quantified the impact on airway diameter size. We first investigated polymers with faster and slower degradation rates than 75:25 PLG. The airway diameters in the PCL tHLOs trended towards being slightly smaller (276 µm) compared to 75:25 PLG tHLOs (333 µm, **Fig 5.4A**). We also transplanted HLOs onto 85:15 PLG polymer which degrades at a rate intermediate of that between 75:25 PLG and PCL[355]. The 85:15 PLG tHLOs had significantly smaller airway diameter (224µm, $p=0.049$) than the 75:25 PLG (**Fig 5.4A, C**). In addition, the 85:15 PLG tHLO had a similar phenotype to the PCL tHLO, with the airway-like structures present adjacent to the

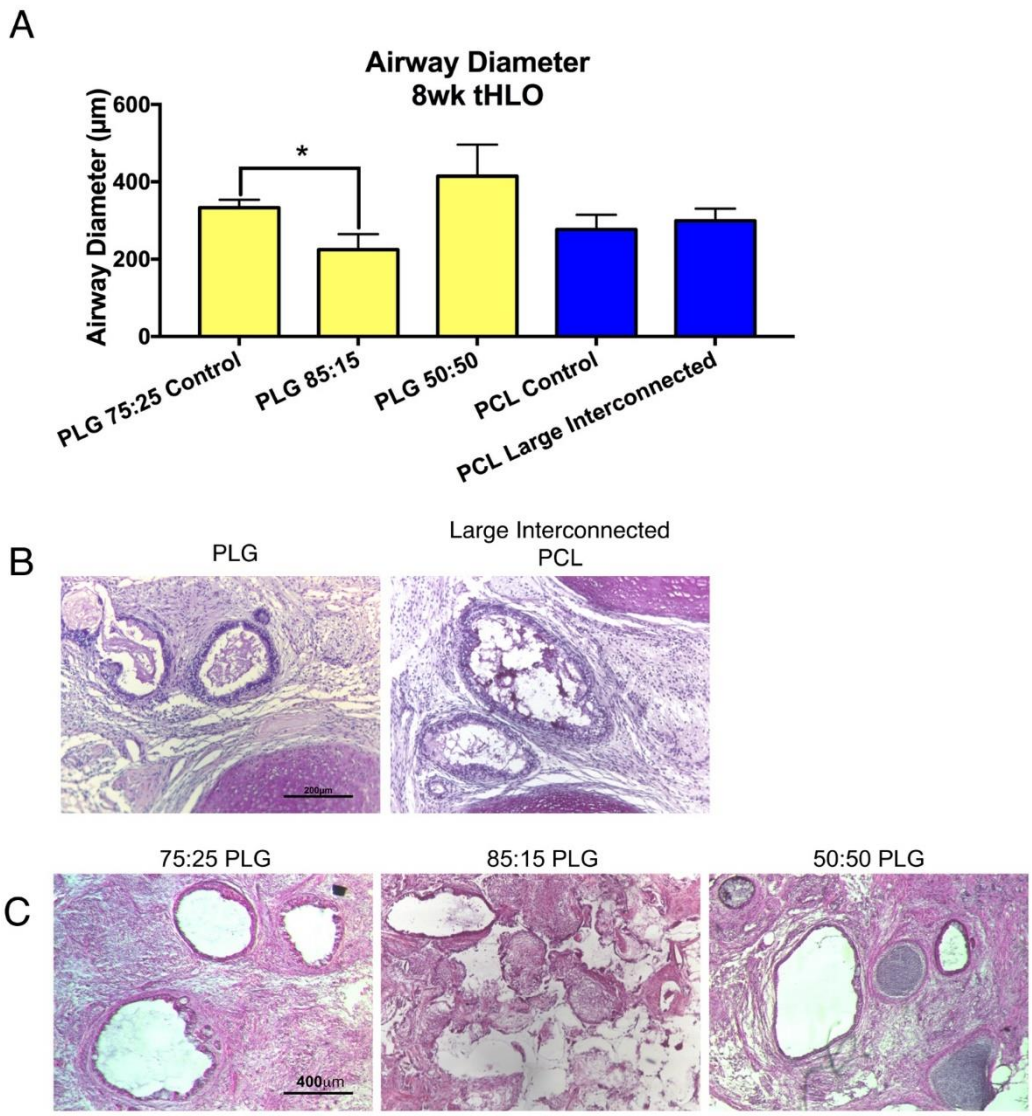

Figure 5.4 *The degradation rate of the scaffold affected airway diameter.*

(A) The average measurement was taken of the longest and shortest diameter for each cross section of an airway structure in a 8wk tHLO. The 85:15 PLG tHLOs (224µm) had the significantly shorter diameter compared to the 75:25 control PLG (333µm) *P≤0.05. The 50:50 PLG tHLO had the longest diameter at 415µm. The PCL control and large interconnected PCL tHLOs had similar diameter at 277µm and 299µm respectively compared to the 85:15 PLG tHLO (224µm). All error bars represent SEM. (B-C) Histology sections of PLG (75:25), large interconnected PCL, 85:15 PLG and 50:50 PLG represent the quantified sections. Scale bars (B) 200µm and (C) 400µm.

scaffold and the tissue within the pores remaining as cell clusters (**Fig 5.4A, C**). We then fabricated a faster degrading polymer scaffold consisting of 50:50 PLG to further investigate whether degradation could support larger airway-like structures[355]. The 50:50 PLG tHLOs trended towards larger airways (414µm) relative to the 75:25 PLG (**Fig 5.4A, C**), though the

difference was not significant. Collectively, the size of the airway structures was influenced by the degradation rate of the scaffold, with slower degrading polymers leading to smaller airway-like structures.

We next tested the hypothesis that an increase in the size of pore interconnections could increase HLO fusion while creating larger airway structure, as HLO fusion may be limited for slow degrading materials that led to smaller airway structures. We obtained PCL scaffolds constructed by 3D printing rods of PCL in a cross-hatch pattern within a 5mm wide, 2mm tall cylinder (same dimensions as the scaffold used in earlier experiments), which has large pore connections (300µm) relative to the PCL scaffolds described previously, which range from 10 – 100 µm[344]. In testing the large interconnected porous scaffolds, the size of the airway structures was similar between PCL scaffolds with varying pore interconnectivity (**Fig 5.4A, B**). These results suggest that while fusion of cells can be aided by adjacent pores and degradation to contribute to the formation of airway structures, pore interconnectivity does not seem to directly determine the size of airway-like structures.

5.4.5 Controlling the tHLO explant size

After 8 weeks, we found the size of the explant was a function of the polymer type and design. The size of the explant for HLOs transplanted on PLG scaffolds reached diameters up to 2.5 cm, which is five times the original scaffold diameter (5 mm). Relative to 75:25 PLG tHLOs, the other tHLO conditions had a significant reduction in explant size. The explant sizes in fast degrading 50:50 PLG, slow degrading 85:15, and large interconnected PCL scaffolds were 0.81 cm, 0.53 cm, and 0.65 cm respectively. The PCL tHLO explant size was significantly smaller than 75:25 PLG tHLOs, with the PCL explants having diameters in the range of 0.5 to 0.6 cm (**Fig 5.5A**). However, the 50:50 PLG tHLOs were significantly larger than the 85:15 PLG tHLO. All together, these data suggested that both the slow and fast degrading PLG caused a reduction in explant size, but the size reduction was more significant in the slow degrading polymers, 85:15 PLG and

PCL. Both the PCL control and PCL large interconnected pores were similar in size (**Fig 5.5A**). Thus, the size of pore interconnections does not appear to significantly impact the explant size.

Proliferation within the explant was subsequently investigated as a contributing factor to the explant size. A significant two-fold change in proliferation (Ki67$^+$cells) in 75:25 PLG tHLO (19.5%) was observed relative to PCL tHLO (8.7%) (**Fig 5.5B-C**). During native lung development, both the branching airway epithelium and surrounding mesenchyme contain proliferating cells[345,356]. ECAD$^+$ was used to differentiate between the mesenchyme and epithelium structures. The increase in proliferation in PLG tHLOs was observed in both the clusters of epithelial cells marked

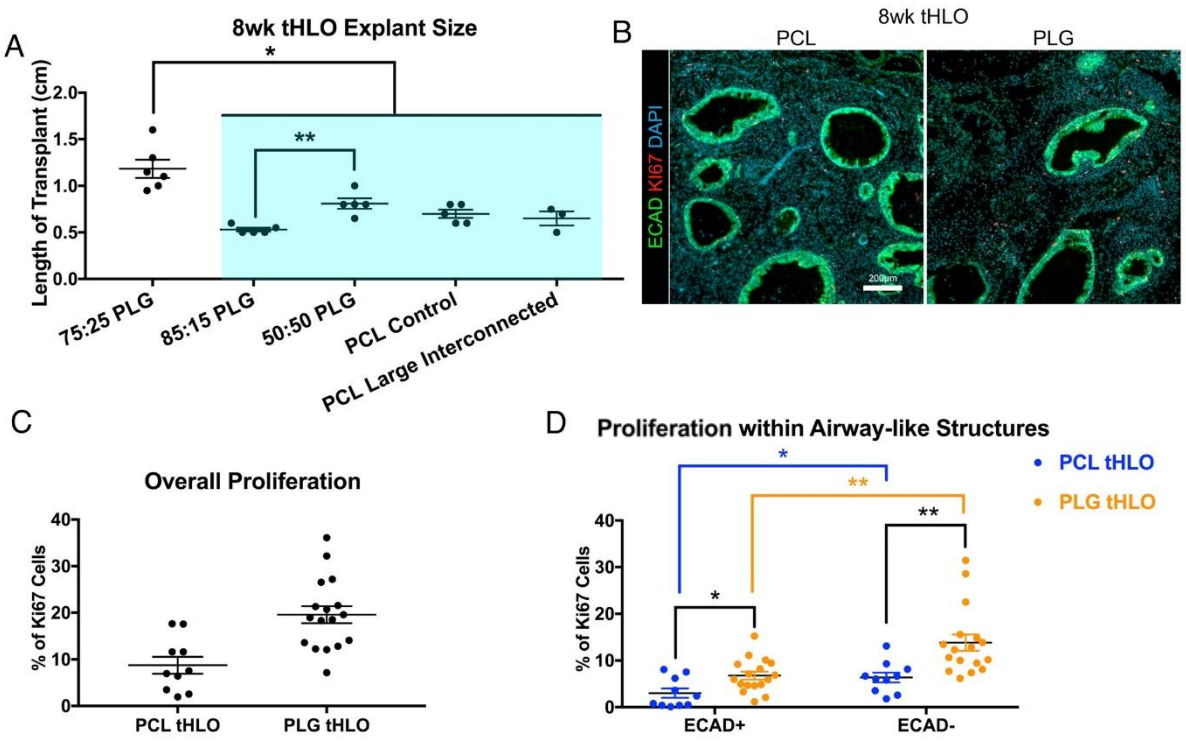

Figure 5.5 *The degradation rate of the scaffold affected explant size of tHLO.*

(A) Overall, the 75:25 PLG had the largest explant size (1.18cm, n=6) after an 8wk transplant compared to both fast (50:50 PLG, n=5) and slow degrading (85:15 and PCL, n=5) *P≤0.05. The fast degrading 50:50 PLG tHLO was significantly larger than the 85:15 PLG tHLO explant *P≤0.005. (B) Ki67$^+$ cells (red) were present within the epithelial airway structures labelled with ECAD (green) and the surrounding tissue both in PCL and 75:15 PLG. (C) 75:25 PLG (19.6% ± 1.8%) had significantly more Ki67$^+$ cells than PCL (8.7% ± 1.8%). D) The 75:25 PLG had significantly more Ki67$^+$ cells in the ECAD$^+$ and ECAD$^-$ areas (ECAD$^+$: 6.7 ± 0.9, ECAD$^-$: 13.8% 1.7) compared to PCL tHLO (ECAD$^+$: 3.009 ± 1.0, ECAD$^-$: 6.4% 1.1). Both for PCL and PLG tHLOs there was significantly more Ki67$^+$ cells in the surrounding tissue (ECAD$^-$) compared to the organized epithelium (ECAD$^+$). **P≤0.005, *P≤0.05 All error bars represent SEM.

by E-Cadherin ($ECAD^+$) within airway-like structures, and the surrounding tissue ($ECAD^-$). Interestingly, both in PLG and PCL tHLOs, proliferation was significantly greater in the tissue adjacent to the scaffold relative to the $ECAD^+$ airway-like structures (**Fig 5.5D**).

5.5 Discussion

In this report, we have demonstrated that the type of material and degradation of the microporous scaffold can affect lung airway formation, airway size, and explant size derived from transplanted HLOs (**Table 5.2**). Previously, 75:25 PLG microporous scaffolds were used to transplant HLOs into the epididymal fat pad[195]. Since no maturation occurred when HLOs were placed into the kidney capsule or sewn in the omentum of an immunocompromised mouse, we hypothesized that the tHLOs needed a surface to grow and expand on in order to mature in airway structures. We then tested this hypothesis and found that the HLOs did not require the support of

Table 5.2: Physico-chemical properties of microporous scaffolds that support HLO maturation into airway structures

Scaffold Material	Pore Size	Interconnected Pore Size	Degradation Rate	Spheroid Engraftment (Fig.1)	Airway Diameter Size (Fig.4)	Tissue Explant Size (Fig.5)
PLG 75:25	250-425µm	10-100µm	Fast	Throughout Scaffold	333µm	1.18cm
PLG 85:15	250-425µm	10-100µm	Medium	Throughout Scaffold	224µm	0.53cm
PLG 50:50	250-425µm	10-100µm	Very Fast	Throughout Scaffold	415µm	0.81cm
PEG	250-425µm	10-100µm	N/A	Within the Pores	No Airway Formation	N/A
PEG-RGD	250-425µm	10-100µm	N/A	Within the Pores	No Airway Formation	N/A
PCL	250-425µm	10-100µm	Slow	Within the Pores	277µm	0.65cm
Large Interconnected PCL	300µm	300µm	Slow	Within the Pores	299µm	0.5cm

the pores to form airway-like structures, but instead needed specific material properties to allow for the development of airway structures. More specifically, the degradation of the material affected airway size and overall explant size of the tHLO.

As the airway structures formed, the individual HLOs fused together to form these structures evident by the GFP^+ and GFP^- HLOs forming into one airway. Interestingly, the buds forming together occurred when the scaffold held its shape (PCL) or degraded (75:25 PLG) over the 8 weeks *in vivo*. Thus, the degradation was not necessary for the HLOs to fuse together to form the airway structures; however, there were no structures within the pores of the scaffolds that held the scaffold structure during the 8 weeks (PCL and 85:15 PLG). The fusion of the HLOs took place either on the surface of the PCL scaffold or as the PLG scaffold degraded. After incorporating a larger interconnected porous design to the PCL scaffold, we observed airway formation within the scaffold. Collectively, the HLOs could only form airway structures if they had the space to fuse and expand together into epithelial tubes. This need of expansion aligns with airway formation during lung development where the airways start as one epithelial bud that continually bifurcates and expands into the surrounding mesenchyme to ultimately form a network of airways[357,358].

The degradation of the material contributed to multiple properties of the organoids: airway size and overall explant size. Deriving variations in airway size will allow the study of airway diseases such as COPD and asthma in both large and small airway models[359]. An airway ranging in size from 200-350µm represents a 5^{th} generation airway in a native human lung while the 4^{th} generation ranges from 400-600µm[360]. Here by changing the degradation we were able to represent two types of airways, 4^{th} and 5^{th} generation size that are observed in the native adult lung. The data with PLG and PCL indicated that the airway size was maximal for 75:25 PLG, with slightly smaller structures for 50:50 PLG and 85:15 PLG, suggesting that degradation plays a role and that maximal size occurs at an intermediate rate of degradation. One mechanism by which degradation can influence airway size is through the fusion of organoids

from adjacent pores. Polymer degradation would influence fusion by increasing the size of the interconnections between pores over time, which would allow for greater connectivity. Polymer degradation would also function to remove the polymer as a substrate for organoid development, which may also influence proliferation and maturation. Collectively, these results are consistent with the general idea that the polymer degradation should be matched with the rate of tissue formation.

Multiple scaffolds maintained the ability to form mature airway structures, which did not form without the presence of a material, yet the explant size was a function of the scaffold properties. PCL scaffolds allowed for the formation of structures at the surface of the material, yet not within the pores of the scaffold. The increased size resulted from an increase of proliferation from the supporting tissue including the mesenchyme with a lesser extent increase of proliferation from the organized epithelium. However, the increased size of the explant did not influence the size of the airway-like structures that formed. The scaffold properties influenced the proliferation of the progenitor cells, that subsequently influenced the overall size of the explant. A more controlled growth of the organoid would allow for longer studies to be performed, since the explant growth will not impede the mouse health. For instance, future studies could use HLOs generated from patient specific hPSCs lines that have Cystic Fibrosis (CF). Patients with CF have mutations in Cystic Fibrosis Transmembrane conductance Regulator (CFTR), which causes excess of mucus within the airways which leads to chronic infection and inflammation of the lung epithelium[361]. With this model, HLOs could be generated from CF patient specific hPCS and studied in the tHLO model that provides a human airway model. Since the explant size is smaller, longer studies can be conducted in order to understand the short and long-term effects of CF on the airway epithelium and surrounding tissue including smooth muscle, cartilage and vasculature.

Microporous scaffolds composed of PEG did not support maturation over the 8 weeks and the HLOs remained as NKX2.1 progenitors. HLOs were seeded onto PEG hydrogels with and

without modification with RGD, a fibronectin binding peptide, in order to investigate if ECM signaling may be a signal directing maturation. The presence of RGD peptide did not impact maturation, suggesting that either adhesion is not a limiting factor in HLO maturation or that the RGD is insufficient to trigger the necessary signaling cascades. The innate immune response, which is active in immunocompromised mice, differed significantly between PEG versus PLG and PCL. The increase in immune cell recruitment in PEG scaffolds could be due in part to hydrogel swelling, which creates a larger volume that can contain more immune cells. This difference in scaffold environments could be a contributing factor that influenced HLOs maturation since it is known that the immune system affects hPSCs and tissue regeneration including adult stem cells[362–364].

Overall, HLO maturation was supported by multiple microporous scaffolds that resulted from fusion of organoid clusters in adjacent pores. Our studies show the physico-chemical properties of the scaffold can be manipulated to influence the properties of explant, such as the number and size of airways structures and the size of the explant. The biomaterials, thus, provide a tool that may be capable of directing tissue formation from organoids for the purpose of modeling normal development, and also for modeling disease states. Specific to airways, controlling airway and total explant size will allow for new models for airway diseases such as asthma, COPD, and CF with the potential to perform long-term studies.

Chapter 6: Regulation of Adipose Tissue Inflammation and Systemic Metabolism in Murine Obesity by Interleukin-4-Expressing Polymer Implants

6.1 Abstract

Dysfunctional adipose tissue, including defects in inflammation and cellular metabolism, plays a central role in the pathogenesis of obesity-related metabolic disease, including type 2 diabetes. Targeting adipose tissue in obesity using biopolymer implants is a novel approach towards developing therapy for metabolic disease. In this report, we study effects of porous poly(lactide-co-glycolide) (PLG) implants coated with interleukin 4 (IL-4)-expressing lentivirus into epididymal adipose tissue of mice fed high-fat diet (HFD) on local adipose tissue inflammation and systemic metabolism, using flow cytometry, immunohistochemistry, qRT-PCR, and *in vivo* systemic metabolic phenotyping. We also studied early and established murine obesity, modeled by 2-week and 10-week HFD respectively. PLG implants carrying an IL-4-expressing lentiviral vector transplanted into the epididymal fat pad of mice induced subtle effects on adipose tissue inflammation and adipogenesis that included increased $CD3^+CD4^+$ T-cell frequency, increased CD206 gene expression, and increased adipocyte hypertrophy, along with reduced fasting blood glucose levels. These effects were observed in early obesity but were not maintained in established obesity. These results show that local delivery of cytokine-expressing biopolymer implants to adipose tissue influences tissue inflammation and systemic metabolism over short time periods. Further study will be required to show more dramatic and durable metabolic effects, but these data demonstrate that modified polymer implants transplanted into adipose tissue have the potential to modulate local tissue and systemic inflammation and metabolism.

6.2 Introduction

Dysfunctional adipose tissue plays a central role in the pathogenesis of obesity-related metabolic disease, including type 2 diabetes. As adipose tissue mass expands beyond a critical point, its nutrient storage capacity is overwhelmed, causing adipocyte metabolic dysfunction and impaired nutrient buffering capacity, leading to systemic nutrient overflow, toxicity in multiple tissues, and metabolic disease. These processes are exacerbated by an inflammatory response directed towards dead and dying adipocytes, potentiating adipose tissue failure. Selective "repair" of adipose tissue metabolic dysfunction and inflammation improves systemic metabolism in murine obesity[365], supporting adipose tissue as a target for therapy. Nonetheless, effective adipose tissue-based therapeutics remain elusive.

Efforts to date directed towards adipose tissue-based therapy include transplant of intact subcutaneous adipose tissue (SAT) into mice, as well as delivery of adipocytes in artificial matrices. Transplant of intact SAT into the visceral cavity of obese mice improves systemic insulin resistance[366–368], but such a strategy is likely not feasible in humans. Engineered adipose tissues using adipocytes or preadipocytes embedded in hydrogels to date are confined to preclinical models[369], and suffer from limitations inherent to cell-based therapy, including limited *in vivo* cell viability and infectious/alloreactive complications associated with non-autologous cell sources. Cell-free therapeutic vectors delivered from artificial polymers eliminate many of these problems. Biomaterial implants have been widely used for engineering the adipose tissue because they are biodegradable, easily fabricated, and capable of delivering molecules for localized release to modulate the microenvironment [370–373]. We previously reported local IL-33 delivery from porous poly(lactide-co-glycolide) (PLG) implants attenuates graft-destructive T cell infiltration of adipose tissue in an islet transplant model[374]. Our goal in this study was to extend these results into a murine model of obesity and test the utility of PLG implants engineered to deliver lentiviral vectors expressing the human cytokine interleukin 4 (IL-4) in modulating local adipose tissue inflammation

and systemic metabolism. We hypothesized that implantation of IL-4-implants into adipose tissue of mice would attenuate tissue inflammation and systemic insulin resistance.

6.3 Materials and Methods

6.3.1 Synthetic polymer implant fabrication

6.3.2 Animals

Animal experiments were approved by University of Michigan Institutional Animal Care and Use Committee consistent with AAALAC regulations and NIH Guidelines for Care and Use of Animals. Eight-week old male C57Bl/6 mice (The Jackson Laboratory, Bar Harbor, ME, USA) were divided into three experimental arms: sham operation, empty implant, and IL-4-implant, and were transplanted into the epididymal fat pads as previously described[278]. Briefly, mice were anesthetized with 2% isoflurane, the abdomen was shaved and sterilized, and epididymal fat pads were delivered through a midline abdominal incision. One implant was wrapped in each epididymal fat pad, then placed back into the peritoneal cavity and the midline incision closed with suture (**Fig 6.1A**). For sham surgery, a midline abdominal incision made, epididymal fat pads were delivered through the incision, then placed back into the peritoneal cavity and the midline incision closed with suture. One week after surgery, mice were placed on a 60% high fat diet (HFD, Research Diets Inc., New Brunswick, NJ, USA, Cat#D12492). Two time-points were studied: 2 weeks HFD and 10 weeks HFD, to model early obesity/initiation and established obesity respectively. Body weights were measured weekly. At the end of each feeding protocol, glucose tolerance testing (GTT) was performed as described[376]. Briefly, after a 6 hour fast, mice received an intraperitoneal injection of 2g/kg of D-glucose, using a 250 mg/ml D-glucose solution in sterile PBS. Blood glucose levels collected by tail vein nick were measured at baseline (before injection, time 0), 15,30, 60, 90, and 120 min after the glucose injection, using a Precision Xtra glucometer (Abbott Laboratories, Inc., Bedford, MA, USA). After GTT, animals were euthanized and tissues collected (epididymal fat pad, subcutaneous inguinal/flank fat pad, and liver) (**Fig 6.1B**).

6.3.3 Adipocyte sizing

Adipocyte area (µm2) was measured using fixed hematoxylin/eosin-stained tissue sections imaged on an Olympus IX-81 fluorescent microscope using Texas Red channel (595-605nM). Images were captured as multiple TIFF-gray-scale images and analyzed with ImageJ software. Adipocyte area was measured in 200-500 cells from multiple slides per specimen and averaged for each tissue sample.

6.3.4 Quantitative real-time polymerase chain reaction (qRT-PCR)

Tissue samples were mechanically homogenized in Trizol® reagent (Life Technologies, Grand Island, NY, USA), RNA isolated using Direct-zol™ RNA MiniPrep Plus (Zymo Research Corp., Irvine, CA, USA), and concentration determined using a NanoDrop ND-1000 spectrophotometer (Nanodrop Technologies Inc., Wilmington, DE, USA). iScript™ Reverse Transcription Supermix was used to transcribe RNA into cDNA. Universal qRT-PCR assays were performed using SYBR Green MasterMix Universal RT (Exiqon Inc., Woburn, MA, USA) and gene target-specific primers (**Table 6.1**). Amplification profile was assessed using a LightCycler® 480 (Roche Inc., Indianapolis, IN, USA). Gene expression was normalized to ribosomal 18S housekeeping gene expression and fold change calculated using the 2-ΔΔCt method(Livak and Schmittgen 2001).

6.3.5 Flow cytometry

eWAT fat pads were washed in ice-cold RPMI media, then minced and digested in 10 mL of 1mg/ml Type II collagenase (Sigma-Aldrich Inc., St. Louis, MO, USA) at 37°C, 30 minutes with vigorous shaking. Tissue homogenate was then strained through a 100µm filter, washed in RPMI media, centrifuged, and the resultant stromal vascular cell fraction pellets isolated and incubated with 0.5mL of 0.1M ammonium chloride buffer for 5 minutes at room temperature to lyse red blood cells and then washed with PBS. In preparation for staining, cells were resuspended in RPMI and incubated in Fc block (anti-CD16/32), (Invitrogen Inc., Carlsbad, CA,

USA, Cat#14-0161) for 5 minutes on ice prior to staining for 30 minutes. Samples were then fixed, stained with antibodies (**Table 6.2**) and analyzed using a LSR Fortessa flow cytometer (Becton, Dickinson & Co., Franklin Lakes, New Jersey, USA). Compensation and data analysis were completed using FlowJo software (FlowJo, LLC, Becton, Dickinson & Co., Franklin Lakes, NJ, USA). Isotype antibodies were used to establish gating.

6.3.6 Statistics

All statistical analyses were conducted using GraphPad Prism graphing and data analysis software (GraphPad Software, Inc., La Jolla, CA, USA). Groups were compared using a one-way ANOVA with Tukey's multiple comparison test. Values were reported as the mean ± SEM. Each experimental arm (sham, empty implant, hIL-4 implant) included 8 mice.

6.4 Results

6.4.1 Implants loaded with hIL-4-expressing lentiviral vectors induce local hIL-4 expression in adipose tissue in early obesity

We studied transplantation of implants into visceral eWAT based on prior data demonstrating the visceral cavity to be a preferred site for influencing systemic metabolism in obesity[382–384]. Local transgene expression of hIL-4 in murine eWAT was quantified using qRT-PCR. At 2 weeks, hIL-4 gene expression in eWAT of hIL-4-implants in mice was significantly increased relative to sham and empty implant mice at 2 weeks (24.4±6.9 versus 1.0±0.6, and 1.7±0.7, P≤0.0.05, respectively), but not 10 weeks (1.9±0.9 versus 1.0±0.2, and 1.8±1.1, respectively) (**Fig 6.1C**). These data demonstrate that lentivirus-modified implants effect adipose tissue transgene expression for at least 2 weeks.

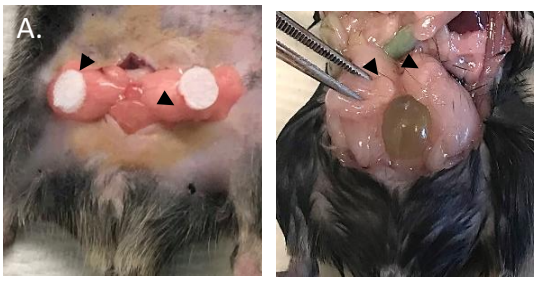

B.

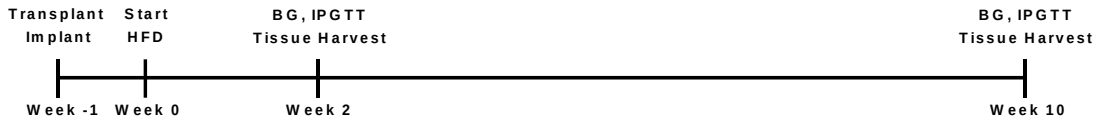

C.

Figure 6.1 *Transfection of adipose tissue with hIL-4-PLG implants*
(A) Synthetic polymer implants into eWAT fat pads. (B) Study design timeline; BG: fasting blood glucose; GTT: intraperitoneal glucose tolerance test. (C) Expression of hIL-4 in murine adipose tissue measured by qRT-PCR at 2 and 10 weeks after implants were transplanted; ordinate: fold difference in transcript level relative to sham mice; *P≤0.05 relative to the sham, ψ P≤0.05 relative to mice receiving empty implants

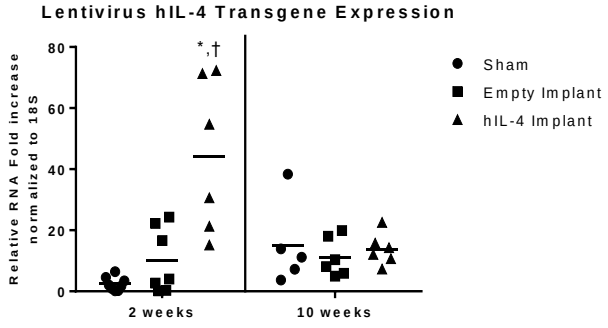

6.4.2 *hIL-4-implants regulate fasting blood glucose levels in early obesity*

We next investigated the effect of adipose tissue delivery of implants on systemic glucose metabolism in obesity. HFD induced obesity in mice consistent with numerous published data, with no difference in body weights between experimental arms (**Fig 6.2A**). sWAT and liver weights after 2 weeks HFD were similar between experimental arms, but eWAT weight was decreased in mice receiving empty implants relative to sham and hIL-4-implant arms (**Fig 6.2A**). No difference in tissue weights were observed after 10 weeks HFD (data not

A.

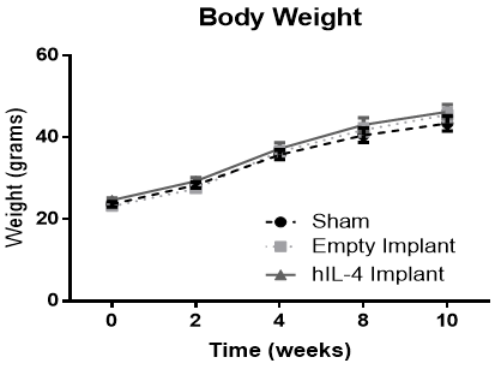
Body Weight
Weight (grams)
60
40
20
0
0
2
4
8
10
Time (weeks)
Sham
Empty Implant
hIL-4 Implant

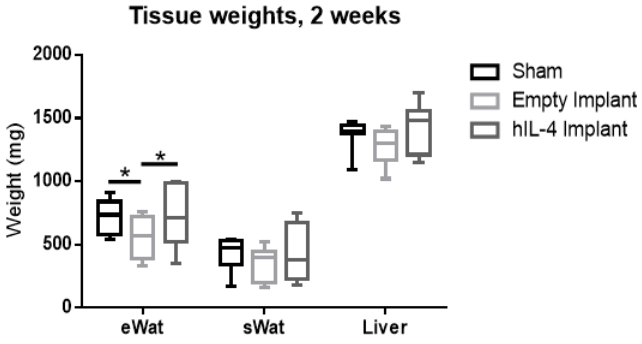
Tissue weights, 2 weeks
Weight (mg)
2000
1500
1000
500
0
*
*
eWat
sWat
Liver
Sham
Empty Implant
hIL-4 Implant

B.

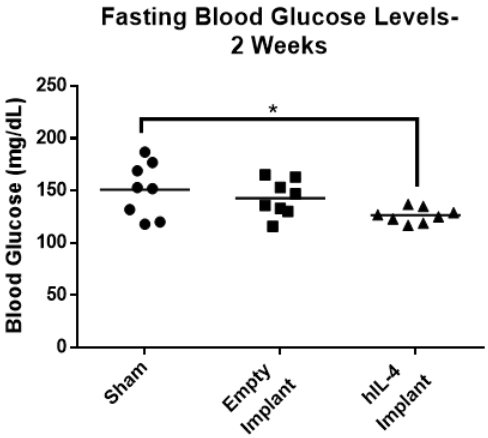
Fasting Blood Glucose Levels- 2 Weeks
Blood Glucose (mg/dL)
250
200
150
100
50
0
*
Sham
Empty Implant
hIL-4 Implant

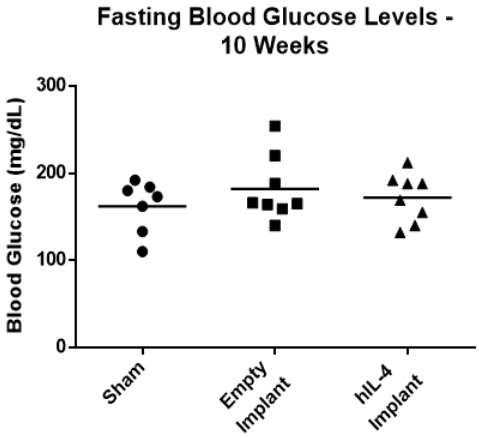
Fasting Blood Glucose Levels - 10 Weeks
Blood Glucose (mg/dL)
300
200
100
0
Sham
Empty Implant
hIL-4 Implant

C.

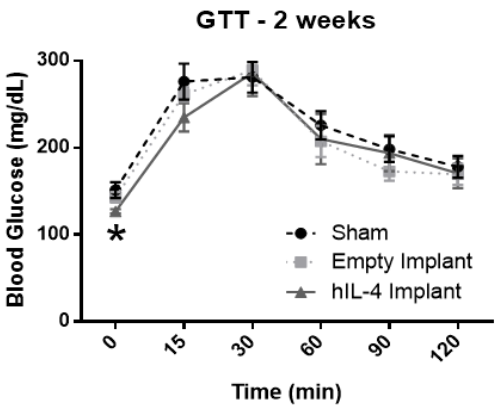
GTT - 2 weeks
Blood Glucose (mg/dL)
300
200
100
0
*
Sham
Empty Implant
hIL-4 Implant
0
15
30
60
90
120
Time (min)

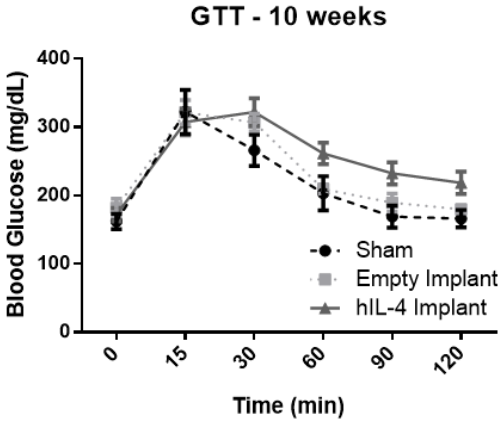
GTT - 10 weeks
Blood Glucose (mg/dL)
400
300
200
100
0
Sham
Empty Implant
hIL-4 Implant
0
15
30
60
90
120
Time (min)

D.

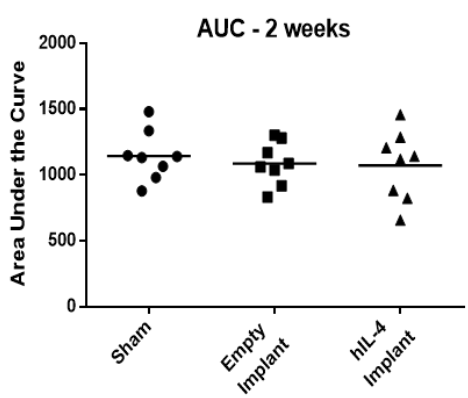
AUC - 2 weeks
Area Under the Curve
2000
1500
1000
500
0
Sham
Empty Implant
hIL-4 Implant

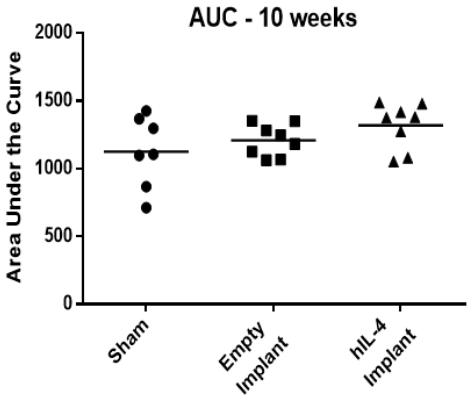
AUC - 10 weeks
Area Under the Curve
2000
1500
1000
500
0
Sham
Empty Implant
hIL-4 Implant

Figure 6.4 *hIL-4-PLG implants regulate systemic glucose metabolism*

(A) Total body weights of mice over course of 10-week study; tissue weights at 2 weeks. (B) Fasting blood glucose levels for sham, empty implant, and hIL-4 implants; *P<0.05 comparing sham and hIL-4-implant arms, using one-way ANOVA with Tukey's multiple comparison test. (C) Glucose tolerance tests (GTT) 2 and 10 weeks after implant; *P≤0.05 comparing sham and hIL-4-implant arms (D) Area under the curves (AUC) for GTT; *P≤0.05 compared to sham arm

shown). At 2 weeks HFD, hIL-4-implants caused a significant decrease in fasting blood glucose levels compared to sham and empty implant mice (**Fig 6.2B**); no difference in GTT results were observed between experimental arms at 2 weeks or 10 weeks (**Fig 6.2C, D**). These results indicate that hIL-4-implants transplanted into eWAT induce subtle but measurable improvement in systemic glucose metabolism in early but not in established obesity.

6.4.3 Implants induce hIL-4-dependent and hIL-4-independent effects on adipose tissue T-cell and macrophage infiltration in early obesity

Given the link between adipose tissue inflammation and metabolism, we next studied the effects of implants on local adipose tissue inflammation. Flow cytometry analysis revealed no difference between sham, empty implant, and hIL-4-implant mice in the frequency of leukocytes ($CD45^+$ cells) in eWAT at 2 or 10 weeks (**Fig 6.3A, B**). At 2 weeks, hIL-4-implant mice showed an increase in $CD4^+CD3^+$ T-cell frequency relative to empty implants and sham mice, but no such difference in T cell frequency was observed at 10 weeks (**Fig 6.3C, D**). No difference in the frequency of total adipose tissue macrophages (ATM, $CD45^+CD64^+$ cells) was observed between all three experimental arms at 2 weeks or 10 weeks (**Fig 6.3E, F**). Mice receiving empty implants manifested an increase in $CD45^+CD64^+CD206^+$ and $CD45^+CD64^+CD206^+CD11c^+$ macrophage subpopulations at 2 weeks relative to sham arm and hIL-4-implant mice, differences that disappeared at 10 weeks (**Fig 6.3G, H**). qRT-PCR analysis of eWAT revealed increased *CD206* expression at 2 weeks in hIL-4-implant and empty implant mice relative to sham mice, along with an increase in *TNFA* expression in empty implant mice relative to sham mice, differences that disappeared at 10 weeks (**Fig 6.4**). Together these data suggest that hIL-4-implants induce increased infiltration of T cells and M2-like ATM in adipose

tissue in early but not established obesity.

A.

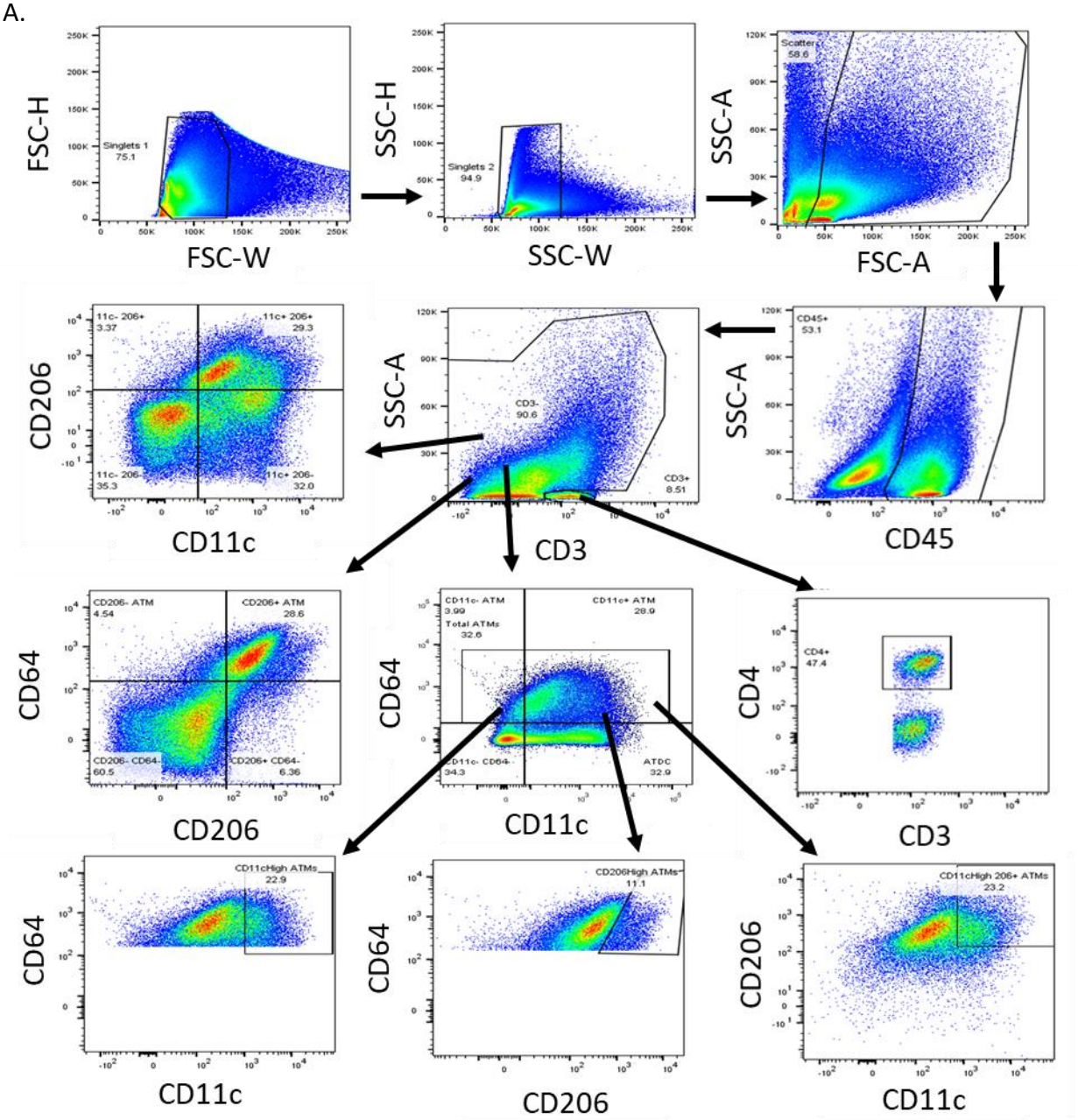

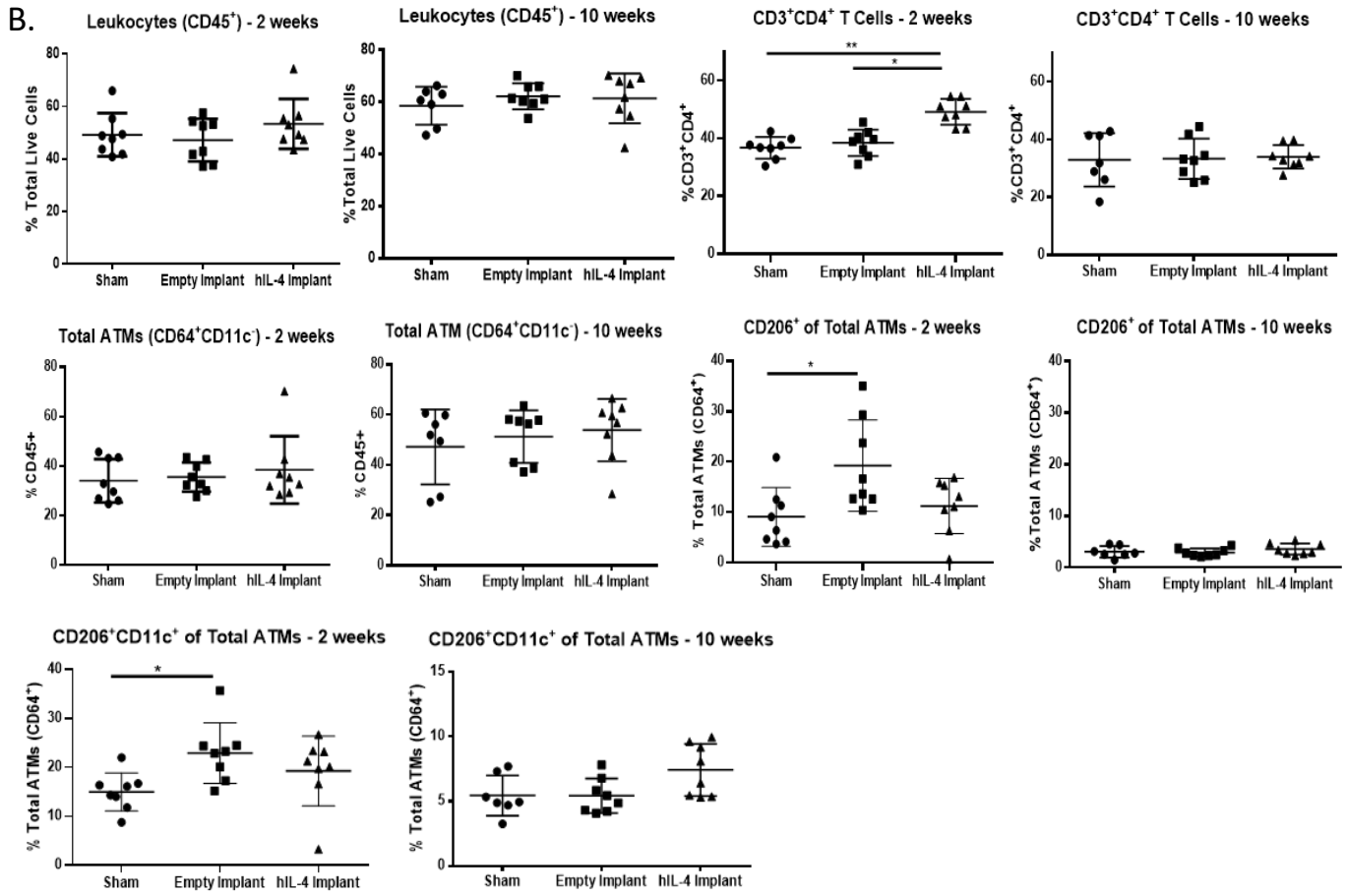

Figure 6.7 *hIL-4-implants regulate adipose tissue inflammation*

(A) Flow cytometry gating strategy. (B) Flow cytometry analysis of $CD45^+$ leukocytes, $CD3^+CD4^+$ T cells, $CD64^+CD11c^-$ ATM, $CD64^+$ $CD11c^-CD206^+$ ATM and $CD64^+CD11c^-CD206^+CD11c^+$ ATM in adipose tissue after 2 weeks and 10 weeks from mice receiving IL-4 coated implants, empty implants, or sham

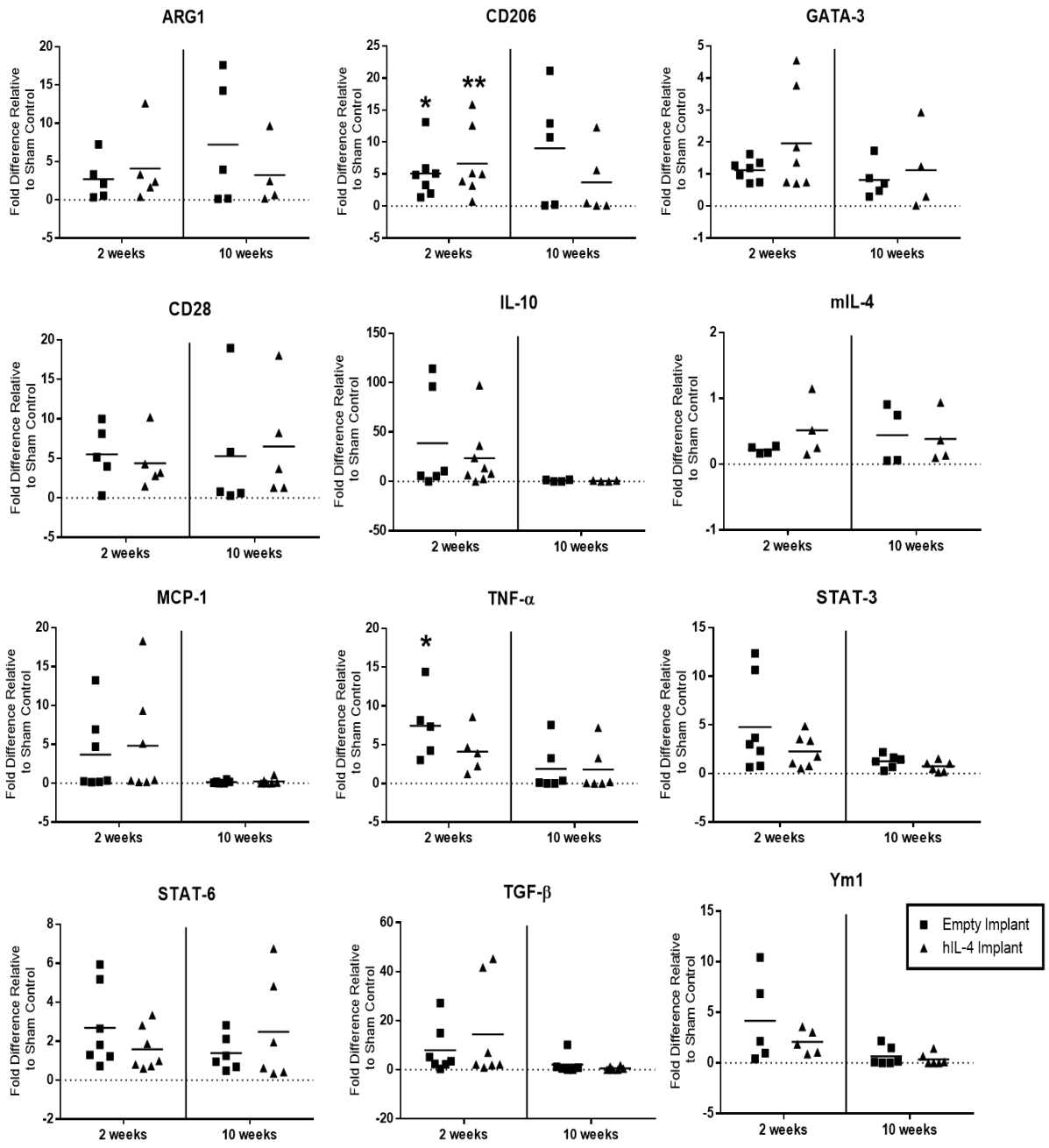

Figure 6.10 *Implants influence obesity-related inflammation in adipose tissue*

Inflammation-related gene expression assessed by qRT-PCR in eWAT; ordinates: fold differences in transcript levels relative to sham arm as referent =1; mean fold differences relative to sham +/- SEM: *CD206*: hIL4: 6.63 +/- 2.07; Empty: 5.08 +/- 1.48; *TNF-α* hIL4: 4.12 +/- 1.27; Empty: 7.44 +/- 1.98; *P≤0.05, **P≤0.01 compared to sham

6.4.4 IL-4-implants induce adipocyte hypertrophy and metabolic gene expression in adipose tissue in early obesity

We next studied the effects of implants on adipose tissue hypertrophy and metabolic gene expression. Histological analysis of adipocyte size in eWAT at 2 weeks HFD revealed larger adipocytes in hIL-4-implant treated mice relative to sham and empty implant mice (959.6±40.4μm^2 versus 788.6±27.2μm^2, P≤0.01, and 828.4±42.0μm^2, P≤0.05, respectively); no differences in adipocyte size were observed between experimental arms at 10 weeks HFD (**Fig 6.5A-C**). qRT-PCR analysis of a panel of metabolic genes demonstrated increased *GLUT-1* expression in eWAT from empty implant and hIL-4-implant mice relative to sham mice at 2 but not 10 weeks, and decreased *ATGL* and *FASN* expression in hIL-4-implant mice relative to sham mice at 2 but not 10 weeks (**Fig 6.5D**). Together these data demonstrate that hIL-4-implants induce adipocyte hypertrophy and alterations in metabolic gene expression in early but not established obesity.

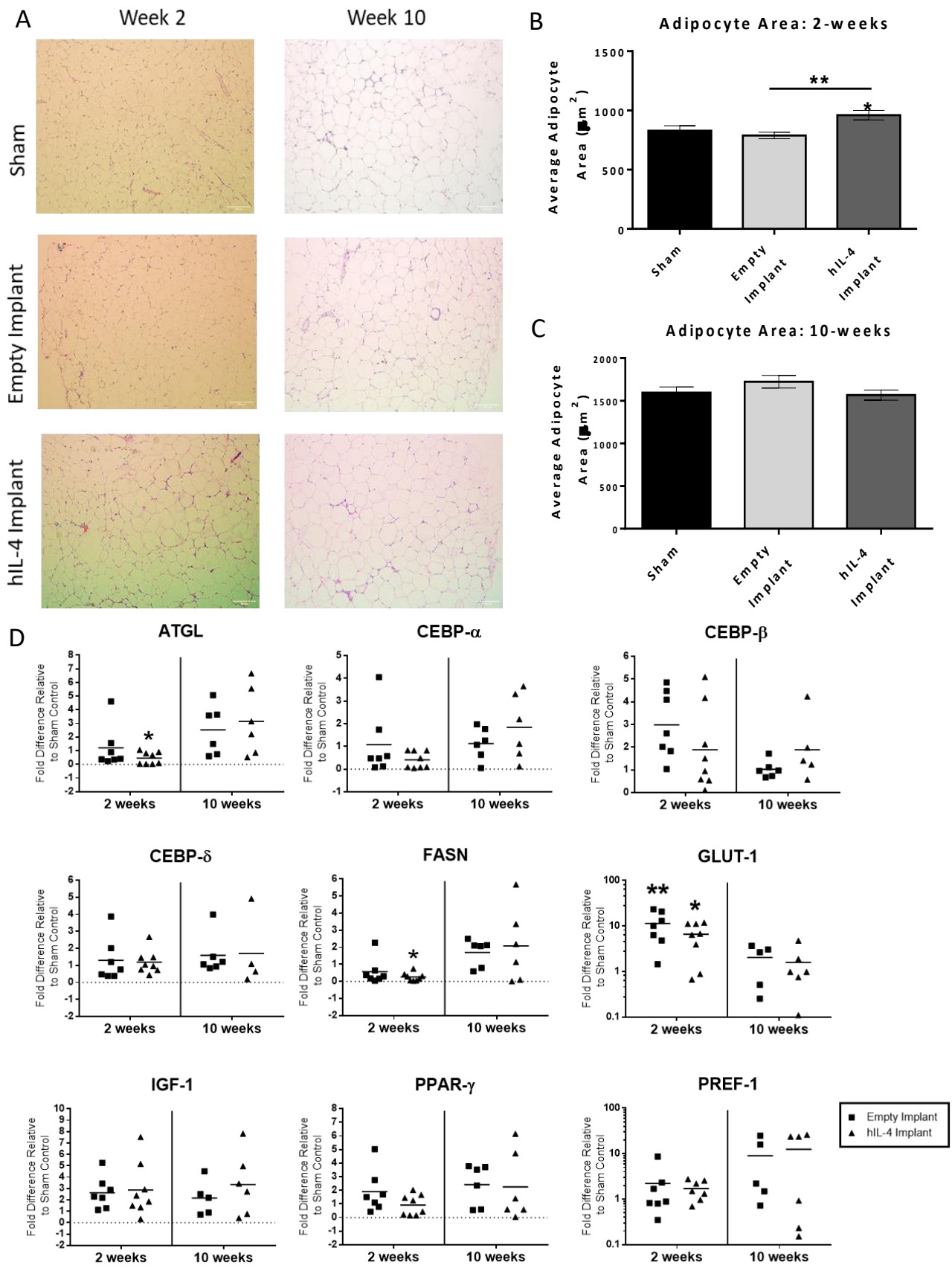
A
Week 2
Week 10
Sham
Empty Implant
hIL-4 Implant
B
Adipocyte Area: 2-weeks
Average Adipocyte Area (μm²)
1500
1000
500
0
**
*
Sham
Empty Implant
hIL-4 Implant
C
Adipocyte Area: 10-weeks
Average Adipocyte Area (μm²)
2000
1500
1000
500
0
Sham
Empty Implant
hIL-4 Implant
D
ATGL
CEBP-α
CEBP-β
CEBP-δ
FASN
GLUT-1
IGF-1
PPAR-γ
PREF-1
Fold Difference Relative to Sham Control
2 weeks
10 weeks
Empty Implant
hIL-4 Implant

Figure 6.13 *PLG implants regulate adipocyte hypertrophy and metabolic gene expression*
(A) Representative H&E stained images of eWAT adipocytes at 2 and 10-weeks; scale bar: 100 μm. (B-C) Mean adipocyte area in eWAT; *P≤0.05 comparing empty implant and hIL-4-implant arms; **P≤0.01 comparing hIL-4 arm to sham arm (D) Metabolic gene expression assessed by qRT-PCR in eWAT; ordinates: fold differences in transcript levels relative to sham arm as referent =1; mean fold differences relative to sham +/- SEM: *ATGL*: hIL4: 0.46 +/- 0.15; Empty: 1.21 +/- 0.59; *FASN*: hIL4: 0.27 +/- 0.09; Empty: 0.57 +/- 0.29; *GLUT-1*: hIL4: 6.62 +/- 1.61; Empty: 11.45 +/- 3.12; *P≤0.05, **P≤0.01 compared to sham

6.5 Discussion

Mechanisms underlying adipose tissue inflammation in obesity are not well-defined, but increased M1-like ATM, along with alterations in T-cells, have been implicated[385,386]. Multiple cytokines regulate macrophage and T-cell mediated inflammation. We studied implants loaded with hIL-4-expressing lentivirus, given prior data demonstrating that the delivery of this construct in the spinal cord led to long-term sustained expression[377]. IL-4 has also been shown to induce Th2 and regulatory T cells and an M2 phenotype in macrophages in multiple model systems[387,388], changes that would be expected to attenuate the adipose tissue inflammatory response associated with obesity. We demonstrate that PLG implants carrying an hIL-4-expressing lentiviral vector regulated adipose tissue inflammation, adipocyte hypertrophy, and systemic insulin resistance in early murine obesity induced by 2 weeks HFD, but that these effects are not maintained in established obesity at 10 weeks HFD.

Prior data by our group demonstrate that similar biomaterial implant-based delivery of lentiviral vectors into murine eWAT in model systems studying gene delivery leads to transgene expression primarily in macrophages, and that turnover of these cells limits the duration of transgene expression[389]. Similarities of these prior models with our experimental design in this manuscript suggest that ATM are the likely target of IL-4 lentivirus transduction in the present model, and that the transient effects of hIL-4 implants on adipose tissue and systemic metabolism in this obesity model are likely the result turnover of ATM beyond the 2-week time-point. In addition, hIL-4 transgene expression was sustained for 12 weeks when delivered in the spinal cord but we did not observe this similar effect when delivered in the eWAT[390]. This suggests the site of lentiviral delivery can affect sustainability and that the transient effect

observed could be partly attributed to the eWAT environment, like inflammation associated with HFD.

We demonstrate increased adipose tissue $CD3^+CD4^+$ T-cells in response to hIL-4 implant transplantation. Prior data by our group demonstrates that the localized delivery of IL-33 from our implants in the eWAT induces a Treg response[391]. Our qRT-PCR results do not demonstrate increased Treg markers in adipose tissue with implants (genes), but nonetheless, subtle alterations in Treg frequency is consistent with an improvement in system glucose metabolism. We also observed subtle changes in ATM phenotype consistent with an M2 shift, a finding consistent with the known effects of IL-4 on macrophage phenotype in multiple systems[387,388], as well as established effects of IL-4 and M2 ATM on metabolism in obesity[386,392,393].

Adipocyte hypertrophy is an adaptive response in early obesity, increasing adipocyte nutrient storage capacity to prevent overflow of lipids into the systemic circulation. hIL-4 implant implantation was associated with increased adipocyte hypertrophy in early obesity, consistent with this concept. hIL-4 implants also induced decreased expression of ATGL and FASN, genes that regulate the rate limiting steps of adipocyte lipolysis and fatty acid synthesis respectively. While increased lipolysis might be expected to decrease adipocyte hypertrophy, it is possible that differences in magnitude of induction of ATGL and FASN activities in response to implants may tip the balance of adipocyte cellular metabolism towards hypertrophy. Further studies will be necessary to define the specific effects of implants on adipocyte cellular metabolism *in vivo*. Interestingly, increased GLUT1 expression was observed in eWAT in mice treated with both empty implants and hIL-4-implant, suggesting that implants induce some changes in tissue function independent of their biocargos. Notably, a single previous report by Hendley et al. studied the effect of implantation of empty (no cytokine vector) PLG implants into eWAT fat pads on metabolism in murine obesity, and confirmed effects on metabolism independent of cytokine cargo, including increased GLUT1 expression[394]. These investigators observed

improved glucose tolerance after 2 weeks of animals receiving implants by a glucose tolerance test, but no improvement in fasting blood glucose levels as we observed in response to hIL-4-implants. In their study, mice received twice the implant dose (4 per mouse), and underwent implant transplantation one week after HFD initiation, compared to our study, in which implants were transplanted one week prior to HFD initiation. These investigators did not test implants loaded with cytokine vector, nor did they study inflammation or longer HFD time-points. These differences may account for the fact that in our study, we saw no effect of empty implants on glucose homeostasis; our data suggest that lower implant doses may require concomitant cytokine delivery to achieve measurable effects on glucose homeostasis.

We demonstrate that PLG implants loaded with hIL-4-expressing lentivirus vectors implanted into eWAT effect modest improvement in systemic glucose homeostasis along with subtle changes in adipose tissue leukocyte infiltration and adipose tissue metabolism in early murine obesity, but that these effects disappear in late obesity. More detailed studies of this model will be necessary to elucidate the precise effects of implants on adipose tissue macrophage and T-cell subpopulations, and determine if refinement of implant dosing and biocargo will have more durable effects on systemic metabolism. Nonetheless, this report demonstrates promise for synthetic polymer implants as a therapeutic tool for obesity.

Table 6.1: qRT-PCR Primers

Gene	Primer	Sequence (5'-3')
Human IL-4	forward	ACATTGTCACTGCAAATCGACACC
	reverse	TGTCTGTTACGGTCAACTCGGTGC
FASN	forward	AGCGGCCATTTCCATTGCCC
	reverse	CCATGCCCAGAGGGTGGTTG
PPAR γ	forward	TGTGGGGATAAAGCATCAGGC
	reverse	CCGGCAGTTAAGATCACACCTAT
ATGL	forward	CTGAGAATCACCATTCCCACATC
	reverse	CACAGCATGTAAGGGGGAGA
C/EBP-α	forward	GTTAGCCATGTGGTAGGAGACA
	reverse	CCCAGCCGTTAGTGAAGAGT
C/EBP-β	forward	CAAGCTGAGCGACGAGTACA
	reverse	AGCTGCTCCACCTTCTTCTG
C/EBP-δ	forward	CCTGGAGGGTTTGTGTTTTCTG
	reverse	CCCCAAAGCTATGTGCCTTTC
18S	forward	GCAATTATTCCCCATGAACG
	reverse	GGCCTCACTAAACCATCCAA
CD28	forward	TGGCTTGCTAGTGACAGTGG
	reverse	CATTGGTGGCCCAGTAGAGG
IL-10	forward	ATGCAGGACTTTAAGGGTTACTTGGGTT
	reverse	ATTCGGAGAGAGAGGTACAAACGAGGTTT
CD206	forward	TCTTTGCCTTTCCCAGTCTCC
	reverse	TGACACCCAGCGGAATTTC
MCP-1	forward	GCCAACTCTCACTGAAGCCA
	reverse	TGCTGCTGGTGATCCTCTTG
TGF-β	forward	ACCGCAACAACGCCATCTAT
	reverse	GTAACGCCAGGAATTGTTGC
Ym1	forward	GATCTCAATATACACAGTGC
	reverse	GAGCTTAGCCAAAGCTGAC
TNF-α	forward	TTGACCTCAGCGCTGAGTTG
	reverse	CCTGTAGCCCACGTCGTAG
GATA-3	forward	GAAGGCATCCAGACCCGAAAC
	reverse	ACCCATGGCGGTGACCATGC
Arg1	forward	GAACACGGCAGTGGCTTTAAC
	reverse	TGCTTAGCTCTGTCTGCTTTGC
Mouse IL-4	forward	TCGGCATTTTGAACGAGGTC
	reverse	GAAAAGCCCGAAAGAGTCTC
Pref-1	forward	GACCCACCCTGTGACCCC
	reverse	CAGGCAGCTCGTGCACCCC
STAT-3	forward	ACCCAACAGCCGCCGTAG
	reverse	CAGACTGGTTGTTTCCATTCAGAT
STAT-6	forward	TGAGGTGGGGACCAGCCGG
	reverse	GTGACCAGGACACACAGCGG
GLUT-1	forward	GCCCCCAGAAGGTTATTGA
	reverse	CGTGGTGAGTGTGGTGGA
IGF-1	forward	AAAGCAGCCCCGCTCTATCC
	reverse	CTTCTGAGTCTTGGGCATGTCA

Table 6.2: Flow Cytometry Antibodies

Target	Channel	Clone	Vendor	Catalog #
CD45	eFluor 450	30-F11	Invitrogen, eBioscience, Carlsbad, CA, USA	48-0451
CD64	PE	X54-4/7.1	BD Biosciences, (Franklin Lakes, NJ, USA	558455
CD11c	APC-eFluor 780	N418	Invitrogen, eBioscience, Carlsbad, CA, USA	47-0114
CD206	Brilliant Violet 605	C068C2	Biolegend Inc., San Diego, CA, USA	141721
CD4	APC	GK1.5	Invitrogen, eBioscience, Carlsbad, CA, USA	17-0041
CD3	PerCP-Cy5.5	145-2C11	Invitrogen, eBioscience, Carlsbad, CA, USA	45-0031
Rat IgG2a K Isotype Control	PerCP-Cy5.5	eBR2a	Invitrogen, eBioscience, Carlsbad, CA, USA	45-4321-80
Rat IgG2b kappa Isotype Control	PE	eB149/10H5	Invitrogen, eBioscience, (Carlsbad, CA, USA	12-4031-82
Rat IgG2b kappa Isotype Control	eFluor 450	eB149/10H5	Invitrogen, eBioscience, Carlsbad, CA, USA	48-4031-82
Rat IgG2b kappa Isotype Control	APC-eFluor 780	eB149/10H5	Invitrogen, eBioscience, Carlsbad, CA, USA	47-4031-82
Rat IgG2a kappa Isotype Control	Brilliant Violet 605	RTK2758	Biolegend Inc., San Diego, CA, USA	400539
Rat IgG2a kappa Isotype Control	APC	eBR2a	Invitrogen, eBioscience, Carlsbad, CA, USA	17-4321-81

Chapter 7: Conclusions and Future Perspectives on Bioengineering Strategies to Advance Organoid-Based Therapies

7.1 Summary and significance of findings

Recent advances in three-dimensional cultures have led to the generation of human organoids, which comprise of tissue structure and cellular organization similar to the native organ, while possessing the specified cell types[32,34,49,52,266,267]. Organoids provide an excellent platform for drug screening and may hold great potential for organ replacement therapies[395–397]. Currently, their major strength comes as a discovery tool to better understand human development and disease. While three-dimensional culture techniques have proved groundbreaking for generating components of the intestine, brain, liver, stomach, and the eye[32,34,49,52,266,267], these approaches have not been applied to the development of functional islets. Traditionally, hPSC-derived cells have been cultured as 3D aggregates on low attachment plates or in suspension cultures[23,274,398]. Yet, during organogenesis the progenitors congregate into structures that are surrounded by a supportive extracellular matrix[27–29].As a result, the field has turned to biomaterials that can spatially enable cell-cell and cell-matrix interactions that are needed for organ formation. However, many organoid cultures utilize reconstituted extracellular matrices, like Matrigel, as scaffolds, which are often poorly chemically defined, not translatable and allow only limited tunability. Thus, synthetic microporous scaffolds were evaluated for organoid cultures as a tunable, 3D culture environment that is more physiologically representative of the architecture of the native environment compared to traditional culture systems.

This dissertation focuses on developing scaffold technologies that can serve as a supportive matrix to promote *in vitro* development and function of islet organoids (Chapter 3 and 4), *in vivo* maturation of lung organoids (Chapter 5) as well as regulate the *in vivo* immune response to support cell transplantation (Chapter 6). The underlying concept is that cellular behavior can be guided by manipulating environmental signals. Adequately controlling the formation of complex tissues remains a challenge partly due to a lack of effective strategies that can drive a complex array of biological signals in a spatially and temporally controlled manner. Thus, this work sought out to design effective biomanufacturing scaffold platforms for organoid transplantation that could overcome these challenges and provide a promising cell-replacement strategy for the treatment of diseases.

In Chapter 3, a microporous polymer scaffold was used in a novel way to support the differentiation of hPSC-derived pancreatic progenitor cells into 3D insulin-producing clusters. Our studies showed scaffolds provide a means to control the cell-cell interactions and can provide matrix-based signals that enable more consistent and efficient maturation of hPSC-derived β-cells. Two different synthetic scaffold materials, PEG and PLG, were utilized for these studies as they provide flexibility in synthesis and modification, have been widely applied for islet transplantation[286–288] and are generally easy to manufacture for large scale production. The microporous structure provided a high surface area-to-volume ratio for polymer–cell interactions and allowed nutrients to diffuse into the scaffold, which facilitated the 3D development of cell clusters. The scaffold also provided a strategy to control cell cluster size that could protect against adverse effects of shear during clinical manufacturing.

Characterization of β-cell development within the scaffolds revealed a correlation with maturation and the scaffold pore size. Clusters forming in pores with diameters greater than 250 μm generated cells with increased expression of insulin and β-cell maturation markers. This relationship may be contributed to larger pores having a greater interconnected porosity, thus, aiding diffusion of growth media as well as enabling a more uniform distribution of seeded cells.

In addition, unlike suspension clusters, the clusters in scaffolds are in close proximity that reflect how islets are organized within the native pancreas and could lead to an increase in cell-cell interactions. E-cadherin gene and protein expression analysis confirmed scaffold cultures enhance cell-cell interactions relative to suspension cultures. Collectively, we show the microporous scaffold controls the formation of clusters and promotes cell-cell interactions that are influential in maturation.

These studies also examined cell-matrix interactions by coating scaffolds with individual ECM components in isolation, as well as, Matrigel, a mixture of ECM proteins, to establish a matrix representative of the native islet extracellular microenvironment. The relationship between cells and their ECM is highly dynamic and reciprocal. The results of this work demonstrated that cell-secreted ECM deposited on the empty scaffold surface provided a niche environment comparable to the ECM-coated scaffolds. This indicates that natural proteins do not need to be introduced on the scaffold prior to cell seeding in order to promote the assembly and function of insulin-producing clusters *in vitro*. More importantly, the matrix deposited by the cells on the PLG scaffold has the potential to mimic more of the dynamic, complex niche environment during pancreatic development compared to the coated ECM proteins that may mask the impact of the adsorbed ECM proteins. β-cell function was demonstrated through glucose-responsive functional tests that showed cells cultured on both PEG and PLG scaffolds had higher insulin secretion than suspension clusters. Collectively, the scaffold design including pore size, biomaterial, and ECM coating was shown to generate functional islet organoids that reflected the native islet architecture and environment. Thus, both scaffold materials are considered amenable to our fundamental objective – supporting β-cell maturation in a 3D environment.

The application of more recent protocols[255,289] to scaffold-based cultures offered the opportunity to further enhance glucose stimulated responses in islet organoids and characterize mechanisms that could improve *in vitro* maturation on the microporous scaffold. Chapter 4

demonstrated that the support of the scaffold microenvironment during organoid maturation could be enhanced by adjusting the differentiation stage of cells seeded on scaffolds as well as the seeding technique. PLG was used for these investigative scaffold culture studies as it generated islet organoids with higher insulin secretion function relative to PEG and was a well-established model for islet transplantation studies[279,310,399]. hPSCs were differentiated using a new protocol described in Velazco-Cruz et al. (2019) to improve cluster maturation compared to the prior protocol described in Rezania et al (2014). By changing protocols, the culture system transitioned to a 3D environment with cell clusters in suspension versus a 2D monolayer prior to scaffold seeding. Scaffold cultures were then seeded with more mature progenitor cells resembling stage 5 pancreatic endoderm and showed enhanced secretion of insulin per cell compared to scaffolds seeded with stage 4 pancreatic progenitors. These results indicate incorporating cells on scaffolds after they have made their early cell fate decisions in the differentiation process could generate more functional organoids.

Prior studies showed how cell-cell and cell-matrix interactions established during the differentiation process played a crucial role during cell development, thus the influence of cell manipulation on organoid maturation was evaluated. hPSCs were cultured on a 2D monolayer that requires less daily manipulation compared to 3D cultures and differentiated to stage 4 pancreatic progenitors then reaggregated in suspension. This reaggregation step on differentiated cells has been shown to increase the percentage of endocrine cells in the culture but also requires established cell interactions to be manipulated. GSIS functional testing of scaffold cultures seeded with cells from reaggregated clusters showed this modified protocol could generate islet organoids with insulin secretion comparable to human islets. However, the modified protocol also generated immature clusters thus the functional variability from this modified protocol needs to be further evaluated. A process step for seeding scaffold cultures was also modified by seeding scaffolds with dense clusters rather than a single cell suspension of dissociated clusters. Relative to suspension clusters, scaffold cultures seeded with dense

clusters showed enhanced expression of β-cell maturation markers after the pancreatic endoderm stage. In addition, scaffolds seeded with dense clusters showed an insulin secretion index that was comparable to the suspension clusters while scaffolds seeded with dissociated cells had decreased function. As a result, less manipulation on pancreatic endoderm clusters combined with maintaining cell-cell contacts and providing ECM signals should be considered in order to improve islet organoid function.

Furthermore, a novel fluorescent insulin reporter stem cell line was developed to give mechanistic insight regarding material design and cell development throughout the *in vitro* differentiation. This engineered hPSC line with the insertion of a superfolder green fluorescent protein in the C-peptide (sfGFP-Cpep) coding sequence helped assess the function of individual clusters by measuring dynamic insulin storage and secretion. Developing an insulin reporter allowed us to carry out non-invasive assessments of maturation during these studies as well as assess heterogeneity in function between clusters rather than relying on traditional methods that either assess an entire cell population or require the study to end. Immunofluorescence imaging of islet organoids in a high glucose solution showed GFP-positive cells in islet organoids exhibited a functional decrease in sfGFP-Cpep (insulin) but varied in intensity, indicative of a heterogenous functional response. This observation was corroborated by ELISA testing that showed islet organoids secreted insulin under glucose-challenged environments, but the insulin secretion index ratio was not comparable to human islets. Incorporating this reporter cell line laid the foundation for using cells to report on the activity of transcription factors (TFs) associated with pancreatic development or β-cell maturation, or the expression of key proteins indicative of function (e.g., insulin) over the course of differentiation. The ability of a reporter to provide a non-invasive, real-time measurement both *in vitro* and *in vivo* enables quantification of the activity for key TFs or promoters throughout the entire maturation process, which can be connected to the material design.

While the polymer scaffold provided a useful model to assess how the ECM influences *in vitro* organoid development, the islet organoids generated would be characterized as early-stage organoids since they still lacked structural and functional similarities to the endogenous counterpart. Similarly, *in vitro* human lung organoid (HLO) cultures only reflect the fetal airway, with adult airway-like structures generated only after *in vivo* transplantation[195]. Prior studies showed HLO transplantation was further enhanced with biomaterial scaffolds, where HLOs had improved tissue structure and cellular differentiation after being transplanted for 8 weeks. Chapter 5 focused on identifying the polymer scaffolds design parameters that directed engraftment and *in vivo* maturation for HLOs, which could then be applied to promote islet organoid *in vivo* development as well.

In order to evaluate the role of polymer material on *in vivo* organoid development, PLG. PEG and PCL scaffolds were generated for organoid cultures. In contrast to PLG scaffolds, transplantation of HLOs on microporous PEG hydrogel scaffolds led to inhibited growth and maturation with transplanted HLOs remaining as immature $NKX2.1^{+}$ lung progenitors. The presence of RGD, a fibronectin binding peptide, bound to the PEG gel did not impact maturation either, suggesting that either adhesion is not a limiting factor in HLO maturation or that the RGD is insufficient to trigger the necessary signaling cascades. On the other hand, HLOs transplanted on PCL led to tube-like structures that resembled both the structure and cellular diversity of an adult airway. Similar to PLG, PCL scaffolds allowed for the formation of structures at the surface of the material, yet, more similar to PEG, tissue formation did not occur within the pores of the scaffold. Each polymer has a different degradation rate with PLG degrading in 2-4 months, PCL degrading over a year and PEG being non-degradable[400]. These variations in organoid growth suggest that polymer degradation contributed to the maturation, and that the size of the airway structures and the total size of the transplanted tissue was influenced by the material degradation rate. Histological staining showed the increased explant size resulted from an increase of proliferation from the supporting tissue including the mesenchyme with a lesser

extent increase of proliferation from the organized epithelium. Thus, scaffold properties were shown to have influenced the proliferation of the progenitor cells, which subsequently influenced the overall size of the explant.

Airway structure formation was evaluated using GFP^+ and GFP^- HLOs to better characterize organoid growth within the scaffolds after transplantation. As the airway structures formed, the individual HLOs fused together to form these structures evident by the GFP^+ and GFP- HLOs forming into one airway. Surprisingly, the buds were able to form together when the scaffold held its shape (PCL) or degraded (75:25 PLG) over the 8 weeks *in vivo*. Thus, the degradation was not necessary for the HLOs to fuse together; however, the HLOs could only form airway structures if they had the space to fuse and expand together into epithelial tubes. Additional studies focused on testing the hypothesis that maximal airway size occurs at an intermediate rate of degradation. Evaluating PLG scaffolds of varying degradation rates confirmed this theory by showing that the airway size was maximal for 75:25 PLG control, with slightly smaller structures for the faster degrading 50:50 PLG and slower degrading 85:15 PLG. One mechanism by which degradation can influence airway size is by increasing the size of the interconnections between pores over time. This would allow for greater fusion of organoids from adjacent pores. Overall, these results are consistent with the general idea that the polymer degradation should be matched with the rate of tissue formation. Our studies show the physico-chemical properties of the scaffold can be manipulated to influence the properties of explant, such as the number and size of airways structures and the size of the explant. Controlling airway and total explant size will allow for new models for airway diseases such as asthma, COPD, and CF with the potential to perform long-term studies. Collectively, these biomaterial platforms were shown to provide a set of tools to promote maturation of the tissues and to control the size and structure of the organoids.

Despite the potential shown here for organoid cultures on microporous scaffolds, immune tolerance remains a major challenge due to the abundance of foreign antigens

recognized by the host immune system and the arduous task of regulating the natural immune response to attack foreign tissues or cells. Using scaffold technologies to develop and transplant organoids, however, allows existing immunosuppressive therapies, or emerging tolerance therapies, to be incorporated into the scaffold to prevent tissue rejection. Towards this goal, Chapter 6 investigates a method for immunomodulatory cytokine delivery from scaffold implants that can be used to modulate a specific set of immune cells for tolerance induction.

PLG microporous implants were loaded with human IL-4 (hIL-4)-expressing lentivirus to induce Th2 and regulatory T cells as well as an M2 phenotype in macrophages in order to attenuate the adipose tissue inflammatory response. Implants were then transplanted in the epididymal fat pad of immunocompetent mice who were given a high fat diet (HFD) to challenge the inflammatory environment. Despite the sustained expression shown in prior studies that used a similar approach to deliver lentivirus in the spinal cord[390], viral delivery of hIL-4 in the epididymal fat pad resulted in short-term, localized transgene expression. Prior data suggested that adipose tissue macrophages (ATM) are the likely target of hIL-4 lentivirus transduction in the present model[389]. Consequently, the transient effects of hIL-4 implants on adipose tissue and systemic metabolism in this obesity model are likely the result of turnover of ATM beyond the 2-week time-point. We also observed subtle changes in the ATM phenotype consistent with an M2 shift, a finding consistent with the known effects of IL-4 on macrophage phenotype in multiple systems[387,388].

PLG implants loaded with hIL-4-expressing lentivirus vectors implanted into eWAT induced a modest improvement in systemic glucose homeostasis, but these effects disappeared in late obesity. The short-term effect on glucose metabolism is likely attributed to the transient viral expression in the local environment. Analyzing the immune response in the fat pad at the 2-week transplant time-point revealed there was an increased $CD3^{+}CD4^{+}$ T-cell population in adipose tissue in response to hIL-4 implant transplantation. hIL-4 implants also induced decreased expression of ATGL and FASN, genes that regulate the rate limiting steps of

adipocyte lipolysis and fatty acid synthesis, respectively. hIL-4 implant transplantation was associated with increased adipocyte hypertrophy in early obesity, consistent with these results. Interestingly, increased GLUT1 expression was observed in fat pads in mice treated with both empty implants and hIL-4-implant, suggesting that implants induce some changes in tissue function independent of their biocargos. More detailed studies of this model will be necessary to elucidate the precise effects of implants on adipose tissue macrophage and T-cell subpopulations and determine if refinement of implant dosing and biocargo will have more durable effects on systemic metabolism. In summary, PLG implants carrying an hIL-4-expressing lentiviral vector regulated adipose tissue inflammation, adipocyte hypertrophy, and systemic insulin resistance in early murine obesity induced by 2 weeks HFD, but these effects were not maintained in established obesity at 10 weeks HFD. These studies demonstrate how a gene delivery system might be used in conjunction with organoid transplantation to create an area of localized immunosuppression that would protect regenerated tissue from immune attack while decreasing or eliminating the requirement for systemic immunosuppression.

The Shea lab is performing groundbreaking research at the interface of biomaterials, tissue engineering, and developmental biology using synthetic microporous scaffolds, and the studies presented in this dissertation advance these technologies with the end goal of translation from bench to clinic. Taken together, this dissertation introduces a novel biomanufacturing platform as an alternative to the traditional suspension culture to improve the development and efficacy of cell-based therapies. These conclusions establish the groundwork for understanding the influential role of the ECM and relevant factors that are necessary to enhance the function of transplanted organoids. In order to further characterize the critical components in the extracellular microenvironment that regulate these effects, additional studies should be carried out, which are described in the next section.

7.2 Future directions

There are several key questions that need to be examined in order for further progress to be made toward the ultimate goal of using synthetic microporous scaffolds for organ transplantation in humans. This section will highlight some recommended new directions for continuing the work detailed in this thesis.

7.2.1 Measure metabolic maturation of mitochondria in islet organoids to characterize function

The process of generating hPSC-derived insulin-expressing cells is well established however little is known about their bioenergetic requirements or how closely their energy metabolism is governed by the constraints of the genetic developmental program. The transition from a pluripotent stem cell through progressive stages of differentiation probably involves dynamic changes in the energy demand for cellular processes, depending on the needs of the individual cell types. ATP generation in aerobic cells is divided between two main pathways: anaerobic glycolysis and mitochondrial oxidative phosphorylation. On the basis of changing energy demands, and the need to limit the production of mitochondrial reactive oxygen species, it might be expected that the relative contribution of these two pathways would change during differentiation.

Characterizing mitochondrial metabolism as hPSCs differentiate down the pancreatic lineage could elucidate key characteristics that indicate whether the islet organoids will be mature or immature. Assessing mitochondrial respiratory function in islet organoids generated under various scaffold conditions as well as in suspension could provide a more complex understanding of maturation as well. Studies have shown that human islets show increased oxygen consumption rate (OCR) upon stimulation with high glucose. The capacity for maturing organoids to raise OCR as efficiently as human islets in response to glucose could be another assessment that the organoids are metabolically mature and effectively engage mitochondrial oxidative phosphorylation for glucose oxidation. In addition, the analysis of individual clusters within the

maturing pancreatic progenitors *in vitro* could provide metabolic markers that will identify pathways or factors that will enhance homogenous maturation.

Some studies suggest that the mitochondrial population increases as a universal phenomenon from the initiation of hPSC differentiation regardless of the differentiation lineage [401]. On the other hand, several energy-consuming processes might be diminished during the early transition to a differentiated state, and it might not be accompanied by a mitochondrial expansion[402–405]. Changes in metabolic regulation *in vitro* might reflect the typical energy requirements of these cell types *in vivo* and, thus, be guided by genetic developmental programs. Future studies should follow the genetic regulators of energy metabolism in tandem with the bioenergetics to clarify the different forces driving mitochondrial function.

7.2.2 Targeted genome editing for iPSC-derived organoids

Future studies may enable iPSCs to culture islet organoids. iPSCs derived from patient's adult cells can undergo CRISPR genome editing to correct a disease-related mutation and then undergo transplantation as functional organ-like units used to advance tissue repair and functionality. Monogenic diabetes occurs at a young age due to mutations in a single gene, leading to impaired function of the pancreatic β-cells. A particular genetic modification (e.g. knockout, knockin) can be generated in a well-differentiating, healthy hPSC line or a candidate mutation can be corrected in patient-derived hiPSCs. A proof-of-concept use of genome editing in the organoid field was recently demonstrated[406]. Effective genome editing of human stem cells in primary intestinal organoids using CRISPR/Cas9 was proven. Then, using CRISPR-Cas9-mediated HDR, intestinal organoids from two patients with cystic fibrosis were genome edited to fix the mutation, the primary cause of the disease. It was shown that the genome-edited intestinal organoid systems expressed the corrected CFTR allele, which subsequently resulted in fully functional proteins in these organoids. This study demonstrates how genome editing of iPSC-derived organoids could be a potential gene therapy strategy, with limited risks to off-target tissue

mutagenesis. It is important to keep in mind, however, some of the challenges that come with translating iPSCs to the clinic. In order for this technology to be successful, we will need to address the cost of manufacturing personalized medicine that meets the regulatory demands of the FDA as well as ensure patient safety.

7.2.3 In vivo imaging of β-cell function in sfGFP-Cpep islet organoids to measure glucose-mediated heterogeneity

While the cellular components required for GSIS are well established, the key signaling pathways that regulate β cell metabolism and insulin secretion *in vivo* remain poorly understood. Analysis of insulin content, or insulin secretion, in real time is difficult for transplanted cells, thus, it is tough to determine when euglycemia is not achieved due to a limited group of highly-responsive insulin-secreting cells or alternatively a large group of minimally-responsive cells. Using the sfGFP-Cpep reporter would address some of these challenges in understanding what factors in the *in vivo* milieu are critical to promoting and maintaining functional maturation.

In vivo imaging of $Ca2^{+}$activity in a recent study revealed heterogeneity of β-cell functional development *in vivo* occurred as two waves propagating from the islet mantle to the core, coordinated by islet vascularization[407]. This asynchronous behavior was also observed in mice with pancreatic sfGFP-Cpep cells where a small subset of islets showed rapid dispossession of a major fraction of their stored sfGFP-Cpep (insulin) content, whereas most islets exhibited no demonstrable loss of sfGFP-Cpep (insulin)[314]. These studies strongly suggest that there are “first responder” islets to an *in vivo* glycemic challenge, which cannot be replicated by islets *in vitro*. This heterogenous response observed in the pancreas could be a major regulator of glucose metabolism but not so easily replicated by transplanted hPSC-derived clusters that are dispersed across a transplant site. Alternatively, the scaffold culture presents a physical structure similar to the pancreas tissue that integrates clusters into connective tissue that might enhance the ability for clusters to function similarly to their endogenous counterpart. Using the sfGFP-Cpep tool, we

have made preliminary attempts at evaluating *in vivo* heterogenous function in hPSC-derived scaffold cultures that can be further improve upon to compare to transplanted suspension clusters and further examine what role an asynchronous response plays in glucose metabolism. These studies can also help provide new insights for the optimization of the differentiation process.

7.2.4 Designing dynamic organoid culture environments through multi-faced scaffolds

Bioengineered scaffold matrices facilitate dynamic variation of mechanical and biochemical properties to guide *in vitro* three-dimensional culture conditions for individual cell types. Studies in Chapters 3, 4 and 5 demonstrate how scaffold cultures can be utilized to develop different organoids as a universal platform. The scaffold's tunable features combined with the enabling of the organoid tissue to remodel the local environment through ECM deposition and material degradation allows the scaffold culture to reflect the specific niche for different organoids. In order to advance the capabilities shown by the synthetic scaffolds, future studies should focus on developing multi-faceted scaffold designs that recapitulate tissue heterogeneity in terms of spatial arrangement and temporal changes. New scaffold designs could incorporate compartmentalized regions in the biomaterial structure that are functionalized with molecular factors that form concentration gradients through the construct and guide organoid development and tissue architecture. The rate the supportive scaffold matrix degrades demonstrated a critical component for *in vivo* HLO growth. Applying new technologies to regulate degradation might allow this technology to be applied to a wider variety of organoid cultures. A number of scaffold designs could be investigated to achieve this control, such as self-assembling peptides and peptide amphiphiles that provide for controllable scaffold gelation, degradation, and presentation of cell adhesion motifs.[408] Hydrogels that are created with bifunctional crosslinkers containing MMP degradable peptide sequences have also been shown to influence differentiations and could provide cells the ability to dynamically remodel their environment as they grow[409]. EphA, a family of receptor tyrosine kinases, along with their Ephrin-A ligands—both of which are localized to the

cell membrane—mediate cell-cell interactions between β-cells to regulate insulin secretion[410]. Inclusion of EphA/Ephrin-A fusion proteins into the scaffold may provide cells a more natural environment by “cloaking” the scaffold with ligands found on mature beta cells to help signal the islet organoids toward a more mature phenotype. Recent advances in biofabrication technologies approaches have also enabled the fabrication of scaffolds that aim to mimic the dynamic nature of the native extracellular matrix.[411]

7.2.5 Expression profiling of sorted cells generated from hPSC-derived islet organoid development

One of the biggest challenges in stem cell research in recent years is the development of differentiation protocols to efficiently generate functional, robust cells for therapeutic applications. In order to learn more about progenitor cells at different stages along the differentiation process in which they become progressively more committed to the final beta cell fate either in suspension or on scaffold cultures, studies can focus on identifying, isolating and characterizing stage specific progenitor cells. Stage specific cell types could be identified by either SRY box 17 (SOX17) or pancreatic and duodenal homeobox 1 (PDX1), two transcription factors which are expressed relatively early in pancreatic differentiation. Characterizing these time points may serve as useful markers for monitoring the differentiation of hPSCs under the influence of different growth factors at different time points. The sorting of precursors at key stages of pancreatic beta cell differentiation enables systematic assessment of the effect of signaling factors, small molecules or other compounds on growth, differentiation and survival of these progenitor cells. The expression profile of these populations could be assessed in order to compare the influence of scaffold and suspension cultures on specific precursor cell types during particular stages of the differentiation. Moreover, it is anticipated that the information gained through these studies will permit more efficient generation of populations enriched with functional beta cells derived from stem cells.

7.2.6 Engineering organoid vascularization within scaffold cultures

Both HLO's and islet organoids were transplanted on PLG microporous scaffolds in the epididymal fat pad, but only the HLO's showed further maturation and tissue organization. While this could be attributed to the level of maturation of organoids prior to transplantation, future studies should assess if this difference in *in vivo* development between organoids could be addressed through enhanced vascularization. During organogenesis, developing tissues interact with a complex network of vasculature which permits not only oxygen, nutrient and waste exchange, but also allows for a structural template for growth. In order to test this, in vivo studies could consist of utilizing a pocket scaffold design that allows for an inner layer protein loaded PLG disk to be inserted between two scaffold culture halves and locally release VEGF within the implant site. An alternative method would be to culture an endothelial-derived scaffold culture and transplant the vascular tissue along with the islet organoid scaffold culture to promote vasculature support to the organoid. The mechanisms that guide the difference in how these two organoids mature in vivo could also be limiting other organoids thus these studies will provide useful observations for the field.

Chapter 8: Appendix

Chapter 8.1: Microporous scaffolds support islet transplantation in non-human primate studies

Clinical islet transplantation has the potential to become a cure for Type 1 Diabetes (T1D). However, a number of barriers limit the widespread application of this technology. A translatable supply of islets and the underlying autoimmune and immune response to the transplanted cells reflect two major barriers; however, a third major challenge is the isolation of a transplantable site for the long-term engraftment and functionality of islets. Clinically, islets are transplanted intrahepatically, which is associated with an instant blood mediated inflammatory response (IBMIR) that can damage the cells. Furthermore, the liver has numerous critical functions and thus little can be done to alter this transplantation site. Extrahepatic sites have been investigated, primarily using encapsulation approaches to protect islets from the host immune response. However, these approaches often lead to the exclusion of blood vessels that would normally revascularize the islets. The Shea lab has been working for over 10 years on islet transplantation on microporous scaffolds that allow for revascularization of the transplanted islets. The ability to revascularize the islets distinguishes this approach from encapsulation systems, as revascularization can provide the nutrients necessary for islet survival while also facilitating the sensing of blood glucose and the distribution of insulin. These microporous scaffolds have also been functionalized to control the local environment, which was initially employed to enhance the engraftment of the transplanted islets (e.g., extracellular matrix proteins, trophic factors). More recently, the scaffolds have also been employed to modulate the innate and adaptive immune responses (e.g., immune cytokines, Tregs) to delay rejection or promote immune tolerance, which is emerging as an essential component for any cell transplantation strategy. These microporous scaffolds will be studied in large animal models,

performed in collaboration with the Oberholzer and Lyubimov laboratories, with the aim of initiating clinical trials using this technology.

Polymer scaffolds, used for the transplantation of islets to mouse models, were scaled to accommodate the transplantation of islets to the omentum of non-human primates (NHP). PLG and PEG polymer scaffolds were scaled up to 35 mm in diameter and 2 mm in thickness (**Fig 8.1.1**) using the same manufacturing techniques previously used for fabricating mouse

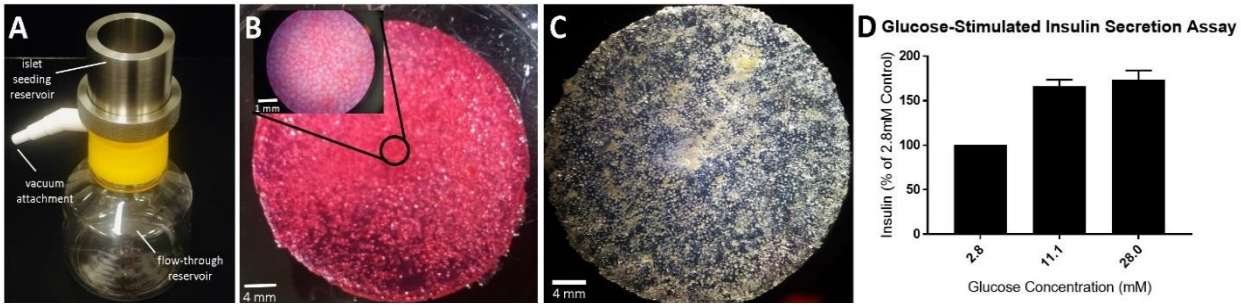

Figure 8.1.1 *Scale-up of scaffolds for NHP studies and optimizing islet seeding.*

An islet seeding device (A) was developed to maximize the islet seeding efficiency. Either 25 mm diameter or 35 mm diameter NHP scaffolds (B) are placed into the islet seeding reservoir and islets suspended in media are added to the reservoir. A vacuum is attached to the attachment to pull through the media to the flow-through reservoir, leaving islets seeded to the scaffold (99% islet seeding efficiency). Human islets seeded to a PEG hydrogel scaffold (C), where islets can be seen as white masses and the PEG scaffold is a translucent blue color. Human islets seeded to PEG hydrogel scaffolds using the islet seeding device remain viable and functional following a 24 hour incubation in media, as indicated by the glucose stimulated insulin secretion assay (D).

scaffolds. Furthermore, standardized GMP manufacturing and sterilization protocols were developed for reproducible scale-up manufacturing of these scaffolds. For NHP scaffold transplantation studies, the scaffolds were sterilized using gamma irradiation and scaffold integrity was examined before and after, and scaffold polymer concentrations were optimized to withstand the sterilization process (**Fig 8.1.2**). Sterilized scaffolds tested for the presence of bacterial contaminants found that sterilized scaffolds were negative for aerobic and anaerobic bacteria, yeast, and fungi (**Fig 8.1.3**). Endotoxin testing was also conducted on sterilized scaffolds and determined no significant presence of endotoxins following sterilization (<10 EU endotoxin level reported for scaffolds; up to 20 EU/device are FDA thresholds for endotoxin levels) (**Fig 8.1.4**).

This was further confirmed by performing a blood panel and showing no significant increases in inflammatory immune cell populations after the transplant. (**Table 8.1.1**). An islet seeding device was developed (**Fig 8.1.1A**) for the reproducible and homogenous seeding of islets to the

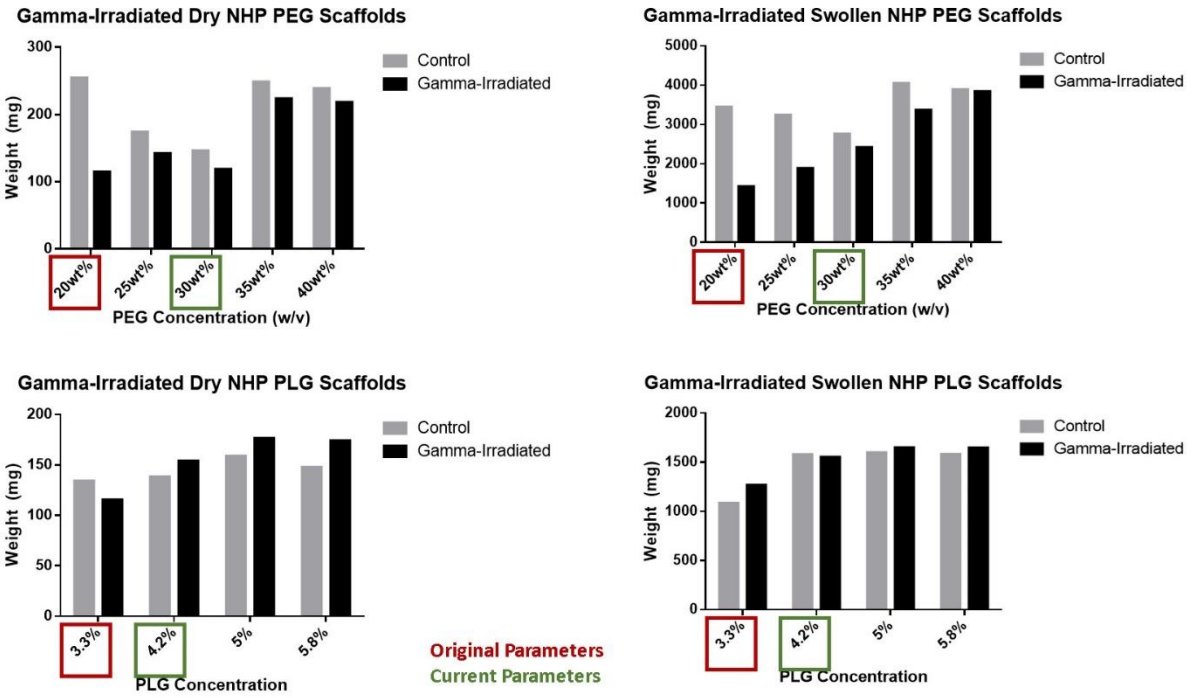

Figure 8.1.2 *Impact of Gamma Irradiation on PEG and PLG Scaffolds*

The process of irradiating scaffolds for sterility had affected their handling with seeding and transplantation. We thus investigated modifications to the formulation such that the scaffolds would have properties similar to what has been used in the past. PEG and PLG scaffolds were fabricated using varying concentrations of polymer and the dry weights and wet (swollen) weights were compared between non-irraditated (control) and gamma-irradiated scaffolds to determine which scaffold fabrication parameters were the least affected by gamma irradiation.

```
01/20/2017  BODY FLUID CULTURE
   R1711  ACC. NO.:    F42176       TRANSPORT TIME:  UNKNO  PRELIMINARY
          SPECIMEN DESCRIPTION:     BODY FLUID
          SPECIAL REQUESTS    :     RECEIVED IN STERILE TUBE

               DIRECT GRAM :   1.    NO WBC, NO ORGANISMS SEEN

               CULTURE         :     1.    NO GROWTH 3 DAYS

01/20/2017  ANAEROBE CULTURE
   R1711  ACC. NO.:    F42176       TRANSPORT TIME:  UNKNO  PRELIMINARY
          SPECIMEN DESCRIPTION:     BODY FLUID
          SPECIAL REQUESTS    :     RECEIVED IN STERILE TUBE

               DIRECT GRAM :   1.    FOR RESULT PLEASE REFER TO DIRECT GRAM STAIN
                                     OF: BODYFLUID FROM 01/20/17

               CULTURE         :     1.    NO ANAEROBES ISOLATED AFTER 3 DAYS

01/20/2017  FUNGUS CULTURE
   R1711  ACC. NO.:    F42176       TRANSPORT TIME:  UNKNO  PRELIMINARY
          SPECIMEN DESCRIPTION:     BODY FLUID
          SPECIAL REQUESTS    :     RECEIVED IN STERILE TUBE

               KOH/CALCOFLU:   1.    NO YEAST OR FUNGAL ELEMENTS SEEN

               CULTURE         :     1.    CULTURE UNDER REVIEW FOR THE NEXT FOUR WEEKS.
                                           CURRENT CULTURE STATUS: NO FUNGUS ISOLATED AT
                                           THIS TIME.
```

Figure 8.1.4 *Bacteriology panel for sterilized PEG scaffold.*

Sterilized scaffolds tested for the presence of bacterial contaminants found that sterilized scaffolds were negative for aerobic and anaerobic bacteria, yeast, and fungi.

```
********* ENDOSAFE Test Record *********
          V7.12C 8/25/2011
DateTime: ..... 01-01-98 @ 12:36:59AM
Device: ..................................... 0304
OperatorID: ................................. PDR
Cartridge: ..................... Endotoxin
Temperature: .. Start: 37.0C  End: 37.0C
Method: ..................................... KX-122
Cartridge Lot#: ................. 6159137
Cartridge Cal Code: ....... 113347306949
Range: ..................................... 1-0.01
Range Time: ................ Sec: 133 073
Onset Times: ........... 210 160 214 164
Slope: -0.409 ..... Intercept: +2.124
Dilution: ................................... 1
Sample Lot: ................................ E002
Sample ID: ..................... JAN 17/17
Sample Rxn Time CV: ........... 1.3% Pass
Spike Value: ............... 0.298 EU/mL
Spike Rxn Time CV: ........... 1.7% Pass
Spike Recovery: ............... 167% Pass
Test Suitability: ..................... Pass
Sample #1 Value: ........... 0.327 EU/mL
Sample #2 Value: ........... 0.312 EU/mL
```

Figure 8.1.3 *Endotoxin testing of sterilized PEG scaffold.*

Sterilized scaffolds tested for presence of endotoxins yielded a negative test for endotoxins (<0.298 EU/mL endotoxin level reported for scaffolds; <0.5 EU/mL or <20 EU/device are FDA thresholds for endotoxin levels for devices directly or indirectly in contact with blood, respectively)

scaffolds. Human islets seeded to PEG hydrogel scaffold (**Fig 8.1.1C**) using the islet seeding

device remain viable and functional following a 24 hour incubation in media, as indicated by the glucose stimulated insulin secretion assay (**FIG 8.1.1D**). Next, scaffolds without islets were transplanted to the bursa omentalis of a non-diabetic NHP to determine the optimal surgical

Table 8.1.1: Comprehensive results of blood panel from a NHP 30 days following transplantation for the immunoreactivity study.

	Pre-Immunosuppression	Post-Immunosuppresion; Pre-Transplant	2 Weeks Post-Transplant	Normal Range	Units
White Blood Cell	7.9	10.58	10.27	[6.9 - 19.0]	x10^3/uL
Red Blood Cell	7.06	6.32	5.69	[5.0 - 7.6]	x10^6/uL
Hemoglobin	14.3	12.9	11.4	[10.3 - 14.4]	g/dL
Hematocrit	47.2	42.2	37.8	[34.3 - 44.1]	%
Mean Corpuscular Volume	66.9	66.7	66.3	[52.9 - 71.5]	fL
Mean Corpuscular Hemoglobin	20.3	20.3	20.0	[16.4 - 21.5]	pg
Mean Corpuscular Hemoglobin Concentration	30.4	30.5	30.2	[28.4 - 33.7]	g/dL
Platelet	266	425	291	[193.2 - 578.2]	x10^3/uL
Mean Platelet Volume	9.8	9.7	9.6	[5.8 - 10.5]	fL
Red Cell Distribution Width	15.3	14.4	13.6	[12.3 - 15.8]	fL
% Neutrophils	51.9	61.2	68.9	[38.0 - 80.8]	%
% Lymphocytes	43.7	35.6	26.8	[27.9 - 66.9]	%
% Monocytes	2.5	1.9	2.4	[0.9 - 7.3]	%
% Eosinophils	0.90	0.50	1.10	[0.2 - 4.6]	%
% Basophils	0.4	0.4	0.2	[0 - 1.0]	%
% Large Unstained Cells	0.6	0.5	0.6	[0 - 2.8]	%
# Neutrophils	4.1	6.48	7.08	[2.8 - 12.1]	x10^3/uL
#Lymphocytes	3.45	3.76	2.75	[2.5 - 7.8]	x10^3/uL
#Monocytes	0.20	0.20	0.25	[0 - 1.0]	x10^3/uL
#Eosinophils	0.07	0.05	0.12	[0.04 - 0.4]	x10^3/uL
#Basophils	0.03	0.04	0.02	[0 - 0.1]	x10^3/uL
#Large Unstained Cells	0.05	0.05	0.06	[0 - 0.4]	x10^3/uL
%Reticulocytes	0.27	0.51	0.56	[0.2 - 1.1]	%
#Reticulocytes	19.1	32.3	31.8	[11.1 - 51.6]	x10^3/uL
Sodium	147	147	146	[137 - 145]	mEq/L
Potassium	3.5	3.3	3.5	[3.5 - 5.5]	mEq/L
Chloride	107	108	105	[98 - 106]	mEq/L
Alkaline Phosphotase	275	243	178	[38 - 126]	U/L
Alanine Aminotransferase	20	30	33	[0 - 30]	U/L
Aspartate Aminotransferase	19	29	46	[0 - 40]	U/L
Bilirubin Test	0.2	0.2	0.23	[0 - 1.0]	mg/dL total
Blood Urea Nitrogen	9	11	16	[7 - 21]	mg/dL
Creatinine	1.2244	1.1531	1.1706	[1.0 - 2.0]	mg/dL
Calcium	9.64	9.82	9.28	[9 - 11] ; [4.5 - 5.5]	mg/dL ; mEq/L
Glucose	66	49	58	[80 - 120]	g/dL
Albumin	4.969	4.568	4.018	[3.5 - 5.5]	U/L
Total Protein	7.675	7.472	6.446	[6.3 - 8.2]	gm/dL
Phosphate	3.9	4.4	4.7	[3 - 4.5] ; [1.8 - 2.3]	mg/dL ; mEq/L
Gamma-Glutamyl Transpeptidase	105.512	102.919	104.833	[8 - 78]	U/L
Globulin	2.98	2.9	2.43	[-99999-99999]	mg/L
Albumin/Globulin Ratio	1.6	1.6	1.7	[-99999-99999]	

procedure: laproscopic or open-surgery; and optimal transplant site: scaffold transplanted on top of bursa omentalis (**Fig 8.1.5A**) or scaffold transplanted to a pocket within the bursa omentalis (**Fig 8.1.5B**). Also, this transplantation of scaffolds (no islets) to the bursa omentalis of non-immunosuppressed NHPs was used for 30-day immunoreactivity study to determine inflammatory response to scaffolds and immune cell profile within scaffolds. The immunoreactivity study demonstrated no significant presence of immune cells or inflammation for PEG and

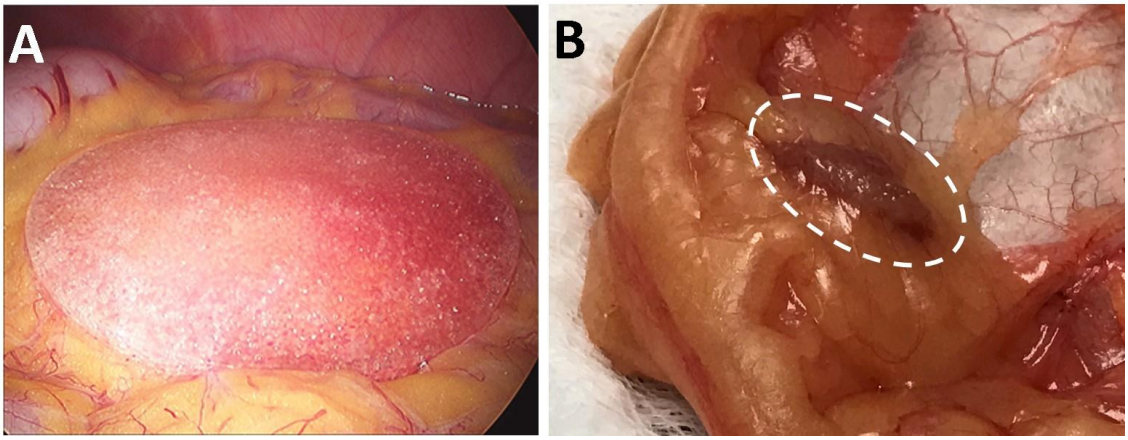

Figure 8.1.6 *PEG hydrogel transplantation to the bursa omentalis of a NHP.*

A PEG hydrogel laproscopically transplanted on top of the bursa omentailis of a NHP immediately following transplantation.A PEG hydrogel (side-view) transplanted to a pocket within the bursa omentalis of a NHP, 30 days following transplantation.

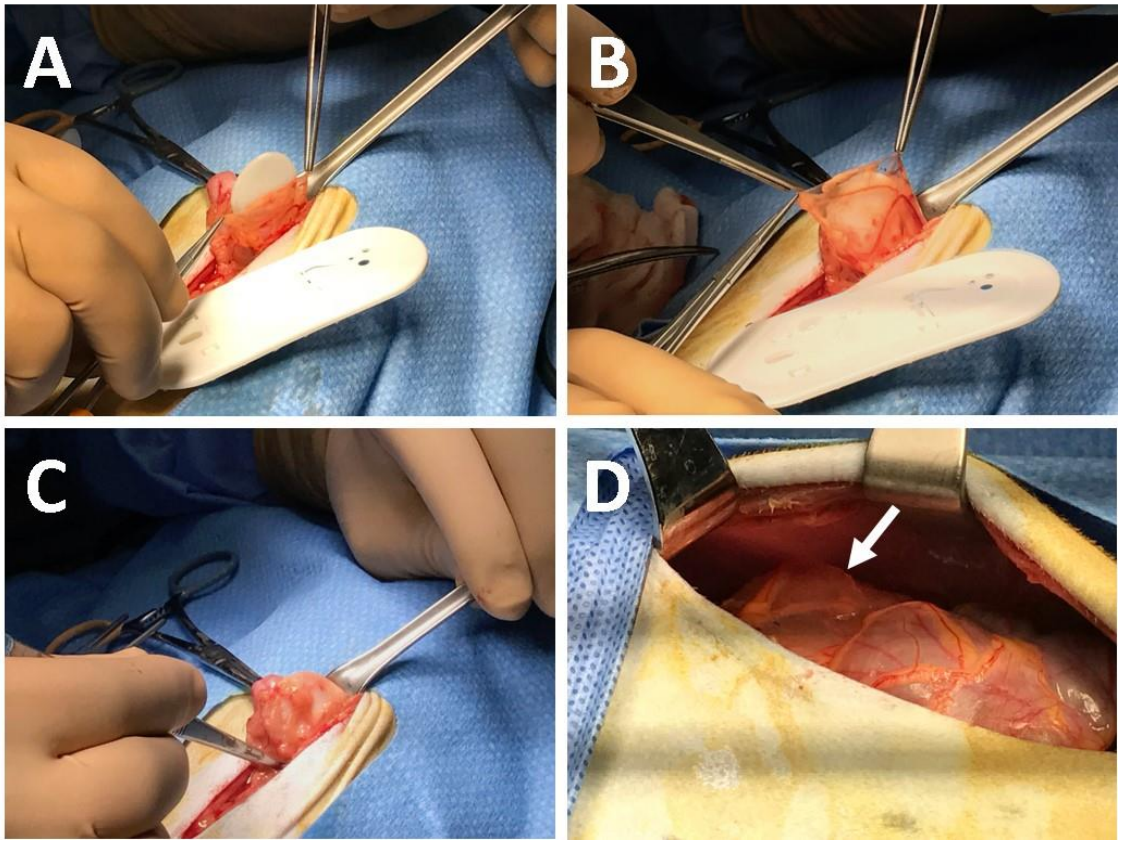

Figure 8.1.5 *Scaffold transplantation to the bursa omentalis of a NHP for 30 day immunoreactivity study.*

An incision was made into the omentum of a NHP to create a pocket in which a scaffold was inserted (A), then wrapped in the omental tissue (B). Scaffold wrapped in the omentum was placed back into the peritoneal space (C) and can be seen transplanted to the omentum prior to suturing the NHP (white arrow, D).

PLG scaffolds, compared to the omentum (control), 30 days following transplantation (**Fig 8.1.6-7**). Previous clinical islet transplantation studies have demonstrated that intraportal islet transplantation provokes an instant blood mediated inflammatory reaction that leads to significant, immediate islet cell loss. Using the omentum as a transplant site with a microporous

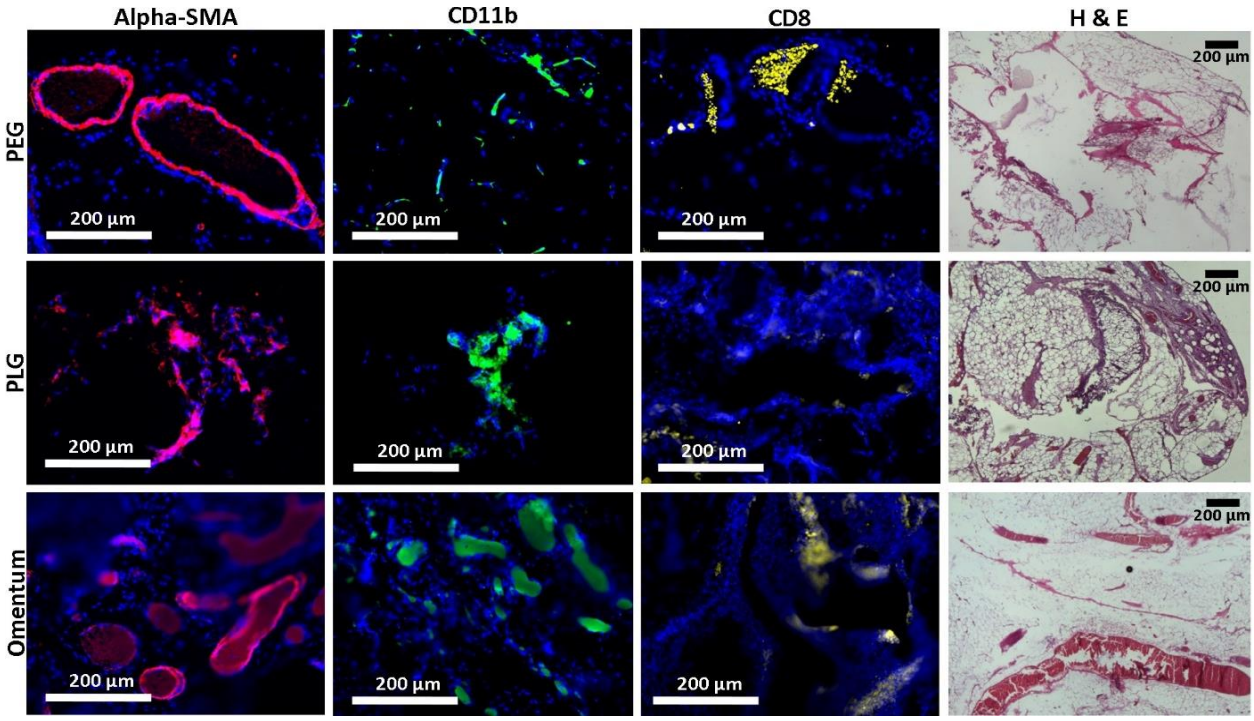

Figure 8.1.7 *Immunohistochemistry Staining for Immune Markers of PLG, PEG Scaffolds and Omentum from Immunoreactivity Study*

Scaffolds, transplanted without islets, and omentum were removed from NHP 30 days following transplantation and stained for alpha-smooth muscle actin (red), CD11b (green) CD8 (yellow), and nuclear counterstain with DAPI (blue). Scale bar = 200 µm. This analysis and others suggest that the material is well tolerated and that inflammation or fibrosis would not obviously limit engraftment or function.

scaffold could reduce the need for using multiple donors to achieve long-term insulin independence after islet transplantation. We showed in this study that the scaffolds are biocompatible in the omentum and, for next steps, plan to obtain toxicology data that is necessary to pursue an IND through the FDA to begin clinical trials for human islet transplantation. UIC has extensive regulatory experience in working with the FDA and has filed several INDs for islet cell transplantation. UIC is currently in the process of biologic license application, and anticipates obtaining licensure for human, isolated cadaveric islets by June

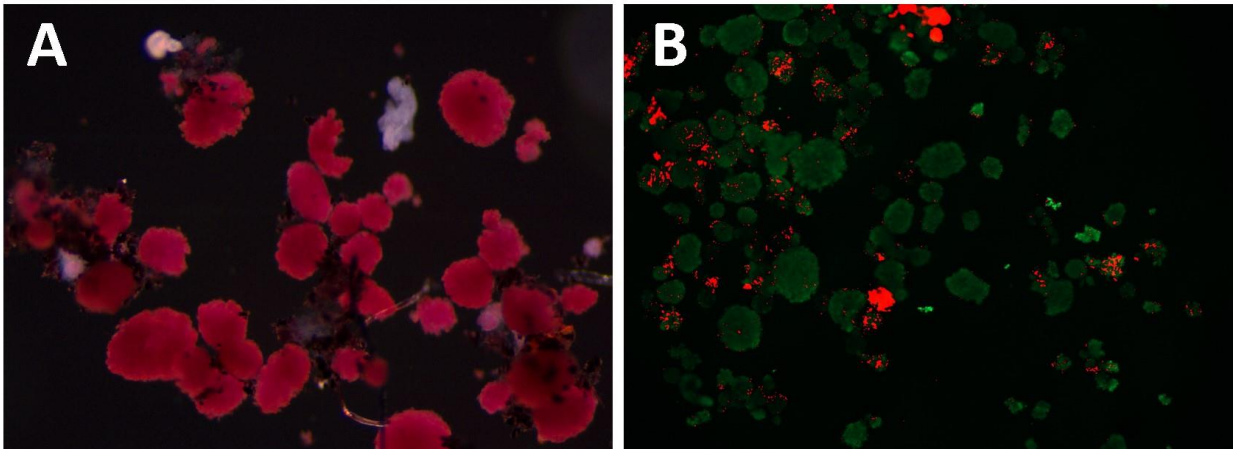

Figure 8.1.8 *NHP islet isolation, purification, and transplantation to diabetic, immunosuppressed NHP*
Islets were isolated from 4 NHP donors and purified. Islet purity was assessed using a DTZ stain (A) and islet viability was assessed using a live/dead stain (B). Islets were seeded to scaffolds using our proprietary islet seeding device 2 days following isolation and transplanted to a diabetic, immunosuppressed NHP.

2017. Having licensure for the human islet cell product would greatly simplify future INDs in testing scaffolds that fall under this device category by the FDA. Transplantation of scaffolds seeded with purified islets (**Fig 8.1.8**) to non-diabetic, immunosuppressed NHPs for 30 days demonstrated that islets were not rejected and were still present 30 days following transplantation. Finally, diabetic, immunosuppressed NHPs transplanted with scaffolds, seeded with islets (non-therapeutic dose), determined that islets remain functional – regulating blood glucose levels (**Fig 8.1.9A**), decreasing demand for exogenous insulin administration (**Fig 1.8.9A**), and producing C-peptide (**Fig 8.1.9B**) – up to 10 days following transplantation, and histology demonstrates the presence of extensive insulin staining 30 days following transplantation (**Fig 8.1.9C**).

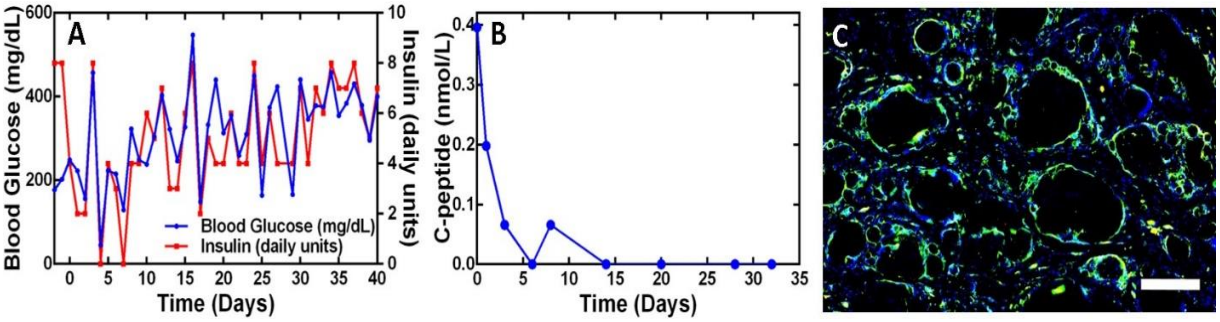

Figure 8.1.9 *Transplantation of allogeneic islets (non-therapeutic dose) using microporous PLG polymer scaffolds to the omentum of NHPs.*

Blood glucose levels and decreased demand for exogenous insulin within the first 30 days following transplantation of a sub-therapeutic dose of islets (A), C-peptide production was also observed within the first 10 days following transplantation (B), and histology demonstrates the presence of extensive insulin staining 30 days following transplantation (insulin = green, DAPI nuclear counterstain = blue, scale bar = 200 µm. (C)

In order to improve the therapeutic function of the transplanted islets on scaffolds, we increased the islet load from 40K IEQ to approx. 110K IEQ. Diabetic, immunosuppressed NHPs were transplanted with scaffolds seeded with an increased islet dose and we found that islets showed a similar result to the lower dose by regulating blood glucose levels (**Fig 8.1.10**), decreasing demand for exogenous insulin administration (**Fig 8.1.10**), and producing C-peptide

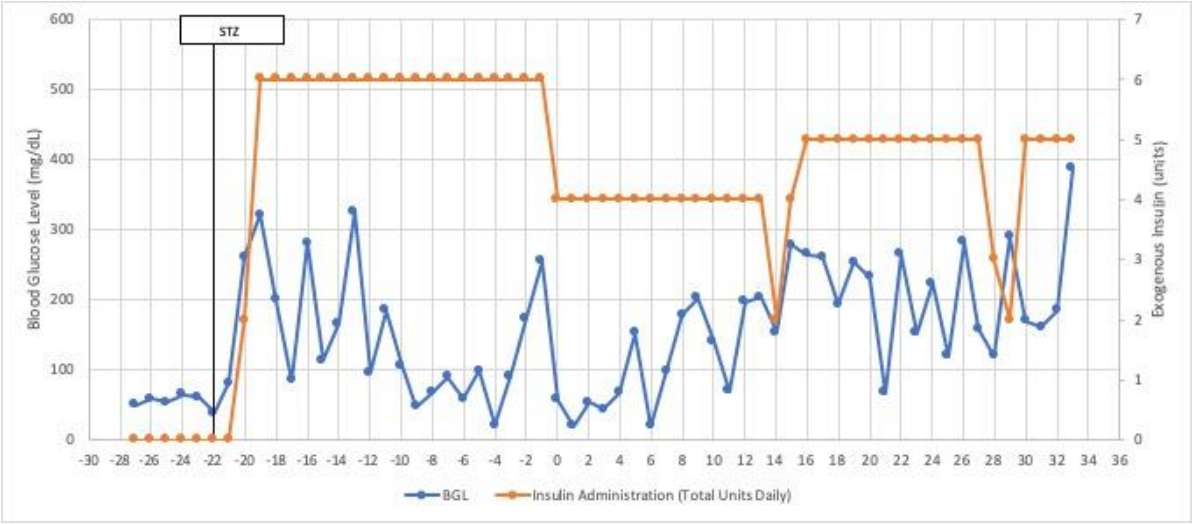

Figure 8.1.10 *Blood Glucose Levels and Daily Insulin Administration for CN9086 Allogeneic Scaffold Transplant Recipient (on Immunosuppression).*

BGLs were well managed (<205 mg/dL) for the first 2 weeks post-transplant. Insulin administration was reduced in the immediate post-transplant period (2 weeks) from 6 units daily to 4 units daily. Transplant dose = approximately 34,186 IEQ/kg

(**Fig 8.1.11**) – up to 12 days following transplantation. IVDTT demonstrated that the transplant

was not able to maintain glucose homeostasis after a 15 day time point in the diabetic monkey (**Fig 8.1.12**). We investigated the immune response to the scaffolds and found no abnormalities

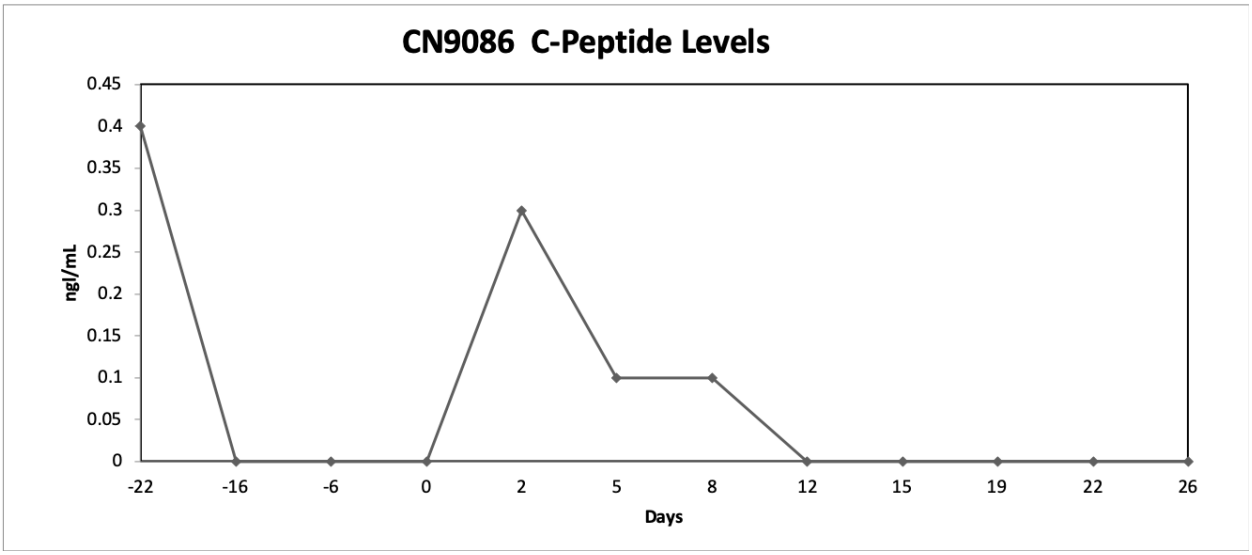

Figure 8.1.11 *C-Peptide Levels for CN9086*

The diabetic NHP recipient maintained detectable C-peptide levels until Day 8 post-transplant. Prior to transplant, loss of islet function was confirmed post-STZ (Day -16). Baseline Reading = Day -22

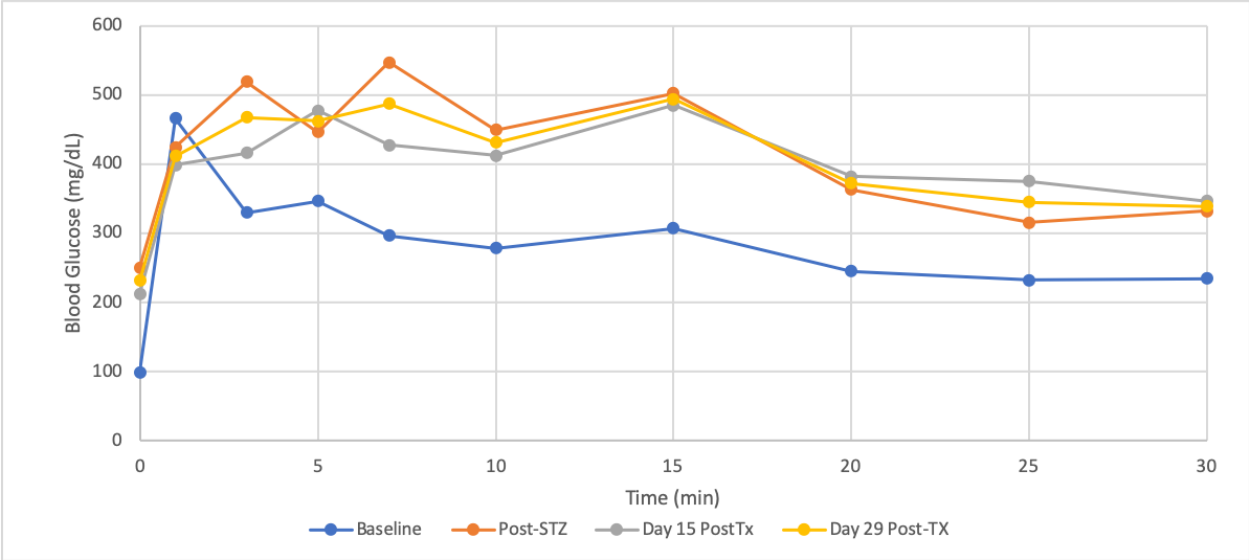

Figure 8.1.12 *Intravenous Dextrose Tolerance Test (IVDTT) to Assess Functional Response of Islets.*

A functional response was not detected at Day 14 or Day 29 post-transplant.

were noted in the CBCs or chemistries which supports the safety of the scaffold implant (**Fig 8.1.13**).

A

Monkey:	CN9086							
Condition:	Pre-STZ	Post-STZ		Tx Day	2 Week Post Tx IVDTT	4 Week Post Tx IVDTT	Normal Range	Units
Day:	-26	-16	-1	0	15	29		
Date:	9/20/19	9/30/19	10/15/19	10/16/19	10/31/19	11/14/19		
WBC	11.36	6.44	6.19	13.85	15.89	14.58	[3.0 - 19.0]	x10^3/uL
RBC	6.24	6.43	6.59	5.75	5.24	5.82	[5.0 - 7.6]	x10^6/uL
HGB	12.4	13.1	13.1	11.8	10.6	11.9	[10.3 - 14.4]	g/dL
HCT	42	43.4	44.1	38	35.8	39.7	[34.3 - 44.1]	%
MCV	67.3	67.4	67	66.2	68.2	68.2	[52.9 - 71.5]	fL
MCH	19.9	20.3	19.9	20.5	20.2	20.4	[16.4 - 21.5]	pg
MCHC	29.6	30.1	29.7	321	29.6	29.9	[28.4 - 33.7]	g/dL
PLT	593	420	364	411	530	445	[193.2 - 578.2]	x10^3/uL
MPV	7.7	7.1	7.4	8.1	8.1	6.9	[5.8 - 10.5]	fL
RDW	13.8	14.6	13.2	12.9	12.7	12.6	[12.3 - 15.8]	%
%NEUT	7	44.8	32.3	83.1	61.1	71.4	[38.0 - 80.8]	%
%LYMPH	99.1	46.2	55.8	15.2	31.2	26.1	[27.9 - 66.9]	%
%MONO	0	4.1	3.4	1.3	3	1.3	[0.9 - 7.3]	%
%EOS	0.1	3.8	6.5	0	3.9	0.9	[0.2 - 4.6]	%
%BASO	0.2	0.1	0.2	0.2	0.5	0.3	[0 - 1.0]	%
%LUC	0	1	1.9	0.2	0.3	0.1	[0 - 2.8]	%
#NEUT	0.08	2.88	2	11.51	9.71	10.41	[2.8 - 12.1]	x10^3/uL
#LYMPH	11.25	2.97	3.45	2.1	4.96	3.81	[2.5 - 7.8]	x10^3/uL
#MONO	0	0.26	0.21	0.19	0.48	0.18	[0 - 1.0]	x10^3/uL
#EOS	0.01	0.24	0.4	0	0.61	0.12	[0.04 - 0.4]	x10^3/uL
#BASO	0.02	0.01	0.01	0.03	0.08	0.04	[0 - 0.1]	x10^3/uL
#LUC	0	0.07	0.11	0.02	0.05	0.02	[0 - 0.4]	x10^3/uL
%RETIC	0.22	0.22	0.35	0.14	0.29	0.35	[0.2 - 1.1]	%
#RETIC	13.8	14.2	23.3	8	15.1	20.6	[11.1 - 51.6]	x10^3/uL

B

Monkey:	CN9086							
Condition:	Pre-STZ	Post-STZ		Tx Day	2 Week Post Tx IVDTT	4 Week Post Tx IVDTT	Normal Range	Units
Day:	-26	-16	-1	0	15	29		
Date:	9/20/19	9/30/19	10/15/19	10/16/19	10/31/19	11/14/19		
Albumin	3.769	4.317	4.394	4.703	4.288	4.396	[3.4-5.0]	g/dL
Alkaline Phosphatase	564	755	134	588	413	414	[83-455]	IU/L
ALT	14	50	45	47	43	69	[3-28]	IU/L
AST	43	25	39	61	28	26	[23-65]	IU/L
Urea Nitrogen (BUN)	11	13	7	17	22	16	[7-21]	mg/dL
Calcium	9.29	9.73	9.81	9.48	9.77	9.5	[8.88-11.8]	mg/dL
Creatinine	0.8487	1.0027	0.9836	1.0351	0.8606	0.9023	[0.81-1.35]	mg/dL
GGT	75	83	71	81	75	84	[49-112]	IU/L
Glucose	98	254	57	22	194	241	[44-100]	mg/dL
I. Phosphorous	4.1	3.9	4.3	3.4	3.9	4	[3-6.2]	mg/dL
Total Bilirubin	0.14	0.18	0.22	0.16	0.22	0.24	[0.15-0.31]	mg/dL
Total Protein	6.83	7.236	7.735	7.838	7.488	7.459	[6.5-8.9]	g/dL
Sodium	146	141	144	145	145	142	[151-188]	mmol/L
Potassium	4.2	4.1	3.9	3.3	4.3	4.7	[3.8-6.4]	mmol/L
Chloride	106	103	108	106	102	104	[110-141]	mmol/L
Globulin	3.061	2.919	3.341	3.135	3.2	3.063	[3.1-3.9]	g/dL
Alb/Glob Ratio	1	1	1	2	1	1		

Figure 8.1.13 *Complete Blood Counts (CBCs) (A) and Blood Chemistries (B) for CN9086 for the Pre- and Post-Transplant Period.*

No abnormalities were noted in the CBCs or chemistries which supports the safety (non-toxicity) of the PLG scaffold implant. Formal toxicology studies are pending later this year.

Scaffolds were explanted at Day33 (**Fig 8.1.14**) and stained for immune cell populations as well as insulin-expressing cells. We found a small population of insulin-expressing cells were present in the scaffold after approximately 30 days and immunes cells were predominantly located around the perimeter of the scaffold colocalized with the remaining islets (**Fig 8.1.15-16**).

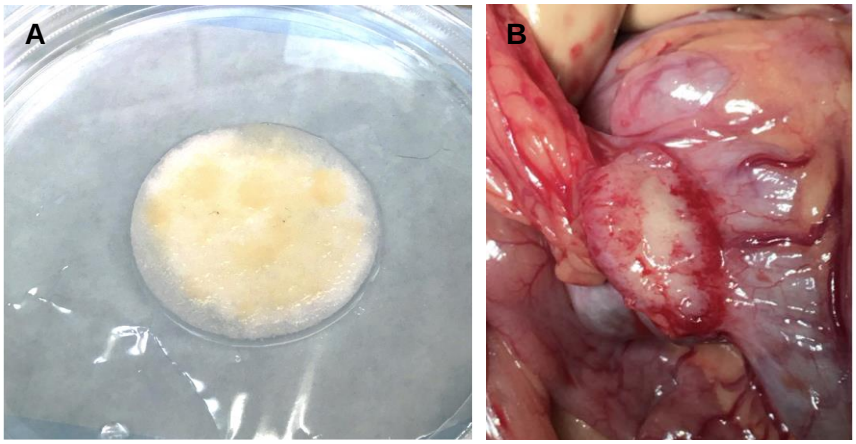

Figure 8.1.14 *Seeded Scaffold Day of Transplant (A) and Explanted Scaffold at Day 33 (B).*
Macroscopically, the scaffold appears vascularized at retrieval. During tissue removal, adhesion of the scaffold-omentum to the colon was observed.

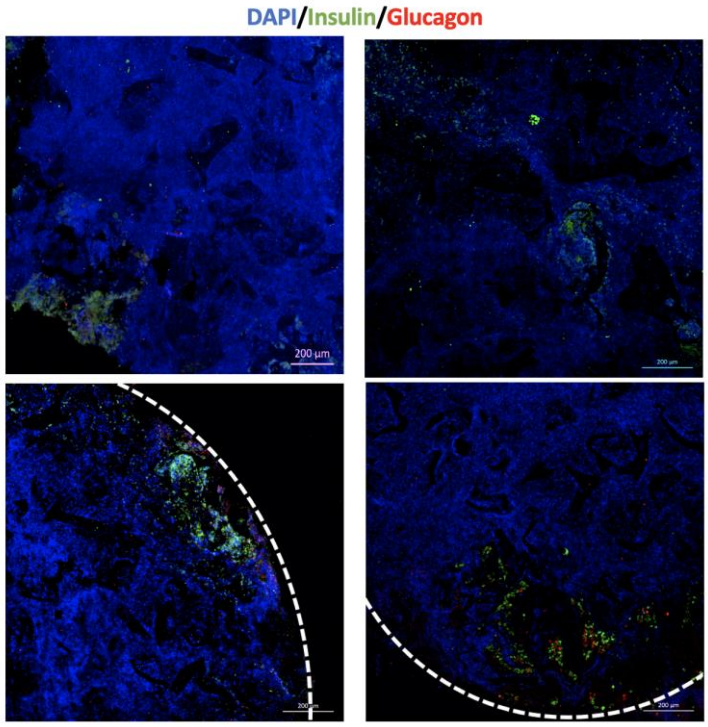

Figure 8.1.15 *Immunohistochemistry of Explanted Scaffold from CN9086 at Day 33.*
Insulin and glucagon positive cells were identified primarily on the perimeter of the scaffold.

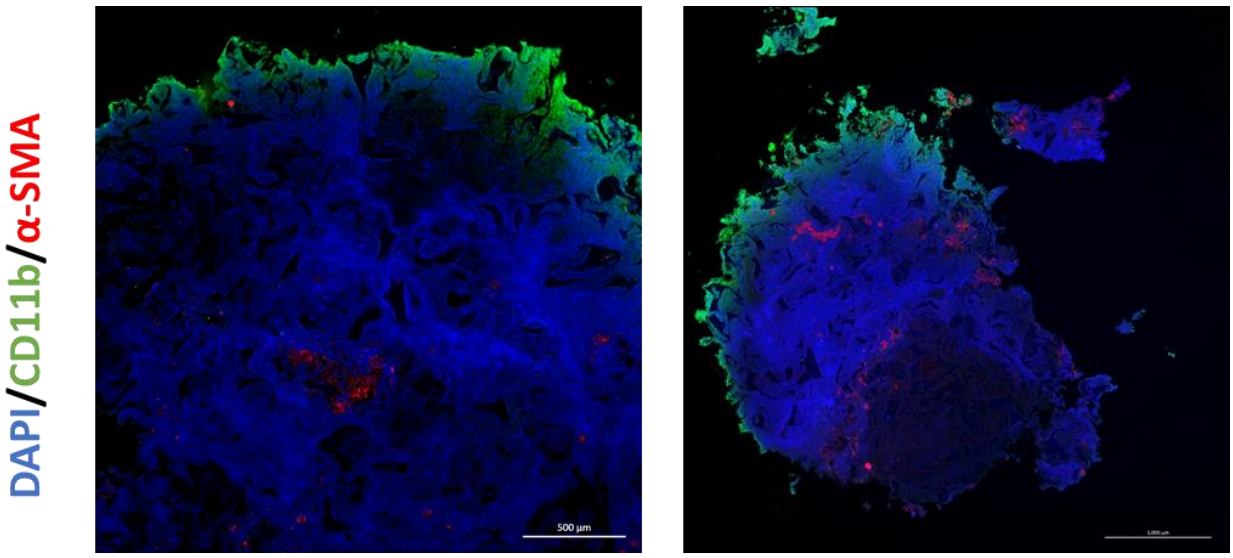

Figure 8.1.16 *Immunohistochemistry shows no significant presence of immune cells or inflammation for PLG scaffolds*

Scaffold in omentum was stained for alpha-smooth muscle actin (red), CD11b (green) and nuclear counterstain with DAPI (blue) with a (A) 10x and (B) 5x objective. Immune cells are localized to the perimeter of the scaffold.

These results led us to evaluate the scaffold's influence on islet function to determine if it was affecting the *in vivo* output. Irradiation had shown to affect the scaffold integrity earlier, thus we

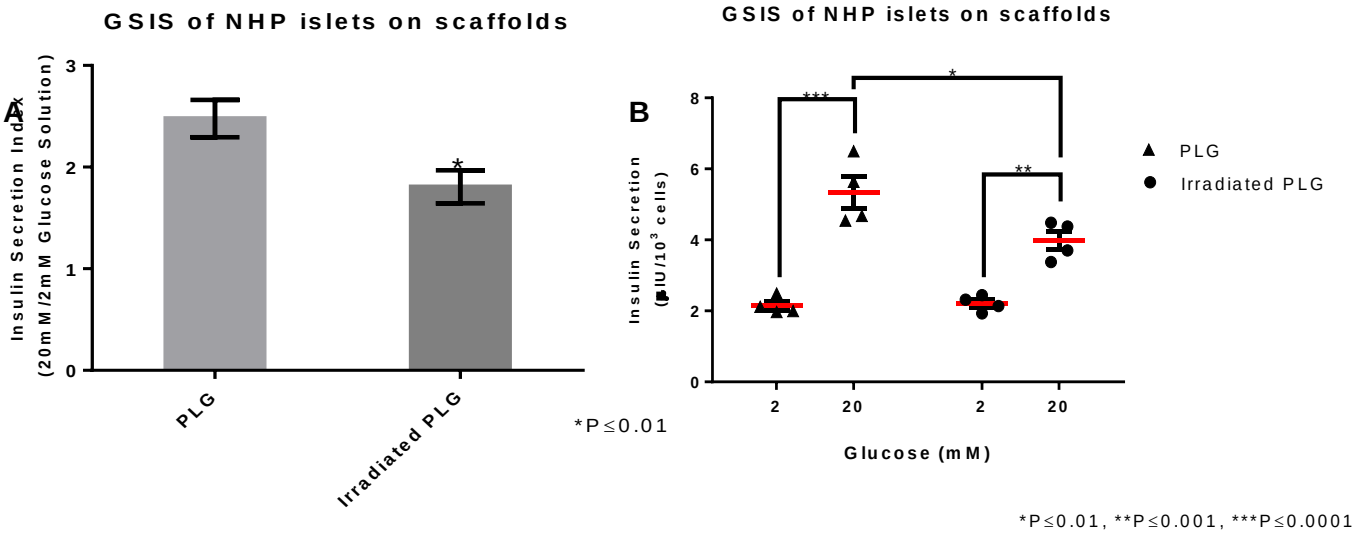

Figure 8.1.17 *NHP islet function on irradiated and non-irradiated PLG scaffolds*

Insulin secretion from NHP islets seeded on irradiated and non-irradiated PLG scaffolds under GSIS static conditions indicate a reduction in insulin secretion index (A) for islets seeded on irradiated scaffolds. (B) We show that the loss of function occurs at higher concentrations of glucose while both scaffolds show similar insulin secretion levels when exposed to low glucose. (n = 4 biological replicates, error bars represent the SEM.)

seeded NHP islets on irradiated and non-irradiated scaffolds and tested insulin secretion under glucose-challenged environments (**Fig 8.1.17**). We found islets seeded on irradiated scaffolds had a significant decrease in insulin secretion relative to islets seeded on non-irradiated scaffolds. This is likely affecting our functional results and suggests that we should further optimize our scaffold material composition to aide either diffusion through the scaffold or islet viability after the scaffold is irradiated.

In the future, upon obtaining an IND through the FDA, we anticipate to conduct a pilot trial with three, brittle, type I diabetic patients presenting with severe, hypoglycemic unawareness qualifying for islet transplantation using UIC's immunosuppressive protocol. The foldable scaffold would be seeded with purified, human islets at a dose of a minimum of 5000 IEN/kg, and then placed laparoscopically on the omentum of the recipients. Patients would receive the UIC protocol of immunosuppression as previously described and be monitored for glycemic control, insulin requirements, C-peptide, fructosamine levels and HbA1c, as well as a series of other metabolic markers to evaluate overall glycemic and metabolic control. At the end of 6 months, the patient would undergo a diagnostic laparoscopy for macroscopic inspection of the abdominal cavity and evaluation of the transplant site. Additionally, these investigations could deliver important clues on whether this transplant site and the use of scaffolds could provide a safe, retrievable site for future, hPSC derived ß-cell transplants into brittle, type I diabetic patients.

We will continue the translation of the research studies in multiple directions. First, the NHP studies will continue towards the goal of eliminating the systemic immunosuppression through applying the immune tolerance strategies that have been demonstrated to work with the transplantation on microporous scaffolds, which includes ECDI-fixation of donor splenocytes or FasL modification of islets, both of which are currently be investigated in non-human primate models and have demonstrated efficacy with microporous scaffolds. Furthermore, the Shea

laboratory is developing nanoparticles for immune tolerance that are aimed as an off-the-shelf alternative to isolating and manipulating splenocytes.

Chapter 8.2: Injectable in situ crosslinked PEG hydrogels with tunable gelation time and affinity-controlled protein release

8.2.1 Abstract

The goal of this work was to develop an injectable protein delivery system for use in the middle ear that can provide localized release of NT-3 growth factors in a controlled and sustained manner. We identified a one-step mixing formulation to prepare injectable in situ forming PEG hydrogels crosslinked by thiol-vinyl sulfone Michael addition that provides convenience and flexibility for gel handling due to its tunable gelation time. PEG hydrogels prepared by this formulation were further demonstrated with high stability, good mechanical rigidity and elasticity, low cytotoxicity, long residence time and low immune responses in vivo. PEG hydrogels were the modified with affinity- peptides specific for NT-3 protein, which were selected by phage display. NT-3 loaded hydrogels provided a controlled release that was dependent upon the peptide affinity and the protein-to-peptide ratio. Collectively, the studies developed an injectable PEG hydrogel formulation that allows for affinity-controlled protein release.

8.2.2 Introduction

Hydrogels have great potential in tissue engineering and local drug delivery[412–414]. Biocompatible hydrogels have been extensively used in cardiac tissue engineering[415], bone and cartilage repair[416], as well as wound healing[417]. Gels have also been loaded with different therapeutic agents such as small drugs, growth factors, and siRNA for local drug delivery to various sites in the body, such as the middle and inner ear[418], the vitreous body and subconjunctival area in the eye[419], and the brain[420] . Drug delivery to these target sites requires low tissue damage in medication administration, flexibility of the hydrogel to adapt to different structures in these sites, and low cytotoxicity[418–420].

Recently, injectable hydrogels have been extensively researched due to their minimally invasive injection method to replace implantation surgery and their ability to match irregular defects in the target sites[421,422]. Injectable hydrogels are formed by sol-gel transition induced by physical (*i.e*. electrostatic interactions and hydrophobic interactions) or chemical (*i.e*. Michael addition and Schiff base reaction) crosslinking reactions after injection[421,422]. External stimuli such as temperature and pH are usually required to drive the gelation through non-covalent physical crosslinking reactions. A major concern in physically crosslinked hydrogels is their low mechanical stability because physical reactions that drive gel formation might be reversed over time, altering their morphology and properties and further causing the collapse of the gel structure[421,422]. In contrast, chemically crosslinked hydrogels formed by irreversible covalent bonds provide higher mechanical strength and higher stability, but the potential damage of local cells and tissues exposed to toxic agents such as initiators in chemical reactions worries people[423]. Controlling the speed of gel formation to provide enough time for handling and injecting is another critical issue in designing injectable chemically crosslinked hydrogels[424].

Easy handling and minimal invasiveness provide facility to use injectable hydrogels. However, the most important factor in the design and use of hydrogels for delivering therapeutic agents is their sustained and controlled drug release[414]. Burst drug release or immobilization of drug diffusion from hydrogels can be the result of an inappropriate ratio of mesh size to drug size[414,422], poor bioadhesion or short residence time of hydrogels in the target sites[425]. Previous studies suggest developing hydrogels with controlled drug release involve changing the network structure of hydrogels by external stimuli to modify drug diffusion and designing cleavable chemical bonds or physical interactions between drugs and polymers to sustain drug release[414].

In this study, we introduced an injectable *in situ* crosslinked poly(ethylene glycol) (PEG) hydrogel *via* Michael addition between 4-arm PEG vinyl sulfone (PEG-4VS) and 4-arm PEG thiol (PEG-4SH)[426]. We found that the thiol-vinyl sulfone reaction provides a tunable gelation time at

different temperatures that makes it suitable for gel handling and injecting, and PEG hydrogels prepared by this method show high mechanical strength, superior bioadhesion, long residence time and good biocompatibility *in vivo*.

Macromolecules show burst release in this type of injectable PEG gels. We then designed gels with affinity-controlled drug release by conjugating the PEG polymers with protein-targeting peptides in order to use their binding affinity to sustain and control protein release from hydrogels. NT-3 was chosen as a model protein in this study. NT-3 is a neuron growth factor that is critical for recovering cochlear function and regenerating inner ear ribbon synapse after hearing injury[427]. NT-3 has been reported locally delivered to round window membrane (the membrane between the middle ear and the inner ear) in the tympanic cavity by hydrogels, and then diffuses through the membrane to inner ear[428]. Because of the irregular structure of the cavity and the high safety requirement for intratympanic administration, injectable hydrogels such as thermo-sensitive Poloxamer 407 (Pluronic F127) have been favored to deliver drugs to inner ears and some formulations have been undergoing pre-clinical or clinical evaluation[428,429]. Poloxamer 407 is a non-ionic poly(ethylene oxide)a-poly(propylene oxide)b-poly(ethylene oxide)a (PEO-PPO-PEO) triblock copolymer that transitions to gels above the lower critical solution temperature (LCST) driven by the increased hydrophobic interaction among PPO blocks[430]. In this study, we used physically crosslinked Poloxamer 407 hydrogels as a control to compare with chemically crosslinked PEG hydrogel to evaluate the potential of this injectable PEG hydrogel to be used as a protein delivery system for inner ear therapy.

NT-3 targeting peptides were screened out from a Ph.D.™-7 phage display peptide library in this study, and their affinity to NT-3 proteins was quantified by a bio-layer interferometry (BLI) based platform. Phage display, a well-established powerful and popular technology, has been extensively used in many fields, including antibody engineering[431,432], ligand screening[433,434], peptide drug discovery and manufacture[435,436], disease molecular diagnostic analysis[437],

biosensing[438] and vaccine research and development[439]. The high capacity and abundance of random phage display library makes it appropriate for high-throughput screening of peptide ligands that specifically bind with the given targets.

Using our protein-loaded, peptide-conjugated PEG hydrogels, we studied how the peptides' affinity and the peptide-to-protein ratio affect the affinity-controlled protein release from PEG hydrogels. Developing injectable hydrogels, of which network morphology and properties could be tuned and the affinity between polymers and payloads can be modified, to control the load and release of therapeutic agents can consequently lead to significant therapeutic efficacy.

8.2.3 Materials and Methods

Materials. 4-arm PEG thiol (20 kD), 4-arm PEG vinylsulfone (20 kD) and 4-arm PEG Maleimide (20 kD) were purchased from JenKem Technology USA, and they all have pentaerythritol core structure. Poloxamer 407, FITC-dextran (40 kD) and L-cysteine were purchased from Sigma-Aldrich. Recombinant human NT-3 and its ELISA kit were from BioLegend. Thiol-functionalized peptides were synthesized by GenScript. Alexa Fluor 488 (AF488) C5 Maleimide, CellTrace FarRed dye and Ellman's reagent were purchased from ThermoFisher Scientific. All the antibodies were from Biolegend.

Preparation of PEG Hydrogel by One-Step Mixing and Hydrogel Crosslinking Efficiency. 4-arm PEG thiol (PEG-4SH) and 4-arm PEG vinyl sulfone (PEG-4VS) were separately dissolved in PBS to prepare 30% (w/v) PEG stock solution. 30% PEG-4SH solution, 30% PEG-4VS solution and PBS were mixed together at 1: 1: 4 or 1: 1: 2 or 1: 1: 1 ratios to prepare cargo-free 10% or 15% or 20% (w/v) PEG hydrogel, respectively. To prepare protein-loaded, peptide-conjugated 20% PEG hydrogels, NT-3 proteins were first mixed with thiol-functionalized targeting peptides at the desired ratios in 10 µl of PBS, and then mixed well with 10 µl of 30% PEG-4SH solution, followed by mixing with 10 µl of 30% PEG-4VS solution. The mixture was then incubated at 37 °C to allow gel formation.

Hydrogel crosslinking efficiency was identified by measuring the unreacted thiols in PEG hydrogels using Ellman's reagent. Briefly, PEG-4SH solution and PEG-4VS solution were mixed at different SH/VS ratios, and then incubated at 37 °C to form hydrogels. 30 µl of PEG hydrogels were immersed in 300 µl of Ellman's reagent solution and then incubated at room temperature on a shaker for 15 min. Absorbance of colored products of thiols reacting with Ellman's reagent was measured at 412 nm on a plate reader (BioTex), and the amount of thiols in PEG hydrogels was quantified by comparison to a standard curve composed of known concentrations of L-cysteine.

Swelling Behavior of PEG Hydrogels. 200 µl of 10% (w/v), 15% and 20% PEG hydrogels (~12 mm in diameter and ~4 mm in height) were dried up at 60 °C for 2 days, and then placed in water at room temperature. At the desired time points, hydrogels were removed from the water, dried the surface quickly with Kimwipe paper and then weighted. Three hydrogels were prepared for each polymer concentration. Swelling degree (H) was calculated by the following equation:

$$H\ (\%) = \frac{m_t - m_0}{m_0} \times 100 \qquad (1)$$

Water content (W) in the hydrogel was calculated by the following equation:

$$W\ (\%) = \frac{m_t - m_0}{m_t} \times 100 \qquad (2)$$

where m_t is the weight of the hydrogel at t time, and m_0 is the weight of the dry hydrogel, and (m_t-m_0) is the water weight (M_t) at t time. $W_{infinite}$ is the water content when the equilibrium is reached.

Elasticity and Rheological Analysis of PEG Hydrogels. The rheological properties of 10%, 15% and 20% PEG hydrogels were measured on a rheometer (Discovery HR-2, TA Instruments). The storage modulus (G′) and loss modulus (G″) were detected keeping strain at 2% with a continuous frequency (0.1−100 rad/s) at room temperature. Hydrogels were measured in the air or in PBS solution.

Bioadhesion and Residence Time of Hydrogels.

In vitro, bioadhesion and residence time of PEG hydrogels and Poloxamer 407 hydrogels were studied on a tissue-treated surface. 30 µl of freshly mixed PEG-4VS/PEG-4SH solution or Poloxamer 407 solution was added to the bottom of tissue-treated 6-well plates, and then placed at a 37 °C incubator for 20 min to allow *in situ* formation of 20% (w/v) hydrogels. To test the adhesion of hydrogels to the tissue-treated surface, we scratched the gels with pipette tips. To identify the residence time of hydrogels in the solution, pre-warmed PBS was added to the plate wells with hydrogels attached to the bottom surface, and the plate was placed on a shaker (20 rpm) in a 37 °C incubator. Hydrogels was imaged at the desired time points.

Ex vivo, bioadhesion of PEG hydrogels to fresh tissue with a flat tissue surface and to a fixed tissue with structure defect (tympanic cavity) was studied. 10-20 µl of 20% (w/v) of PEG-4VS/PEG-4SH mixed solution that included 5 molar% of AF488-C5 Maleimide was loaded to the hypodermis layer (subcutaneous tissue) of fresh skin, the inner side of the skull or the large intestine extracted from BALB/c mice. These gels were then incubated for 20 min to allow *in situ* gel formation at room temperature. Next, we tested the adhesion of gels to the skin by trying to separate them with a forceps. In another study, human temporal bones that were preserved in formalin solution were rinsed with PBS and dried up by Kimwipe paper. And then ~5 µl of mixed solution was applied to the round window niche of each temporal bone, waiting for 20 min to allow *in situ* gel formation at room temperature. We tested the attachment of hydrogels to the tympanic cavity with a forceps, and then we immersed the human temporal bones in PBS and rocked on a shaker (20 rpm) at room temperature. Fluorescence of AF488-labeled PEG hydrogels were imaged by a fluorescence microscope (Nikon) at days 1, 2, 9 after gel formation.

***In vivo* Imaging of Hydrogels (Solution *vs.* PEG hydrogels *vs.* Poloxamer 407 hydrogels).** PEG-4SH, PEG-4VS and Poloxamer 407 solutions were sterilized by filtering through 0.22 µm membranes (Millipore). 5 µl of 5 mM FarRed dye was added to 100 µl of ice-cold PBS

solution, and freshly mixed 20% (w/v) PEG-4SH/PEG-4VS solution and 20% (w/v) Poloxamer 407 solution. And then 50 µl of each solution was subcutaneously injected to the back of BALB/c mice with 1 ml syringes with 27 G needles (the body temperature of mice is about 36 °C). Each mouse received one injection at the right side and another injection at the left side of the back. Mice bearing fluorescent hydrogels were imaged at the desired time points by IVIS (PerkinElmer). The first imaging was performed 3 hours after injection. The reduction in the fluorescence intensity of solutions or hydrogels *in vivo* was quantified and plotted over time.

H&E Staining Tissue samples from subcutaneous fat in mice were cryopreserved in isopentane and cooled on dry ice, processed, and embedded within OCT embedding medium (Tissue-Tek, Sakura Finetech, Torrance, CA). Sections of 14 µm were stained with hematoxylin and eosin (H&E). Immunohistochemical stains were fixed with 4% paraformaldehyde for 30 min, blocked and permeabilized for 30-min with staining buffer (5% donkey serum, Jackson Immunoresearch; 017-000-121) and 0.1% Triton-X 100 (Acros Organics; 327371000 in PBS), stained overnight with primary antibodies at 4 °C, stained for 4 h with secondary antibodies at 4 °C, and treated with mounting solution DAPI Fluoromount-G (SouthernBiotech; 0100-20). Digital images were acquired with a MicroFire digital camera (Optronics, Goleta, CA) connected to an Olympus BX-41 fluorescence microscope (Olympus, Center Valley, PA, United States).

Immunofluorescent Staining. Shaved skin tissues (from epidermis to hypodermis) where the gel solution or PBS solution was injected to were collected, minced to small pieces and then digested in 2 mg/ml Liberase TM (Roche) for 30 min. Liberase was neutralized with FACS buffer, PBS containing 0.5% Bovine serum albumin and 2 mM EDTA. And then cells were isolated by passing the tissues through 70 µm strainers (BD Bioscience). Red blood cells were lysed using 0.2% sodium chloride solution, followed by neutralization with 1.6% sodium chloride solution. For analysis of immune cell populations, 1 million cells were suspended in 100 µl of FACS solution and blocked with 1 µg anti-mouse CD16/32 antibody for 30 min at 4 °C. Cells were then stained

with antibody cocktail solution at 4 °C for 1 h, and then fixed with 4% paraformaldehyde (PFA) and measured by Bio-Rad ZE5 cell analyzer. 100 µl of antibody cocktail solution included 0.4 µg Brilliant Violet 510 anti-mouse/human CD11b antibody, 0.25 µg Brilliant Violet 605 anti-mouse CD11c antibody, 0.25 µg FITC anti-mouse Ly6C antibody, 0.25 µg PE anti-mouse Ly6G antibody, 0.25 µg PE/Cy7 anti-mouse F4/80 antibody, and 0.25 µg Alexa Fluor 700 anti-mouse CD45 antibody.

Identification of NT-3-Targeting Peptides by Phage Display The Ph.D.-7 peptide library (NEB, New England Biolabs, USA, E8100S) was used to screen for NT-3 binding peptides according to the manufacturer's instructions with slight modifications. In short, 96-well plates were coated with 150 µL/well of the recombinant NT-3 protein (Peprotech) at a concentration of 30 µg/mL. Biopanning was carried out by incubating the phage display library. After washing away the unbound phage with Tris-buffered saline (TBS $^{+}$ 0.1% Tween 20), bound phages were eluted in TBS and titrated as described in the standard protocol, and then subjected to the next round of panning. The second, third and fourth rounds of panning were done under more stringent conditions using shorter incubation times (40 min, 25 min and 20 min in the 2, 3 and 4th round, respectively). After four rounds of panning, individual clones were randomly picked and amplified in E. coli ER2738 strain to prepare their DNA.

Individual positive phage clones were amplified, and phage single-stranded DNA was extracted and purified using M13 Phage DNA Rapid Extraction Kit (Spin-column, Signalway Biotechnology, USA). DNA was sequenced by the Genomics Core Facility in the Center for Genetic Medicine (Chicago, IL) using the 96 gIII sequencing primer 5′-CCCTCATAGTTAGCGTAACG-3′ provided by the Ph.D.-7 peptide library kit to identify common peptide sequences among the clones and thus the extent of consensus. Amino acid sequences were deduced from phage display peptide DNA sequences by ExPASy Translate tool (http://web.expasy.org/translate/). Three peptide sequences were randomly picked from this pool.

These phages and a non-consensus control peptide, OVA(323–339) containing a C-terminal cysteine, were synthesized and purified by Genemed Synthesis (San Antonio, TX).

Binding Analysis of NT-3-Targeting Peptides The binding kinetics between the selected phage display peptides and target protein NT-3 were studied using a Biolayer Interferometry based instrument, Octet Red (ForteBio). The biotinylation of NT-3 was prepared by incubating NT-3 with EZ-Link NHS-LC-LC-biotin (Pierce) at a 1:1 molar ratio for 2 hours on ice, followed by dialysis to remove the excess biotin reagent. Super Streptavidin (SSA) sensors were equilibrated for 10 min in black 96-well microplates (VWR, Radnor, PA, USA) containing 200 µL/well of PBS buffer. Then, SSA-coated tips were saturated with 10 µg/mL biotinylated NT-3 at capture levels of 0.70 ± 0.15 nm. Purified binding phage display peptides at concentrations ranging from 1nM to 200µM were associated to protein-saturated sensors followed by dissociation in buffer. Reference binding sensors containing only the control peptide were corrected for baseline drift. Nanometer shift data were analyzed in Data Analysis 6.4 (ForteBio, Menlo Park, CA, USA). To estimate a direct binding affinity via the kinetic rate constants ($KD = K_{on}/K_{off}$, where KD = equilibrium dissociation rate constant, k_{on} = association rate constant, and k_{off} = dissociation rate constant) the buffer-subtracted octet data were fitted globally to a simple 1:1 Langmuir model.

Cumulative *in vitro* Drug Release. Transwell permeable inserts that separate two chambers were used to mimic the round window membrane. Boyden chambers and Transwell inserts (6.5 mm diameter, 8 µm pore size, Corning), were pre-coated with 1% BSA overnight at room temperature. Then 30 µl of dextran-loaded or NT-3-loaded PEG hydrogel prepared in the mold was transferred to the surface of the Transwell permeable insert and the lower chamber was filled 0.5 ml of pre-warmed PBS containing 1% bovine serum albumin (BSA) that blocks nonspecific binding to released proteins to well surface. Plates were rocked at 20 rpm in a 37°C incubator with full humidity. At the desired time points, 100 µl of solution was collected from the lower chamber followed by supplementing 100 µl of PBS containing 1% BSA. Released NT-3

proteins were quantified by ELISA (R&D systems) while released FITC-dextran and FITC-casein proteins were quantified by their fluorescence intensity measured by a plate reader (BioTek). Accumulative released amount of NT-3, dextran and casein was compared with the initial loading amount of macromolecules to obtain the drug release ratios.

8.2.4 Results and Discussion

Gelation Time of PEG Hydrogels at Different Temperatures

The injectable PEG hydrogel was prepared by one-step mixing of PEG-4VS and PEG-4SH solutions at a 1: 1 molar ratio (**Schematic 8.2.1A**). By measuring the free unreacted thiols in PEG hydrogels using Ellman's reagent, the conversion of thiol groups in 10%, 15% and 20% (w/v) PEG hydrogels was identified to be 99%, 100% and 100%, respectively (**Table 8.2.S1**), demonstrating the high efficiency of the thiol-vinyl sulfone reaction in gel formation, consistent with previous reports[440].

We found this Michael addition reaction between thiol (SH) and vinyl sulfone (VS) crosslinked PEG polymers at a moderate reaction rate and therefore provided ample time for gel handling and allowed the formation of a uniform gel structure. Gelation time of the PEG-4VS/PEG-4SH mixed solution was further evaluated by changing the polymer concentration and temperature. At body temperature (37°C), the gelation times of 60 µl of 10%-20% PEG hydrogels ranged from 5 min to 15 min, and their gelation time increased to 18-46 min at room temperature (25°C), and further increased to several hours at 4°C (**Table 8.2.1**). The slow gelation of PEG hydrogels at room temperature and 4°C provides sufficient time and convenience for operators to prepare, handle and inject the mixed solution and also allows well mixing of two components to prepare uniform gels[441] (**Fig 8.2.S1**). The moderate gelation time of PEG hydrogels at 37 °C enables the mixed solution to spread out and fill the space in the target site before gel formation occurs[442].

These features are no longer available when the crosslinking is too fast. This was shown when we compared SH-VS reaction with SH-maleimide (MAL) Michael addition reaction in the preparation of PEG hydrogels using a one-step mixing method. The SH-MAL gelation rate made it difficult to uniformly mix PEG-4SH and PEG-4MAL solutions because significant crosslinking occurred when the two solutions came into contact. The fast reaction did not provide enough time for mixing and gel injection, and poor mixing produced SH-MAL crosslinked PEG gels with non-uniform internal morphology (**Fig 8.2.S1**) and lower conversion of thiol groups than VS-SH crosslinked hydrogels (*e.g.* 89% in VS-MAL crosslinking *vs*. 100% in VS-SH crosslinking, 20% hydrogel, **Table 8.2.S1**). Collectively, the Michael addition reaction between thiol and vinyl sulfone efficiently crosslinked 4-arm PEG polymers at a moderate reaction rate, providing PEG hydrogels with tunable gelation time at different temperatures.

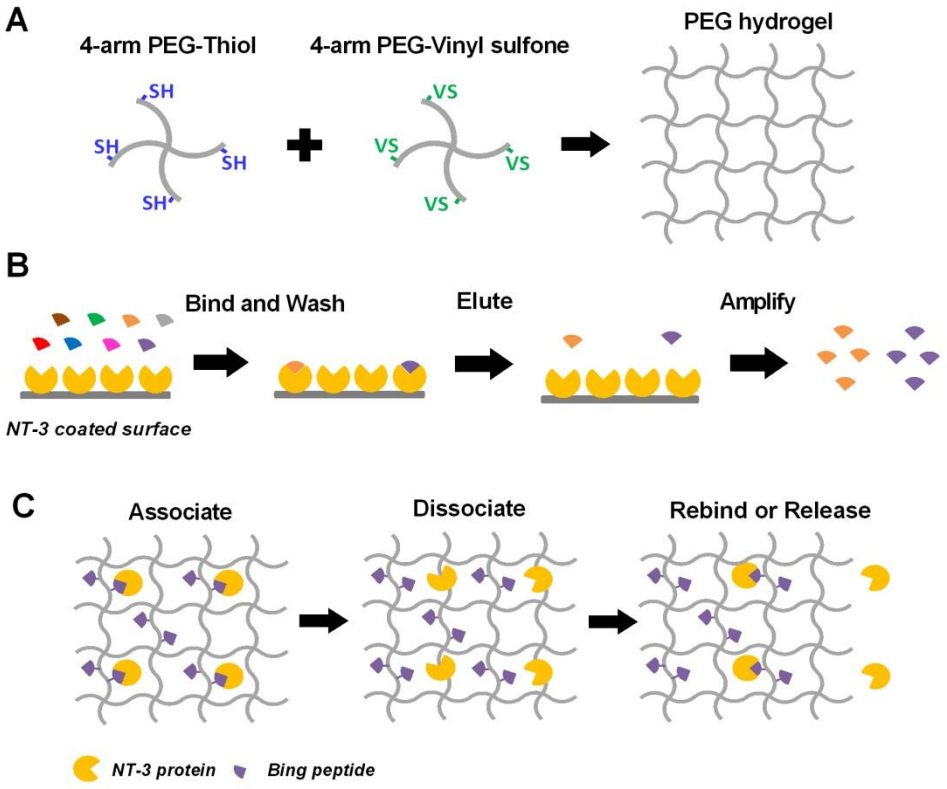

Schematic 8.2.1. (A) Schematic representation of preparing PEG hydrogel by one-step mixing through Micheal addition. (B) Schematic view of phage display to screen peptides that specifically

bind to our model drug, human NT-3 proteins. (C) Schematic representation of affinity-controlled protein release from PEG hydrogels that are chemically conjugated with NT-3 targeting peptides and physically loaded with NT-3 proteins.

Table 8.2.1: Gelation time of PEG-4SH/PEG-4VS mixed solutions at different conditions.

PEG concentration (w/v)	10%	15%	20%
37°C	~15 min	~7 min	~5 min
25°C	~46 min	~27 min	~18 min
4°C	~6.5 h	~3.5 h	~2 h

Viscoelastic and Swelling Properties of PEG Hydrogels

Physicochemical properties of hydrogels determine their diverse *in vivo* applications[421,422,425]. We subsequently characterized the rheological properties and swelling behaviors of VS-SH Michael addition reaction crosslinked PEG hydrogels. We measured the storage modulus (G') and loss modulus (G") of pre-fabricated 10%, 15% and 20% PEG hydrogels at a constant 2% oscillation strain at room temperature in the air (**Fig 8.2.1A-B**) and in PBS solution (**Fig 8.2.1C-D**). Greater G' values than G" values indicate the elastic property of PEG gels[443]. The G' of all hydrogels were independent of angular frequency except a slight decrease for 10% gels at a high frequency region (30-100 rad/s), demonstrating the good stability of PEG gels. A higher polymer concentration increased the G' values, as seen by the average G' value of 20% compared to 15% and 10% gels between 0.01 and 100 rad/s in the air (684.5, 478.3, and 259.1 Pa, respectively) (**Table 8.2.2, Fig 8.2.1A,C**). This indicates that 20% PEG gels have a higher degree of crosslinking and a higher mechanical rigidity than 15% and 10% gels (24).

The G" of PEG gels also depended on the polymer concentration. The G" values of all PEG hydrogels were constant between 0.25 and 30 rad/s, but the average G" values of 20% gels (1.6 Pa) and 15% gels (1.5 Pa) were greater than that of 10% gels (0.5 Pa) in this frequency region in

the air (**Table 8.2.2, Fig 8.2.1A**). However, the influence of polymer concentration on the G" values seemed less significant in the aqueous solution (**Fig 8.2.1C**). We further plotted the damping factor (tan δ), the ratio of G" to G', as a function of angular frequency (**Fig 8.2.1B,D**). The tan δ values of all hydrogels are independent of frequency between 0.25 and 30 rad/s with an average value ranging from 0.002 to 0.003 (**Table 8.2.2**), an indicator of ideally elastic solid materials (tan δ < 0.01)[443]. When angular frequency is above 30 rad/s, the tan δ values of all hydrogels increased rapidly as the angular frequency increased (**Fig 8.2.1B,D**), suggesting the energy dissipation caused by intermolecular friction was proportional to the frequency[444].

Next, we characterized the swelling behavior of the PEG hydrogels. Swelling behavior reflects the water diffusion in the matrix and is another indicator of the relative crosslinking density, where stiffer networks exhibit lower swelling[445]. This property is critical for predicting drug release behaviors from hydrogels as well as evaluating their use in tissue engineering[446,447]. We measured the weight gain of 10%, 15% and 20% dried PEG hydrogels placed in water at room temperature and plotted their swelling ratio (H) and water content (W) as a function of swelling time (t) (**Fig 8.2.1E-F**). All three types of PEG hydrogels reached equilibrium at ~120 min. After 24 h, the swelling ratios of 10%, 15% and 20% PEG hydrogels were around 2222%, 1993% and 1718% (**Fig 8.2.1E**), respectively, but their water contents were all close to 95% (**Fig 8.2.1F**). Thus, an increase in polymer concentration decreased the swelling ratio of PEG hydrogels but did not significantly influence the water content in PEG hydrogels at equilibrium. The decreased swelling ratio at a high PEG concentration (20% *vs.* 15% and 10%) indicated the decreased capacity of 20% PEG hydrogels to deform themselves due to their more restricted structure with a higher degree of crosslinking[445], consistent with their higher mechanical rigidity demonstrated in the rheological study.

The time-programed swelling behavior of PEG hydrogels in water (**Fig 8.2.1E**) shows second-order kinetics, which can be expressed as[448]:

$$\frac{dW_t}{dt} = K(W_{infinite} - W_t)^2 \qquad (3)$$

where K is the kinetics rate constant, and W_t and $W_{infinite}$ denote the water content at time t and at infinite time (at equilibrium), respectively. After integration between the limits (t = 0 and W_t = 0) and rearranging, the above equation can be also expressed as[448]:

$$\frac{t}{W_t} = \frac{1}{KW_{infinite}^2} + \frac{t}{W_{infinite}} \qquad (4)$$

We plotted the variation of t/W_t against time in **Fig 8.2.1G** and then calculated $W_{infinite}$ and K (**Table 8.2.2**) by linear regression with $R^2 > 0.99$. We found the polymer concentration doesn't significantly change $W_{infinite}$, but the kinetics rate constant K decreased from 0.0466 min^{-1} for 10% PEG gels, to 0.0377 min^{-1} for 15% PEG gels, and 0.0263 min^{-1} for 20% PEG gels, indicating decelerated swelling rate of PEG gels at a higher polymer concentration due to the less flexible structure.

We also studied the rate of water transportation in PEG hydrogels using the following empirical Ritger-Peppas equation[414,448]:

$$\frac{M_t}{M_{infinite}} = kt^n \qquad (5)$$

which can be written as (3, 29):

$$\log\frac{M_t}{M_{infinite}} = \log k + n\log t \qquad (6)$$

where M_t and $M_{infinite}$ denote the water weight diffused into the gel at time t and at infinite time, respectively. k is a constant and n is a characteristic exponent that reflects the diffusion mechanism. We plotted the variance of log ($M_t/M_{infinite}$) as a function of log (t) and obtained the n value by linear regression with $R^2 > 0.99$. n values range from 0.54 to 0.56 for 10-20% PEG hydrogels (**Table 8.2.2**), indicating non-Fickian diffusion ($0.5 < n < 1$) in PEG hydrogels which

occurs when the water diffusion and polymer relaxation rates are comparable[449]. Overall, VS-SH crosslinked PEG hydrogels are ideally elastic materials with good mechanical rigidity and high-water content (95%). In addition, water transportation in PEG hydrogels showed non-Fickian diffusion.

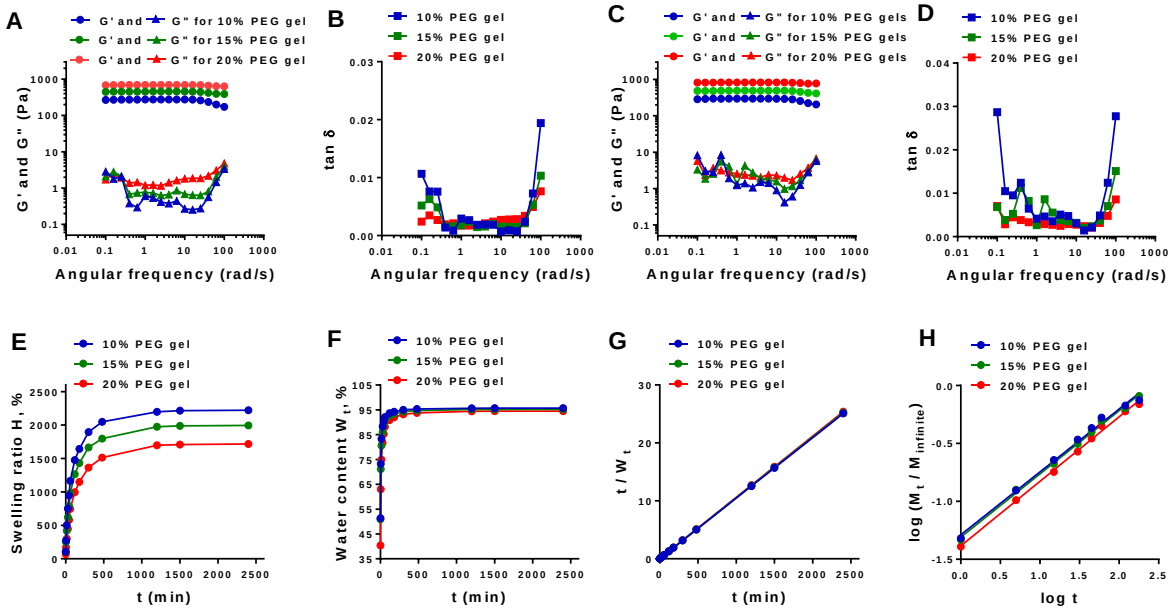

Figure 8.2.1 *Rheological properties and swelling behaviors of PEG gels with different polymer concentrations.*

(A-D) Rheological analysis of 10%, 15% and 20% PEG hydrogels in the air (A, B) or in the PBS solution (C, D). Measurements were performed at room temperature. G': storage modulus; G": loss modulus. tan δ: damping factor, tan δ = G" / G'. (E) Swelling isotherms of 10%, 15% and 20% PEG hydrogels in water at room temperature; H (%): swelling ratio; (F) Water content in different PEG hydrogels over time; W_t (%): water content at time t; (G) Experimental data of water content and time t plotted according to Equation (4) for different PEG hydrogels. Three curves overlap. (H) Experimental data of water weight and time t plotted according to Equation (6) for different PEG hydrogels; M_t: water weight at time t; $M_{infinite}$: water weight at equilibrium.

Table 8.2.2: **Characteristics of PEG hydrogels crosslinked by SH-VS Michael addition**

Polymer concentration (w/v)	10%	15%	20%
[1]**Average G' (Pa, 0.01-100 rad/s)**	259.1	478.3	684.5
[2]**Average G" (Pa, 0.25-30 rad/s)**	0.5	1.4	1.6
[3]**Average tan δ (0.25-30 rad/s)**	0.0020	0.0029	0.0023

$^{4}W_{infinite}$ (%)	96.1	95.2	96.2
^{5}K (min^{-1})	0.47	0.38	0.25
^{6}n	0.54	0.55	0.56

$^{1}G'$: storage modulus; $^{2}G'$: loss modulus; $^{3}\tan\delta$: damping factor, $\tan\delta = G'' / G'$; $^{4}W_{infinite}$: water content when hydrogels reach equilibrium, from equation (4); ^{5}K: kinetic rate constant, from equation (4); ^{6}n: diffusion exponent, from equation (6).

Bioadhesion of PEG Hydrogels and Macromolecular Release from PEG Hydrogels

In addition to physicochemical properties, the interactions of hydrogels with biological tissues through bioadhesion are also important for their *in vivo* applications[432]. One challenge with using injectable biomaterials is the discontinuity in the interfacial region between biomaterials and tissue, which can affect the therapeutic efficacy of the gel[433]. As a result, our next studies assessed the adhesion of gels to a tissue-treated petri dish surface then fresh tissues with a flat surface (hypodermis, skull and large intestine) and fixed tissue with structure defects (tympanic cavity in the middle ear). We prepared *in situ* formed PEG gels on a tissue-treated surface and then tried to separate the gel using a tip or forceps (**Fig 8.2.2A**). Mechanical forces failed to remove PEG gels from the surface even after a scratch test was performed. Alternatively, the Poloxamer gel bound to the tissue-treated surface by physical bioadhesive forces[433] but it began to detach from the surface after the scratch test due to its low mechanical strength (**Fig 8.2.2A**).

Since this study demonstrated the PEG gel's ability to adhere to a tissue-treated surface, we sought to verify these results by testing the gel's bioadhesion to different tissue samples. The surface of the hypodermis (subcutaneous area), skull and large intestine is mainly composed of adipose tissue, connective tissue and epithelial tissue, respectively. Similar to the tissue-treated petri dish surface, mechanical forces were not able to remove PEG gels from the tissues regardless of the tissue type, structure and property of target site (flat *vs.* cavity, fresh *vs*. fixed tissues), indicating their good bioadhesion (**Fig 8.2.2B-C**). Tight attachment of PEG gels to tissues might result from chemical bonds formed between PEG-VS/PEG-SH and tissue-derived biomolecules that includes thiol during *in situ* chemical crosslinking. Good bioadhesion is

associated with long residence time of hydrogels *in vivo*, which is critical for sustained local drug delivery[432]. We tested gel's residence time *in vitro* and *ex vivo* by immersing PEG gels that were attached to tissue-treated surface or fixed tissue in PBS and rocked them at 37 °C or room temperature. And we found PEG gels continued to have a consistent size and good attachment to both a tissue-treated surface and real tissues over a long time (**Fig 8.2.2A,C**) while Poloxamer 407 gels quickly dissolved in PBS (**Fig 8.2.2A**).

Longer residence time of PEG hydrogels in the aqueous solution than Poloxamer 407 gels suggests the gels would have a more sustained drug release. In an *in vitro* drug release model, we prepared in situ formed gels on the Transwell insert (6.5 mm in diameter, with 8 μm pores), and then filled the lower chamber with PBS solution containing 1% BSA. The release of 40 kD FITC-dextran and 24 kD FITC-casein protein from the PEG and Poloxamer gels at the air-liquid surface were compared. Due to the dissolving of 20% Poloxamer 407 gels, gels are collapsed fast, resulting in > 90% of release of dextran and casein at 8 h (**Fig 8.2.2D**). In contrast, only 16%, 27% and 43% of dextran were released from 20%, 15% and 10% PEG gels at 8 h, respectively.

Similar to the behavior of water diffusion into dried PEG gels (**Fig 8.2.1E**), the behavior of macromolecule release from PEG gels also shows second-order kinetics (**Fig 8.2.2D**). We then defined R_t as the ratio of cumulative released drug at time t vs. total drugs, and then plotted the t/R_t over time (**Fig 8.2.2E**). The kinetics rate constant K of dextran or casein release from PEG gels with different polymer concentrations were obtained with linear regression $R^2 > 0.99$ according to Equation (4) with the replacement of W_t to R_t (**Fig 8.2.2E** and **Tables 8.2.2**). Similar to the reduced water diffusion into dried 20% PEG gels compared to 10% and 15% gels (K values in the swelling of 10%, 15% and 20% PEG gels are 466, 377, 263 min^{-1}, **Table 8.2.1**), a higher polymer concentration in PEG hydrogels also showed slower dextran and casein release from 20% PEG gels than from 15% and 10% gels. The K values in the release of dextran from 10%, 15% and 20% PEG gels are 2.3 d^{-1}, 1.9 d^{-1} and 1.6 d^{-1}, respectively. (**Table 8.2.2**). Dextran release

from 20% Poloxamer gels are 11-fold faster than that from 20% PEG gels, respectively. Strong bioadhesion, long residence time and water-insolubility of *in situ* VS-SH Michael addition reaction crosslinked PEG hydrogels imply their suitability for a broad range of *in vivo* applications.

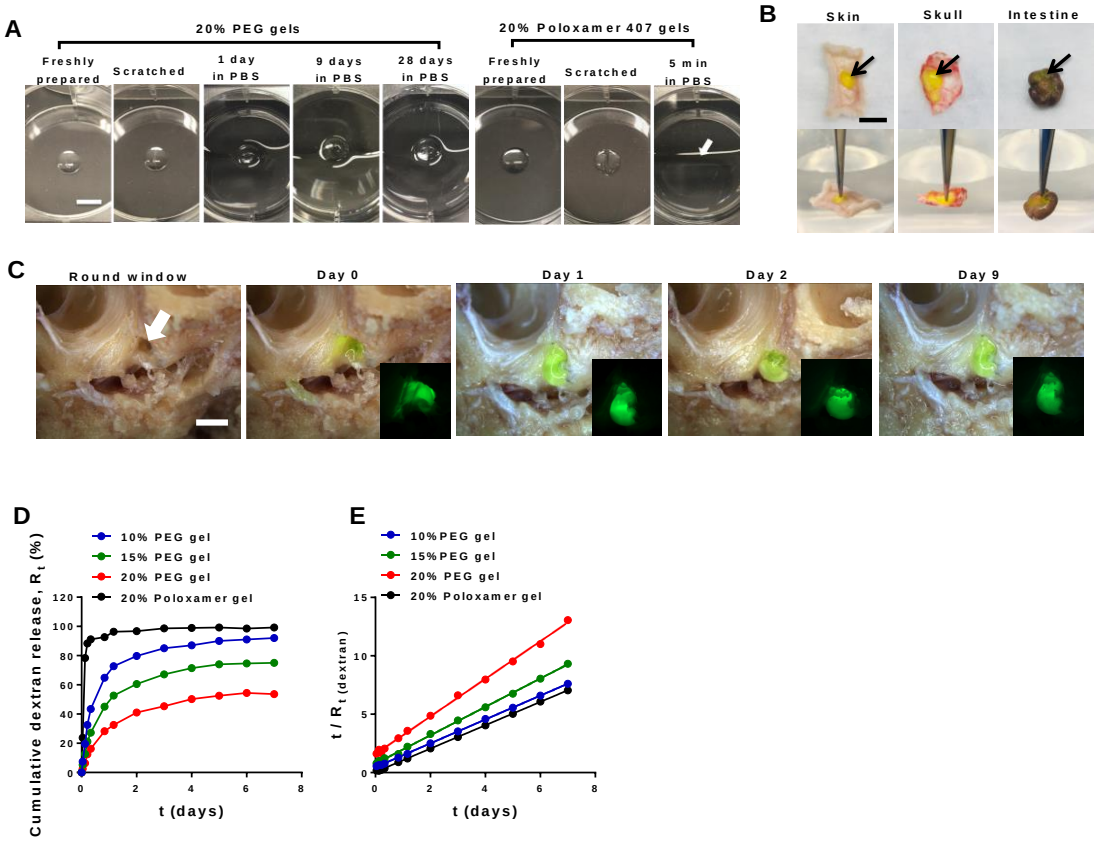

Figure 8.2.2 *Bioadhesion and in vitro residence time analysis of PEG hydrogels*

(A) Morphology of freshly prepared PEG and Poloxamer 407 hydrogels, gels scratched by a tip and gels that were incubated in PBS solution 37 °C for the desired times. *In situ* formed PEG gels bind tightly to tissue-treated surface and continue to have similar size and morphology in PBS over 28 days. Poloxamer 407 gels disappeared in pre-warmed PBS solution in 5 min (The arrow indicates the original location of the gel). Scale bar = 5 mm. (B) Adhesion of *in situ* formed AF488-labeled PEG hydrogels (green, indicated by arrows) to different fresh tissues, including hypodermis, skull and large intestine. Gels do not detach the tissue when they are lifted with a forceps (the horizontal level is indicated by the water level in the lower panels). Scale bar = 5 mm. (C) Residence of AF488-labeled 20% PEG hydrogels (green) in the tympanic cavity over 9 days in PBS. The arrow indicates the round window in the tympanic cavity of middle ear. Scale bar = 5 mm. (D, E) *in vitro* cumulative release of FITC-dextran (D) from 10%, 15% and 20% PEG hydrogels and 20% Poloxamer 407 hydrogels. And the ratio of cumulative released dextran (E) to total drugs, R_t, plotted against time t according to Equation (4) for different hydrogels.

Table 8.2.3 Quantitative analysis of *in vivo* Far-Red decay and *in vitro* NT-3 protein release from PEG and Poloxamer 407 hydrogels

	Far-Red fluorescence reduction *in vivo*			Cumulative NT-3 release *in vitro*				
	20% PEG	20% Poloxamer	Dye solution	10% PEG	15% PEG	20% PEG	20% PEG with peptides[2]	20% Poloxamer
[1]K	1.1 d^{-1}	5.3 d^{-1}	9.7 d^{-1}	4.5 d^{-1}	3.9 d^{-1}	3.1 d^{-1}	1.8 d^{-1}	13.8 d^{-1}

[1]K: kinetic rate constant, from equation (4). [2]NLKEPYA peptides are conjugated to PEG hydrogels at a NT-3: peptides = 1: 50 molar ratio.

In vivo Gel Degradation and Immune Responses to PEG Hydrogels

The injectability and the superior characteristics of PEG hydrogels to Poloxamer 407 gels were further demonstrated by their *in vivo* behaviors. FarRed dye-loaded 20% PEG-4VS/PEG-4SH mixed solution and ice-cold 20% Poloxamer 407 solution (control) were subcutaneously (*s.c*.) injected to the back of mice to allow gel formation at the body temperature of mice (~36 °C). We observed a fine shape of PEG hydrogels in the subcutaneous area with FarRed fluorescence uniformly distributed in the gel after gel formation (Day 0, 3 h after injection), indicating the similar thickness of the gel at different areas. The PEG gel showed minimal degradation demonstrated by the shape and size of PEG hydrogels not changing over 28 days. This could be due to their good mechanical strength and the stability of gels *in vivo* (**Fig 8.2.3A**, hydrogels on the right side of the mouse back are shown in **Fig 8.2.S2**).

In contrast, similar to *s.c*. injected PBS solution, *in situ* formed Poloxamer 407 gels had no definite shape and no uniform thickness, as seen by the uneven fluorescence distribution of the FarRed dye (Day 0). This is partly due to the reversible physical forces driving crosslinking and the gels' low mechanical rigidity. These properties resulted in easy deformation of Poloxamer 407 gels under the skin during gel formation. In contrast to the PEG hydrogels that had a consistent fluorescent shape over a month, fluorescent Poloxamer 407 gels decreased their size and

intensity significantly over time (**Fig 8.2.3A, 8.2.S2**). We extracted gels at day 28 after *s.c*. injection. As shown in **Fig 8.2.3B**, most Poloxamer 407 gels disappeared due to water-solubility or gel degradation[430], indicating their short residence time in the *s.c.* area. In contrast, fluorescent PEG gels had a similar size at day 28 *vs*. as day 0 (**Fig 8.2.3B**), consistent with *in vitro* results (**Fig 8.2.2A**).

Gel's residence time, degradation and water solubility also influence the drug release behavior *in vivo*. We quantified and compared the decay of the FarRed signal in different gels. *In vitro*, FarRed dyes dissolved in PBS solution are resistant to photo-bleaching over time, as seen by the consistent fluorescence intensity of FarRed dye solution preserved in a tube at room temperature over a month (**Fig 8.2.S3**). *In vivo*, decreased fluorescence of FarRed dye can be ascribed to that dyes are adsorbed and quenched by cells and tissues when dyes are diffused out the gel or when hydrogels degrade. PEG hydrogels lost ~33% of FarRed fluorescence in the first 3 days, following by the slow attenuation of fluorescence. In contrast, Poloxamer 407 hydrogels and injected PBS solution lost ~82% and ~92% of FarRed fluorescence, respectively, in the first 3 days (**Fig 8.2.3C**). Because the decay of FarRed fluorescence *in vivo* shows second-order kinetics in gels or solutions (**Fig 8.2.3C**), we then defined F_t is the fluorescence reduction ratio at day t after *s.c*. injection, and then plotted the t/F_t *vs*. t according to Equation (4) with the replacement of W_t to F_t. As shown in **Fig 8.2.3D**, t/F_t *vs*. t shows linear regression with $R^2 > 0.99$ in all the three conditions *in vivo* (**Table 8.2.3**), and the kinetics rate constant of FarRed loss in Poloxamer 407 gels ($K = 5.3\ d^{-1}$) is ~5-fold faster than in PEG gels ($K = 1.1\ d^{-1}$), consistent with the *in vitro* drug release data (**Fig 8.2.2D-G, Table 8.2.3**). Good mechanical strength, water insolubility and non-degradation contribute to the long residence time of PEG hydrogels *in vivo*, resulting in sustained FarRed release from hydrogels.

We subsequently studied the foreign body responses to *in situ* formed PEG hydrogels that reflect the *in vivo* biocompatibility of hydrogels[450]. The frequency of immune cell subsets in the

skin tissue surrounding PEG gels at different time points were analyzed and then compared with control tissues, such as normal skin and skin tissues that were touched with PBS or Poloxamer gel for a month. A total of four major immune cell populations were characterized in this study, including $CD11b^{+}F4/80^{+}$ macrophages, $CD11b^{+}Ly6G^{+}$ polymorphonuclear neutrophils (pMN), $F4/80^{-}Ly6C^{+}$ monocytes and $F4/80^{-}CD11c^{+}$ dendritic cells (DCs) (**Fig 8.2.S4**). In the skin tissue touching *in situ* formed PEG hydrogels, we observed doubled frequency of $CD45^{+}$ leukocytes at day1 after injection compared with normal tissues due to the acute inflammation that occurs after s.c. implantation[450] (**Fig 8.2.3E**). Increased leukocytes mainly result from the recruitment of pMN and monocytes, as seen by a 6-fold increase in pMN and a 4-fold increase in monocytes relative to normal skin (**Fig 8.2.3F**). But this acute immune response to PEG gels at day1 didn't cause evitable tissue redness or ulceration, indicating the low tissue damage during injection and *in situ* PEG gel formation (**Fig 8.2.S5**). After alleviating the acute inflammation over a month, leukocytes, pMN and monocytes in the skin tissues dropped greatly, and their frequencies (PEG, day28) are close to normal skin tissue or tissues treated with PBS solution (**Fig 8.2.3F**), indicating the good biocompatibility of PEG hydrogels *in vivo*. In contrast to PEG gels, the frequency of DCs in the skin tissue surrounding Poloxamer gels is higher than all the other groups at day28 (**Fig 8.2.3F**), resulting in a slightly higher leukocytes population (**Fig 8.2.3E**). This is probably because gradually degraded Poloxamer gels were regarded as foreign objects and hence were taken up by DCs for antigen-presenting, which stimulates the recruitment of DCs to gel sites over a long time[451]. Overall, *in situ* formed PEG hydrogels initiate acute inflammation after injection, which is common for *s.c*. implants[450], but the immune responses were greatly alleviated in a month, demonstrating the good biocompatibility of PEG hydrogels *in vivo*.

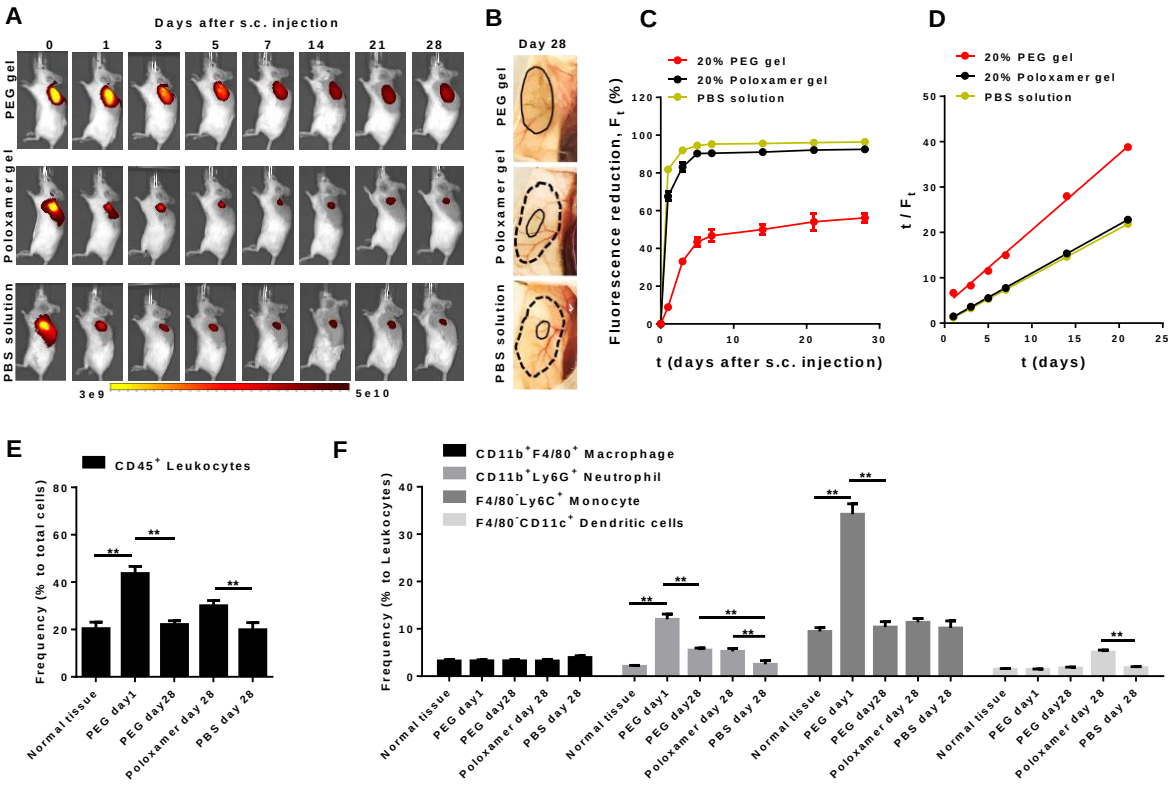

Figure 8.2. 3 *In vivo fluorescence analysis of FarRed-loaded PBS solution, PEG hydrogels and Poloxamer hydrogels over time.*

(A) Whole-animal images of *s. c.* injected solutions or hydrogels on the left back of mice. (B) Morphology of FarRed-loaded gels at day 28 post *s.c.* injection; solid line distinguishes the PEG gel edge or FarRed traces at day 28 while dash line indicates the original size the gel/solution at day 0. Scale bar = 5 mm. (C) Quantitative image analysis of fluorescence reduction over time; Ft: fluorescence reduction at day t. F_t values were averaged by the two gels at the mouse back. (D) Experimental data of the fluorescence reduction F_t and time t plotted according to Equation (4) for different hydrogels. (E, F) Flow analysis of the frequency of immune cell subsets in the skin tissues surrounding the PEG gel at day 1 and day 28 after injection.

Screening and Identifying NT-3 Binding Peptides

We employed an affinity-controlled NT-3 release system from the injectable *in situ* crosslinking PEG hydrogel to prevent a significant burst release while providing sustained release profiles. Unlike Poloxamer 407 hydrogels, the SH and VS groups on PEG allow chemically conjugation to thiol-functionalized peptides that can reversibly associate with NT-3 to control release. We screened short peptides that can selectively bind NT-3 using a Ph.D.-7™ phage

display peptide library (**Schematic 8.2.1B**). Following four rounds of biopanning, the amounts of output phages on NT-3 coated wells *vs.* control proteins (bovine serum albumin (BSA) and casein) were determined by titration (**Fig 8.2.4A**). The output for NT-3 coated well was at approximately 10^5-fold higher than BSA and casein (from 1.3×10^8 to 1.4×10^4 and 2.0×10^3, respectively), suggesting that the phages had a specific affinity to NT-3. After the fourth round of panning, a total of 17 phage clones were randomly selected and amplified, and the DNA of these selected clones was extracted and sequenced (**Table 8.2.4**). Three peptides, including NLKEPYA, ADARYKS, and SLTEPSS were picked from the fourth-round phage pool, and all three showed strong NT-3 binding in a monoclonal phage ELISA assay compared to casein proteins (control) (**Fig 8.2.4B**).

The affinity and binding kinetics of the three peptides were quantified by binding analysis using Octet RED platform that is based on bioluminescence imaging (BLI) to evaluate biomaterial interactions. In this test, NT-3 proteins were immobilized to the super streptavidin coated biosensor surface, and soluble peptides were injected at concentrations ranging from 10 to 200 µM. Real-time association and dissociation of these peptides to immobilized NT-3 are shown in **Fig 8.2.4C** and the association rate k_{on}, the dissociation rate k_{off} and the binding affinity K_D ($K_D = k_{off} / k_{on}$) are summarized in **Table 8.2.5**. The binding analysis identified that NLKEPYA peptides (K_D = 2.8 µM) and SLTEPSS (K_D = 7.5 µM) show superior binding affinity for NT-3 than the ADARYKS peptide (K_D = 24.0 µM). Although the ADARYKS peptide had a similar k_{on} value to the other two peptides, its k_{off} value was much greater, resulting in a higher K_D value that indicates its poor affinity for NT-3 (**Table 8.2.5**).

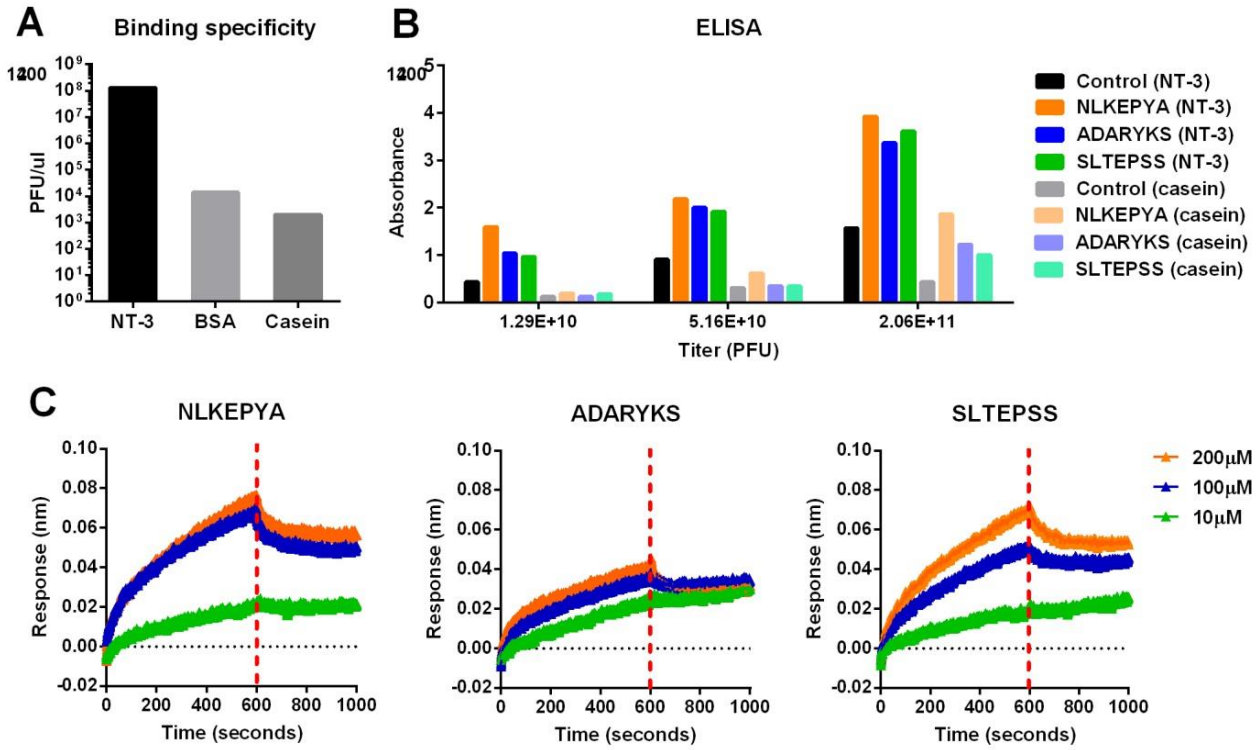

Figure 8.2.5 *Identification of NT-3 binding peptides.*

(A) Plots of round 4 phage output on plates coated overnight with NT-3, BSA, or casein. (B) ELISA measurements of NLKEPYA, ADARYKS and SLTEPSS peptides or control Ph.D.™-7 peptide binding to NT-3 or casein (control). (C) Binding kinetics for NLKEPYA, ADARYKS and SLTEPSS peptides at 10, 100 and 200 μM concentrations to NT-3 proteins. k_{on}, k_{off} and K_D are summarized in **Table 8.2.5**.

Table 8.2.4: Sequencing results of 17 positive phage colonies that show specific binding to NT-3 proteins.

Round	Sample	Sequence
4	1	DHINLTR
4	2	THNKLLV
4	3	LLAPPYW
4	4	ANPTFFS
4	5	FHSTDPS
4	6	SPLHSNY
4	7	AWPYVTL

4	8	LSAFGTH
4	9	NLKEPYA
4	10	TQMWAMG
4	11	ADARYKS
4	12	LITNGHL
4	13	GSTSFSK
4	14	MNDAFRN
4	15	NQRVDKV
4	16	YRAIPSP
4	17	SLTEPSS

Table 8.2.5: Binding kinetics and binding affinity of NT-3 targeting peptides

Peptides	k_{on} ($\times 10^3$, $M^{-1}s^{-1}$)	k_{off} ($\times 10^{-2}$, s^{-1})	K_D (μM)
NLKEPYA	3.99	1.37	2.8
ADARYKS	5.24	15.5	24.0
SLTEPSS	3.37	3.39	7.5

Peptide-Conjugated PEG Hydrogels Show Affinity-Controlled NT-3 Release

The kinetics and pattern of NT-3 release from unmodified PEG hydrogels, at multiple percentages of PEG, was initially evaluated. We added 1 μM of NT-3 proteins in PEG-4SH/PEG-4VS solutions to allow physical protein loading during gel formation. Protein loading does not significantly change the gelation time of PEG (data not shown). Protein release was studied at the air-liquid surface in a Boyden chamber that mimics the round window membrane. In this model, protein-loaded hydrogels were *in situ* formed on the Transwell membrane insert in the upper Boyden chamber while the lower chamber was filled with PBS buffer containing 1% BSA. NT-3 proteins are released from gels that are placed at the air-liquid surface, and then diffuse

through the membrane to the buffer in the lower chamber. We quantified the amount of NT-3 accumulated in the lower chamber at different time points with ELISA, and then plotted time-programmed cumulative NT-3 release from 10%, 15%, and 20% unmodified PEG hydrogels or Poloxamer 407 hydrogels. NT-3 release from PEG hydrogels showed second-order kinetics, including the burst release in the first 24 hours followed by the slow release afterwards (**Fig 8.2.5A**). We defined R_t as the ratio of cumulative released NT-3 amount at t time *vs*. total NT-3 loaded in the gel, and then plotted t/R_t against time (**Fig 8.2.5B**). The kinetic rate constant (K) of NT-3 release from PEG gels was obtained according to Equation (4) where W_t was replaced to R_t, with linear regression $R^2 > 0.98$. A correlation between release rates and polymer concentrations were observed with higher polymer concentration decelerating the NT-3 release. Specifically, K values for NT-3 release from 10%, 15% and 20% PEG hydrogels are 4.5 d^{-1}, 3.9 d^{-1} and 3.1 d^{-1}, respectively (**Table 8.2.3**). These results are consistent with the observation that water diffusion into dried 20% PEG hydrogels is slower than 10% and 15% hydrogels (**Table 8.2.2**) because 20% hydrogels have a more constrained structure and a relatively smaller pore size inside the hydrogels, which limit the payloads or solutions to diffuse in or out. In contrast to stable PEG hydrogels, Poloxamer 407 hydrogels gradually dissolve and collapse at the air-liquid surface, causing a > 90% of release of payloads in 8 hours, while at this time point, only 8% of NT-3 proteins were released from 20% PEG hydrogels. Afterwards, NT-3 was continuously released from PEG hydrogels and 25% of NT-3 is released from 20% PEG hydrogels in a week (**Fig 8.2.5A**). NT-3 release from 20% Poloxamer hydrogels (K = 13.8 d^{-1}) is ~4.5-fold faster than from 20% PEG hydrogels (K = 3.1 d^{-1}, **Table 8.2.3**), comparable to the ~5-fold faster loss of Far-Red fluorescence from Poloxamer hydrogels than from PEG hydrogels *in vivo*.

Next, release from the affinity PEG hydrogels was analyzed using the three peptides with varying affinity for NT-3 (**Table 8.2.5**) that were separately conjugated to 20% PEG hydrogels at a protein: peptide = 1:50 molar ratio. NLKEPYA and SLTEPSS peptides, which have high affinity

to NT-3 (K_D < 10 μM, **Table 8.2.5**), suppressed protein release in the first 8 hours and 2 days , while the lower affinity ADARYK (K_D = 24 μM) did not significantly change NT-3 release in the first 2 days (**Fig 8.2.5C**). For the NLKEPYA-conjugated PEG hydrogels, release exhibited second-order kinetics similar to the unmodified PEG hydrogels, except for a slower release profile (**Fig 8.2.5D**). Quantitatively, the kinetic constant K calculated from Equation (4) for NT-3 release from 20% PEG hydrogels decreased from 3.2 d^{-1} to 1.1 d^{-1} after conjugation with NLKEPYA peptides at a protein: peptide = 1: 50 molar ratio (**Fig 8.2.5E, Table 8.2.3**), suggesting a ~3-fold lower NT-3 release by peptides and thus demonstrating that reversible binding within the gel can successfully control the release of NT-3 (**Schematic 8.2.1C**). In addition to peptide affinity, we also observed that a higher protein-to-peptide ratio in the gel can further decelerate the NT-3 release, yet it plateaus at protein-to-peptide ratios below 1/100 (**Fig 8.2.5F**)

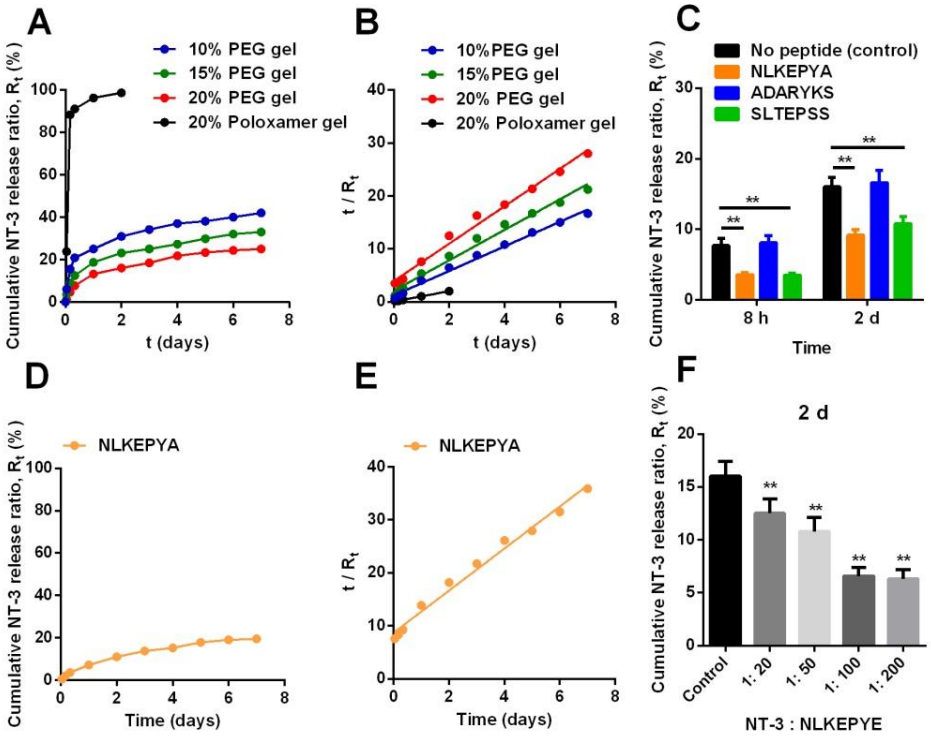

Figure 8.2.8 *in vitro NT-3 protein release from unmodified or peptide-conjugated PEG hydrogels*

(A) Cumulative NT-3 release from 10%, 15% and 20% of unmodified PEG hydrogels and 20% Poloxamer 407 hydrogels over 7 days. R_t: released ratio, R_t = released protein amount at t time / total protein amount. (B) Experimental data of R_t in (A) and time t plotted according to Equation (4). (C) Cumulative NT-3 release from 20% PEG hydrogels conjugated with NLKEPYA, ADARYKS, or SLTEPSS at a protein: peptide = 1: 50 molar ratio in 8 hours and 2 days. (D) Cumulative NT-3 release from 20% PEG hydrogels conjugated with NLKEPYA at a protein: peptide = 1: 50 molar ratio over a week. (E) Experimental data of R_t in (C) and time t plotted according to Equation (4). (F) Cumulative NT-3 release from 20% PEG hydrogels conjugated with NLKEPYA at different protein: peptide molar ratios in 2 days.

8.2.5 Conclusions

In this study, we identified a one-step mixing formulation to prepare injectable *in situ* crosslinking PEG hydrogels by using SH-VS Michael addition that has a moderate reaction rate. Tunable gelation time of this PEG-4SH/PEG-4VS formulation, depending on temperature and polymer concentrations, provides time for handling at room temperature, yet efficient gelation at body temperature. PEG hydrogels crosslinked by SH-VS Michael addition were elastic and stable, with good mechanical rigidity and high-water content. Water transportation in PEG hydrogels showed non-Fickian diffusion. The gels have better bioadhesion, longer *in vivo* residence time and better biocompatibility compared to physically crosslinked Poloxamer 407 hydrogels.

This injectable chemically crosslinked PEG hydrogel formulation is suitable for delivering drugs to biological sites that have irregular structure and require low cytotoxicity, such as the tympanic cavity in the middle ear. We verified the potential of this formulation to deliver NT-3 protein to the round window membrane in the middle ear. Unmodified PEG hydrogels release NT-3 proteins at second-order kinetics. The affinity PEG hydrogels, which were conjugated with peptides that specifically bind NT-3, suppressed the burst release. NT-3 release from PEG hydrogels separately conjugated with three peptides of varying affinity demonstrated sustained protein release from the hydrogels, with tuning of the affinity-controlled release possible through the protein-to-peptide ratio.

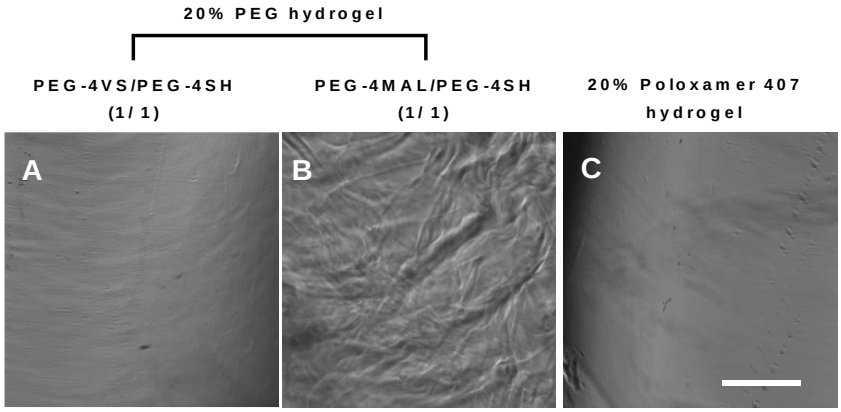

Figure 8.2.S1 *Hydrogel morphology observed under the microscope showing the uniform internal structure (A, C) and non-uniform internal structure (B). Scale bar = 5 µm.*

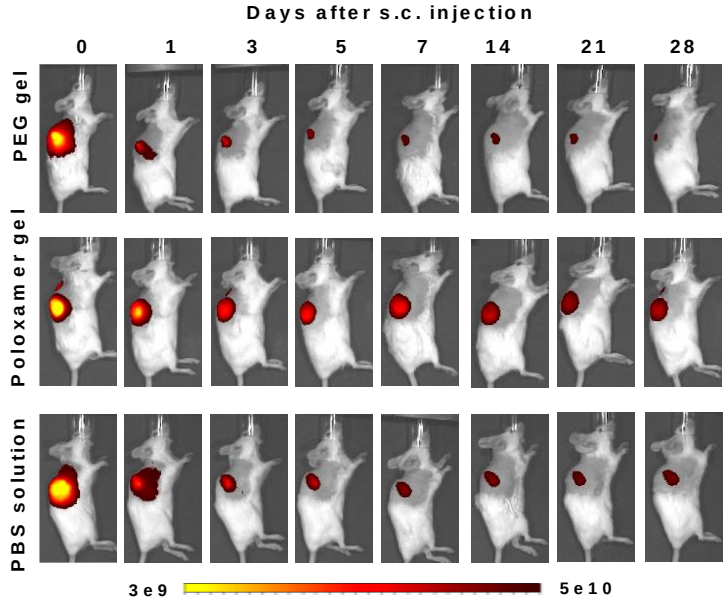

Figure 8.2.S2 *Whole-animal images of s. c. injected hydrogels or solutions on right back of mice.*

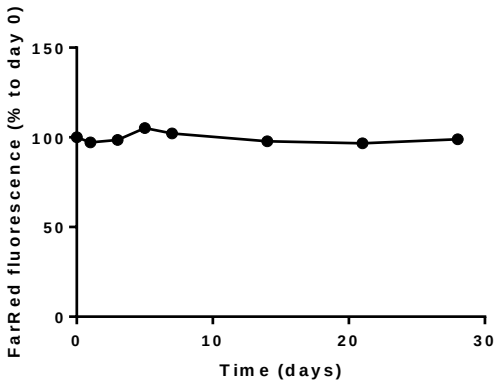

Figure 8.2.S3 *Fluorescence intensity of the FarRed solution that was preserved in a tube at room temperature over a month.*

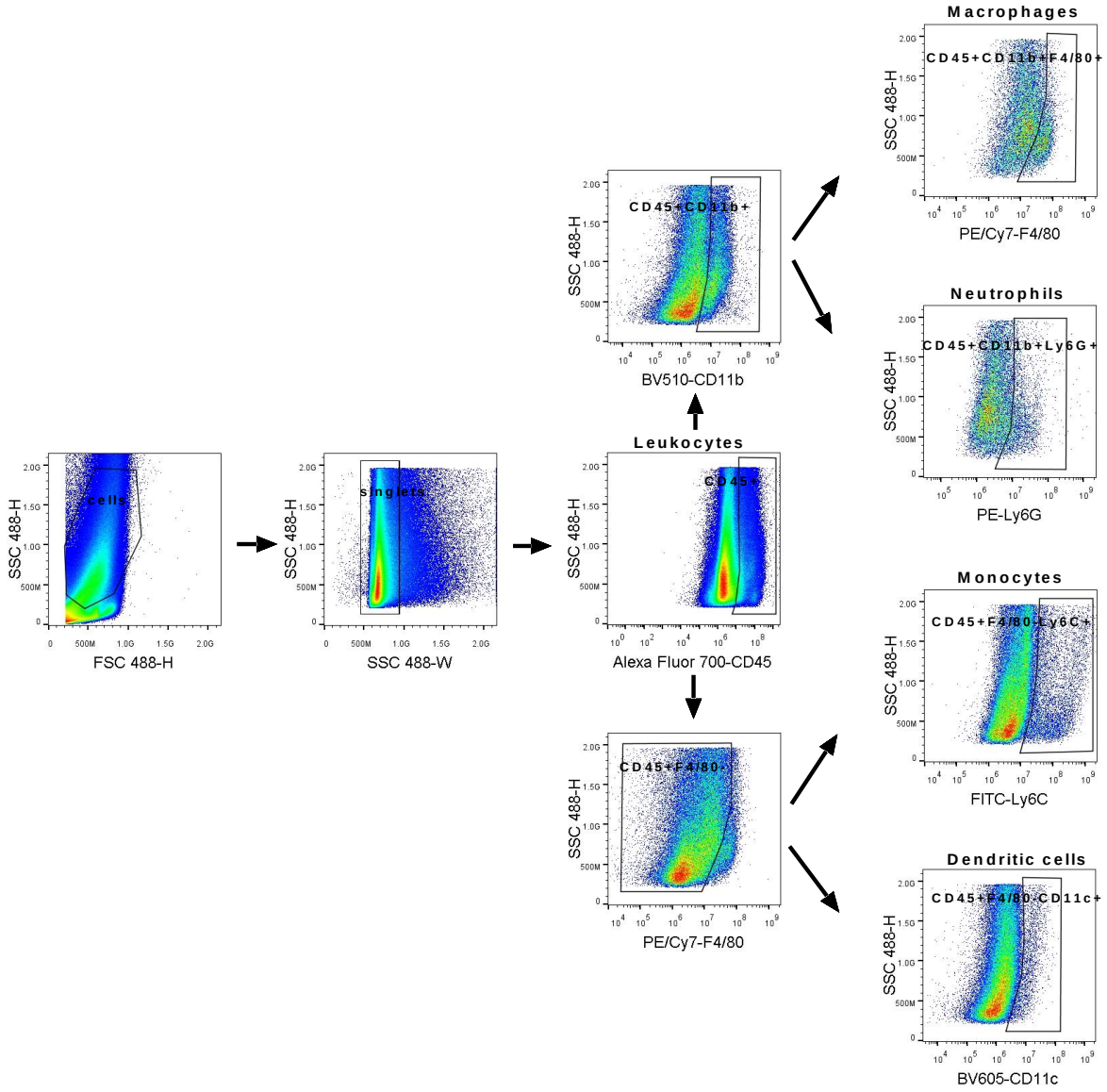

Figure 8.2.S4 *Gating strategies for flow cytometric analysis of immune cell markers showing identification of cells*

Singlets gated by side scatter, $CD45^+$ leukocytes gated as $AF700^+$, $CD11b^+F4/80^+$ macrophages gated as $BV510^+PE/Cy7^+$, $CD11b^+Ly6G^+$ polymorphnuclear neutrophils (pMN) gated as $BV510^+PE^+$, $F4/80^-Ly6C^+$ monocytes gated as $PE/Cy7^-FITC^+$, and $F4/80^-CD11c^+$ dendritic cells gated as $PE/Cy7^-BV605^+$. All gates were set according to appropriate positive and negative controls. Each arrow indicates a nested gate where the positive population from the previous plot is represented on the subsequent plot. BV: brilliant violet.

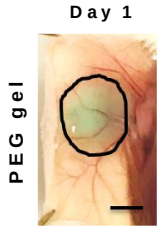

Figure 8.2.S5 *Morphology of FarRed-loaded PEG gel at day 1 post s.c. injection. Solid line distinguishes the gel edge. Scale bar = 5 mm.*

Table 8.2.S1: Thiol conversation in PEG hydrogels

PEG concentration (w/v)	Formulation (molar ratio)	Thiol Conversation
10%	PEG-4VS/PEG-4SH (1: 1)	99%
15%	PEG-4VS/PEG-4SH (1: 1)	100%
20%	PEG-4VS/PEG-4SH (1: 1)	100%
20%	PEG-4MAL/PEG-4SH (1: 1)	89%

References

(1) Szot, C. S.; Buchanan, C. F.; Freeman, J. W.; Rylander, M. N. 3D in Vitro Bioengineered Tumors Based on Collagen I Hydrogels. *Biomaterials* **2011**, *32* (31), 7905–7912. https://doi.org/10.1016/j.biomaterials.2011.07.001.

(2) Miralles, F.; Czernichow, P.; Scharfmann, R. Follistatin Regulates the Relative Proportions of Endocrine versus Exocrine Tissue during Pancreatic Development. *Dev. Camb. Engl.* **1998**, *125* (6), 1017–1024.

(3) Montesano, R.; Mouron, P.; Amherdt, M.; Orci, L. Collagen Matrix Promotes Reorganization of Pancreatic Endocrine Cell Monolayers into Islet-like Organoids. *J. Cell Biol.* **1983**, *97* (3), 935–939. https://doi.org/10.1083/jcb.97.3.935.

(4) Sainz, B.; TenCate, V.; Uprichard, S. L. Three-Dimensional Huh7 Cell Culture System for the Study of Hepatitis C Virus Infection. *Virol. J.* **2009**, *6*, 103. https://doi.org/10.1186/1743-422X-6-103.

(5) Yamada, K. M.; Cukierman, E. Modeling Tissue Morphogenesis and Cancer in 3D. *Cell* **2007**, *130* (4), 601–610. https://doi.org/10.1016/j.cell.2007.08.006.

(6) Griffith, L. G.; Swartz, M. A. Capturing Complex 3D Tissue Physiology in Vitro. *Nat. Rev. Mol. Cell Biol.* **2006**, *7* (3), 211–224. https://doi.org/10.1038/nrm1858.

(7) Derda, R.; Laromaine, A.; Mammoto, A.; Tang, S. K. Y.; Mammoto, T.; Ingber, D. E.; Whitesides, G. M. Paper-Supported 3D Cell Culture for Tissue-Based Bioassays. *Proc. Natl. Acad. Sci. U. S. A.* **2009**, *106* (44), 18457–18462. https://doi.org/10.1073/pnas.0910666106.

(8) Cukierman, E.; Pankov, R.; Yamada, K. M. Cell Interactions with Three-Dimensional Matrices. *Curr. Opin. Cell Biol.* **2002**, *14* (5), 633–639. https://doi.org/10.1016/s0955-0674(02)00364-2.

(9) Kim, J. B.; Stein, R.; O'Hare, M. J. Three-Dimensional in Vitro Tissue Culture Models of Breast Cancer — a Review. *Breast Cancer Res. Treat.* **2004**, *85* (3), 281–291. https://doi.org/10.1023/B:BREA.0000025418.88785.2b.

(10) Li, H.-Y.; Chang, S.-P.; Yuan, C.-C.; Chao, H.-T.; Ng, H.-T.; Sung, Y.-J. Establishment of an Efficient Method to Quantify Embryo Attachment to Endometrial Epithelial Cell Monolayers. *In Vitro Cell. Dev. Biol. Anim.* **2002**, *38* (9), 505–511. https://doi.org/10.1290/1071-2690(2002)038<0505:EOAEMT>2.0.CO;2.

(11) Vinci, M.; Gowan, S.; Boxall, F.; Patterson, L.; Zimmermann, M.; Court, W.; Lomas, C.; Mendiola, M.; Hardisson, D.; Eccles, S. A. Advances in Establishment and Analysis of Three-Dimensional Tumor Spheroid-Based Functional Assays for Target Validation and Drug Evaluation. *BMC Biol.* **2012**, *10*, 29. https://doi.org/10.1186/1741-7007-10-29.

(12) Kelm, J. M.; Djonov, V.; Ittner, L. M.; Fluri, D.; Born, W.; Hoerstrup, S. P.; Fussenegger, M. Design of Custom-Shaped Vascularized Tissues Using Microtissue Spheroids as

Minimal Building Units. *Tissue Eng.* **2006**, *12* (8), 2151–2160. https://doi.org/10.1089/ten.2006.12.2151.

(13) Asghari, F.; Samiei, M.; Adibkia, K.; Akbarzadeh, A.; Davaran, S. Biodegradable and Biocompatible Polymers for Tissue Engineering Application: A Review. *Artif. Cells Nanomedicine Biotechnol.* **2017**, *45* (2), 185–192. https://doi.org/10.3109/21691401.2016.1146731.

(14) Rozario, T.; DeSimone, D. W. The Extracellular Matrix In Development and Morphogenesis: A Dynamic View. *Dev. Biol.* **2010**, *341* (1), 126–140. https://doi.org/10.1016/j.ydbio.2009.10.026.

(15) Xiao, G.; Jiang, D.; Gopalakrishnan, R.; Franceschi, R. T. Fibroblast Growth Factor 2 Induction of the Osteocalcin Gene Requires MAPK Activity and Phosphorylation of the Osteoblast Transcription Factor, Cbfa1/Runx2. *J. Biol. Chem.* **2002**, *277* (39), 36181–36187. https://doi.org/10.1074/jbc.M206057200.

(16) Geiger, B.; Bershadsky, A.; Pankov, R.; Yamada, K. M. Transmembrane Crosstalk between the Extracellular Matrix--Cytoskeleton Crosstalk. *Nat. Rev. Mol. Cell Biol.* **2001**, *2* (11), 793–805. https://doi.org/10.1038/35099066.

(17) Ge, C.; Xiao, G.; Jiang, D.; Franceschi, R. T. Critical Role of the Extracellular Signal-Regulated Kinase-MAPK Pathway in Osteoblast Differentiation and Skeletal Development. *J. Cell Biol.* **2007**, *176* (5), 709–718. https://doi.org/10.1083/jcb.200610046.

(18) National Diabetes Statistics Report 2020. Estimates of Diabetes and Its Burden in the United States. **2020**, 32.

(19) Vaithilingam, V.; Sundaram, G.; Tuch, B. E. Islet Cell Transplantation. *Curr. Opin. Organ Transplant.* **2008**, *13* (6), 633–638. https://doi.org/10.1097/MOT.0b013e328317a48b.

(20) Fiorina, P.; Shapiro, A. M. J.; Ricordi, C.; Secchi, A. The Clinical Impact of Islet Transplantation. *Am. J. Transplant. Off. J. Am. Soc. Transplant. Am. Soc. Transpl. Surg.* **2008**, *8* (10), 1990–1997. https://doi.org/10.1111/j.1600-6143.2008.02353.x.

(21) Shapiro, A. M. J.; Ricordi, C.; Hering, B. J.; Auchincloss, H.; Lindblad, R.; Robertson, R. P.; Secchi, A.; Brendel, M. D.; Berney, T.; Brennan, D. C.; Cagliero, E.; Alejandro, R.; Ryan, E. A.; DiMercurio, B.; Morel, P.; Polonsky, K. S.; Reems, J.-A.; Bretzel, R. G.; Bertuzzi, F.; Froud, T.; Kandaswamy, R.; Sutherland, D. E. R.; Eisenbarth, G.; Segal, M.; Preiksaitis, J.; Korbutt, G. S.; Barton, F. B.; Viviano, L.; Seyfert-Margolis, V.; Bluestone, J.; Lakey, J. R. T. International Trial of the Edmonton Protocol for Islet Transplantation. *N. Engl. J. Med.* **2006**, *355* (13), 1318–1330. https://doi.org/10.1056/NEJMoa061267.

(22) Alejandro, R.; Barton, F. B.; Hering, B. J.; Wease, S.; Collaborative Islet Transplant Registry Investigators. 2008 Update from the Collaborative Islet Transplant Registry. *Transplantation* **2008**, *86* (12), 1783–1788. https://doi.org/10.1097/TP.0b013e3181913f6a.

(23) Rezania, A.; Bruin, J. E.; Arora, P.; Rubin, A.; Batushansky, I.; Asadi, A.; O'Dwyer, S.; Quiskamp, N.; Mojibian, M.; Albrecht, T.; Yang, Y. H. C.; Johnson, J. D.; Kieffer, T. J. Reversal of Diabetes with Insulin-Producing Cells Derived in Vitro from Human Pluripotent Stem Cells. *Nat. Biotechnol.* **2014**, *32* (11), 1121–1133. https://doi.org/10.1038/nbt.3033.

(24) Pagliuca, F. W.; Millman, J. R.; Gürtler, M.; Segel, M.; Van Dervort, A.; Ryu, J. H.; Peterson, Q. P.; Greiner, D.; Melton, D. A. Generation of Functional Human Pancreatic β Cells In Vitro. *Cell* **2014**, *159* (2), 428–439. https://doi.org/10.1016/j.cell.2014.09.040.
(25) Velazco-Cruz, L.; Song, J.; Maxwell, K. G.; Goedegebuure, M. M.; Augsornworawat, P.; Hogrebe, N. J.; Millman, J. R. Acquisition of Dynamic Function in Human Stem Cell-Derived β Cells. *Stem Cell Rep.* **2019**, *12* (2), 351–365. https://doi.org/10.1016/j.stemcr.2018.12.012.
(26) Pagliuca, F. W.; Melton, D. A. How to Make a Functional β-Cell. *Dev. Camb. Engl.* **2013**, *140* (12), 2472–2483. https://doi.org/10.1242/dev.093187.
(27) Stendahl, J. C.; Kaufman, D. B.; Stupp, S. I. Extracellular Matrix in Pancreatic Islets: Relevance to Scaffold Design and Transplantation. *Cell Transplant.* **2009**, *18* (1), 1–12. https://doi.org/10.3727/096368909788237195.
(28) Gibly, R. F.; Graham, J. G.; Luo, X.; Lowe, W. L.; Hering, B. J.; Shea, L. D. Advancing Islet Transplantation: From Engraftment to the Immune Response. *Diabetologia* **2011**, *54* (10), 2494. https://doi.org/10.1007/s00125-011-2243-0.
(29) Cantarelli, E.; Piemonti, L. Alternative Transplantation Sites for Pancreatic Islet Grafts. *Curr. Diab. Rep.* **2011**, *11* (5), 364–374. https://doi.org/10.1007/s11892-011-0216-9.
(30) Clause, K. C.; Barker, T. H. Extracellular Matrix Signaling in Morphogenesis and Repair. *Curr. Opin. Biotechnol.* **2013**, *24* (5), 830–833. https://doi.org/10.1016/j.copbio.2013.04.011.
(31) Gjorevski, N.; Sachs, N.; Manfrin, A.; Giger, S.; Bragina, M. E.; Ordóñez-Morán, P.; Clevers, H.; Lutolf, M. P. Designer Matrices for Intestinal Stem Cell and Organoid Culture. *Nature* **2016**, *539* (7630), 560–564. https://doi.org/10.1038/nature20168.
(32) Dye, B. R.; Hill, D. R.; Ferguson, M. A.; Tsai, Y.-H.; Nagy, M. S.; Dyal, R.; Wells, J. M.; Mayhew, C. N.; Nattiv, R.; Klein, O. D.; White, E. S.; Deutsch, G. H.; Spence, J. R. In Vitro Generation of Human Pluripotent Stem Cell Derived Lung Organoids. *eLife* **2015**, *4*, e05098. https://doi.org/10.7554/eLife.05098.
(33) Watson, C. L.; Mahe, M. M.; Múnera, J.; Howell, J. C.; Sundaram, N.; Poling, H. M.; Schweitzer, J. I.; Vallance, J. E.; Mayhew, C. N.; Sun, Y.; Grabowski, G.; Finkbeiner, S. R.; Spence, J. R.; Shroyer, N. F.; Wells, J. M.; Helmrath, M. A. An in Vivo Model of Human Small Intestine Using Pluripotent Stem Cells. *Nat. Med.* **2014**, *20* (11), 1310–1314. https://doi.org/10.1038/nm.3737.
(34) Spence, J. R.; Mayhew, C. N.; Rankin, S. A.; Kuhar, M. F.; Vallance, J. E.; Tolle, K.; Hoskins, E. E.; Kalinichenko, V. V.; Wells, S. I.; Zorn, A. M.; Shroyer, N. F.; Wells, J. M. Directed Differentiation of Human Pluripotent Stem Cells into Intestinal Tissue in Vitro. *Nature* **2011**, *470* (7332), 105–109. https://doi.org/10.1038/nature09691.
(35) Mahe, M. M.; Sundaram, N.; Watson, C. L.; Shroyer, N. F.; Helmrath, M. A. Establishment of Human Epithelial Enteroids and Colonoids from Whole Tissue and Biopsy. *J. Vis. Exp. JoVE* **2015**, No. 97. https://doi.org/10.3791/52483.
(36) Sato, T.; Clevers, H. Primary Mouse Small Intestinal Epithelial Cell Cultures. *Methods Mol. Biol. Clifton NJ* **2013**, *945*, 319–328. https://doi.org/10.1007/978-1-62703-125-7_19.
(37) Kovbasnjuk, O.; Zachos, N. C.; In, J.; Foulke-Abel, J.; Ettayebi, K.; Hyser, J. M.; Broughman, J. R.; Zeng, X.-L.; Middendorp, S.; de Jonge, H. R.; Estes, M. K.; Donowitz, M.

Human Enteroids: Preclinical Models of Non-Inflammatory Diarrhea. *Stem Cell Res. Ther.* **2013**, *4 Suppl 1*, S3. https://doi.org/10.1186/scrt364.

(38) Leslie, J. L.; Huang, S.; Opp, J. S.; Nagy, M. S.; Kobayashi, M.; Young, V. B.; Spence, J. R. Persistence and Toxin Production by Clostridium Difficile within Human Intestinal Organoids Result in Disruption of Epithelial Paracellular Barrier Function. *Infect. Immun.* **2015**, *83* (1), 138–145. https://doi.org/10.1128/IAI.02561-14.

(39) Finkbeiner, S. R.; Zeng, X.-L.; Utama, B.; Atmar, R. L.; Shroyer, N. F.; Estes, M. K. Stem Cell-Derived Human Intestinal Organoids as an Infection Model for Rotaviruses. *mBio* **2012**, *3* (4), e00159-00112. https://doi.org/10.1128/mBio.00159-12.

(40) Munot, K.; Kotler, D. P. Small Intestinal Infections. *Curr. Gastroenterol. Rep.* **2016**, *18* (6), 31. https://doi.org/10.1007/s11894-016-0502-4.

(41) Czerwinski, M.; Spence, J. R. Hacking the Matrix. *Cell Stem Cell* **2017**, *20* (1), 9–10. https://doi.org/10.1016/j.stem.2016.12.010.

(42) Yan, Y.; Yang, D.; Zarnowska, E. D.; Du, Z.; Werbel, B.; Valliere, C.; Pearce, R. A.; Thomson, J. A.; Zhang, S.-C. Directed Differentiation of Dopaminergic Neuronal Subtypes from Human Embryonic Stem Cells. *STEM CELLS* **2005**, *23* (6), 781–790. https://doi.org/10.1634/stemcells.2004-0365.

(43) Wichterle, H.; Lieberam, I.; Porter, J. A.; Jessell, T. M. Directed Differentiation of Embryonic Stem Cells into Motor Neurons. *Cell* **2002**, *110* (3), 385–397. https://doi.org/10.1016/S0092-8674(02)00835-8.

(44) Laflamme, M. A.; Chen, K. Y.; Naumova, A. V.; Muskheli, V.; Fugate, J. A.; Dupras, S. K.; Reinecke, H.; Xu, C.; Hassanipour, M.; Police, S.; O'Sullivan, C.; Collins, L.; Chen, Y.; Minami, E.; Gill, E. A.; Ueno, S.; Yuan, C.; Gold, J.; Murry, C. E. Cardiomyocytes Derived from Human Embryonic Stem Cells in Pro-Survival Factors Enhance Function of Infarcted Rat Hearts. *Nat. Biotechnol.* **2007**, *25* (9), 1015–1024. https://doi.org/10.1038/nbt1327.

(45) Lian, X.; Zhang, J.; Azarin, S. M.; Zhu, K.; Hazeltine, L. B.; Bao, X.; Hsiao, C.; Kamp, T. J.; Palecek, S. P. Directed Cardiomyocyte Differentiation from Human Pluripotent Stem Cells by Modulating Wnt/β-Catenin Signaling under Fully Defined Conditions. *Nat. Protoc.* **2013**, *8* (1), 162–175. https://doi.org/10.1038/nprot.2012.150.

(46) Lian, X.; Hsiao, C.; Wilson, G.; Zhu, K.; Hazeltine, L. B.; Azarin, S. M.; Raval, K. K.; Zhang, J.; Kamp, T. J.; Palecek, S. P. Robust Cardiomyocyte Differentiation from Human Pluripotent Stem Cells via Temporal Modulation of Canonical Wnt Signaling. *Proc. Natl. Acad. Sci.* **2012**, *109* (27), E1848–E1857. https://doi.org/10.1073/pnas.1200250109.

(47) Cai, J.; Zhao, Y.; Liu, Y.; Ye, F.; Song, Z.; Qin, H.; Meng, S.; Chen, Y.; Zhou, R.; Song, X.; Guo, Y.; Ding, M.; Deng, H. Directed Differentiation of Human Embryonic Stem Cells into Functional Hepatic Cells. *Hepatology* **2007**, *45* (5), 1229–1239. https://doi.org/10.1002/hep.21582.

(48) Song, Z.; Cai, J.; Liu, Y.; Zhao, D.; Yong, J.; Duo, S.; Song, X.; Guo, Y.; Zhao, Y.; Qin, H.; Yin, X.; Wu, C.; Che, J.; Lu, S.; Ding, M.; Deng, H. Efficient Generation of Hepatocyte-like Cells from Human Induced Pluripotent Stem Cells. *Cell Res.* **2009**, *19* (11), 1233–1242. https://doi.org/10.1038/cr.2009.107.

(49) Nakano, T.; Ando, S.; Takata, N.; Kawada, M.; Muguruma, K.; Sekiguchi, K.; Saito, K.; Yonemura, S.; Eiraku, M.; Sasai, Y. Self-Formation of Optic Cups and Storable Stratified

Neural Retina from Human ESCs. *Cell Stem Cell* **2012**, *10* (6), 771–785. https://doi.org/10.1016/j.stem.2012.05.009.

(50) Xia, Y.; Sancho-Martinez, I.; Nivet, E.; Esteban, C. R.; Campistol, J. M.; Belmonte, J. C. I. The Generation of Kidney Organoids by Differentiation of Human Pluripotent Cells to Ureteric Bud Progenitor–like Cells. *Nat. Protoc.* **2014**, *9* (11), 2693–2704. https://doi.org/10.1038/nprot.2014.182.

(51) Lancaster, M. A.; Renner, M.; Martin, C.-A.; Wenzel, D.; Bicknell, L. S.; Hurles, M. E.; Homfray, T.; Penninger, J. M.; Jackson, A. P.; Knoblich, J. A. Cerebral Organoids Model Human Brain Development and Microcephaly. *Nature* **2013**, *501* (7467), 373–379. https://doi.org/10.1038/nature12517.

(52) Lancaster, M. A.; Renner, M.; Martin, C.-A.; Wenzel, D.; Bicknell, L. S.; Hurles, M. E.; Homfray, T.; Penninger, J. M.; Jackson, A. P.; Knoblich, J. A. Cerebral Organoids Model Human Brain Development and Microcephaly. *Nature* **2013**, *501* (7467). https://doi.org/10.1038/nature12517.

(53) Qian, X.; Nguyen, H. N.; Song, M. M.; Hadiono, C.; Ogden, S. C.; Hammack, C.; Yao, B.; Hamersky, G.; Jacob, F.; Zhong, C.; Yoon, K.; Jeang, W.; Lin, L.; Li, Y.; Thakor, J.; Berg, D.; Zhang, C.; Kang, E.; Chickering, M.; Naeun, D.; Ho, C.-Y.; Wen, Z.; Christian, K. M.; Shi, P.-Y.; Maher, B. J.; Wu, H.; Jin, P.; Tang, H.; Song, H.; Ming, G. Brain Region-Specific Organoids Using Mini-Bioreactors for Modeling ZIKV Exposure. *Cell* **2016**, *165* (5), 1238–1254. https://doi.org/10.1016/j.cell.2016.04.032.

(54) Greggio, C.; De Franceschi, F.; Figueiredo-Larsen, M.; Gobaa, S.; Ranga, A.; Semb, H.; Lutolf, M.; Grapin-Botton, A. Artificial Three-Dimensional Niches Deconstruct Pancreas Development in Vitro. *Dev. Camb. Engl.* **2013**, *140* (21), 4452–4462. https://doi.org/10.1242/dev.096628.

(55) Ciancanelli, M. J.; Huang, S. X. L.; Luthra, P.; Garner, H.; Itan, Y.; Volpi, S.; Lafaille, F. G.; Trouillet, C.; Schmolke, M.; Albrecht, R. A.; Israelsson, E.; Lim, H. K.; Casadio, M.; Hermesh, T.; Lorenzo, L.; Leung, L. W.; Pedergnana, V.; Boisson, B.; Okada, S.; Picard, C.; Ringuier, B.; Troussier, F.; Chaussabel, D.; Abel, L.; Pellier, I.; Notarangelo, L. D.; García-Sastre, A.; Basler, C. F.; Geissmann, F.; Zhang, S.-Y.; Snoeck, H.-W.; Casanova, J.-L. Infectious Disease. Life-Threatening Influenza and Impaired Interferon Amplification in Human IRF7 Deficiency. *Science* **2015**, *348* (6233), 448–453. https://doi.org/10.1126/science.aaa1578.

(56) Dekkers, J. F.; Wiegerinck, C. L.; de Jonge, H. R.; Bronsveld, I.; Janssens, H. M.; de Winter-de Groot, K. M.; Brandsma, A. M.; de Jong, N. W. M.; Bijvelds, M. J. C.; Scholte, B. J.; Nieuwenhuis, E. E. S.; van den Brink, S.; Clevers, H.; van der Ent, C. K.; Middendorp, S.; Beekman, J. M. A Functional CFTR Assay Using Primary Cystic Fibrosis Intestinal Organoids. *Nat. Med.* **2013**, *19* (7), 939–945. https://doi.org/10.1038/nm.3201.

(57) Ranga, A.; Girgin, M.; Meinhardt, A.; Eberle, D.; Caiazzo, M.; Tanaka, E. M.; Lutolf, M. P. Neural Tube Morphogenesis in Synthetic 3D Microenvironments. *Proc. Natl. Acad. Sci.* **2016**, *113* (44), E6831–E6839. https://doi.org/10.1073/pnas.1603529113.

(58) Lu, P.; Takai, K.; Weaver, V. M.; Werb, Z. Extracellular Matrix Degradation and Remodeling in Development and Disease. *Cold Spring Harb. Perspect. Biol.* **2011**, *3* (12). https://doi.org/10.1101/cshperspect.a005058.

(59) Levental, K. R.; Yu, H.; Kass, L.; Lakins, J. N.; Egeblad, M.; Erler, J. T.; Fong, S. F. T.; Csiszar, K.; Giaccia, A.; Weninger, W.; Yamauchi, M.; Gasser, D. L.; Weaver, V. M. Matrix Crosslinking Forces Tumor Progression by Enhancing Integrin Signaling. *Cell* **2009**, *139* (5), 891–906. https://doi.org/10.1016/j.cell.2009.10.027.

(60) Xu, Y.; Chen, C.; Hellwarth, P. B.; Bao, X. Biomaterials for Stem Cell Engineering and Biomanufacturing. *Bioact. Mater.* **2019**, *4*, 366–379. https://doi.org/10.1016/j.bioactmat.2019.11.002.

(61) Lutolf, M. P.; Gilbert, P. M.; Blau, H. M. Designing Materials to Direct Stem-Cell Fate. *Nature* **2009**, *462* (7272), 433–441. https://doi.org/10.1038/nature08602.

(62) Song, X.; Zhu, C.; Fan, D.; Mi, Y.; Li, X.; Fu, R. Z.; Duan, Z.; Wang, Y.; Feng, R. R. A Novel Human-Like Collagen Hydrogel Scaffold with Porous Structure and Sponge-Like Properties. *Polymers* **2017**, *9* (12), 638. https://doi.org/10.3390/polym9120638.

(63) Liu, M.; Zeng, X.; Ma, C.; Yi, H.; Ali, Z.; Mou, X.; Li, S.; Deng, Y.; He, N. Injectable Hydrogels for Cartilage and Bone Tissue Engineering. *Bone Res.* **2017**, *5*, 17014. https://doi.org/10.1038/boneres.2017.14.

(64) Chen, N.; Zhang, Z.; Soontornworajit, B.; Zhou, J.; Wang, Y. Cell Adhesion on an Artificial Extracellular Matrix Using Aptamer-Functionalized PEG Hydrogels. *Biomaterials* **2012**, *33* (5), 1353–1362. https://doi.org/10.1016/j.biomaterials.2011.10.062.

(65) Rape, A. D.; Zibinsky, M.; Murthy, N.; Kumar, S. A Synthetic Hydrogel for the High-Throughput Study of Cell–ECM Interactions. *Nat. Commun.* **2015**, *6*, 8129. https://doi.org/10.1038/ncomms9129.

(66) Fang, Y.; Eglen, R. M. Three-Dimensional Cell Cultures in Drug Discovery and Development. *Slas Discov.* **2017**, *22* (5), 456–472. https://doi.org/10.1177/1087057117696795.

(67) Kratochvil, M. J.; Seymour, A. J.; Li, T. L.; Paşca, S. P.; Kuo, C. J.; Heilshorn, S. C. Engineered Materials for Organoid Systems. *Nat. Rev. Mater.* **2019**, *4* (9), 606–622. https://doi.org/10.1038/s41578-019-0129-9.

(68) Oksdath, M.; Perrin, S. L.; Bardy, C.; Hilder, E. F.; DeForest, C. A.; Arrua, R. D.; Gomez, G. A. Review: Synthetic Scaffolds to Control the Biochemical, Mechanical, and Geometrical Environment of Stem Cell-Derived Brain Organoids. *APL Bioeng.* **2018**, *2* (4). https://doi.org/10.1063/1.5045124.

(69) Kornmuller, A.; Brown, C. F. C.; Yu, C.; Flynn, L. E. Fabrication of Extracellular Matrix-Derived Foams and Microcarriers as Tissue-Specific Cell Culture and Delivery Platforms. *J. Vis. Exp. JoVE* **2017**, No. 122. https://doi.org/10.3791/55436.

(70) DeQuach, J. A.; Yuan, S. H.; Goldstein, L. S. B.; Christman, K. L. Decellularized Porcine Brain Matrix for Cell Culture and Tissue Engineering Scaffolds. *Tissue Eng. Part A* **2011**, *17* (21–22), 2583–2592. https://doi.org/10.1089/ten.TEA.2010.0724.

(71) Gilbert, T. W.; Sellaro, T. L.; Badylak, S. F. Decellularization of Tissues and Organs. *Biomaterials* **2006**, *27* (19), 3675–3683. https://doi.org/10.1016/j.biomaterials.2006.02.014.

(72) Crapo, P. M.; Gilbert, T. W.; Badylak, S. F. An Overview of Tissue and Whole Organ Decellularization Processes. *Biomaterials* **2011**, *32* (12), 3233–3243. https://doi.org/10.1016/j.biomaterials.2011.01.057.

(73) Kim, B. S.; Choi, J. S.; Kim, J. D.; Choi, Y. C.; Cho, Y. W. Recellularization of Decellularized Human Adipose-Tissue-Derived Extracellular Matrix Sheets with Other Human Cell Types. *Cell Tissue Res.* **2012**, *348* (3), 559–567. https://doi.org/10.1007/s00441-012-1391-y.

(74) Shridhar, A.; Gillies, E.; Amsden, B. G.; Flynn, L. E. Composite Bioscaffolds Incorporating Decellularized ECM as a Cell-Instructive Component Within Hydrogels as In Vitro Models and Cell Delivery Systems. *Methods Mol. Biol. Clifton NJ* **2018**, *1577*, 183–208. https://doi.org/10.1007/7651_2017_36.

(75) Singelyn, J. M.; DeQuach, J. A.; Seif-Naraghi, S. B.; Littlefield, R. B.; Schup-Magoffin, P. J.; Christman, K. L. Naturally Derived Myocardial Matrix as an Injectable Scaffold for Cardiac Tissue Engineering. *Biomaterials* **2009**, *30* (29), 5409–5416. https://doi.org/10.1016/j.biomaterials.2009.06.045.

(76) Turner, A. E. B.; Flynn, L. E. Design and Characterization of Tissue-Specific Extracellular Matrix-Derived Microcarriers. *Tissue Eng. Part C Methods* **2012**, *18* (3), 186–197. https://doi.org/10.1089/ten.TEC.2011.0246.

(77) Russo, V.; Omidi, E.; Samani, A.; Hamilton, A.; Flynn, L. E. Porous, Ventricular Extracellular Matrix-Derived Foams as a Platform for Cardiac Cell Culture. *BioResearch Open Access* **2015**, *4* (1), 374–388. https://doi.org/10.1089/biores.2015.0030.

(78) Yu, C.; Bianco, J.; Brown, C.; Fuetterer, L.; Watkins, J. F.; Samani, A.; Flynn, L. E. Porous Decellularized Adipose Tissue Foams for Soft Tissue Regeneration. *Biomaterials* **2013**, *34* (13), 3290–3302. https://doi.org/10.1016/j.biomaterials.2013.01.056.

(79) Pati, F.; Jang, J.; Ha, D.-H.; Won Kim, S.; Rhie, J.-W.; Shim, J.-H.; Kim, D.-H.; Cho, D.-W. Printing Three-Dimensional Tissue Analogues with Decellularized Extracellular Matrix Bioink. *Nat. Commun.* **2014**, *5*, 3935. https://doi.org/10.1038/ncomms4935.

(80) DeQuach, J. A.; Mezzano, V.; Miglani, A.; Lange, S.; Keller, G. M.; Sheikh, F.; Christman, K. L. Simple and High Yielding Method for Preparing Tissue Specific Extracellular Matrix Coatings for Cell Culture. *PLOS ONE* **2010**, *5* (9), e13039. https://doi.org/10.1371/journal.pone.0013039.

(81) Rajabi-Zeleti, S.; Jalili-Firoozinezhad, S.; Azarnia, M.; Khayyatan, F.; Vahdat, S.; Nikeghbalian, S.; Khademhosseini, A.; Baharvand, H.; Aghdami, N. The Behavior of Cardiac Progenitor Cells on Macroporous Pericardium-Derived Scaffolds. *Biomaterials* **2014**, *35* (3), 970–982. https://doi.org/10.1016/j.biomaterials.2013.10.045.

(82) Flynn, L. E. The Use of Decellularized Adipose Tissue to Provide an Inductive Microenvironment for the Adipogenic Differentiation of Human Adipose-Derived Stem Cells. *Biomaterials* **2010**, *31* (17), 4715–4724. https://doi.org/10.1016/j.biomaterials.2010.02.046.

(83) Robb, K. P.; Shridhar, A.; Flynn, L. E. Decellularized Matrices As Cell-Instructive Scaffolds to Guide Tissue-Specific Regeneration. *ACS Biomater. Sci. Eng.* **2018**, *4* (11), 3627–3643. https://doi.org/10.1021/acsbiomaterials.7b00619.

(84) Kleinman, H. K.; McGarvey, M. L.; Liotta, L. A.; Robey, P. G.; Tryggvason, K.; Martin, G. R. Isolation and Characterization of Type IV Procollagen, Laminin, and Heparan Sulfate Proteoglycan from the EHS Sarcoma. *Biochemistry* **1982**, *21* (24), 6188–6193. https://doi.org/10.1021/bi00267a025.

(85) Lancaster, M. A.; Knoblich, J. A. Organogenesis in a Dish: Modeling Development and Disease Using Organoid Technologies. *Science* **2014**, *345* (6194), 1247125. https://doi.org/10.1126/science.1247125.
(86) Birgersdotter, A.; Sandberg, R.; Ernberg, I. Gene Expression Perturbation in Vitro--a Growing Case for Three-Dimensional (3D) Culture Systems. *Semin. Cancer Biol.* **2005**, *15* (5), 405–412. https://doi.org/10.1016/j.semcancer.2005.06.009.
(87) Eiraku, M.; Takata, N.; Ishibashi, H.; Kawada, M.; Sakakura, E.; Okuda, S.; Sekiguchi, K.; Adachi, T.; Sasai, Y. Self-Organizing Optic-Cup Morphogenesis in Three-Dimensional Culture. *Nature* **2011**, *472* (7341), 51–56. https://doi.org/10.1038/nature09941.
(88) Eiraku, M.; Watanabe, K.; Matsuo-Takasaki, M.; Kawada, M.; Yonemura, S.; Matsumura, M.; Wataya, T.; Nishiyama, A.; Muguruma, K.; Sasai, Y. Self-Organized Formation of Polarized Cortical Tissues from ESCs and Its Active Manipulation by Extrinsic Signals. *Cell Stem Cell* **2008**, *3* (5), 519–532. https://doi.org/10.1016/j.stem.2008.09.002.
(89) Gattazzo, F.; Urciuolo, A.; Bonaldo, P. Extracellular Matrix: A Dynamic Microenvironment for Stem Cell Niche. *Biochim. Biophys. Acta* **2014**, *1840* (8), 2506–2519. https://doi.org/10.1016/j.bbagen.2014.01.010.
(90) Sato, T.; Vries, R. G.; Snippert, H. J.; van de Wetering, M.; Barker, N.; Stange, D. E.; van Es, J. H.; Abo, A.; Kujala, P.; Peters, P. J.; Clevers, H. Single Lgr5 Stem Cells Build Crypt-Villus Structures in Vitro without a Mesenchymal Niche. *Nature* **2009**, *459* (7244), 262–265. https://doi.org/10.1038/nature07935.
(91) Slaughter, B. V; Khurshid, S. S.; Fisher, O. Z.; Khademhosseini, A.; Peppas, N. A. Hydrogels in Regenerative Medicine. *Adv. Mater. Deerfield Beach Fla* **2009**, *21* (32–33), 3307–3329. https://doi.org/10.1002/adma.200802106.
(92) Hoffman, A. S. Hydrogels for Biomedical Applications. *Adv. Drug Deliv. Rev.* **2012**, *64* (null), 18–23. https://doi.org/10.1016/j.addr.2012.09.010.
(93) Hollister, S. J. Porous Scaffold Design for Tissue Engineering. *Nat. Mater.* **2005**, *4* (7), 518–524. https://doi.org/10.1038/nmat1421.
(94) Drury, J. L.; Mooney, D. J. Hydrogels for Tissue Engineering: Scaffold Design Variables and Applications. *Biomaterials* **2003**, *24* (24), 4337–4351. https://doi.org/10.1016/S0142-9612(03)00340-5.
(95) Jhon, M. S.; Andrade, J. D. Water and Hydrogels. *J. Biomed. Mater. Res.* **1973**, *7* (6), 509–522. https://doi.org/10.1002/jbm.820070604.
(96) Molinaro, G.; Leroux, J.-C.; Damas, J.; Adam, A. Biocompatibility of Thermosensitive Chitosan-Based Hydrogels: An in Vivo Experimental Approach to Injectable Biomaterials. *Biomaterials* **2002**, *23* (13), 2717–2722.
(97) Noguchi, T.; Yamamuro, T.; Oka, M.; Kumar, P.; Kotoura, Y.; Hyon, S.; Ikada, Y. Poly(Vinyl Alcohol) Hydrogel as an Artificial Articular Cartilage: Evaluation of Biocompatibility. *J. Appl. Biomater. Off. J. Soc. Biomater.* **1991**, *2* (2), 101–107. https://doi.org/10.1002/jab.770020205.
(98) de Vos, P.; Lazarjani, H. A.; Poncelet, D.; Faas, M. M. Polymers in Cell Encapsulation from an Enveloped Cell Perspective. *Adv. Drug Deliv. Rev.* **2014**, *67–68* (4), 15–34. https://doi.org/10.1016/j.addr.2013.11.005.
(99) Lee, K. Y.; Mooney, D. J. Hydrogels for Tissue Engineering. *Chem. Rev.* **2001**, *101* (7), 1869–1879.

(100) Ahearne, M.; Wilson, S. L.; Liu, K.-K.; Rauz, S.; El Haj, A. J.; Yang, Y. Influence of Cell and Collagen Concentration on the Cell-Matrix Mechanical Relationship in a Corneal Stroma Wound Healing Model. *Exp. Eye Res.* **2010**, *91* (5), 584–591. https://doi.org/10.1016/j.exer.2010.07.013.

(101) Bott, K.; Upton, Z.; Schrobback, K.; Ehrbar, M.; Hubbell, J. A.; Lutolf, M. P.; Rizzi, S. C. The Effect of Matrix Characteristics on Fibroblast Proliferation in 3D Gels. *Biomaterials* **2010**, *31* (32), 8454–8464. https://doi.org/10.1016/j.biomaterials.2010.07.046.

(102) Nöth, U.; Schupp, K.; Heymer, A.; Kall, S.; Jakob, F.; Schütze, N.; Baumann, B.; Barthel, T.; Eulert, J.; Hendrich, C. Anterior Cruciate Ligament Constructs Fabricated from Human Mesenchymal Stem Cells in a Collagen Type I Hydrogel. *Cytotherapy* **2005**, *7* (5), 447–455. https://doi.org/10.1080/14653240500319093.

(103) Ahearne, M.; Yang, Y.; El Haj, A. J.; Then, K. Y.; Liu, K.-K. Characterizing the Viscoelastic Properties of Thin Hydrogel-Based Constructs for Tissue Engineering Applications. *J. R. Soc. Interface* **2005**, *2* (5), 455–463. https://doi.org/10.1098/rsif.2005.0065.

(104) Bader, R. A. Synthesis and Viscoelastic Characterization of Novel Hydrogels Generated via Photopolymerization of 1,2-Epoxy-5-Hexene Modified Poly(Vinyl Alcohol) for Use in Tissue Replacement. *Acta Biomater.* **2008**, *4* (4), 967–975. https://doi.org/10.1016/j.actbio.2008.02.015.

(105) Pierschbacher, M. D.; Ruoslahti, E. Cell Attachment Activity of Fibronectin Can Be Duplicated by Small Synthetic Fragments of the Molecule. *Nature* **1984**, *309* (5963), 30–33. https://doi.org/10.1038/309030a0.

(106) Knight, C. G.; Morton, L. F.; Peachey, A. R.; Tuckwell, D. S.; Farndale, R. W.; Barnes, M. J. The Collagen-Binding A-Domains of Integrins Alpha(1)Beta(1) and Alpha(2)Beta(1) Recognize the Same Specific Amino Acid Sequence, GFOGER, in Native (Triple-Helical) Collagens. *J. Biol. Chem.* **2000**, *275* (1), 35–40. https://doi.org/10.1074/jbc.275.1.35.

(107) Tashiro, K.; Sephel, G. C.; Weeks, B.; Sasaki, M.; Martin, G. R.; Kleinman, H. K.; Yamada, Y. A Synthetic Peptide Containing the IKVAV Sequence from the A Chain of Laminin Mediates Cell Attachment, Migration, and Neurite Outgrowth. *J. Biol. Chem.* **1989**, *264* (27), 16174–16182.

(108) Graf, J.; Iwamoto, Y.; Sasaki, M.; Martin, G. R.; Kleinman, H. K.; Robey, F. A.; Yamada, Y. Identification of an Amino Acid Sequence in Laminin Mediating Cell Attachment, Chemotaxis, and Receptor Binding. *Cell* **1987**, *48* (6), 989–996. https://doi.org/10.1016/0092-8674(87)90707-0.

(109) Benitez, P. L.; Mascharak, S.; Proctor, A. C.; Heilshorn, S. C. Use of Protein-Engineered Fabrics to Identify Design Rules for Integrin Ligand Clustering in Biomaterials. *Integr. Biol. Quant. Biosci. Nano Macro* **2016**, *8* (1), 50–61. https://doi.org/10.1039/c5ib00258c.

(110) Wang, X.; Yan, C.; Ye, K.; He, Y.; Li, Z.; Ding, J. Effect of RGD Nanospacing on Differentiation of Stem Cells. *Biomaterials* **2013**, *34* (12), 2865–2874. https://doi.org/10.1016/j.biomaterials.2013.01.021.

(111) Oria, R.; Wiegand, T.; Escribano, J.; Elosegui-Artola, A.; Uriarte, J. J.; Moreno-Pulido, C.; Platzman, I.; Delcanale, P.; Albertazzi, L.; Navajas, D.; Trepat, X.; García-Aznar, J. M.; Cavalcanti-Adam, E. A.; Roca-Cusachs, P. Force Loading Explains Spatial Sensing of

Ligands by Cells. *Nature* **2017**, *552* (7684), 219–224. https://doi.org/10.1038/nature24662.
(112) Wade, R. J.; Bassin, E. J.; Gramlich, W. M.; Burdick, J. A. Nanofibrous Hydrogels with Spatially Patterned Biochemical Signals to Control Cell Behavior. *Adv. Mater. Deerfield Beach Fla* **2015**, *27* (8), 1356–1362. https://doi.org/10.1002/adma.201404993.
(113) Arnold, M.; Cavalcanti-Adam, E. A.; Glass, R.; Blümmel, J.; Eck, W.; Kantlehner, M.; Kessler, H.; Spatz, J. P. Activation of Integrin Function by Nanopatterned Adhesive Interfaces. *Chemphyschem Eur. J. Chem. Phys. Phys. Chem.* **2004**, *5* (3), 383–388. https://doi.org/10.1002/cphc.200301014.
(114) Kloxin, A. M.; Kasko, A. M.; Salinas, C. N.; Anseth, K. S. Photodegradable Hydrogels for Dynamic Tuning of Physical and Chemical Properties. *Science* **2009**, *324* (5923), 59–63. https://doi.org/10.1126/science.1169494.
(115) Salinas, C. N.; Anseth, K. S. The Influence of the RGD Peptide Motif and Its Contextual Presentation in PEG Gels on Human Mesenchymal Stem Cell Viability. *J. Tissue Eng. Regen. Med.* **2008**, *2* (5), 296–304. https://doi.org/10.1002/term.95.
(116) Lutolf, M. P.; Hubbell, J. A. Synthesis and Physicochemical Characterization of End-Linked Poly(Ethylene Glycol)-Co-Peptide Hydrogels Formed by Michael-Type Addition. *Biomacromolecules* **2003**, *4* (3), 713–722. https://doi.org/10.1021/bm025744e.
(117) Cruz-Acuña, R.; Quirós, M.; Farkas, A. E.; Dedhia, P. H.; Huang, S.; Siuda, D.; García-Hernández, V.; Miller, A. J.; Spence, J. R.; Nusrat, A.; García, A. J. Synthetic Hydrogels for Human Intestinal Organoid Generation and Colonic Wound Repair. *Nat. Cell Biol.* **2017**, *19* (11), 1326–1335. https://doi.org/10.1038/ncb3632.
(118) Gobaa, S.; Hoehnel, S.; Roccio, M.; Negro, A.; Kobel, S.; Lutolf, M. P. Artificial Niche Microarrays for Probing Single Stem Cell Fate in High Throughput. *Nat. Methods* **2011**, *8* (11), 949–955. https://doi.org/10.1038/nmeth.1732.
(119) Gjorevski, N.; Ranga, A.; Lutolf, M. P. Bioengineering Approaches to Guide Stem Cell-Based Organogenesis. *Dev. Camb. Engl.* **2014**, *141* (9), 1794–1804. https://doi.org/10.1242/dev.101048.
(120) Lancaster, M. A.; Corsini, N. S.; Wolfinger, S.; Gustafson, E. H.; Phillips, A. W.; Burkard, T. R.; Otani, T.; Livesey, F. J.; Knoblich, J. A. Guided Self-Organization and Cortical Plate Formation in Human Brain Organoids. *Nat. Biotechnol.* **2017**, *35* (7), 659–666. https://doi.org/10.1038/nbt.3906.
(121) Sampaziotis, F.; Justin, A. W.; Tysoe, O. C.; Sawiak, S.; Godfrey, E. M.; Upponi, S. S.; Gieseck, R. L.; de Brito, M. C.; Berntsen, N. L.; Gómez-Vázquez, M. J.; Ortmann, D.; Yiangou, L.; Ross, A.; Bargehr, J.; Bertero, A.; Zonneveld, M. C. F.; Pedersen, M. T.; Pawlowski, M.; Valestrand, L.; Madrigal, P.; Georgakopoulos, N.; Pirmadjid, N.; Skeldon, G. M.; Casey, J.; Shu, W.; Materek, P. M.; Snijders, K. E.; Brown, S. E.; Rimland, C. A.; Simonic, I.; Davies, S. E.; Jensen, K. B.; Zilbauer, M.; Gelson, W. T. H.; Alexander, G. J.; Sinha, S.; Hannan, N. R. F.; Wynn, T. A.; Karlsen, T. H.; Melum, E.; Markaki, A. E.; Saeb-Parsy, K.; Vallier, L. Reconstruction of the Mouse Extrahepatic Biliary Tree Using Primary Human Extrahepatic Cholangiocyte Organoids. *Nat. Med.* **2017**, *23* (8), 954–963. https://doi.org/10.1038/nm.4360.

(122) Cheung, H.-Y.; Lau, K.-T.; Lu, T.-P.; Hui, D. A Critical Review on Polymer-Based Bio-Engineered Materials for Scaffold Development. *Compos. Part B Eng.* **2007**, *38* (3), 291–300. https://doi.org/10.1016/j.compositesb.2006.06.014.
(123) Billiet, T.; Gevaert, E.; De Schryver, T.; Cornelissen, M.; Dubruel, P. The 3D Printing of Gelatin Methacrylamide Cell-Laden Tissue-Engineered Constructs with High Cell Viability. *Biomaterials* **2014**, *35* (1), 49–62. https://doi.org/10.1016/j.biomaterials.2013.09.078.
(124) Ma, P. X.; Choi, J. W. Biodegradable Polymer Scaffolds with Well-Defined Interconnected Spherical Pore Network. *Tissue Eng.* **2001**, *7* (1), 23–33. https://doi.org/10.1089/107632701300003269.
(125) Sun, T.; Norton, D.; McKean, R. J.; Haycock, J. W.; Ryan, A. J.; MacNeil, S. Development of a 3D Cell Culture System for Investigating Cell Interactions with Electrospun Fibers. *Biotechnol. Bioeng.* **2007**, *97* (5), 1318–1328. https://doi.org/10.1002/bit.21309.
(126) Loh, Q. L.; Choong, C. Three-Dimensional Scaffolds for Tissue Engineering Applications: Role of Porosity and Pore Size. *Tissue Eng. Part B Rev.* **2013**, *19* (6), 485–502. https://doi.org/10.1089/ten.teb.2012.0437.
(127) Wise, J. K.; Yarin, A. L.; Megaridis, C. M.; Cho, M. Chondrogenic Differentiation of Human Mesenchymal Stem Cells on Oriented Nanofibrous Scaffolds: Engineering the Superficial Zone of Articular Cartilage. *Tissue Eng. Part A* **2009**, *15* (4), 913–921. https://doi.org/10.1089/ten.tea.2008.0109.
(128) Parikh, S. A.; Edelman, E. R. Endothelial Cell Delivery for Cardiovascular Therapy. *Adv. Drug Deliv. Rev.* **2000**, *42* (1–2), 139–161.
(129) Yow, K.-H.; Ingram, J.; Korossis, S. A.; Ingham, E.; Homer-Vanniasinkam, S. Tissue Engineering of Vascular Conduits. *Br. J. Surg.* **2006**, *93* (6), 652–661. https://doi.org/10.1002/bjs.5343.
(130) Villalona, G. A.; Udelsman, B.; Duncan, D. R.; McGillicuddy, E.; Sawh-Martinez, R. F.; Hibino, N.; Painter, C.; Mirensky, T.; Erickson, B.; Shinoka, T.; Breuer, C. K. Cell-Seeding Techniques in Vascular Tissue Engineering. *Tissue Eng. Part B Rev.* **2010**, *16* (3), 341–350. https://doi.org/10.1089/ten.teb.2009.0527.
(131) Tokatlian, T.; Cam, C.; Siegman, S. N.; Lei, Y.; Segura, T. Design and Characterization of Microporous Hyaluronic Acid Hydrogels for in Vitro Gene Transfer to MMSCs. *Acta Biomater.* **2012**, *8* (11), 3921–3931. https://doi.org/10.1016/j.actbio.2012.07.014.
(132) Ozbolat, I. T.; Hospodiuk, M. Current Advances and Future Perspectives in Extrusion-Based Bioprinting. *Biomaterials* **2016**, *76*, 321–343. https://doi.org/10.1016/j.biomaterials.2015.10.076.
(133) Kolesky, D. B.; Truby, R. L.; Gladman, A. S.; Busbee, T. A.; Homan, K. A.; Lewis, J. A. 3D Bioprinting of Vascularized, Heterogeneous Cell-Laden Tissue Constructs. *Adv. Mater. Deerfield Beach Fla* **2014**, *26* (19), 3124–3130. https://doi.org/10.1002/adma.201305506.
(134) Wang, L.; Shansky, J.; Borselli, C.; Mooney, D.; Vandenburgh, H. Design and Fabrication of a Biodegradable, Covalently Crosslinked Shape-Memory Alginate Scaffold for Cell and Growth Factor Delivery. *Tissue Eng. Part A* **2012**, *18* (19–20), 2000–2007. https://doi.org/10.1089/ten.TEA.2011.0663.

(135) Silva, E. A.; Kim, E.-S.; Kong, H. J.; Mooney, D. J. Material-Based Deployment Enhances Efficacy of Endothelial Progenitor Cells. *Proc. Natl. Acad. Sci.* **2008**, *105* (38), 14347–14352. https://doi.org/10.1073/pnas.0803873105.
(136) Bidarra, S. J.; Barrias, C. C.; Granja, P. L. Injectable Alginate Hydrogels for Cell Delivery in Tissue Engineering. *Acta Biomater.* **2014**, *10* (4), 1646–1662. https://doi.org/10.1016/j.actbio.2013.12.006.
(137) González-Díaz, E. C.; Varghese, S. Hydrogels as Extracellular Matrix Analogs. *Gels* **2016**, *2* (3), 20. https://doi.org/10.3390/gels2030020.
(138) Hunt, N. C.; Grover, L. M. Cell Encapsulation Using Biopolymer Gels for Regenerative Medicine. *Biotechnol. Lett.* **2010**, *32* (6), 733–742. https://doi.org/10.1007/s10529-010-0221-0.
(139) Bayoussef, Z.; Dixon, J. E.; Stolnik, S.; Shakesheff, K. M. Aggregation Promotes Cell Viability, Proliferation, and Differentiation in an in Vitro Model of Injection Cell Therapy. *J. Tissue Eng. Regen. Med.* **2012**, *6* (10), e61-73. https://doi.org/10.1002/term.482.
(140) Nicodemus, G. D.; Bryant, S. J. Cell Encapsulation in Biodegradable Hydrogels for Tissue Engineering Applications. *Tissue Eng. Part B Rev.* **2008**, *14* (2), 149–165. https://doi.org/10.1089/ten.teb.2007.0332.
(141) Living Cell Technologies. Products - DIABECELL - Development to date.
(142) Dosier, C. R.; Uhrig, B. A.; Willett, N. J.; Krishnan, L.; Li, M.-T. A.; Stevens, H. Y.; Schwartz, Z.; Boyan, B. D.; Guldberg, R. E. Effect of Cell Origin and Timing of Delivery for Stem Cell-Based Bone Tissue Engineering Using Biologically Functionalized Hydrogels. *Tissue Eng. Part A* **2014**, *21* (1–2), 156–165. https://doi.org/10.1089/ten.tea.2014.0057.
(143) Smith, T. T.; Moffett, H. F.; Stephan, S. B.; Opel, C. F.; Dumigan, A. G.; Jiang, X.; Pillarisetty, V. G.; Pillai, S. P. S.; Wittrup, K. D.; Stephan, M. T. Biopolymers Codelivering Engineered T Cells and STING Agonists Can Eliminate Heterogeneous Tumors. *J. Clin. Invest.* **2017**, *127* (6), 2176–2191. https://doi.org/10.1172/JCI87624.
(144) Kim, J.; Perez, A. S.; Claflin, J.; David, A.; Zhou, H.; Shikanov, A. Synthetic Hydrogel Supports the Function and Regeneration of Artificial Ovarian Tissue in Mice. *Npj Regen. Med.* **2016**, *1*, npjregenmed201610. https://doi.org/10.1038/npjregenmed.2016.10.
(145) Han, L.-H.; Conrad, B.; Chung, M. T.; Deveza, L.; Jiang, X.; Wang, A.; Butte, M. J.; Longaker, M. T.; Wan, D.; Yang, F. Microribbon-Based Hydrogels Accelerate Stem Cell-Based Bone Regeneration in a Mouse Critical-Size Cranial Defect Model. *J. Biomed. Mater. Res. A* **2016**, *104* (6), 1321–1331. https://doi.org/10.1002/jbm.a.35715.
(146) Crawford, D. C.; DeBerardino, T. M.; Williams, R. J. NeoCart, an Autologous Cartilage Tissue Implant, Compared with Microfracture for Treatment of Distal Femoral Cartilage Lesions: An FDA Phase-II Prospective, Randomized Clinical Trial after Two Years. *J. Bone Joint Surg. Am.* **2012**, *94* (11), 979–989. https://doi.org/10.2106/JBJS.K.00533.
(147) Huebsch, N.; Lippens, E.; Lee, K.; Mehta, M.; Koshy, S. T.; Darnell, M. C.; Desai, R.; Madl, C. M.; Xu, M.; Zhao, X.; Chaudhuri, O.; Verbeke, C.; Kim, W. S.; Alim, K.; Mammoto, A.; Ingber, D. E.; Duda, G. N.; Mooney, D. J. Matrix Elasticity of Void-Forming Hydrogels Controls Transplanted Stem Cell-Mediated Bone Formation. *Nat. Mater.* **2015**, *14* (12), 1269–1277. https://doi.org/10.1038/nmat4407.
(148) Du, C.; Narayanan, K.; Leong, M. F.; Wan, A. C. A. Induced Pluripotent Stem Cell-Derived Hepatocytes and Endothelial Cells in Multi-Component Hydrogel Fibers for Liver Tissue

Engineering. *Biomaterials* **2014**, *35* (23), 6006–6014. https://doi.org/10.1016/j.biomaterials.2014.04.011.
(149) Joosten, E. a. j.; Veldhuis, W. b.; Hamers, F. p. t. Collagen Containing Neonatal Astrocytes Stimulates Regrowth of Injured Fibers and Promotes Modest Locomotor Recovery after Spinal Cord Injury. *J. Neurosci. Res.* **2004**, *77* (1), 127–142. https://doi.org/10.1002/jnr.20088.
(150) Jha, A. K.; Tharp, K. M.; Browne, S.; Ye, J.; Stahl, A.; Yeghiazarians, Y.; Healy, K. E. Matrix Metalloproteinase-13 Mediated Degradation of Hyaluronic Acid-Based Matrices Orchestrates Stem Cell Engraftment through Vascular Integration. *Biomaterials* **2016**, *89* (Supplement C), 136–147. https://doi.org/10.1016/j.biomaterials.2016.02.023.
(151) Moshayedi, P.; Nih, L. R.; Llorente, I. L.; Berg, A. R.; Cinkornpumin, J.; Lowry, W. E.; Segura, T.; Carmichael, S. T. Systematic Optimization of an Engineered Hydrogel Allows for Selective Control of Human Neural Stem Cell Survival and Differentiation after Transplantation in the Stroke Brain. *Biomaterials* **2016**, *105* (Supplement C), 145–155. https://doi.org/10.1016/j.biomaterials.2016.07.028.
(152) Takehara, N.; Tsutsumi, Y.; Tateishi, K.; Ogata, T.; Tanaka, H.; Ueyama, T.; Takahashi, T.; Takamatsu, T.; Fukushima, M.; Komeda, M.; Yamagishi, M.; Yaku, H.; Tabata, Y.; Matsubara, H.; Oh, H. Controlled Delivery of Basic Fibroblast Growth Factor Promotes Human Cardiosphere-Derived Cell Engraftment to Enhance Cardiac Repair for Chronic Myocardial Infarction. *J. Am. Coll. Cardiol.* **2008**, *52* (23), 1858–1865. https://doi.org/10.1016/j.jacc.2008.06.052.
(153) Nguyen, M. K.; Jeon, O.; Krebs, M. D.; Schapira, D.; Alsberg, E. Sustained Localized Presentation of RNA Interfering Molecules from in Situ Forming Hydrogels to Guide Stem Cell Osteogenic Differentiation. *Biomaterials* **2014**, *35* (24), 6278–6286. https://doi.org/10.1016/j.biomaterials.2014.04.048.
(154) Mulyasasmita, W.; Cai, L.; Dewi, R. E.; Jha, A.; Ullmann, S. D.; Luong, R. H.; Huang, N. F.; Heilshorn, S. C. Avidity-Controlled Hydrogels for Injectable Co-Delivery of Induced Pluripotent Stem Cell-Derived Endothelial Cells and Growth Factors. *J. Controlled Release* **2014**, *191*, 71–81. https://doi.org/10.1016/j.jconrel.2014.05.015.
(155) Mayfield, A. E.; Tilokee, E. L.; Latham, N.; McNeill, B.; Lam, B.-K.; Ruel, M.; Suuronen, E. J.; Courtman, D. W.; Stewart, D. J.; Davis, D. R. The Effect of Encapsulation of Cardiac Stem Cells within Matrix-Enriched Hydrogel Capsules on Cell Survival, Post-Ischemic Cell Retention and Cardiac Function. *Biomaterials* **2014**, *35* (1), 133–142. https://doi.org/10.1016/j.biomaterials.2013.09.085.
(156) Menasché, P.; Vanneaux, V.; Hagège, A.; Bel, A.; Cholley, B.; Cacciapuoti, I.; Parouchev, A.; Benhamouda, N.; Tachdjian, G.; Tosca, L.; Trouvin, J.-H.; Fabreguettes, J.-R.; Bellamy, V.; Guillemain, R.; Suberbielle Boissel, C.; Tartour, E.; Desnos, M.; Larghero, J. Human Embryonic Stem Cell-Derived Cardiac Progenitors for Severe Heart Failure Treatment: First Clinical Case Report. *Eur. Heart J.* **2015**, *36* (30), 2011–2017. https://doi.org/10.1093/eurheartj/ehv189.
(157) Alexaki, V.-I.; Simantiraki, D.; Panayiotopoulou, M.; Rasouli, O.; Venihaki, M.; Castana, O.; Alexakis, D.; Kampa, M.; Stathopoulos, E. N.; Castanas, E. Adipose Tissue-Derived Mesenchymal Cells Support Skin Reepithelialization through Secretion of KGF-1 and

PDGF-BB: Comparison with Dermal Fibroblasts. *Cell Transplant.* **2012**, *21* (11), 2441–2454. https://doi.org/10.3727/096368912X637064.

(158) Vegas, A. J.; Veiseh, O.; Doloff, J. C.; Ma, M.; Tam, H. H.; Bratlie, K.; Li, J.; Bader, A. R.; Langan, E.; Olejnik, K.; Fenton, P.; Kang, J. W.; Hollister-Locke, J.; Bochenek, M. A.; Chiu, A.; Siebert, S.; Tang, K.; Jhunjhunwala, S.; Aresta-Dasilva, S.; Dholakia, N.; Thakrar, R.; Vietti, T.; Chen, M.; Cohen, J.; Siniakowicz, K.; Qi, M.; McGarrigle, J.; Graham, A. C.; Lyle, S.; Harlan, D. M.; Greiner, D. L.; Oberholzer, J.; Weir, G. C.; Langer, R.; Anderson, D. G. Combinatorial Hydrogel Library Enables Identification of Materials That Mitigate the Foreign Body Response in Primates. *Nat. Biotechnol.* **2016**, *34* (3), 345–352. https://doi.org/10.1038/nbt.3462.

(159) Passemard, S.; Szabó, L.; Noverraz, F.; Montanari, E.; Gonelle-Gispert, C.; Bühler, L. H.; Wandrey, C.; Gerber-Lemaire, S. Synthesis Strategies to Extend the Variety of Alginate-Based Hybrid Hydrogels for Cell Microencapsulation. *Biomacromolecules* **2017**, *18* (9), 2747–2755. https://doi.org/10.1021/acs.biomac.7b00665.

(160) Gattás-Asfura, K. M.; Stabler, C. L. Chemoselective Cross-Linking and Functionalization of Alginate via Staudinger Ligation. *Biomacromolecules* **2009**, *10* (11), 3122–3129. https://doi.org/10.1021/bm900789a.

(161) Veiseh, O.; Doloff, J. C.; Ma, M.; Vegas, A. J.; Tam, H. H.; Bader, A. R.; Li, J.; Langan, E.; Wyckoff, J.; Loo, W. S.; Jhunjhunwala, S.; Chiu, A.; Siebert, S.; Tang, K.; Hollister-Lock, J.; Aresta-Dasilva, S.; Bochenek, M.; Mendoza-Elias, J.; Wang, Y.; Qi, M.; Lavin, D. M.; Chen, M.; Dholakia, N.; Thakrar, R.; Lacík, I.; Weir, G. C.; Oberholzer, J.; Greiner, D. L.; Langer, R.; Anderson, D. G. Size- and Shape-Dependent Foreign Body Immune Response to Materials Implanted in Rodents and Non-Human Primates. *Nat. Mater.* **2015**, *14* (6), 643–651. https://doi.org/10.1038/nmat4290.

(162) Tuch, B. E.; Keogh, G. W.; Williams, L. J.; Wu, W.; Foster, J. L.; Vaithilingam, V.; Philips, R. Safety and Viability of Microencapsulated Human Islets Transplanted into Diabetic Humans. *Diabetes Care* **2009**, *32* (10), 1887–1889. https://doi.org/10.2337/dc09-0744.

(163) Hwang, P. T. J.; Shah, D. K.; Garcia, J. A.; Bae, C. Y.; Lim, D.-J.; Huiszoon, R. C.; Alexander, G. C.; Jun, H.-W. Progress and Challenges of the Bioartificial Pancreas. *Nano Converg.* **2016**, *3* (1), 28. https://doi.org/10.1186/s40580-016-0088-4.

(164) Boettler, T.; Schneider, D.; Cheng, Y.; Kadoya, K.; Brandon, E. P.; Martinson, L.; Von Herrath, M. Pancreatic Tissue Transplanted in TheraCyte™ Encapsulation Devices Is Protected and Prevents Hyperglycemia in a Mouse Model of Immune-Mediated Diabetes. *Cell Transplant.* **2016**, *25* (3), 609–614. https://doi.org/10.3727/096368915X688939.

(165) US National Library of Medicine. A Safety, Tolerability, and Efficacy Study of VC-01™ Combination Product in Subjects With Type I Diabetes Mellitus - No Study Results Posted - ClinicalTrials.gov.

(166) Schweicher, J.; Nyitray, C.; Desai, T. A. Membranes to Achieve Immunoprotection of Transplanted Islets. *Front. Biosci. Landmark Ed.* **2014**, *19*, 49–76.

(167) Wee, null; Gombotz, null. Protein Release from Alginate Matrices. *Adv. Drug Deliv. Rev.* **1998**, *31* (3), 267–285.

(168) Orive, G.; Tam, S. K.; Pedraz, J. L.; Hallé, J.-P. Biocompatibility of Alginate-Poly-L-Lysine Microcapsules for Cell Therapy. *Biomaterials* **2006**, *27* (20), 3691–3700. https://doi.org/10.1016/j.biomaterials.2006.02.048.
(169) Günther, M. I.; Weidner, N.; Müller, R.; Blesch, A. Cell-Seeded Alginate Hydrogel Scaffolds Promote Directed Linear Axonal Regeneration in the Injured Rat Spinal Cord. *Acta Biomater.* **2015**, *27*, 140–150. https://doi.org/10.1016/j.actbio.2015.09.001.
(170) Qiao, S.; Liu, Y.; Han, F.; Guo, M.; Hou, X.; Ye, K.; Deng, S.; Shen, Y.; Zhao, Y.; Wei, H.; Song, B.; Yao, L.; Tian, W. An Intelligent Neural Stem Cell Delivery System for Neurodegenerative Diseases Treatment. *Adv. Healthc. Mater.* **2018**, e1800080–e1800080. https://doi.org/10.1002/adhm.201800080.
(171) Desai, T.; Shea, L. D. Advances in Islet Encapsulation Technologies. *Nat. Rev. Drug Discov.* **2016**, *advance on*. https://doi.org/10.1038/nrd.2016.232.
(172) Rokstad, A. M.; Brekke, O.-L.; Steinkjer, B.; Ryan, L.; Kolláriková, G.; Strand, B. L.; Skjåk-Bræk, G.; Lacík, I.; Espevik, T.; Mollnes, T. E. Alginate Microbeads Are Complement Compatible, in Contrast to Polycation Containing Microcapsules, as Revealed in a Human Whole Blood Model. *Acta Biomater.* **2011**, *7* (6), 2566–2578. https://doi.org/10.1016/j.actbio.2011.03.011.
(173) Rokstad, A. M.; Brekke, O.-L.; Steinkjer, B.; Ryan, L.; Kolláriková, G.; Strand, B. L.; Skjåk-Bræk, G.; Lambris, J. D.; Lacík, I.; Mollnes, T. E.; Espevik, T. The Induction of Cytokines by Polycation Containing Microspheres by a Complement Dependent Mechanism. *Biomaterials* **2013**, *34* (3), 621–630. https://doi.org/10.1016/j.biomaterials.2012.10.012.
(174) Jacobs-Tulleneers-Thevissen, D.; Chintinne, M.; Ling, Z.; Gillard, P.; Schoonjans, L.; Delvaux, G.; Strand, B. L.; Gorus, F.; Keymeulen, B.; Pipeleers, D. Sustained Function of Alginate-Encapsulated Human Islet Cell Implants in the Peritoneal Cavity of Mice Leading to a Pilot Study in a Type 1 Diabetic Patient. *Diabetologia* **2013**, *56* (7), 1605–1614. https://doi.org/10.1007/s00125-013-2906-0.
(175) Tuch, B. E.; Keogh, G. W.; Williams, L. J.; Wu, W.; Foster, J. L.; Vaithilingam, V.; Philips, R. Safety and Viability of Microencapsulated Human Islets Transplanted into Diabetic Humans. *Diabetes Care* **2009**, *32* (10), 1887–1889. https://doi.org/10.2337/dc09-0744.
(176) Veiseh, O.; Doloff, J. C.; Ma, M.; Vegas, A. J.; Tam, H. H.; Bader, A. R.; Li, J.; Langan, E.; Wyckoff, J.; Loo, W. S.; Jhunjhunwala, S.; Chiu, A.; Siebert, S.; Tang, K.; Hollister-Lock, J.; Aresta-Dasilva, S.; Bochenek, M.; Mendoza-Elias, J.; Wang, Y.; Qi, M.; Lavin, D. M.; Chen, M.; Dholakia, N.; Thakrar, R.; Lacík, I.; Weir, G. C.; Oberholzer, J.; Greiner, D. L.; Langer, R.; Anderson, D. G. Size- and Shape-Dependent Foreign Body Immune Response to Materials Implanted in Rodents and Non-Human Primates. *Nat. Mater.* **2015**, *14* (6), 643–651. https://doi.org/10.1038/nmat4290.
(177) Gattás-Asfura, K. M.; Stabler, C. L. Chemoselective Cross-Linking and Functionalization of Alginate via Staudinger Ligation. *Biomacromolecules* **2009**, *10* (11), 3122–3129. https://doi.org/10.1021/bm900789a.
(178) Passemard, S.; Szabó, L.; Noverraz, F.; Montanari, E.; Gonelle-Gispert, C.; Bühler, L. H.; Wandrey, C.; Gerber-Lemaire, S. Synthesis Strategies to Extend the Variety of Alginate-Based Hybrid Hydrogels for Cell Microencapsulation. *Biomacromolecules* **2017**, *18* (9), 2747–2755. https://doi.org/10.1021/acs.biomac.7b00665.

(179) Vegas, A. J.; Veiseh, O.; Doloff, J. C.; Ma, M.; Tam, H. H.; Bratlie, K.; Li, J.; Bader, A. R.; Langan, E.; Olejnik, K.; Fenton, P.; Kang, J. W.; Hollister-Locke, J.; Bochenek, M. A.; Chiu, A.; Siebert, S.; Tang, K.; Jhunjhunwala, S.; Aresta-Dasilva, S.; Dholakia, N.; Thakrar, R.; Vietti, T.; Chen, M.; Cohen, J.; Siniakowicz, K.; Qi, M.; McGarrigle, J.; Lyle, S.; Harlan, D. M.; Greiner, D. L.; Oberholzer, J.; Weir, G. C.; Langer, R.; Anderson, D. G. Combinatorial Hydrogel Library Enables Identification of Materials That Mitigate the Foreign Body Response in Primates. *Nat. Biotechnol.* **2016**, *34* (3), 345–352. https://doi.org/10.1038/nbt.3462.

(180) Vegas, A. J.; Veiseh, O.; Gürtler, M.; Millman, J. R.; Pagliuca, F. W.; Bader, A. R.; Doloff, J. C.; Li, J.; Chen, M.; Olejnik, K.; Tam, H. H.; Jhunjhunwala, S.; Langan, E.; Aresta-Dasilva, S.; Gandham, S.; McGarrigle, J. J.; Bochenek, M. A.; Hollister-Lock, J.; Oberholzer, J.; Greiner, D. L.; Weir, G. C.; Melton, D. A.; Langer, R.; Anderson, D. G. Long-Term Glycemic Control Using Polymer-Encapsulated Human Stem Cell-Derived Beta Cells in Immune-Competent Mice. *Nat. Med.* **2016**, *22* (3), 306–311. https://doi.org/10.1038/nm.4030.

(181) Manzoli, V.; Villa, C.; Bayer, A. L.; Morales, L. C.; Molano, R. D.; Torrente, Y.; Ricordi, C.; Hubbell, J. A.; Tomei, A. A. Immunoisolation of Murine Islet Allografts in Vascularized Sites through Conformal Coating with Polyethylene Glycol. *Am. J. Transplant.* n/a-n/a. https://doi.org/10.1111/ajt.14547.

(182) Shikanov, A.; Smith, R. M.; Xu, M.; Woodruff, T. K.; Shea, L. D. Hydrogel Network Design Using Multifunctional Macromers to Coordinate Tissue Maturation in Ovarian Follicle Culture. *Biomaterials* **2011**, *32* (10), 2524–2531. https://doi.org/10.1016/j.biomaterials.2010.12.027.

(183) Khansari, M. M.; Sorokina, L. V.; Mukherjee, P.; Mukhtar, F.; Shirdar, M. R.; Shahidi, M.; Shokuhfar, T. Classification of Hydrogels Based on Their Source: A Review and Application in Stem Cell Regulation. *JOM* **2017**, *69* (8), 1340–1347. https://doi.org/10.1007/s11837-017-2412-9.

(184) David, A.; Day, J.; Shikanov, A. Immunoisolation to Prevent Tissue Graft Rejection: Current Knowledge and Future Use. *Exp. Biol. Med.* **2016**, *241* (9), 955–961. https://doi.org/10.1177/1535370216647129.

(185) Rios, P. D.; Zhang, X.; Luo, X.; Shea, L. D. Mold-Casted Non-Degradable, Islet Macro-Encapsulating Hydrogel Devices for Restoration of Normoglycemia in Diabetic Mice. *Biotechnol. Bioeng.* **2016**, *113* (11), 2485–2495. https://doi.org/10.1002/bit.26005.

(186) Lovett, M.; Lee, K.; Edwards, A.; Kaplan, D. L. Vascularization Strategies for Tissue Engineering. *Tissue Eng. Part B Rev.* **2009**, *15* (3), 353–370. https://doi.org/10.1089/ten.teb.2009.0085.

(187) Rouwkema, J.; Boer, J. De; Blitterswijk, C. A. Van. Endothelial Cells Assemble into a 3-Dimensional Prevascular Network in a Bone Tissue Engineering Construct. *Tissue Eng.* **2006**, *12* (9), 2685–2693. https://doi.org/10.1089/ten.2006.12.2685.

(188) Duan, Y.; Liu, Z.; O'Neill, J.; Wan, L. Q.; Freytes, D. O.; Vunjak-Novakovic, G. Hybrid Gel Composed of Native Heart Matrix and Collagen Induces Cardiac Differentiation of Human Embryonic Stem Cells without Supplemental Growth Factors. *J Cardiovasc. Transl. Res.* **2011**, *4* (5), 605–615. https://doi.org/10.1007/s12265-011-9304-0.

(189) El-Sherbiny, I. M.; Yacoub, M. H. Hydrogel Scaffolds for Tissue Engineering: Progress and Challenges. *Glob. Cardiol. Sci. Pract.* **2013**, *2013* (3), 316–342. https://doi.org/10.5339/gcsp.2013.38.
(190) Ahn, G.; Park, J. H.; Kang, T.; Lee, J. W.; Kang, H.-W.; Cho, D.-W. Effect of Pore Architecture on Oxygen Diffusion in 3D Scaffolds for Tissue Engineering. *J. Biomech. Eng.* **2010**, *132* (10), 104506. https://doi.org/10.1115/1.4002429.
(191) Malda, J.; Klein, T. J.; Upton, Z. The Roles of Hypoxia in the in Vitro Engineering of Tissues. *Tissue Eng.* **2007**, *13* (9), 2153–2162. https://doi.org/10.1089/ten.2006.0417.
(192) Wang, C.; Varshney, R. R.; Wang, D.-A. Therapeutic Cell Delivery and Fate Control in Hydrogels and Hydrogel Hybrids. *Adv. Drug Deliv. Rev.* **2010**, *62* (7–8), 699–710. https://doi.org/10.1016/j.addr.2010.02.001.
(193) Naganuma, T.; Traversa, E. The Effect of Cerium Valence States at Cerium Oxide Nanoparticle Surfaces on Cell Proliferation. *Biomaterials* **2014**, *35* (15), 4441–4453. https://doi.org/10.1016/j.biomaterials.2014.01.074.
(194) Sokic, S.; Christenson, M.; Larson, J.; Papavasiliou, G. In Situ Generation of Cell-Laden Porous MMP-Sensitive PEGDA Hydrogels by Gelatin Leaching. *Macromol. Biosci.* **2014**, *14* (5), 731–739. https://doi.org/10.1002/mabi.201300406.
(195) Dye, B. R.; Dedhia, P. H.; Miller, A. J.; Nagy, M. S.; White, E. S.; Shea, L. D.; Spence, J. R. A Bioengineered Niche Promotes in Vivo Engraftment and Maturation of Pluripotent Stem Cell Derived Human Lung Organoids. *eLife* **2016**, *5*, e19732. https://doi.org/10.7554/eLife.19732.
(196) Aurora, M.; Spence, J. R. HPSC-Derived Lung and Intestinal Organoids as Models of Human Fetal Tissue. *Dev. Biol.* **2016**, *420* (2), 230–238. https://doi.org/10.1016/j.ydbio.2016.06.006.
(197) Schlieve, C. R.; Fowler, K. L.; Thornton, M.; Huang, S.; Hajjali, I.; Hou, X.; Grubbs, B.; Spence, J. R.; Grikscheit, T. C. Neural Crest Cell Implantation Restores Enteric Nervous System Function and Alters the Gastrointestinal Transcriptome in Human Tissue-Engineered Small Intestine. *Stem Cell Rep.* **2017**, *9* (3), 883–896. https://doi.org/10.1016/j.stemcr.2017.07.017.
(198) Holloway, E. M.; Capeling, M. M.; Spence, J. R. Biologically Inspired Approaches to Enhance Human Organoid Complexity. *Development* **2019**, *146* (8). https://doi.org/10.1242/dev.166173.
(199) Sivashanmugam, A.; Arun Kumar, R.; Vishnu Priya, M.; Nair, S. V.; Jayakumar, R. An Overview of Injectable Polymeric Hydrogels for Tissue Engineering. *Eur. Polym. J.* **2015**, *72* (Supplement C), 543–565. https://doi.org/10.1016/j.eurpolymj.2015.05.014.
(200) Sideris, E.; Griffin, D. R.; Ding, Y.; Li, S.; Weaver, W. M.; Di Carlo, D.; Hsiai, T.; Segura, T. Particle Hydrogels Based on Hyaluronic Acid Building Blocks. *ACS Biomater. Sci. Eng.* **2016**, *2* (11), 2034–2041. https://doi.org/10.1021/acsbiomaterials.6b00444.
(201) Griffin, D. R.; Weaver, W. M.; Scumpia, P. O.; Di Carlo, D.; Segura, T. Accelerated Wound Healing by Injectable Microporous Gel Scaffolds Assembled from Annealed Building Blocks. *Nat. Mater.* **2015**, *14* (7), 737–744. https://doi.org/10.1038/nmat4294.
(202) Nih, L. R.; Sideris, E.; Carmichael, S. T.; Segura, T. Injection of Microporous Annealing Particle (MAP) Hydrogels in the Stroke Cavity Reduces Gliosis and Inflammation and

Promotes NPC Migration to the Lesion. *Adv. Mater.* **2017**, *29* (32), 1606471. https://doi.org/10.1002/adma.201606471.
(203) Mealy, J. E.; Chung, J. J.; Jeong, H.-H.; Issadore, D.; Lee, D.; Atluri, P.; Burdick, J. A. Injectable Granular Hydrogels with Multifunctional Properties for Biomedical Applications. *Adv. Mater. 30* (20), 1705912. https://doi.org/10.1002/adma.201705912.
(204) Wang, L.; Lu, S.; Lam, J.; Kasper, F. K.; Mikos, A. G. Fabrication of Cell-Laden Macroporous Biodegradable Hydrogels with Tunable Porosities and Pore Sizes. *Tissue Eng. Part C Methods* **2015**, *21* (3), 263–273. https://doi.org/10.1089/ten.TEC.2014.0224.
(205) Huang, B. J.; Hu, J. C.; Athanasiou, K. A. Cell-Based Tissue Engineering Strategies Used in the Clinical Repair of Articular Cartilage. *Biomaterials* **2016**, *98*, 1–22. https://doi.org/10.1016/j.biomaterials.2016.04.018.
(206) Lee, Y. H. D.; Suzer, F.; Thermann, H. Autologous Matrix-Induced Chondrogenesis in the Knee: A Review. *Cartilage* **2014**, *5* (3), 145–153. https://doi.org/10.1177/1947603514529445.
(207) Corporation, H. Histogenics Completes Enrollment for Phase 3 Clinical Trial of Neocart® to Treat Knee Cartilage Damage.
(208) Khetan, S.; Guvendiren, M.; Legant, W. R.; Cohen, D. M.; Chen, C. S.; Burdick, J. A. Degradation-Mediated Cellular Traction Directs Stem Cell Fate in Covalently Crosslinked Three-Dimensional Hydrogels. *Nat. Mater.* **2013**, *12* (5), 458–465. https://doi.org/10.1038/nmat3586.
(209) Caliari, S. R.; Burdick, J. A. A Practical Guide to Hydrogels for Cell Culture. *Nat. Methods* **2016**, *13* (5), 405–414. https://doi.org/10.1038/nmeth.3839.
(210) Lima, A. C.; Batista, P.; Valente, T. A. M.; Silva, A. S.; Correia, I. J.; Mano, J. F. Novel Methodology Based on Biomimetic Superhydrophobic Substrates to Immobilize Cells and Proteins in Hydrogel Spheres for Applications in Bone Regeneration. *Tissue Eng. Part A* **2012**, *19* (9–10), 1175–1187. https://doi.org/10.1089/ten.tea.2012.0249.
(211) Zhu, J.; Marchant, R. E. Design Properties of Hydrogel Tissue-Engineering Scaffolds. *Expert Rev. Med. Devices* **2011**, *8* (5), 607–626. https://doi.org/10.1586/erd.11.27.
(212) Burdick, J. A.; Chung, C.; Jia, X.; Randolph, M. A.; Langer, R. Controlled Degradation and Mechanical Behavior of Photopolymerized Hyaluronic Acid Networks. *Biomacromolecules* **2005**, *6* (1), 386–391. https://doi.org/10.1021/bm049508a.
(213) Lei, Y.; Gojgini, S.; Lam, J.; Segura, T. The Spreading, Migration and Proliferation of Mouse Mesenchymal Stem Cells Cultured inside Hyaluronic Acid Hydrogels. *Biomaterials* **2011**, *32* (1), 39–47. https://doi.org/10.1016/j.biomaterials.2010.08.103.
(214) Gojgini, S.; Tokatlian, T.; Segura, T. Utilizing Cell-Matrix Interactions to Modulate Gene Transfer to Stem Cells inside Hyaluronic Acid Hydrogels. *Mol. Pharm.* **2011**, *8* (5), 1582–1591. https://doi.org/10.1021/mp200171d.
(215) Lutolf, M. P.; Lauer-Fields, J. L.; Schmoekel, H. G.; Metters, a T.; Weber, F. E.; Fields, G. B.; Hubbell, J. a. Synthetic Matrix Metalloproteinase-Sensitive Hydrogels for the Conduction of Tissue Regeneration: Engineering Cell-Invasion Characteristics. *Proc. Natl. Acad. Sci. U. S. A.* **2003**, *100* (9), 5413–5418. https://doi.org/10.1073/pnas.0737381100.
(216) Sridhar, B. V.; Brock, J. L.; Silver, J. S.; Leight, J. L.; Randolph, M. A.; Anseth, K. S. Development of a Cellularly Degradable PEG Hydrogel to Promote Articular Cartilage

Extracellular Matrix Deposition. *Adv. Healthc. Mater.* **2015**, *4* (5), 702–713. https://doi.org/10.1002/adhm.201400695.
(217) Athanasiou, K. A.; Darling, E. M.; Hu, J. C. Articular Cartilage Tissue Engineering. *Synth. Lect. Tissue Eng.* **2009**, *1* (1), 1–182. https://doi.org/10.2200/S00212ED1V01Y200910TIS003.
(218) Weaver, J. D.; Headen, D. M.; Aquart, J.; Johnson, C. T.; Shea, L. D.; Shirwan, H.; García, A. J. Vasculogenic Hydrogel Enhances Islet Survival, Engraftment, and Function in Leading Extrahepatic Sites. *Sci. Adv.* **2017**, *3* (6), e1700184. https://doi.org/10.1126/sciadv.1700184.
(219) McKenzie, M.; Betts, D.; Suh, A.; Bui, K.; Kim, L. D.; Cho, H. Hydrogel-Based Drug Delivery Systems for Poorly Water-Soluble Drugs. *Mol. Basel Switz.* **2015**, *20* (11), 20397–20408. https://doi.org/10.3390/molecules201119705.
(220) Kondiah, P. J.; Choonara, Y. E.; Kondiah, P. P. D.; Marimuthu, T.; Kumar, P.; du Toit, L. C.; Pillay, V. A Review of Injectable Polymeric Hydrogel Systems for Application in Bone Tissue Engineering. *Molecules* **2016**, *21* (11), 1580. https://doi.org/10.3390/molecules21111580.
(221) Gutowska, A.; Jeong, B.; Jasionowski, M. Injectable Gels for Tissue Engineering. *Anat. Rec.* **2001**, *263* (4), 342–349.
(222) Jones, D. S.; Andrews, G. P.; Caldwell, D. L.; Lorimer, C.; Gorman, S. P.; McCoy, C. P. Novel Semi-Interpenetrating Hydrogel Networks with Enhanced Mechanical Properties and Thermoresponsive Engineered Drug Delivery, Designed as Bioactive Endotracheal Tube Biomaterials. *Eur. J. Pharm. Biopharm. Off. J. Arbeitsgemeinschaft Pharm. Verfahrenstechnik EV* **2012**, *82* (3), 563–571. https://doi.org/10.1016/j.ejpb.2012.07.019.
(223) Wintgens, V.; Amiel, C. Physical Gelation of Amphiphilic Poly(N-Isopropylacrylamide): Influence of the Hydrophobic Groups. *Macromol. Chem. Phys.* **2008**, *209* (15), 1553–1563. https://doi.org/10.1002/macp.200800093.
(224) Li, X.; Zhou, J.; Liu, Z.; Chen, J.; Lü, S.; Sun, H.; Li, J.; Lin, Q.; Yang, B.; Duan, C.; Xing, M. (Mengqiu); Wang, C. A PNIPAAm-Based Thermosensitive Hydrogel Containing SWCNTs for Stem Cell Transplantation in Myocardial Repair. *Biomaterials* **2014**, *35* (22), 5679–5688. https://doi.org/10.1016/j.biomaterials.2014.03.067.
(225) Gaffey, A. C.; Chen, M. H.; Venkataraman, C. M.; Trubelja, A.; Rodell, C. B.; Dinh, P. V.; Hung, G.; MacArthur, J. W.; Soopan, R. V.; Burdick, J. A.; Atluri, P. Injectable Shear-Thinning Hydrogels Used to Deliver Endothelial Progenitor Cells, Enhance Cell Engraftment, and Improve Ischemic Myocardium. *J. Thorac. Cardiovasc. Surg.* **2015**, *150* (5), 1268–1276. https://doi.org/10.1016/j.jtcvs.2015.07.035.
(226) Weaver, J. D.; Headen, D. M.; Aquart, J.; Johnson, C. T.; Shea, L. D.; Shirwan, H.; García, A. J. Vasculogenic Hydrogel Enhances Islet Survival, Engraftment, and Function in Leading Extrahepatic Sites. *Sci. Adv.* **2017**, *3* (6), e1700184. https://doi.org/10.1126/sciadv.1700184.
(227) Xu, Y.; Fu, M.; Li, Z.; Fan, Z.; Li, X.; Liu, Y.; Anderson, P. M.; Xie, X.; Liu, Z.; Guan, J. A Prosurvival and Proangiogenic Stem Cell Delivery System to Promote Ischemic Limb Regeneration. *Acta Biomater.* **2016**, *31*, 99–113. https://doi.org/10.1016/j.actbio.2015.12.021.

(228) Cui, H.; Webber, M. J.; Stupp, S. I. Self-Assembly of Peptide Amphiphiles: From Molecules to Nanostructures to Biomaterials. *Biopolymers* **2010**, *94* (1), 1–18. https://doi.org/10.1002/bip.21328.
(229) Moore, A. N.; Hartgerink, J. D. Self-Assembling Multidomain Peptide Nanofibers for Delivery of Bioactive Molecules and Tissue Regeneration. *Acc. Chem. Res.* **2017**, *50* (4), 714–722. https://doi.org/10.1021/acs.accounts.6b00553.
(230) Lee, J.-E.; Park, J.-C.; Lee, K. H.; Oh, S. H.; Suh, H. Laminin Modified Infection-Preventing Collagen Membrane Containing Silver Sulfadiazine-Hyaluronan Microparticles. *Artif. Organs* **2002**, *26* (6), 521–528. https://doi.org/10.1046/j.1525-1594.2002.06890.x.
(231) Huebsch, N.; Lippens, E.; Lee, K.; Mehta, M.; Koshy, S. T.; Darnell, M. C.; Desai, R.; Madl, C. M.; Xu, M.; Zhao, X.; Chaudhuri, O.; Verbeke, C.; Kim, W. S.; Alim, K.; Mammoto, A.; Ingber, D. E.; Duda, G. N.; Mooney, D. J. Matrix Elasticity of Void-Forming Hydrogels Controls Transplanted Stem Cell-Mediated Bone Formation. *Nat. Mater.* **2015**, *14* (12), 1269–1277. https://doi.org/10.1038/nmat4407.
(232) Kim, J.; Perez, A. S.; Claflin, J.; David, A.; Zhou, H.; Shikanov, A. Synthetic Hydrogel Supports the Function and Regeneration of Artificial Ovarian Tissue in Mice. *Npj Regen. Med.* **2016**, *1* (1), 1–8. https://doi.org/10.1038/npjregenmed.2016.10.
(233) Moshayedi, P.; Nih, L. R.; Llorente, I. L.; Berg, A. R.; Cinkornpumin, J.; Lowry, W. E.; Segura, T.; Carmichael, S. T. Systematic Optimization of an Engineered Hydrogel Allows for Selective Control of Human Neural Stem Cell Survival and Differentiation after Transplantation in the Stroke Brain. *Biomaterials* **2016**, *105*, 145–155. https://doi.org/10.1016/j.biomaterials.2016.07.028.
(234) Jha, A. K.; Tharp, K. M.; Browne, S.; Ye, J.; Stahl, A.; Yeghiazarians, Y.; Healy, K. E. Matrix Metalloproteinase-13 Mediated Degradation of Hyaluronic Acid-Based Matrices Orchestrates Stem Cell Engraftment through Vascular Integration. *Biomaterials* **2016**, *89*, 136–147. https://doi.org/10.1016/j.biomaterials.2016.02.023.
(235) Joosten, E. a. J.; Veldhuis, W. B.; Hamers, F. P. T. Collagen Containing Neonatal Astrocytes Stimulates Regrowth of Injured Fibers and Promotes Modest Locomotor Recovery after Spinal Cord Injury. *J. Neurosci. Res.* **2004**, *77* (1), 127–142. https://doi.org/10.1002/jnr.20088.
(236) Du, C.; Narayanan, K.; Leong, M. F.; Wan, A. C. A. Induced Pluripotent Stem Cell-Derived Hepatocytes and Endothelial Cells in Multi-Component Hydrogel Fibers for Liver Tissue Engineering. *Biomaterials* **2014**, *35* (23), 6006–6014. https://doi.org/10.1016/j.biomaterials.2014.04.011.
(237) Dziki, J. L.; Badylak, S. F. Immunomodulatory Biomaterials. *Curr. Opin. Biomed. Eng.* **2018**, *6*, 51–57. https://doi.org/10.1016/j.cobme.2018.02.005.
(238) Meissner, T.; Strominger, J.; Cowan, C. The Universal Donor Stem Cell: Removing the Immune Barrier to Transplantation Using CRISPR/Cas9 (TRAN1P.946). *J. Immunol.* **2015**, *194* (1 Supplement), 140.28-140.28.
(239) Centers for Disease Control and Prevention 2017 Diabetes Report Card. *CDC* **2015**, 16.
(240) Daneman, D. Type 1 Diabetes. *Lancet Lond. Engl.* **2006**, *367* (9513), 847–858. https://doi.org/10.1016/S0140-6736(06)68341-4.

(241) Tiwari, N.; Thakur, A. K.; Kumar, V.; Dey, A.; Kumar, V. Therapeutic Targets for Diabetes Mellitus: An Update. *Clin. Pharmacol. Biopharm.* **2014**, *3* (1). https://doi.org/10.4172/2167-065X.1000117.

(242) Pambianco, G.; Costacou, T.; Ellis, D.; Becker, D. J.; Klein, R.; Orchard, T. J. The 30-Year Natural History of Type 1 Diabetes Complications: The Pittsburgh Epidemiology of Diabetes Complications Study Experience. *Diabetes* **2006**, *55* (5), 1463–1469. https://doi.org/10.2337/db05-1423.

(243) Bittencourt, M. S.; Hajjar, L. A. Insulin Therapy in Insulin Resistance: Could It Be Part of a Lethal Pathway? *Atherosclerosis* **2015**, *240* (2), 400–401. https://doi.org/10.1016/j.atherosclerosis.2015.04.013.

(244) Kalra, S.; Mukherjee, J. J.; Venkataraman, S.; Bantwal, G.; Shaikh, S.; Saboo, B.; Das, A. K.; Ramachandran, A. Hypoglycemia: The Neglected Complication. *Indian J. Endocrinol. Metab.* **2013**, *17* (5), 819–834. https://doi.org/10.4103/2230-8210.117219.

(245) Ryan, E. A.; Paty, B. W.; Senior, P. A.; Bigam, D.; Alfadhli, E.; Kneteman, N. M.; Lakey, J. R. T.; Shapiro, A. M. J. Five-Year Follow-up after Clinical Islet Transplantation. *Diabetes* **2005**, *54* (7), 2060–2069. https://doi.org/10.2337/diabetes.54.7.2060.

(246) Shapiro, A. M. J.; Ricordi, C.; Hering, B. J.; Auchincloss, H.; Lindblad, R.; Robertson, R. P.; Secchi, A.; Brendel, M. D.; Berney, T.; Brennan, D. C.; Cagliero, E.; Alejandro, R.; Ryan, E. A.; DiMercurio, B.; Morel, P.; Polonsky, K. S.; Reems, J.-A.; Bretzel, R. G.; Bertuzzi, F.; Froud, T.; Kandaswamy, R.; Sutherland, D. E. R.; Eisenbarth, G.; Segal, M.; Preiksaitis, J.; Korbutt, G. S.; Barton, F. B.; Viviano, L.; Seyfert-Margolis, V.; Bluestone, J.; Lakey, J. R. T. International Trial of the Edmonton Protocol for Islet Transplantation. *N. Engl. J. Med.* **2006**, *355* (13), 1318–1330. https://doi.org/10.1056/NEJMoa061267.

(247) Hering, B. J.; Clarke, W. R.; Bridges, N. D.; Eggerman, T. L.; Alejandro, R.; Bellin, M. D.; Chaloner, K.; Czarniecki, C. W.; Goldstein, J. S.; Hunsicker, L. G.; Kaufman, D. B.; Korsgren, O.; Larsen, C. P.; Luo, X.; Markmann, J. F.; Naji, A.; Oberholzer, J.; Posselt, A. M.; Rickels, M. R.; Ricordi, C.; Robien, M. A.; Senior, P. A.; Shapiro, A. M. J.; Stock, P. G.; Turgeon, N. A.; Clinical Islet Transplantation Consortium. Phase 3 Trial of Transplantation of Human Islets in Type 1 Diabetes Complicated by Severe Hypoglycemia. *Diabetes Care* **2016**, *39* (7), 1230–1240. https://doi.org/10.2337/dc15-1988.

(248) Brennan, D. C.; Kopetskie, H. A.; Sayre, P. H.; Alejandro, R.; Cagliero, E.; Shapiro, A. M. J.; Goldstein, J. S.; DesMarais, M. R.; Booher, S.; Bianchine, P. J. Long-Term Follow-Up of the Edmonton Protocol of Islet Transplantation in the United States. *Am. J. Transplant. Off. J. Am. Soc. Transplant. Am. Soc. Transpl. Surg.* **2016**, *16* (2), 509–517. https://doi.org/10.1111/ajt.13458.

(249) O'Connell, P. J.; Holmes-Walker, D. J.; Goodman, D.; Hawthorne, W. J.; Loudovaris, T.; Gunton, J. E.; Thomas, H. E.; Grey, S. T.; Drogemuller, C. J.; Ward, G. M.; Torpy, D. J.; Coates, P. T.; Kay, T. W.; Australian Islet Transplant Consortium. Multicenter Australian Trial of Islet Transplantation: Improving Accessibility and Outcomes. *Am. J. Transplant. Off. J. Am. Soc. Transplant. Am. Soc. Transpl. Surg.* **2013**, *13* (7), 1850–1858. https://doi.org/10.1111/ajt.12250.

(250) Lablanche, S.; Borot, S.; Wojtusciszyn, A.; Bayle, F.; Tétaz, R.; Badet, L.; Thivolet, C.; Morelon, E.; Frimat, L.; Penfornis, A.; Kessler, L.; Brault, C.; Colin, C.; Tauveron, I.; Bosco,

D.; Berney, T.; Benhamou, P.-Y. Five-Year Metabolic, Functional, and Safety Results of Patients With Type 1 Diabetes Transplanted With Allogenic Islets Within the Swiss-French GRAGIL Network. *Diabetes Care* **2015**, *38* (9), 1714–1722. https://doi.org/10.2337/dc15-0094.

(251) Stegall, M. D.; Lafferty, K. J.; Kam, I.; Gill, R. G. Evidence of Recurrent Autoimmunity in Human Allogeneic Islet Transplantation. *Transplantation* **1996**, *61* (8), 1272–1274.

(252) Shapiro, A. M. J. Immune Antibody Monitoring Predicts Outcome in Islet Transplantation. *Diabetes* **2013**, *62* (5), 1377–1378. https://doi.org/10.2337/db13-0019.

(253) Rezania, A.; Bruin, J. E.; Riedel, M. J.; Mojibian, M.; Asadi, A.; Xu, J.; Gauvin, R.; Narayan, K.; Karanu, F.; O'Neil, J. J.; Ao, Z.; Warnock, G. L.; Kieffer, T. J. Maturation of Human Embryonic Stem Cell–Derived Pancreatic Progenitors Into Functional Islets Capable of Treating Pre-Existing Diabetes in Mice. *Diabetes* **2012**, *61* (8), 2016–2029. https://doi.org/10.2337/db11-1711.

(254) Kroon, E.; Martinson, L. A.; Kadoya, K.; Bang, A. G.; Kelly, O. G.; Eliazer, S.; Young, H.; Richardson, M.; Smart, N. G.; Cunningham, J.; Agulnick, A. D.; D'Amour, K. A.; Carpenter, M. K.; Baetge, E. E. Pancreatic Endoderm Derived from Human Embryonic Stem Cells Generates Glucose-Responsive Insulin-Secreting Cells in Vivo. *Nat. Biotechnol.* **2008**, *26* (4), 443–452. https://doi.org/10.1038/nbt1393.

(255) Velazco-Cruz, L.; Song, J.; Maxwell, K. G.; Goedegebuure, M. M.; Augsornworawat, P.; Hogrebe, N. J.; Millman, J. R. Acquisition of Dynamic Function in Human Stem Cell-Derived β Cells. *Stem Cell Rep.* **2019**. https://doi.org/10.1016/j.stemcr.2018.12.012.

(256) Rezania, A.; Bruin, J. E.; Arora, P.; Rubin, A.; Batushansky, I.; Asadi, A.; O'Dwyer, S.; Quiskamp, N.; Mojibian, M.; Albrecht, T.; Yang, Y. H. C.; Johnson, J. D.; Kieffer, T. J. Reversal of Diabetes with Insulin-Producing Cells Derived in Vitro from Human Pluripotent Stem Cells. *Nat. Biotechnol.* **2014**, *32* (11), 1121–1133. https://doi.org/10.1038/nbt.3033.

(257) Pagliuca, F. W.; Millman, J. R.; Gürtler, M.; Segel, M.; Van Dervort, A.; Ryu, J. H.; Peterson, Q. P.; Greiner, D.; Melton, D. A. *Cell* **2014**, *159* (2), 428–439. https://doi.org/10.1016/j.cell.2014.09.040.

(258) Pepper, A. R.; Bruni, A.; Pawlick, R.; O'Gorman, D.; Kin, T.; Thiesen, A.; Shapiro, A. M. J. Post-Transplant Characterization of Long-Term Functional HESC-Derived Pancreatic Endoderm Grafts. *Diabetes* **2018**. https://doi.org/10.2337/db18-0788.

(259) Nostro, M. C.; Sarangi, F.; Ogawa, S.; Holtzinger, A.; Corneo, B.; Li, X.; Micallef, S. J.; Park, I.-H.; Basford, C.; Wheeler, M. B.; Daley, G. Q.; Elefanty, A. G.; Stanley, E. G.; Keller, G. Stage-Specific Signaling through TGFβ Family Members and WNT Regulates Patterning and Pancreatic Specification of Human Pluripotent Stem Cells. *Dev. Camb. Engl.* **2011**, *138* (5), 861–871. https://doi.org/10.1242/dev.055236.

(260) Kunisada, Y.; Tsubooka-Yamazoe, N.; Shoji, M.; Hosoya, M. Small Molecules Induce Efficient Differentiation into Insulin-Producing Cells from Human Induced Pluripotent Stem Cells. *Stem Cell Res.* **2012**, *8* (2), 274–284. https://doi.org/10.1016/j.scr.2011.10.002.

(261) Chen, K. G.; Mallon, B. S.; McKay, R. D. G.; Robey, P. G. Human Pluripotent Stem Cell Culture: Considerations for Maintenance, Expansion, and Therapeutics. *Cell Stem Cell* **2014**, *14* (1), 13–26. https://doi.org/10.1016/j.stem.2013.12.005.

(262) Moore, K. A.; Lemischka, I. R. Stem Cells and Their Niches. *Science* **2006**, *311* (5769), 1880–1885. https://doi.org/10.1126/science.1110542.
(263) Banerjee, A.; Arha, M.; Choudhary, S.; Ashton, R. S.; Bhatia, S. R.; Schaffer, D. V.; Kane, R. S. The Influence of Hydrogel Modulus on the Proliferation and Differentiation of Encapsulated Neural Stem Cells. *Biomaterials* **2009**, *30* (27), 4695–4699. https://doi.org/10.1016/j.biomaterials.2009.05.050.
(264) Lawrence, B. J.; Madihally, S. V. Cell Colonization in Degradable 3D Porous Matrices. *Cell Adhes. Migr.* **2008**, *2* (1), 9–16. https://doi.org/10.4161/cam.2.1.5884.
(265) Bose, B.; Sudheer, P. S. In Vitro Differentiation of Pluripotent Stem Cells into Functional β Islets Under 2D and 3D Culture Conditions and In Vivo Preclinical Validation of 3D Islets. *Methods Mol. Biol. Clifton NJ* **2016**, *1341*, 257–284. https://doi.org/10.1007/7651_2015_230.
(266) McCracken, K. W.; Catá, E. M.; Crawford, C. M.; Sinagoga, K. L.; Schumacher, M.; Rockich, B. E.; Tsai, Y.-H.; Mayhew, C. N.; Spence, J. R.; Zavros, Y.; Wells, J. M. Modelling Human Development and Disease in Pluripotent Stem-Cell-Derived Gastric Organoids. *Nature* **2014**, *516* (7531), 400–404. https://doi.org/10.1038/nature13863.
(267) Takebe, T.; Sekine, K.; Enomura, M.; Koike, H.; Kimura, M.; Ogaeri, T.; Zhang, R.-R.; Ueno, Y.; Zheng, Y.-W.; Koike, N.; Aoyama, S.; Adachi, Y.; Taniguchi, H. Vascularized and Functional Human Liver from an IPSC-Derived Organ Bud Transplant. *Nature* **2013**, *499* (7459), 481–484. https://doi.org/10.1038/nature12271.
(268) Meng, X.; Leslie, P.; Zhang, Y.; Dong, J. Stem Cells in a Three-Dimensional Scaffold Environment. *SpringerPlus* **2014**, *3* (1), 80. https://doi.org/10.1186/2193-1801-3-80.
(269) Gao, S. Y. The Generation of Definitive Endoderm from Human Embryonic Stem Cells on 3D Biodegradable Poly(Lactic-Co-Glycolic Acid) Scaffolds and Its Comparison to Those Generated on 2D Monolayer Cultures. *Open Stem Cell J.* **2011**, *3* (1), 23–27. https://doi.org/10.2174/1876893801103010023.
(270) Loh, Q. L.; Choong, C. Three-Dimensional Scaffolds for Tissue Engineering Applications: Role of Porosity and Pore Size. *Tissue Eng. Part B Rev.* **2013**, *19* (6), 485–502. https://doi.org/10.1089/ten.teb.2012.0437.
(271) Crawford, D. C.; Heveran, C. M.; Cannon, W. D.; Foo, L. F.; Potter, H. G. An Autologous Cartilage Tissue Implant NeoCart for Treatment of Grade III Chondral Injury to the Distal Femur: Prospective Clinical Safety Trial at 2 Years. *Am. J. Sports Med.* **2009**, *37* (7), 1334–1343. https://doi.org/10.1177/0363546509333011.
(272) Lien, S.-M.; Ko, L.-Y.; Huang, T.-J. Effect of Pore Size on ECM Secretion and Cell Growth in Gelatin Scaffold for Articular Cartilage Tissue Engineering. *Acta Biomater.* **2009**, *5* (2), 670–679. https://doi.org/10.1016/j.actbio.2008.09.020.
(273) Griffon, D. J.; Sedighi, M. R.; Schaeffer, D. V.; Eurell, J. A.; Johnson, A. L. Chitosan Scaffolds: Interconnective Pore Size and Cartilage Engineering. *Acta Biomater.* **2006**, *2* (3), 313–320. https://doi.org/10.1016/j.actbio.2005.12.007.
(274) Vegas, A. J.; Veiseh, O.; Gürtler, M.; Millman, J. R.; Pagliuca, F. W.; Bader, A. R.; Doloff, J. C.; Li, J.; Chen, M.; Olejnik, K.; Tam, H. H.; Jhunjhunwala, S.; Langan, E.; Aresta-Dasilva, S.; Gandham, S.; McGarrigle, J. J.; Bochenek, M. A.; Hollister-Lock, J.; Oberholzer, J.; Greiner, D. L.; Weir, G. C.; Melton, D. A.; Langer, R.; Anderson, D. G. Long-Term Glycemic Control Using Polymer-Encapsulated Human Stem Cell-Derived Beta Cells in

Immune-Competent Mice. *Nat. Med.* **2016**, *22* (3), 306–311. https://doi.org/10.1038/nm.4030.
(275) Shih, H. P.; Wang, A.; Sander, M. Pancreas Organogenesis: From Lineage Determination to Morphogenesis. *Annu. Rev. Cell Dev. Biol.* **2013**, *29* (1), 81–105. https://doi.org/10.1146/annurev-cellbio-101512-122405.
(276) Aamodt, K. I.; Powers, A. C. Signals in the Pancreatic Islet Microenvironment Influence β-Cell Proliferation. *Diabetes Obes. Metab.* **2017**, *19* (S1), 124–136. https://doi.org/10.1111/dom.13031.
(277) Kasputis, T.; Clough, D.; Noto, F.; Rychel, K.; Dye, B.; Shea, L. D. Microporous Polymer Scaffolds for the Transplantation of Embryonic Stem Cell Derived Pancreatic Progenitors to a Clinically Translatable Site for the Treatment of Type I Diabetes. *ACS Biomater. Sci. Eng.* **2018**, *4* (5), 1770–1778. https://doi.org/10.1021/acsbiomaterials.7b00912.
(278) Rios, P. D.; Skoumal, M.; Liu, J.; Youngblood, R.; Kniazeva, E.; Garcia, A. J.; Shea, L. D. Evaluation of Encapsulating and Microporous Nondegradable Hydrogel Scaffold Designs on Islet Engraftment in Rodent Models of Diabetes. *Biotechnol. Bioeng.* **2018**, *115* (9), 2356–2364. https://doi.org/10.1002/bit.26741.
(279) Salvay, D. M.; Rives, C. B.; Zhang, X.; Chen, F.; Kaufman, D. B.; Lowe, W. L.; Shea, L. D. Extracellular Matrix Protein-Coated Scaffolds Promote the Reversal of Diabetes After Extrahepatic Islet Transplantation. *Transplantation* **2008**, *85* (10), 1456–1464. https://doi.org/10.1097/TP.0b013e31816fc0ea.
(280) Yap, W. T.; Salvay, D. M.; Silliman, M. A.; Zhang, X.; Bannon, Z. G.; Kaufman, D. B.; Lowe, W. L.; Shea, L. D. Collagen IV-Modified Scaffolds Improve Islet Survival and Function and Reduce Time to Euglycemia. *Tissue Eng. Part A* **2013**, *19* (21–22), 2361–2372. https://doi.org/10.1089/ten.tea.2013.0033.
(281) Rogers, G. J.; Hodgkin, M. N.; Squires, P. E. E-Cadherin and Cell Adhesion: A Role in Architecture and Function in the Pancreatic Islet. *Cell. Physiol. Biochem. Int. J. Exp. Cell. Physiol. Biochem. Pharmacol.* **2007**, *20* (6), 987–994. https://doi.org/10.1159/000110459.
(282) Jaques, F.; Jousset, H.; Tomas, A.; Prost, A.-L.; Wollheim, C. B.; Irminger, J.-C.; Demaurex, N.; Halban, P. A. Dual Effect of Cell-Cell Contact Disruption on Cytosolic Calcium and Insulin Secretion. *Endocrinology* **2008**, *149* (5), 2494–2505. https://doi.org/10.1210/en.2007-0974.
(283) Carvell, M. J.; Marsh, P. J.; Persaud, S. J.; Jones, P. M. E-Cadherin Interactions Regulate Beta-Cell Proliferation in Islet-like Structures. *Cell. Physiol. Biochem. Int. J. Exp. Cell. Physiol. Biochem. Pharmacol.* **2007**, *20* (5), 617–626. https://doi.org/10.1159/000107545.
(284) Michel, R.; Pasche, S.; Textor, M.; Castner, D. G. Influence of PEG Architecture on Protein Adsorption and Conformation. *Langmuir* **2005**, *21* (26), 12327–12332. https://doi.org/10.1021/la051726h.
(285) Jeong, J. H.; Lim, D. W.; Han, D. K.; Park, T. G. Synthesis, Characterization and Protein Adsorption Behaviors of PLGA/PEG Di-Block Co-Polymer Blend Films. *Colloids Surf. B Biointerfaces* **2000**, *18* (3), 371–379. https://doi.org/10.1016/S0927-7765(99)00162-9.
(286) Salvay, D. M.; Rives, C. B.; Zhang, X.; Chen, F.; Kaufman, D. B.; Lowe, W. L.; Shea, L. D. Extracellular Matrix Protein-Coated Scaffolds Promote the Reversal of Diabetes After

Extrahepatic Islet Transplantation: *Transplantation* **2008**, *85* (10), 1456–1464. https://doi.org/10.1097/TP.0b013e31816fc0ea.

(287) Yap, W. T.; Salvay, D. M.; Silliman, M. A.; Zhang, X.; Bannon, Z. G.; Kaufman, D. B.; Lowe, W. L.; Shea, L. D. Collagen IV-Modified Scaffolds Improve Islet Survival and Function and Reduce Time to Euglycemia. *Tissue Eng. Part A* **2013**, *19* (21–22), 2361–2372. https://doi.org/10.1089/ten.tea.2013.0033.

(288) Blomeier, H.; Zhang, X.; Rives, C.; Brissova, M.; Hughes, E.; Baker, M.; Powers, A. C.; Kaufman, D. B.; Shea, L. D.; Lowe, W. L. Polymer Scaffolds as Synthetic Microenvironments for Extrahepatic Islet Transplantation. *Transplantation* **2006**, *82* (4), 452–459. https://doi.org/10.1097/01.tp.0000231708.19937.21.

(289) Nair, G. G.; Liu, J. S.; Russ, H. A.; Tran, S.; Saxton, M. S.; Chen, R.; Juang, C.; Li, M.; Nguyen, V. Q.; Giacometti, S.; Puri, S.; Xing, Y.; Wang, Y.; Szot, G. L.; Oberholzer, J.; Bhushan, A.; Hebrok, M. Recapitulating Endocrine Cell Clustering in Culture Promotes Maturation of Human Stem-Cell-Derived β Cells. *Nat. Cell Biol.* **2019**, *21* (2), 263. https://doi.org/10.1038/s41556-018-0271-4.

(290) Lehmann, R.; Zuellig, R. A.; Kugelmeier, P.; Baenninger, P. B.; Moritz, W.; Perren, A.; Clavien, P.-A.; Weber, M.; Spinas, G. A. Superiority of Small Islets in Human Islet Transplantation. *Diabetes* **2007**, *56* (3), 594–603. https://doi.org/10.2337/db06-0779.

(291) Farhat, B.; Almelkar, A.; Ramachandran, K.; Williams, S. J.; Huang, H.-H.; Zamierowksi, D.; Novikova, L.; Stehno-Bittel, L. Small Human Islets Comprised of More β-Cells with Higher Insulin Content than Large Islets. *Islets* **2013**, *5* (2), 87–94. https://doi.org/10.4161/isl.24780.

(292) Mendelsohn, A. D.; Nyitray, C.; Sena, M.; Desai, T. A. Size-Controlled Insulin Secreting Cell Clusters. *Acta Biomater.* **2012**, *8* (12), 4278–4284. https://doi.org/10.1016/j.actbio.2012.08.010.

(293) Mendelsohn, A. D.; Nyitray, C.; Sena, M.; Desai, T. A. Size-Controlled Insulin-Secreting Cell Clusters. *Acta Biomater.* **2012**, *8* (12), 4278–4284. https://doi.org/10.1016/j.actbio.2012.08.010.

(294) Rogers, G. J.; Hodgkin, M. N.; Squires, P. E. E-Cadherin and Cell Adhesion: A Role in Architecture and Function in the Pancreatic Islet. *Cell. Physiol. Biochem.* **2007**, *20* (6), 987–994. https://doi.org/10.1159/000110459.

(295) Jiang, J.; Au, M.; Lu, K.; Eshpeter, A.; Korbutt, G.; Fisk, G.; Majumdar, A. S. Generation of Insulin-Producing Islet-Like Clusters from Human Embryonic Stem Cells. *STEM CELLS* **2007**, *25* (8), 1940–1953. https://doi.org/10.1634/stemcells.2006-0761.

(296) Shim, J. H.; Kim, S. E.; Woo, D. H.; Kim, S. K.; Oh, C. H.; McKay, R.; Kim, J. H. Directed Differentiation of Human Embryonic Stem Cells towards a Pancreatic Cell Fate. *Diabetologia* **2007**, *50* (6), 1228–1238. https://doi.org/10.1007/s00125-007-0634-z.

(297) Phillips, B. W.; Hentze, H.; Rust, W. L.; Chen, Q.-P.; Chipperfield, H.; Tan, E.-K.; Abraham, S.; Sadasivam, A.; Soong, P. L.; Wang, S. T.; Lim, R.; Sun, W.; Colman, A.; Dunn, N. R. Directed Differentiation of Human Embryonic Stem Cells into the Pancreatic Endocrine Lineage. *Stem Cells Dev.* **2007**, *16* (4), 561–578. https://doi.org/10.1089/scd.2007.0029.

(298) Serra, M.; Brito, C.; Correia, C.; Alves, P. M. Process Engineering of Human Pluripotent Stem Cells for Clinical Application. *Trends Biotechnol.* **2012**, *30* (6), 350–359. https://doi.org/10.1016/j.tibtech.2012.03.003.

(299) Sargent, C. Y.; Berguig, G. Y.; Kinney, M. A.; Hiatt, L. A.; Carpenedo, R. L.; Berson, R. E.; McDevitt, T. C. Hydrodynamic Modulation of Embryonic Stem Cell Differentiation by Rotary Orbital Suspension Culture. *Biotechnol. Bioeng.* **2010**, *105* (3), 611–626. https://doi.org/10.1002/bit.22578.

(300) Zhao, F.; Grayson, W. L.; Ma, T.; Irsigler, A. Perfusion Affects the Tissue Developmental Patterns of Human Mesenchymal Stem Cells in 3D Scaffolds. *J. Cell. Physiol.* **2009**, *219* (2), 421–429. https://doi.org/10.1002/jcp.21688.

(301) He, H.; Liu, X.; Peng, L.; Gao, Z.; Ye, Y.; Su, Y.; Zhao, Q.; Wang, K.; Gong, Y.; He, F. Promotion of Hepatic Differentiation of Bone Marrow Mesenchymal Stem Cells on Decellularized Cell-Deposited Extracellular Matrix https://www.hindawi.com/journals/bmri/2013/406871/ (accessed Jan 24, 2019). https://doi.org/10.1155/2013/406871.

(302) Riopel, M.; Wang, R. Collagen Matrix Support of Pancreatic Islet Survival and Function. *Front. Biosci. Landmark Ed.* **2014**, *19*, 77–90.

(303) Darribère, T.; Skalski, M.; Cousin, H. L.; Gaultier, A.; Montmory, C.; Alfandari, D. Integrins: Regulators of Embryogenesis. *Biol. Cell* **2000**, *92* (1), 5–25.

(304) D'Amour, K. A.; Agulnick, A. D.; Eliazer, S.; Kelly, O. G.; Kroon, E.; Baetge, E. E. Efficient Differentiation of Human Embryonic Stem Cells to Definitive Endoderm. *Nat. Biotechnol.* **2005**, *23* (12), 1534–1541. https://doi.org/10.1038/nbt1163.

(305) Engineered materials for organoid systems | Nature Reviews Materials https://www.nature.com/articles/s41578-019-0129-9 (accessed Oct 21, 2019).

(306) Giobbe, G. G.; Crowley, C.; Luni, C.; Campinoti, S.; Khedr, M.; Kretzschmar, K.; Santis, M. M. D.; Zambaiti, E.; Michielin, F.; Meran, L.; Hu, Q.; Son, G. van; Urbani, L.; Manfredi, A.; Giomo, M.; Eaton, S.; Cacchiarelli, D.; Li, V. S. W.; Clevers, H.; Bonfanti, P.; Elvassore, N.; Coppi, P. D. Extracellular Matrix Hydrogel Derived from Decellularized Tissues Enables Endodermal Organoid Culture. *Nat. Commun.* **2019**, *10* (1), 1–14. https://doi.org/10.1038/s41467-019-13605-4.

(307) Chung, C.; Beecham, M.; Mauck, R. L.; Burdick, J. A. The Influence of Degradation Characteristics of Hyaluronic Acid Hydrogels on In Vitro Neocartilage Formation by Mesenchymal Stem Cells. *Biomaterials* **2009**, *30* (26), 4287–4296. https://doi.org/10.1016/j.biomaterials.2009.04.040.

(308) Wang, W.; Jin, S.; Ye, K. Development of Islet Organoids from H9 Human Embryonic Stem Cells in Biomimetic 3D Scaffolds. *Stem Cells Dev.* **2016**, *26* (6), 394–404. https://doi.org/10.1089/scd.2016.0115.

(309) Gibly, R. F.; Graham, J. G.; Luo, X.; Jr, W. L. L.; Hering, B. J.; Shea, L. D. Advancing Islet Transplantation: From Engraftment to the Immune Response. *Diabetologia* **2011**, *54* (10), 2494–2505. https://doi.org/10.1007/s00125-011-2243-0.

(310) Hlavaty, K. A.; Gibly, R. F.; Zhang, X.; Rives, C. B.; Graham, J. G.; Lowe, W. L.; Luo, X.; Shea, L. D. Enhancing Human Islet Transplantation by Localized Release of Trophic Factors From PLG Scaffolds. *Am. J. Transplant.* **2014**, *14* (7), 1523–1532. https://doi.org/10.1111/ajt.12742.

(311) Youngblood, R. L.; Sampson, J. P.; Lebioda, K. R.; Shea, L. D. Microporous Scaffolds Support Assembly and Differentiation of Pancreatic Progenitors into β-Cell Clusters. *Acta Biomater.* **2019**. https://doi.org/10.1016/j.actbio.2019.06.032.

(312) Nair, G. G.; Liu, J. S.; Russ, H. A.; Tran, S.; Saxton, M. S.; Chen, R.; Juang, C.; Li, M.; Nguyen, V. Q.; Giacometti, S.; Puri, S.; Xing, Y.; Wang, Y.; Szot, G. L.; Oberholzer, J.; Bhushan, A.; Hebrok, M. Recapitulating Endocrine Cell Clustering in Culture Promotes Maturation of Human Stem-Cell-Derived β Cells. *Nat. Cell Biol.* **2019**, *21* (2), 263. https://doi.org/10.1038/s41556-018-0271-4.

(313) Fishman, B.; Segev, H.; Kopper, O.; Nissenbaum, J.; Schulman, M.; Benvenisty, N.; Itskovitz-Eldor, J.; Kitsberg, D. Targeting Pancreatic Progenitor Cells in Human Embryonic Stem Cell Differentiation for the Identification of Novel Cell Surface Markers. *Stem Cell Rev. Rep.* **2012**, *8* (3), 792–802. https://doi.org/10.1007/s12015-012-9363-x.

(314) Zhu, S.; Larkin, D.; Lu, S.; Inouye, C.; Haataja, L.; Anjum, A.; Kennedy, R.; Castle, D.; Arvan, P. Monitoring C-Peptide Storage and Secretion in Islet β-Cells In Vitro and In Vivo. *Diabetes* **2016**, *65* (3), 699–709. https://doi.org/10.2337/db15-1264.

(315) Haataja, L.; Snapp, E.; Wright, J.; Liu, M.; Hardy, A. B.; Wheeler, M. B.; Markwardt, M. L.; Rizzo, M.; Arvan, P. Proinsulin Intermolecular Interactions during Secretory Trafficking in Pancreatic β Cells. *J. Biol. Chem.* **2013**, *288* (3), 1896–1906. https://doi.org/10.1074/jbc.M112.420018.

(316) Pédelacq, J.-D.; Cabantous, S.; Tran, T.; Terwilliger, T. C.; Waldo, G. S. Engineering and Characterization of a Superfolder Green Fluorescent Protein. *Nat. Biotechnol.* **2006**, *24* (1), 79–88. https://doi.org/10.1038/nbt1172.

(317) Schneider, C. A.; Rasband, W. S.; Eliceiri, K. W. NIH Image to ImageJ: 25 Years of Image Analysis. *Nat. Methods* **2012**, *9* (7), 671–675. https://doi.org/10.1038/nmeth.2089.

(318) Dye, B. R.; Youngblood, R. L.; Oakes, R. S.; Kasputis, T.; Clough, D. W.; Spence, J. R.; Shea, L. D. Human Lung Organoids Develop into Adult Airway-like Structures Directed by Physico-Chemical Biomaterial Properties. *Biomaterials* **2020**, 119757. https://doi.org/10.1016/j.biomaterials.2020.119757.

(319) Hang, Y.; Yamamoto, T.; Benninger, R. K. P.; Brissova, M.; Guo, M.; Bush, W.; Piston, D. W.; Powers, A. C.; Magnuson, M.; Thurmond, D. C.; Stein, R. The MafA Transcription Factor Becomes Essential to Islet β-Cells Soon After Birth. *Diabetes* **2014**, *63* (6), 1994–2005. https://doi.org/10.2337/db13-1001.

(320) Zhang, C.; Moriguchi, T.; Kajihara, M.; Esaki, R.; Harada, A.; Shimohata, H.; Oishi, H.; Hamada, M.; Morito, N.; Hasegawa, K.; Kudo, T.; Engel, J. D.; Yamamoto, M.; Takahashi, S. MafA Is a Key Regulator of Glucose-Stimulated Insulin Secretion. *Mol. Cell. Biol.* **2005**, *25* (12), 4969–4976. https://doi.org/10.1128/MCB.25.12.4969-4976.2005.

(321) Wang, H.; Brun, T.; Kataoka, K.; Sharma, A. J.; Wollheim, C. B. MAFA Controls Genes Implicated in Insulin Biosynthesis and Secretion. *Diabetologia* **2007**, *50* (2), 348–358. https://doi.org/10.1007/s00125-006-0490-2.

(322) Matsuoka, T.; Artner, I.; Henderson, E.; Means, A.; Sander, M.; Stein, R. The MafA Transcription Factor Appears to Be Responsible for Tissue-Specific Expression of Insulin. *Proc. Natl. Acad. Sci.* **2004**, *101* (9), 2930–2933. https://doi.org/10.1073/pnas.0306233101.

(323) Zhu, S.; Larkin, D.; Lu, S.; Inouye, C.; Haataja, L.; Anjum, A.; Kennedy, R.; Castle, D.; Arvan, P. Monitoring C-Peptide Storage and Secretion in Islet β-Cells In Vitro and In Vivo. *Diabetes* **2016**, *65* (3), 699–709. https://doi.org/10.2337/db15-1264.

(324) Haataja, L.; Snapp, E.; Wright, J.; Liu, M.; Hardy, A. B.; Wheeler, M. B.; Markwardt, M. L.; Rizzo, M.; Arvan, P. Proinsulin Intermolecular Interactions during Secretory Trafficking in Pancreatic β Cells. *J. Biol. Chem.* **2013**, *288* (3), 1896–1906. https://doi.org/10.1074/jbc.M112.420018.

(325) Veres, A.; Faust, A. L.; Bushnell, H. L.; Engquist, E. N.; Kenty, J. H.-R.; Harb, G.; Poh, Y.-C.; Sintov, E.; Gürtler, M.; Pagliuca, F. W.; Peterson, Q. P.; Melton, D. A. Charting Cellular Identity during Human in Vitro β-Cell Differentiation. *Nature* **2019**, *569* (7756), 368–373. https://doi.org/10.1038/s41586-019-1168-5.

(326) Hohmeier, H. E.; An, J.; Newgard, C. B. Improving Human β-Cell Maturation in Vitro. *Nat. Cell Biol.* **2019**, *21* (2), 119–121. https://doi.org/10.1038/s41556-019-0277-6.

(327) Turner, D. A.; Girgin, M.; Alonso-Crisostomo, L.; Trivedi, V.; Baillie-Johnson, P.; Glodowski, C. R.; Hayward, P. C.; Collignon, J.; Gustavsen, C.; Serup, P.; Steventon, B.; P, M. L.; Arias, A. M. Anteroposterior Polarity and Elongation in the Absence of Extra-Embryonic Tissues and of Spatially Localised Signalling in Gastruloids: Mammalian Embryonic Organoids. *Dev. Camb. Engl.* **2017**, *144* (21), 3894–3906. https://doi.org/10.1242/dev.150391.

(328) Bonner-Weir, S.; Sullivan, B. A.; Weir, G. C. Human Islet Morphology Revisited. *J. Histochem. Cytochem.* **2015**, *63* (8), 604–612. https://doi.org/10.1369/0022155415570969.

(329) Steiner, D. J.; Kim, A.; Miller, K.; Hara, M. Pancreatic Islet Plasticity: Interspecies Comparison of Islet Architecture and Composition. *Islets* **2010**, *2* (3), 135–145.

(330) Solchaga, L. A. A Rapid Seeding Technique for the Assembly of Large Cell/ Scaffold Composite Constructs. **2007**, 21.

(331) Miller, A. J.; Hill, D. R.; Nagy, M. S.; Aoki, Y.; Dye, B. R.; Chin, A. M.; Huang, S.; Zhu, F.; White, E. S.; Lama, V.; Spence, J. R. In Vitro Induction and In Vivo Engraftment of Lung Bud Tip Progenitor Cells Derived from Human Pluripotent Stem Cells. *Stem Cell Rep.* **2018**, *10* (1), 101–119. https://doi.org/10.1016/j.stemcr.2017.11.012.

(332) Chen, Y.-W.; Huang, S. X.; de Carvalho, A. L. R. T.; Ho, S.-H.; Islam, M. N.; Volpi, S.; Notarangelo, L. D.; Ciancanelli, M.; Casanova, J.-L.; Bhattacharya, J.; Liang, A. F.; Palermo, L. M.; Porotto, M.; Moscona, A.; Snoeck, H.-W. A Three-Dimensional Model of Human Lung Development and Disease from Pluripotent Stem Cells. *Nat. Cell Biol.* **2017**, *19* (5), 542–549. https://doi.org/10.1038/ncb3510.

(333) Tadokoro, T.; Wang, Y.; Barak, L. S.; Bai, Y.; Randell, S. H.; Hogan, B. L. M. IL-6/STAT3 Promotes Regeneration of Airway Ciliated Cells from Basal Stem Cells. *Proc. Natl. Acad. Sci. U. S. A.* **2014**, *111* (35), E3641-3649. https://doi.org/10.1073/pnas.1409781111.

(334) Danahay, H.; Pessotti, A. D.; Coote, J.; Montgomery, B. E.; Xia, D.; Wilson, A.; Yang, H.; Wang, Z.; Bevan, L.; Thomas, C.; Petit, S.; London, A.; LeMotte, P.; Doelemeyer, A.; Vélez-Reyes, G. L.; Bernasconi, P.; Fryer, C. J.; Edwards, M.; Capodieci, P.; Chen, A.; Hild, M.; Jaffe, A. B. Notch2 Is Required for Inflammatory Cytokine-Driven Goblet Cell Metaplasia in the Lung. *Cell Rep.* **2015**, *10* (2), 239–252. https://doi.org/10.1016/j.celrep.2014.12.017.

(335) Rock, J. R.; Onaitis, M. W.; Rawlins, E. L.; Lu, Y.; Clark, C. P.; Xue, Y.; Randell, S. H.; Hogan, B. L. M. Basal Cells as Stem Cells of the Mouse Trachea and Human Airway

Epithelium. *Proc. Natl. Acad. Sci. U. S. A.* **2009**, *106* (31), 12771–12775. https://doi.org/10.1073/pnas.0906850106.
(336) McCauley, K. B.; Hawkins, F.; Serra, M.; Thomas, D. C.; Jacob, A.; Kotton, D. N. Efficient Derivation of Functional Human Airway Epithelium from Pluripotent Stem Cells via Temporal Regulation of Wnt Signaling. *Cell Stem Cell* **2017**, *20* (6), 844-857.e6. https://doi.org/10.1016/j.stem.2017.03.001.
(337) Miller, A. J.; Yu, Q.; Czerwinski, M.; Tsai, Y.-H.; Conway, R. F.; Wu, A.; Holloway, E. M.; Walker, T.; Glass, I. A.; Treutlein, B.; Camp, J. G.; Spence, J. R. Basal Stem Cell Fate Specification Is Mediated by SMAD Signaling in the Developing Human Lung. *bioRxiv* **2018**, 461103. https://doi.org/10.1101/461103.
(338) Finkbeiner, S. R.; Hill, D. R.; Altheim, C. H.; Dedhia, P. H.; Taylor, M. J.; Tsai, Y.-H.; Chin, A. M.; Mahe, M. M.; Watson, C. L.; Freeman, J. J.; Nattiv, R.; Thomson, M.; Klein, O. D.; Shroyer, N. F.; Helmrath, M. A.; Teitelbaum, D. H.; Dempsey, P. J.; Spence, J. R. Transcriptome-Wide Analysis Reveals Hallmarks of Human Intestine Development and Maturation In Vitro and In Vivo. *Stem Cell Rep.* **2015**, *4* (6), 1140–1155. https://doi.org/10.1016/j.stemcr.2015.04.010.
(339) Camp, J. G.; Badsha, F.; Florio, M.; Kanton, S.; Gerber, T.; Wilsch-Bräuninger, M.; Lewitus, E.; Sykes, A.; Hevers, W.; Lancaster, M.; Knoblich, J. A.; Lachmann, R.; Pääbo, S.; Huttner, W. B.; Treutlein, B. Human Cerebral Organoids Recapitulate Gene Expression Programs of Fetal Neocortex Development. *Proc. Natl. Acad. Sci. U. S. A.* **2015**, *112* (51), 15672–15677. https://doi.org/10.1073/pnas.1520760112.
(340) Takasato, M.; Er, P. X.; Chiu, H. S.; Maier, B.; Baillie, G. J.; Ferguson, C.; Parton, R. G.; Wolvetang, E. J.; Roost, M. S.; Chuva de Sousa Lopes, S. M.; Little, M. H. Kidney Organoids from Human IPS Cells Contain Multiple Lineages and Model Human Nephrogenesis. *Nature* **2015**, *526* (7574), 564–568. https://doi.org/10.1038/nature15695.
(341) Hrvatin, S.; O'Donnell, C. W.; Deng, F.; Millman, J. R.; Pagliuca, F. W.; DiIorio, P.; Rezania, A.; Gifford, D. K.; Melton, D. A. Differentiated Human Stem Cells Resemble Fetal, Not Adult, β Cells. *Proc. Natl. Acad. Sci. U. S. A.* **2014**, *111* (8), 3038–3043. https://doi.org/10.1073/pnas.1400709111.
(342) Campeau, E.; Ruhl, V. E.; Rodier, F.; Smith, C. L.; Rahmberg, B. L.; Fuss, J. O.; Campisi, J.; Yaswen, P.; Cooper, P. K.; Kaufman, P. D. A Versatile Viral System for Expression and Depletion of Proteins in Mammalian Cells. *PLOS ONE* **2009**, *4* (8), e6529. https://doi.org/10.1371/journal.pone.0006529.
(343) Blomeier, H.; Zhang, X.; Rives, C.; Brissova, M.; Hughes, E.; Baker, M.; Powers, A. C.; Kaufman, D. B.; Shea, L. D.; Lowe, W. L. Polymer Scaffolds as Synthetic Microenvironments for Extrahepatic Islet Transplantation. *Transplantation* **2006**, *82* (4), 452–459. https://doi.org/10.1097/01.tp.0000231708.19937.21.
(344) Rao, S. S.; Bushnell, G. G.; Azarin, S. M.; Spicer, G.; Aguado, B. A.; Stoehr, J. R.; Jiang, E. J.; Backman, V.; Shea, L. D.; Jeruss, J. S. Enhanced Survival with Implantable Scaffolds That Capture Metastatic Breast Cancer Cells In Vivo. *Cancer Res.* **2016**, *76* (18), 5209–5218. https://doi.org/10.1158/0008-5472.CAN-15-2106.
(345) Rockich, B. E.; Hrycaj, S. M.; Shih, H. P.; Nagy, M. S.; Ferguson, M. A. H.; Kopp, J. L.; Sander, M.; Wellik, D. M.; Spence, J. R. Sox9 Plays Multiple Roles in the Lung Epithelium

during Branching Morphogenesis. *Proc. Natl. Acad. Sci. U. S. A.* **2013**, *110* (47), E4456-4464. https://doi.org/10.1073/pnas.1311847110.

(346) Y, Y.; Pe, L.; Eh, F. A New Site for Islet Transplantation--a Peritoneal-Omental Pouch. *Transplantation* **1983**, *36* (2), 181–182. https://doi.org/10.1097/00007890-198308000-00014.

(347) Schmidt, C. Pancreatic Islets Find a New Transplant Home in the Omentum. *Nat. Biotechnol.* **2017**, *35* (1), 8. https://doi.org/10.1038/nbt0117-8.

(348) Litbarg, N. O.; Gudehithlu, K. P.; Sethupathi, P.; Arruda, J. A. L.; Dunea, G.; Singh, A. K. Activated Omentum Becomes Rich in Factors That Promote Healing and Tissue Regeneration. *Cell Tissue Res.* **2007**, *328* (3), 487–497. https://doi.org/10.1007/s00441-006-0356-4.

(349) Park, Y.; Chen, Y.; Ordovas, L.; Verfaillie, C. M. Hepatic Differentiation of Human Embryonic Stem Cells on Microcarriers. *J. Biotechnol.* **2014**, *174*, 39–48. https://doi.org/10.1016/j.jbiotec.2014.01.025.

(350) Williams, H. E.; Huxley, J.; Claybourn, M.; Booth, J.; Hobbs, M.; Meehan, E.; Clark, B. The Effect of γ-Irradiation and Polymer Composition on the Stability of PLG Polymer and Microspheres; 2006. https://doi.org/10.1016/j.polymdegradstab.2006.01.006.

(351) Morrisey, E. E.; Hogan, B. L. M. Preparing for the First Breath: Genetic and Cellular Mechanisms in Lung Development. *Dev. Cell* **2010**, *18* (1), 8–23. https://doi.org/10.1016/j.devcel.2009.12.010.

(352) Miller, A. J.; Spence, J. R. In Vitro Models to Study Human Lung Development, Disease and Homeostasis. *Physiol. Bethesda Md* **2017**, *32* (3), 246–260. https://doi.org/10.1152/physiol.00041.2016.

(353) Sung, H.-J.; Meredith, C.; Johnson, C.; Galis, Z. S. The Effect of Scaffold Degradation Rate on Three-Dimensional Cell Growth and Angiogenesis. *Biomaterials* **2004**, *25* (26), 5735–5742. https://doi.org/10.1016/j.biomaterials.2004.01.066.

(354) Mondal, D.; Griffith, M.; Venkatraman, S. S. Polycaprolactone-Based Biomaterials for Tissue Engineering and Drug Delivery: Current Scenario and Challenges. *Int. J. Polym. Mater. Polym. Biomater.* **2016**, *65* (5), 255–265. https://doi.org/10.1080/00914037.2015.1103241.

(355) Makadia, H. K.; Siegel, S. J. Poly Lactic-Co-Glycolic Acid (PLGA) as Biodegradable Controlled Drug Delivery Carrier. *Polymers* **2011**, *3* (3), 1377–1397. https://doi.org/10.3390/polym3031377.

(356) Dye, B. R.; Miller, A. J.; Spence, J. R. How to Grow a Lung: Applying Principles of Developmental Biology to Generate Lung Lineages from Human Pluripotent Stem Cells. *Curr. Pathobiol. Rep.* **2016**, *4* (2), 47–57. https://doi.org/10.1007/s40139-016-0102-x.

(357) Metzger, R. J.; Klein, O. D.; Martin, G. R.; Krasnow, M. A. The Branching Programme of Mouse Lung Development. *Nature* **2008**, *453* (7196), 745–750. https://doi.org/10.1038/nature07005.

(358) Rawlins, E. L. The Building Blocks of Mammalian Lung Development. *Dev. Dyn.* **2011**, *240* (3), 463–476. https://doi.org/10.1002/dvdy.22482.

(359) Athanazio, R. Airway Disease: Similarities and Differences between Asthma, COPD and Bronchiectasis. *Clinics* **2012**, *67* (11), 1335–1343. https://doi.org/10.6061/clinics/2012(11)19.

(360) Lewis, T. A.; Tzeng, Y.-S.; McKinstry, E. L.; Tooker, A. C.; Hong, K.; Sun, Y.; Mansour, J.; Handler, Z.; Albert, M. S. Quantification of Airway Diameters and 3D Airway Tree Rendering from Dynamic Hyperpolarized 3He Magnetic Resonance Imaging. *Magn. Reson. Med.* **2005**, *53* (2), 474–478. https://doi.org/10.1002/mrm.20349.

(361) Cutting, G. R. Cystic Fibrosis Genetics: From Molecular Understanding to Clinical Application. *Nat. Rev. Genet.* **2015**, *16* (1), 45–56. https://doi.org/10.1038/nrg3849.

(362) Aurora, A. B.; Olson, E. N. Immune Modulation of Stem Cells and Regeneration. *Cell Stem Cell* **2014**, *15* (1), 14–25. https://doi.org/10.1016/j.stem.2014.06.009.

(363) Kizil, C.; Kyritsis, N.; Brand, M. Effects of Inflammation on Stem Cells: Together They Strive? *EMBO Rep.* **2015**, *16* (4), 416–426. https://doi.org/10.15252/embr.201439702.

(364) Pearl, J. I.; Kean, L. S.; Davis, M. M.; Wu, J. C. Pluripotent Stem Cells: Immune to the Immune System? *Sci. Transl. Med.* **2012**, *4* (164), 164ps25. https://doi.org/10.1126/scitranslmed.3005090.

(365) Morley, T. S.; Xia, J. Y.; Scherer, P. E. Selective Enhancement of Insulin Sensitivity in the Mature Adipocyte Is Sufficient for Systemic Metabolic Improvements. *Nat. Commun.* **2015**, *6* (1), 1–11. https://doi.org/10.1038/ncomms8906.

(366) Tran, T. T.; Yamamoto, Y.; Gesta, S.; Kahn, C. R. Beneficial Effects of Subcutaneous Fat Transplantation on Metabolism. *Cell Metab.* **2008**, *7* (5), 410–420. https://doi.org/10.1016/j.cmet.2008.04.004.

(367) Hocking, S. L.; Stewart, R. L.; Brandon, A. E.; Suryana, E.; Stuart, E.; Baldwin, E. M.; Kolumam, G. A.; Modrusan, Z.; Junutula, J. R.; Gunton, J. E.; Medynskyj, M.; Blaber, S. P.; Karsten, E.; Herbert, B. R.; James, D. E.; Cooney, G. J.; Swarbrick, M. M. Subcutaneous Fat Transplantation Alleviates Diet-Induced Glucose Intolerance and Inflammation in Mice. *Diabetologia* **2015**, *58* (7), 1587–1600. https://doi.org/10.1007/s00125-015-3583-y.

(368) Foster, M. T.; Softic, S.; Caldwell, J.; Kohli, R.; deKloet, A. D.; Seeley, R. J. Subcutaneous Adipose Tissue Transplantation in Diet-Induced Obese Mice Attenuates Metabolic Dysregulation While Removal Exacerbates It. *Physiol. Rep.* **2013**, *1* (2). https://doi.org/10.1002/phy2.15.

(369) Tharp, K. M.; Jha, A. K.; Kraiczy, J.; Yesian, A.; Karateev, G.; Sinisi, R.; Dubikovskaya, E. A.; Healy, K. E.; Stahl, A. Matrix-Assisted Transplantation of Functional Beige Adipose Tissue. *Diabetes* **2015**, *64* (11), 3713–3724. https://doi.org/10.2337/db15-0728.

(370) Kelmendi-Doko, A.; Rubin, J. P.; Klett, K.; Mahoney, C.; Wang, S.; Marra, K. G. Controlled Dexamethasone Delivery via Double-Walled Microspheres to Enhance Long-Term Adipose Tissue Retention. *J. Tissue Eng.* **2017**, *8*, 2041731417735402. https://doi.org/10.1177/2041731417735402.

(371) Zhang, S.; Lu, Q.; Cao, T.; Toh, W. S. Adipose Tissue and Extracellular Matrix Development by Injectable Decellularized Adipose Matrix Loaded with Basic Fibroblast Growth Factor. *Plast. Reconstr. Surg.* **2016**, *137* (4), 1171–1180. https://doi.org/10.1097/PRS.0000000000002019.

(372) Masuda, T.; Furue, M.; Matsuda, T. Photocured, Styrenated Gelatin-Based Microspheres for de Novo Adipogenesis through Corelease of Basic Fibroblast Growth Factor, Insulin, and Insulin-Like Growth Factor I. *Tissue Eng.* **2004**, *10* (3–4), 523–535. https://doi.org/10.1089/107632704323061889.

(373) Mahoney, C. M.; Imbarlina, C.; Yates, C. C.; Marra, K. G. Current Therapeutic Strategies for Adipose Tissue Defects/Repair Using Engineered Biomaterials and Biomolecule Formulations. *Front. Pharmacol.* **2018**, *9*. https://doi.org/10.3389/fphar.2018.00507.
(374) Liu, J. M. H.; Zhang, X.; Joe, S.; Luo, X.; Shea, L. D. Evaluation of Biomaterial Scaffold Delivery of IL-33 as a Localized Immunomodulatory Agent to Support Cell Transplantation in Adipose Tissue. *J. Immunol. Regen. Med.* **2018**, *1*, 1–12. https://doi.org/10.1016/j.regen.2018.01.003.
(375) Youngblood, R. L.; Sampson, J.; Lebioda, K. L.; Spicer, G. L.; Shea, L. D. Microporous Scaffolds Drive Assembly and Maturation of Progenitors into β-Cell Clusters. *bioRxiv* **2019**, 560979. https://doi.org/10.1101/560979.
(376) Thomas, A. M.; Seidlits, S. K.; Goodman, A. G.; Kukushliev, T. V.; Hassani, D. M.; Cummings, B. J.; Anderson, A. J.; Shea, L. D. Sonic Hedgehog and Neurotrophin-3 Increase Oligodendrocyte Numbers and Myelination after Spinal Cord Injury. *Integr. Biol.* **2014**, *6* (7), 694–705. https://doi.org/10.1039/c4ib00009a.
(377) Park, J.; Decker, J. T.; Margul, D. J.; Smith, D. R.; Cummings, B. J.; Anderson, A. J.; Shea, L. D. Local Immunomodulation with Anti-Inflammatory Cytokine-Encoding Lentivirus Enhances Functional Recovery after Spinal Cord Injury. *Mol. Ther.* **2018**, *26* (7), 1756–1770. https://doi.org/10.1016/j.ymthe.2018.04.022.
(378) Dull, T.; Zufferey, R.; Kelly, M.; Mandel, R. J.; Nguyen, M.; Trono, D.; Naldini, L. A Third-Generation Lentivirus Vector with a Conditional Packaging System. *J. Virol.* **1998**, *72* (11), 8463–8471.
(379) Shin, S.; Salvay, D. M.; Shea, L. D. Lentivirus Delivery by Adsorption to Tissue Engineering Scaffolds. *J. Biomed. Mater. Res. A* **2010**, *93* (4), 1252–1259. https://doi.org/10.1002/jbm.a.32619.
(380) Thomas, A. M.; Seidlits, S. K.; Goodman, A. G.; Kukushliev, T. V.; Hassani, D. M.; Cummings, B. J.; Anderson, A. J.; Shea, L. D. Sonic Hedgehog and Neurotrophin-3 Increase Oligodendrocyte Numbers and Myelination after Spinal Cord Injury. *Integr. Biol.* **2014**, *6* (7), 694–705. https://doi.org/10.1039/c4ib00009a.
(381) Tuinstra, H. M.; Aviles, M. O.; Shin, S.; Holland, S. J.; Zelivyanskaya, M. L.; Fast, A. G.; Ko, S. Y.; Margul, D. J.; Bartels, A. K.; Boehler, R. M.; Cummings, B. J.; Anderson, A. J.; Shea, L. D. Multifunctional, Multichannel Bridges That Deliver Neurotrophin Encoding Lentivirus for Regeneration Following Spinal Cord Injury. *Biomaterials* **2012**, *33* (5), 1618–1626. https://doi.org/10.1016/j.biomaterials.2011.11.002.
(382) Foster, M. T.; Softic, S.; Caldwell, J.; Kohli, R.; deKloet, A. D.; Seeley, R. J. Subcutaneous Adipose Tissue Transplantation in Diet-Induced Obese Mice Attenuates Metabolic Dysregulation While Removal Exacerbates It. *Physiol. Rep.* **2013**, *1* (2). https://doi.org/10.1002/phy2.15.
(383) Hocking, S. L.; Stewart, R. L.; Brandon, A. E.; Suryana, E.; Stuart, E.; Baldwin, E. M.; Kolumam, G. A.; Modrusan, Z.; Junutula, J. R.; Gunton, J. E.; Medynskyj, M.; Blaber, S. P.; Karsten, E.; Herbert, B. R.; James, D. E.; Cooney, G. J.; Swarbrick, M. M. Subcutaneous Fat Transplantation Alleviates Diet-Induced Glucose Intolerance and Inflammation in Mice. *Diabetologia* **2015**, *58* (7), 1587–1600. https://doi.org/10.1007/s00125-015-3583-y.

(384) Tran, T. T.; Yamamoto, Y.; Gesta, S.; Kahn, C. R. Beneficial Effects of Subcutaneous Fat Transplantation on Metabolism. *Cell Metab.* **2008**, *7* (5), 410–420. https://doi.org/10.1016/j.cmet.2008.04.004.

(385) Cho, K. W.; Morris, D. L.; DelProposto, J. L.; Geletka, L.; Zamarron, B.; Martinez-Santibanez, G.; Meyer, K. A.; Singer, K.; O'Rourke, R. W.; Lumeng, C. N. An MHC II-Dependent Activation Loop between Adipose Tissue Macrophages and CD4+ T Cells Controls Obesity-Induced Inflammation. *Cell Rep.* **2014**, *9* (2), 605–617. https://doi.org/10.1016/j.celrep.2014.09.004.

(386) Lumeng, C. N.; Bodzin, J. L.; Saltiel, A. R. Obesity Induces a Phenotypic Switch in Adipose Tissue Macrophage Polarization. *J. Clin. Invest.* **2007**, *117* (1), 175–184. https://doi.org/10.1172/JCI29881.

(387) Geginat, J.; Paroni, M.; Maglie, S.; Alfen, J. S.; Kastirr, I.; Gruarin, P.; De Simone, M.; Pagani, M.; Abrignani, S. Plasticity of Human CD4 T Cell Subsets. *Front. Immunol.* **2014**, *5*. https://doi.org/10.3389/fimmu.2014.00630.

(388) Mills, C. D. M1 and M2 Macrophages: Oracles of Health and Disease. *Crit. Rev. Immunol.* **2012**, *32* (6), 463–488. https://doi.org/10.1615/critrevimmunol.v32.i6.10.

(389) Boehler, R. M.; Shin, S.; Fast, A. G.; Gower, R. M.; Shea, L. D. A PLG/HAp Composite Scaffold for Lentivirus Delivery. *Biomaterials* **2013**, *34* (21), 5431–5438. https://doi.org/10.1016/j.biomaterials.2013.04.009.

(390) Park, J.; Decker, J. T.; Smith, D. R.; Cummings, B. J.; Anderson, A. J.; Shea, L. D. Reducing Inflammation through Delivery of Lentivirus Encoding for Anti-Inflammatory Cytokines Attenuates Neuropathic Pain after Spinal Cord Injury. *J. Controlled Release* **2018**, *290*, 88–101. https://doi.org/10.1016/j.jconrel.2018.10.003.

(391) Liu, J. M. H.; Zhang, X.; Joe, S.; Luo, X.; Shea, L. D. Evaluation of Biomaterial Scaffold Delivery of IL-33 as a Localized Immunomodulatory Agent to Support Cell Transplantation in Adipose Tissue. *J. Immunol. Regen. Med.* **2018**, *1*, 1–12. https://doi.org/10.1016/j.regen.2018.01.003.

(392) Stafeev, I. S.; Michurina, S. S.; Podkuychenko, N. V.; Vorotnikov, A. V.; Menshikov, M. Y.; Parfyonova, Y. V. Interleukin-4 Restores Insulin Sensitivity in Lipid-Induced Insulin-Resistant Adipocytes. *Biochem. Biokhimiia* **2018**, *83* (5), 498–506. https://doi.org/10.1134/S0006297918050036.

(393) Tsao, C.-H.; Shiau, M.-Y.; Chuang, P.-H.; Chang, Y.-H.; Hwang, J. Interleukin-4 Regulates Lipid Metabolism by Inhibiting Adipogenesis and Promoting Lipolysis. *J. Lipid Res.* **2014**, *55* (3), 385–397. https://doi.org/10.1194/jlr.M041392.

(394) Hendley, M. A.; Murphy, K. P.; Isely, C.; Struckman, H. L.; Annamalai, P.; Gower, R. M. The Host Response to Poly(Lactide-Co-Glycolide) Scaffolds Protects Mice from Diet Induced Obesity and Glucose Intolerance. *Biomaterials* **2019**, *217*, 119281. https://doi.org/10.1016/j.biomaterials.2019.119281.

(395) Watanabe, M.; Buth, J. E.; Vishlaghi, N.; Torre-Ubieta, L. de la; Taxidis, J.; Khakh, B. S.; Coppola, G.; Pearson, C. A.; Yamauchi, K.; Gong, D.; Dai, X.; Damoiseaux, R.; Aliyari, R.; Liebscher, S.; Schenke-Layland, K.; Caneda, C.; Huang, E. J.; Zhang, Y.; Cheng, G.; Geschwind, D. H.; Golshani, P.; Sun, R.; Novitch, B. G. Self-Organized Cerebral Organoids with Human-Specific Features Predict Effective Drugs to Combat Zika Virus Infection. *Cell Rep.* **2017**, *21* (2), 517–532. https://doi.org/10.1016/j.celrep.2017.09.047.

(396) Dekkers, J. F.; Wiegerinck, C. L.; de Jonge, H. R.; Bronsveld, I.; Janssens, H. M.; de Winter-de Groot, K. M.; Brandsma, A. M.; de Jong, N. W. M.; Bijvelds, M. J. C.; Scholte, B. J.; Nieuwenhuis, E. E. S.; van den Brink, S.; Clevers, H.; van der Ent, C. K.; Middendorp, S.; Beekman, J. M. A Functional CFTR Assay Using Primary Cystic Fibrosis Intestinal Organoids. *Nat. Med.* **2013**, *19* (7), 939–945. https://doi.org/10.1038/nm.3201.

(397) Czerniecki, S. M.; Cruz, N. M.; Harder, J. L.; Menon, R.; Annis, J.; Otto, E. A.; Gulieva, R. E.; Islas, L. V.; Kim, Y. K.; Tran, L. M.; Martins, T. J.; Pippin, J. W.; Fu, H.; Kretzler, M.; Shankland, S. J.; Himmelfarb, J.; Moon, R. T.; Paragas, N.; Freedman, B. S. High-Throughput Screening Enhances Kidney Organoid Differentiation from Human Pluripotent Stem Cells and Enables Automated Multidimensional Phenotyping. *Cell Stem Cell* **2018**, *22* (6), 929-940.e4. https://doi.org/10.1016/j.stem.2018.04.022.

(398) Pagliuca, F. W.; Millman, J. R.; Gürtler, M.; Segel, M.; Van Dervort, A.; Ryu, J. H.; Peterson, Q. P.; Greiner, D.; Melton, D. A. Generation of Functional Human Pancreatic β Cells in Vitro. *Cell* **2014**, *159* (2), 428–439. https://doi.org/10.1016/j.cell.2014.09.040.

(399) Blomeier, H.; Zhang, X.; Rives, C.; Brissova, M.; Hughes, E.; Baker, M.; Powers, A. C.; Kaufman, D. B.; Shea, L. D.; Lowe, W. L. Polymer Scaffolds as Synthetic Microenvironments for Extrahepatic Islet Transplantation. *Transplantation* **2006**, *82* (4), 452–459. https://doi.org/10.1097/01.tp.0000231708.19937.21.

(400) Saad, B.; Suter, U. W. Biodegradable Polymeric Materials. In *Encyclopedia of Materials: Science and Technology*; Buschow, K. H. J., Cahn, R. W., Flemings, M. C., Ilschner, B., Kramer, E. J., Mahajan, S., Veyssière, P., Eds.; Elsevier: Oxford, 2001; pp 551–555. https://doi.org/10.1016/B0-08-043152-6/00105-4.

(401) Facucho-Oliveira, J. M.; St John, J. C. The Relationship between Pluripotency and Mitochondrial DNA Proliferation during Early Embryo Development and Embryonic Stem Cell Differentiation. *Stem Cell Rev. Rep.* **2009**, *5* (2), 140–158. https://doi.org/10.1007/s12015-009-9058-0.

(402) Armstrong, J. S. Mitochondrial Medicine: Pharmacological Targeting of Mitochondria in Disease. *Br. J. Pharmacol.* **2007**, *151* (8), 1154–1165. https://doi.org/10.1038/sj.bjp.0707288.

(403) Becker, K. A.; Ghule, P. N.; Therrien, J. A.; Lian, J. B.; Stein, J. L.; van Wijnen, A. J.; Stein, G. S. Self-Renewal of Human Embryonic Stem Cells Is Supported by a Shortened G1 Cell Cycle Phase. *J. Cell. Physiol.* **2006**, *209* (3), 883–893. https://doi.org/10.1002/jcp.20776.

(404) Efroni, S.; Duttagupta, R.; Cheng, J.; Dehghani, H.; Hoeppner, D. J.; Dash, C.; Bazett-Jones, D. P.; Le Grice, S.; McKay, R. D. G.; Buetow, K. H.; Gingeras, T. R.; Misteli, T.; Meshorer, E. Global Transcription in Pluripotent Embryonic Stem Cells. *Cell Stem Cell* **2008**, *2* (5), 437–447. https://doi.org/10.1016/j.stem.2008.03.021.

(405) Meshorer, E.; Misteli, T. Chromatin in Pluripotent Embryonic Stem Cells and Differentiation. *Nat. Rev. Mol. Cell Biol.* **2006**, *7* (7), 540–546. https://doi.org/10.1038/nrm1938.

(406) Schwank, G.; Koo, B.-K.; Sasselli, V.; Dekkers, J. F.; Heo, I.; Demircan, T.; Sasaki, N.; Boymans, S.; Cuppen, E.; van der Ent, C. K.; Nieuwenhuis, E. E. S.; Beekman, J. M.; Clevers, H. Functional Repair of CFTR by CRISPR/Cas9 in Intestinal Stem Cell Organoids of Cystic Fibrosis Patients. *Cell Stem Cell* **2013**, *13* (6), 653–658. https://doi.org/10.1016/j.stem.2013.11.002.

(407) Zhao, J.; Zong, W.; Zhao, Y.; Gou, D.; Liang, S.; Shen, J.; Wu, Y.; Zheng, X.; Wu, R.; Wang, X.; Niu, F.; Wang, A.; Zhang, Y.; Xiong, J.-W.; Chen, L.; Liu, Y. In Vivo Imaging of β-Cell Function Reveals Glucose-Mediated Heterogeneity of β-Cell Functional Development. *eLife* **2019**, *8*, e41540. https://doi.org/10.7554/eLife.41540.

(408) Bahlmann, L. C.; Fokina, A.; Shoichet, M. S. Dynamic Bioengineered Hydrogels as Scaffolds for Advanced Stem Cell and Organoid Culture. *MRS Commun.* **2017**, *7* (3), 472–486. https://doi.org/10.1557/mrc.2017.72.

(409) Feng, Q.; Zhu, M.; Wei, K.; Bian, L. Cell-Mediated Degradation Regulates Human Mesenchymal Stem Cell Chondrogenesis and Hypertrophy in MMP-Sensitive Hyaluronic Acid Hydrogels. *PLOS ONE* **2014**, *9* (6), e99587. https://doi.org/10.1371/journal.pone.0099587.

(410) Konstantinova, I.; Nikolova, G.; Ohara-Imaizumi, M.; Meda, P.; Kučera, T.; Zarbalis, K.; Wurst, W.; Nagamatsu, S.; Lammert, E. EphA-Ephrin-A-Mediated β Cell Communication Regulates Insulin Secretion from Pancreatic Islets. *Cell* **2007**, *129* (2), 359–370. https://doi.org/10.1016/j.cell.2007.02.044.

(411) Ahadian, S.; Khademhosseini, A. Smart Scaffolds in Tissue Regeneration. *Regen. Biomater.* **2018**, *5* (3), 125–128. https://doi.org/10.1093/rb/rby007.

(412) Hunt, J. A.; Chen, R.; van Veen, T.; Bryan, N. Hydrogels for Tissue Engineering and Regenerative Medicine. *J Mater Chem B* **2014**, *2* (33), 5319–5338. https://doi.org/10.1039/C4TB00775A.

(413) Youngblood, R. L.; Truong, N. F.; Segura, T.; Shea, L. D. It's All in the Delivery: Designing Hydrogels for Cell and Non-Viral Gene Therapies. *Mol. Ther.* **2018**, *26* (9), 2087–2106. https://doi.org/10.1016/j.ymthe.2018.07.022.

(414) Li, J.; Mooney, D. J. Designing Hydrogels for Controlled Drug Delivery. *Nat. Rev. Mater.* **2016**, *1* (12), 16071. https://doi.org/10.1038/natrevmats.2016.71.

(415) Camci-Unal, G.; Annabi, N.; Dokmeci, M. R.; Liao, R.; Khademhosseini, A. Hydrogels for Cardiac Tissue Engineering. *NPG Asia Mater.* **2014**, *6* (5), e99–e99. https://doi.org/10.1038/am.2014.19.

(416) Liu, M.; Zeng, X.; Ma, C.; Yi, H.; Ali, Z.; Mou, X.; Li, S.; Deng, Y.; He, N. Injectable Hydrogels for Cartilage and Bone Tissue Engineering. *Bone Res.* **2017**, *5* (1), 17014. https://doi.org/10.1038/boneres.2017.14.

(417) Kamoun, E. A.; Kenawy, E.-R. S.; Chen, X. A Review on Polymeric Hydrogel Membranes for Wound Dressing Applications: PVA-Based Hydrogel Dressings. *J. Adv. Res.* **2017**, *8* (3), 217–233. https://doi.org/10.1016/j.jare.2017.01.005.

(418) Liu, H.; Hao, J.; Li, K. S. Current Strategies for Drug Delivery to the Inner Ear. *Acta Pharm. Sin. B* **2013**, *3* (2), 86–96. https://doi.org/10.1016/j.apsb.2013.02.003.

(419) Chang, D.; Park, K.; Famili, A. Hydrogels for Sustained Delivery of Biologics to the Back of the Eye. *Drug Discov. Today* **2019**, *24* (8), 1470–1482. https://doi.org/10.1016/j.drudis.2019.05.037.

(420) Basso, J.; Miranda, A.; Nunes, S.; Cova, T.; Sousa, J.; Vitorino, C.; Pais, A. Hydrogel-Based Drug Delivery Nanosystems for the Treatment of Brain Tumors. *Gels* **2018**, *4* (3), 62. https://doi.org/10.3390/gels4030062.

(421) Lee, J. H. Injectable Hydrogels Delivering Therapeutic Agents for Disease Treatment and Tissue Engineering. *Biomater. Res.* **2018**, *22* (1), 27. https://doi.org/10.1186/s40824-018-0138-6.
(422) Dimatteo, R.; Darling, N. J.; Segura, T. In Situ Forming Injectable Hydrogels for Drug Delivery and Wound Repair. *Adv. Drug Deliv. Rev.* **2018**, *127*, 167–184. https://doi.org/10.1016/j.addr.2018.03.007.
(423) Mironi-Harpaz, I.; Yingquan Wang, D.; Venkatraman, S.; Seliktar, D. Photopolymerization of Cell-Encapsulating Hydrogels: Crosslinking Efficiency versus Cytotoxicity. *Acta Biomater.* **2012**, *8* (5), 1838–1848. https://doi.org/10.1016/j.actbio.2011.12.034.
(424) Patenaude, M.; Campbell, S.; Kinio, D.; Hoare, T. Tuning Gelation Time and Morphology of Injectable Hydrogels Using Ketone–Hydrazide Cross-Linking. *Biomacromolecules* **2014**, *15* (3), 781–790. https://doi.org/10.1021/bm401615d.
(425) Sosnik, A.; Seremeta, K. Polymeric Hydrogels as Technology Platform for Drug Delivery Applications. *Gels* **2017**, *3* (3), 25. https://doi.org/10.3390/gels3030025.
(426) P. Nair, D.; Podgórski, M.; Chatani, S.; Gong, T.; Xi, W.; R. Fenoli, C.; N. Bowman, C. The Thiol-Michael Addition Click Reaction: A Powerful and Widely Used Tool in Materials Chemistry. *Chem. Mater.* **2014**, *26* (1), 724–744. https://doi.org/10.1021/cm402180t.
(427) Wan, G.; Gómez-Casati, M. E.; Gigliello, A. R.; Liberman, M. C.; Corfas, G. Neurotrophin-3 Regulates Ribbon Synapse Density in the Cochlea and Induces Synapse Regeneration after Acoustic Trauma. *eLife* **2014**, *3*, e03564. https://doi.org/10.7554/eLife.03564.
(428) Suzuki, J.; Corfas, G.; Liberman, M. C. Round-Window Delivery of Neurotrophin 3 Regenerates Cochlear Synapses after Acoustic Overexposure. *Sci. Rep.* **2016**, *6* (1), 24907. https://doi.org/10.1038/srep24907.
(429) Kechai, N. E.; Florence, A.; Mamelle, E.; Nquyen, Y.; Ferrary, E.; Bochot, A. Recent Advances in Local Drug Delivery to the Inner Ear. *Int. J. Pharm.* **2015**, *494* (1), 83–101. https://doi.org/10.1016/j.ijpharm.2015.08.015.
(430) Giuliano, E.; Paolino, D.; Fresta, M.; Cosco, D. Mucosal Applications of Poloxamer 407-Based Hydrogels: An Overview. *Pharmaceutics* **2018**, *10* (3), 159. https://doi.org/10.3390/pharmaceutics10030159.
(431) Wang, X.; Zhong, P.; Luo, P. P.; Wang, K. C. Antibody Engineering Using Phage Display with a Coiled-Coil Heterodimeric Fv Antibody Fragment. *PLoS ONE* **2011**, *6* (4), e19023. https://doi.org/10.1371/journal.pone.0019023.
(432) Frei, J. C.; Lai, J. R. Protein and Antibody Engineering by Phage Display. In *Methods in Enzymology*; Elsevier, 2016; Vol. 580, pp 45–87. https://doi.org/10.1016/bs.mie.2016.05.005.
(433) Mehdizadeh, M.; Yang, J. Design Strategies and Applications of Tissue Bioadhesives: Design Strategies and Applications of Tissue …. *Macromol. Biosci.* **2013**, *13* (3), 271–288. https://doi.org/10.1002/mabi.201200332.
(434) Odermatt, A.; Audigé, A.; Frick, C.; Vogt, B.; Frey, B. M.; Frey, F. J.; Mazzucchelli, L. Identification of Receptor Ligands by Screening Phage- Display Peptide Libraries Ex Vivo on Microdissected Kidney Tubules. *J Am Soc Nephrol* **2001**, 9.
(435) Mohrlüder, J.; Stangler, T.; Hoffmann, Y.; Wiesehan, K.; Mataruga, A.; Willbold, D. Identification of Calreticulin as a Ligand of GABARAP by Phage Display Screening of a

Peptide Library. *FEBS J.* **2007**, *274* (21), 5543–5555. https://doi.org/10.1111/j.1742-4658.2007.06073.x.
(436) Liu, J. K.; Teng, Q.; Garrity-Moses, M.; Federici, T.; Tanase, D.; Imperiale, M. J.; Boulis, N. M. A Novel Peptide Defined through Phage Display for Therapeutic Protein and Vector Neuronal Targeting. *Neurobiol. Dis.* **2005**, *19* (3), 407–418. https://doi.org/10.1016/j.nbd.2005.01.022.
(437) Molek, P.; Strukelj, B.; Bratkovic, T. Peptide Phage Display as a Tool for Drug Discovery: Targeting Membrane Receptors. *Molecules* **2011**, *16* (1), 857–887. https://doi.org/10.3390/molecules16010857.
(438) Wang, X.; Li, G.; Ren, Y.; Ren, X. Phages Bearing Affinity Peptides to Bovine Rotavirus Differentiate the Virus from Other Viruses. *PLoS ONE* **2011**, *6* (12), e28667. https://doi.org/10.1371/journal.pone.0028667.
(439) Wu, J.; Park, J. P.; Dooley, K.; Cropek, D. M.; West, A. C.; Banta, S. Rapid Development of New Protein Biosensors Utilizing Peptides Obtained via Phage Display. *PLoS ONE* **2011**, *6* (10), e24948. https://doi.org/10.1371/journal.pone.0024948.
(440) Chatani, S.; P. Nair, D.; N. Bowman, C. Relative Reactivity and Selectivity of Vinyl Sulfones and Acrylates towards the Thiol–Michael Addition Reaction and Polymerization. *Polym. Chem.* **2013**, No. 4, 1048–1055. https://doi.org/10.1039/c2py20826a.
(441) Hiemstra, C.; J. van der Aa, L.; Zhong, Z.; Dijkstra, P.; Feijen, J. Novel in Situ Forming, Degradable Dextran Hydrogels by Michael Addition Chemistry: Synthesis, Rheology, and Degradation. *Macromolecules* **2007**, *40* (4), 1165–1173. https://doi.org/10.1021/ma062468d.
(442) Yu, Y.; Lau, L. C. M.; Lo, A. C.; Chau, Y. Injectable Chemically Crosslinked Hydrogel for the Controlled Release of Bevacizumab in Vitreous: A 6-Month In Vivo Study. *Transl. Vis. Sci. Technol.* **2015**, *4* (2), 5. https://doi.org/10.1167/tvst.4.2.5.
(443) Yan, C.; Pochan, D. J. Rheological Properties of Peptide-Based Hydrogels for Biomedical and Other Applications. *Chem. Soc. Rev.* **2010**, *39* (9), 3528. https://doi.org/10.1039/b919449p.
(444) Zhu, L.; Qiu, J.; Sakai, E. A High Modulus Hydrogel Obtained from Hydrogen Bond Reconstruction and Its Application in Vibration Damper. *RSC Adv.* **2017**, No. 69, 4. https://doi.org/10.1039/c7ra08272j.
(445) Mario Grassi; Gabriele Grassi. Mathematical Modelling and Controlled Drug Delivery: Matrix Systems. *Curr. Drug Deliv.* **2005**, *2* (1), 97–116. https://doi.org/10.2174/1567201052772906.
(446) Kim, S. W.; Bae, Y. H.; Okano, T. Hydrogels: Swelling, Drug Loading, and Release. *Pharm. Res.* **1992**, *9* (3), 283–290. https://doi.org/10.1023/A:1015887213431.
(447) Park, H.; Guo, X.; Temenoff, J. S.; Tabata, Y.; Caplan, A. I.; Kasper, F. K.; Mikos, A. G. Effect of Swelling Ratio of Injectable Hydrogel Composites on Chondrogenic Differentiation of Encapsulated Rabbit Marrow Mesenchymal Stem Cells In Vitro. *Biomacromolecules* **2009**, *10* (3), 541–546. https://doi.org/10.1021/bm801197m.
(448) Katime, I.; Mendizábal, E. Swelling Properties of New Hydrogels Based on the Dimethyl Amino Ethyl Acrylate Methyl Chloride Quaternary Salt with Acrylic Acid and 2-

Methylene Butane-1,4-Dioic Acid Monomers in Aqueous Solutions. *Mater. Sci. Appl.* **2010**, *01* (03), 162–167. https://doi.org/10.4236/msa.2010.13026.

(449) Ritger, P. L.; Peppas, N. A. A Simple Equation for Description of Solute Release I. Fickian and Non-Fickian Release from Non-Swellable Devices in the Form of Slabs, Spheres, Cylinders or Discs. *J. Controlled Release* **1987**, *5* (1), 23–36. https://doi.org/10.1016/0168-3659(87)90034-4.

(450) Anderson, J. M.; Rodriguez, A.; Chang, D. T. Foreign Body Reaction to Biomaterials. *Semin. Immunol.* **2008**, *20* (2), 86–100. https://doi.org/10.1016/j.smim.2007.11.004.

(451) Keselowsky, B. G.; Lewis, J. S. Dendritic Cells in the Host Response to Implanted Materials. *Semin. Immunol.* **2017**, *29*, 33–40. https://doi.org/10.1016/j.smim.2017.04.002.